# Radiation Induced Segregation in High Chromium Ferritic/Martensitic Steels

By

Kevin G. Field

A dissertation submitted in partial fulfilment of the requirements for the degree of

Doctor of Philosophy

(Materials Science)

at the

University of Wisconsin - Madison

2012

Date of final oral examination: 11/9/12

The dissertation is approved by the following members of the Final Oral Committee:

Todd Allen, Associate Professor, Engineering Physics

Jake Blanchard, Professor, Engineering Physics

Paul Voyles, Associate Professor, Materials Science and Engineering

John Perepezko, Professor, Materials Science and Engineering

Dane Morgan, Associate Professor, Materials Science and Engineering

*To my family*

# Acknowledgments

This dissertation would not have come to fruition without the help of many. First, I would like to thank my academic adviser, Dr. Todd Allen for the opportunity to complete this work and the guidance he provided. Secondly, I would like to thank Dr. Kumar Sridharan and Dr. Jeremy Busby for the thoughtful discussions, encouragement, and guidance throughout the process. My thesis committee should also be thanked for their time and support. I would also like to thank my collaborators on the project: Dr. Dane Morgan, Leland Barnard and Dr. Janelle Wharry. I would also like to recognize my professors at Michigan Technological University for providing a strong foundation in materials science.

Much of the work contained within these pages was completed at user facilities or away from the University of Wisconsin. I would like to thank the following people for assisting me while conducting research at their institutions: Dr. Chad Parish, Dr. Ed Kenik, Dr. Jim Bentley, Dr. Greg Lumpkin, Dr. Mark Blackford, Dr. Heather Chichester, Dr. Brandon Miller, Joanna Taylor, Jatu Burns and Dr. Jim Cole. Of those listed, a special note should be made for Dr. Jim Bentley and Dr. Chad Parish. Dr. Jim Bentley served as a mentor through the early stages and developed my practical electron microscopy skills. Dr. Chad Parish has been instrumental in teaching the complexities of analytical electron microscopy. I would also like to thank Paul and Tricia for making me feel at home after a long day of sitting in a dark room taking data at ORNL. Their kindness and gratitude kept me sane through long weeks away from my friends, family, and home.

I would like to acknowledge all my colleagues at the University of Wisconsin. There are too many to list here but a few certainly standout. I would like to thank Kim Kriewaldt for his assistance in the ion beam. I would like to recognize Dr. Alicia Certain and Tyler Gerczak for not only their assistance in the lab but their continuing friendship outside of it. Without their help and support, this work would not have been possible.

Lastly I would like to acknowledge my family for their support. My mother deserves special mention for her years of guidance, patience, support and putting up with raising two boys. Everyday I'm amazed how she handled two boys who can solve complex mathematical equations but for some reason could never figure out the intricate details of completing laundry. I would like to thank my big brother, Chris, for the motivation, guidance, and continuing sibling rivalry. Finally, I would like to thank Beth for being there at start and sticking with me through this adventure.

For those mentioned and those who I may have forgotten, *thank you!*

# Contents

# List of Figures

# List of Tables

# List of Abbreviations and Symbols

| | |
|---|---|
| ADF | Annular Dark Field |
| AES | Auger Electron Spectroscopy |
| APT | Atom Probe Tomography |
| ATR | Advanced Test Reactor |
| BCC | Body Centered Cubic |
| C | Carbon |
| CAES | Center for Advanced Energy Studies |
| CBED | Convergent Beam Electron Diffraction |
| Cr | Chromium |
| CSL | Coincident Site Lattice |
| EBR-II | Experimental Breeder Reactor II |
| EBSD | Electron Back Scatter Diffraction |
| EDM | Electrical Discharge Machining |
| EDS | Energy Dispersive X-Ray Spectroscopy |
| EFPD | Effective Full Power Days |
| EFTEM | Energy Filtered Transmission Electron Microscopy |
| EMSL | Environmental Molecular Sciences Laboratory |
| EP v 1.1 | Euclid's Phantasies, a beta software for indexing Kikuchi patterns |
| F/M | Ferritic/Martensitic |
| FCC | Face Centered Cubic |
| FEG-STEM | Field Emission Gun Scanning Transmission Electron Microscopy |

| | |
|---|---|
| FFT | Fast Fourier Transform |
| FFTF | Fast Flux Test Facility |
| FIB | Focused Ion Beam |
| FWHM | Full Width at Half-Maximum |
| HAGB | High Angle Grain Boundary |
| HIP | Hot Isostatic Pressing |
| IK | Inverse Kirkendall |
| INL | Idaho National Laboratory |
| LAGB | Low Angle Grain Boundary |
| MIBL | University of Michigan Ion Beam Laboratory |
| MIK | Inverse Kirkendall model |
| Mo | Molybdenum |
| MSC | Materials Science Center |
| NEC | National Electrostatics Corporation |
| NF-ODS | Nano-featured Oxide Dispersion Strengthened |
| O | Oxygen |
| ORNL | Oak Ridge National Laboratory |
| PKA | Primary Knock-on Atom |
| PNNL | Pacific Northwest National Laboratory |
| RGB | Red, Green, Blue; standard colors used for image overlay maps |
| RIS | Radiation-Induced Segregation |
| SEM | Scanning Electron Microscopy |

| | |
|---|---|
| ShaRE | Shared Research Equipment User Facility |
| SiC | Silicon Carbide |
| SNICS | Source of Negative Ions via Cesium Sputtering |
| SRIM | Stopping Range of Ion in Matter |
| STEM | Scanning Transmission Electron Microscopy |
| TEM | Transmission Electron Microscopy |
| Ti | Titanium |
| TIA | TEM Imaging and Analysis software distributed by FEI |
| UW-IBL | University of Wisconsin Ion Beam Laboratory |
| W | Tungsten |
| Y | Yttrium |
| $\alpha$ | Thermodynamic factor |
| $\alpha_{tilt}$ | Grain boundary tilt to the incident electron probe |
| $\delta$ | Interplanar distance |
| $\delta$ | Thickness of a grain boundary |
| $\Delta\theta$ | Change in misorientation angle to the reference CSL |
| $\gamma_b$ | Grain boundary energy per unit area of a boundary |
| $\gamma_b^{CSL}$ | Grain boundary energy of a reference coincident site lattice |
| $\gamma_{Cr}$ | Chromium activity coefficient |
| $\gamma_{Fe}$ | Iron activity coefficient |
| $\varepsilon$ | Damage efficiency |
| $\Phi$ | Incident particle flux |

| | |
|---|---|
| $\mu$ | Shear modulus |
| $\nu$ | Poisson ratio |
| $\nu(T)$ | Number of displaced atoms from a collision |
| $\nu_m$ | Maximum deviation from the exact CSL in degrees |
| $\nu_o$ | Attempt frequency |
| $\nu_o$ | Upper threshold misorientation for a low angle grain boundary |
| $\Omega$ | Average alloy atomic volume |
| $\phi(E_i)$ | Energy-dependent particle flux |
| $\rho$ | Specimen density |
| $\rho_D$ | Dislocation density |
| $\sigma(E_i, T)$ | Probability of an incident particle imparting energy into a struck lattice atom |
| $\sigma_D(E_i)$ | Energy dependent displacement cross section |
| $\theta$ | Misorientation angle |
| $A$ | Mean atomic weight |
| $a$ | Lattice parameter |
| $b$ | Burgers vector |
| $b_B$ | Secondary grain boundary Burgers vector |
| $C$ | Elemental concentration in weight percent or atomic percent |
| $C_j$ | Site fraction |
| $C_k$ | Site fraction |
| $C_x$ | Solute concentration |
| $d$ | Defect type in a grain boundary |

| | |
|---|---|
| $d$ | Diffusivity of an element within an alloy |
| $d$ | Dislocation spacing |
| $d_0$ | Diffusivity pre-exponential factor |
| $d^{i/v}_{Cr/Fe}$ | Partial diffusion coefficient of specific element-defect |
| $d^{v/i,gb}_{Fe/Cr,0}$ | Pre-exponential factor for grain boundary diffusion of a specific species |
| $d^{v/i,gb}_{Fe/Cr}$ | Effective grain boundary diffusivity coefficient |
| $d_{GB}$ | Secondary grain boundary spacing on a grain boundary |
| $D_{SRIM}$ | Displaced lattice atoms per incident particle per unit length traveled as calculated using SRIM |
| $dpa$ | Displacements per atom |
| $E$ | Electron accelerating voltage in volts |
| $E^{k,d}_a$ | Migration activation energy of a specific solute and defect type |
| $E_c$ | Energy of a dislocation core |
| $E^b_c$ | Energy of a secondary grain boundary dislocation core |
| $E_d$ | Displacement energy for a lattice atom |
| $E^{v/i,gb}_{Fe/Cr}$ | Activation energy for grain boundary diffusion of a specific species |
| $E_i$ | Incident particle energy |
| $f^{GB}_d$ | Correlation factor for a specific defect type |
| $g_d$ | Dimensionless constant based on atomic structure |
| $g_o$ | Geometrical parameter based on grain boundary structure |
| $I$ | Integrated characterisitic X-ray intensity |
| $I$ | Total electron flux in a incident electron probe |

| | |
|---|---|
| $J_j$ | Flux of specific species |
| $J^0_{v,i}$ | Flux of defects within the interaction distance of a grain boundary |
| $J^1_{v,i}$ | Flux of defects outside the interaction distance of a grain boundary |
| $J^{gb}_{v,i}$ | Flux of defects within a grain boundary |
| $k$ | Boltzmann factor |
| $k$ | Component type |
| $K_o$ | Displacement rate |
| $K_o$ | Dose rate in dpa/s |
| $k_{CrFe}$ | Correlation factor for Cr and Fe, also known as a k-factor |
| $M$ | Particle mass |
| $m$ | Multiple sink correction factor |
| $M_f$ | Martensite finish |
| $M_s$ | Martensite start |
| $N$ | Lattice atom density |
| $N$ | Number of counts in an EDS peak above background |
| $P_{input}$ | Model input variable used for senstivity analysis |
| $R$ | A 3 x 3 rotation matrix which describes the rotation and axis to bring two rotation matrices into coincidence |
| $r$ | Measured full width at half maximum of an incident electron probe |
| $R_d$ | Damage rate |
| $R_{ID}$ | Rate of vacancies loss to dislocations |
| $r_{rD}$ | Radius capture of defect species |

| | |
|---|---|
| $R_R$ | Rate coefficient for recombination of vacancies and interstitials |
| $R_{VD}$ | Rate of vacancies loss to dislocations |
| $S$ | Sink strength |
| $S$ | Standard deviation |
| $S_X^P$ | Normalized significance of each input parameter |
| $T$ | Recoil energy |
| $T$ | Temperature |
| $t$ | Specimen thickness |
| $U$ | A 3 x 3 rotation matrix |
| $u$ | Misorientation axis |
| $X$ | Model-calculated output used for senstivity analysis |
| $Z$ | Coordination number of the crystal structure |
| $Z$ | Mean atomic number |
| $z$ | Sink capture efficiency |
| $Z_{dD}$ | Bias factor for point defect loss to dislocations |

# Chapter 1

# Introduction

Instabilities in fossil fuel commodities and their production of green house gases has pushed investigations into new and existing energy technologies which have a stable market and significantly reduce carbon emissions. Nuclear energy is one of these technologies. Currently, the global nuclear reactor fleet produces 20% of the world's electricity with limited production of green-house gases [1]. As the global appetite for electricity keeps increasing, so too will the demand for nuclear energy. To meet these demands, a road map for nuclear energy has been developed [2]. The road map stresses new goals for nuclear power systems including increased thermal efficiency by utilizing high-temperature reactors, improved fuels and coolants, utilization of process heat for industrial applications, improved safety, reduced waste, and increases in proliferation resistance.

The current generation of commercial light water nuclear reactors cannot satisfy these goals without major reconfigurations. Due to this, new nuclear reactor designs are being developed. These new reactor designs will operate at higher temperature, have more intense radiation fields, and have more corrosive environments over the current global fleet of nuclear reactors [2]. Core internals, including cladding and structural components, must use materials capable of operating within these very aggressive environments. Many conventional materials, including ones already in-service in light water reactors, will not meet the requirements set by the new reactor designs. The result is many non-traditional materials have become interesting candidate materials for new advanced fission and fusion nuclear reactor designs.

One candidate material class is high chromium ferritic/martensitic (F/M) steels. The high Cr F/M steel class is broad but most alloys share some common characteristics and heritage. Most

of the F/M steels for nuclear applications were developed by the fossil fuel industry for high temperature applications and then adopted and adapted by the nuclear industry. High Cr F/M steels are typically Cr-Mo steels with a body-centered-cubic (BCC) crystal structure and 9-12 % Cr, 1-2 % Mo, 0.1-.2 % C (in weight percent) and minor element additions. A summary of several of the candidate F/M steels and their compositions are in Table 1.1 [3]. These steels have the high temperature strength and thermal properties to resist failure under thermal stresses [3]. The creep strength of F/M steels has continuously improved over the past several decades and most recently seen a significant increase with the development of nano-featured oxide dispersion strengthen (NF-ODS) steels. Beyond their excellent elevated temperature mechanical properties, F/M steels main advantage for nuclear applications is their resistance to swelling compared to austenitic stainless steels.

The vast majority of advanced F/M steels research comes from research conducted by the fossil fuel industry over the last 40-50 years. Due to this, a comprehensive materials properties database exists for F/M steels in the unirradiated state within the available literature. The same cannot be said about the irradiated state [3]. F/M steels were first widely used in the United States in fast fission experimental reactors, including the Fast Flux Test Facility (FFTF) and Experimental Breeder Reactor II (EBR-II), in the 1970s. The void swelling resistance was an attractive property in these applications as these reactors pushed the obtainable dose above the acceptable total volumetric expansion of core internals comprised of austenitic stainless steels. In the late 1970s, F/M steels were also considered for fusion reactor programs. As these programs started to decline in the 1990s, so did the motivation to continue research on irradiated F/M steels. Recently, renewed interest has lead to continuing the original research conducted in the 1970s and 1980s on steels irradiated within these programs. Unfortunately, the result is a non-comprehensive database on the performance of F/M steels within a nuclear reactor environment.

Nowhere are the gaps in understanding irradiated F/M steels more evident than understanding the primary mechanism for radiation-induced segregation (RIS). RIS occurs during irradiation

due to certain alloying elements coupling with the vacancy and/or interstitial flux to a defect sink leading to segregation at the sink. The majority of RIS studies have been carried out on austenitic stainless steels with a face-centered-cubic (FCC) crystal structure. The result of these studies have been reviewed in several publications and textbooks and show RIS can significantly change the distribution of alloying elements within the microstructure leading to microstructural variations and precipitation of embrittling phases [4–6]. As a result, understanding RIS in F/M steels has seen increased focus to develop the same understanding in the F/M steel system as austenitic stainless steels to determine if embrittlement can occur in F/M steels during nuclear reactor service conditions.

The lack of continuity in conducting RIS studies in F/M steels and advances in materials science over the past 40 decades has led to a highly disjointed database. Most importantly, previous work lacks details on the segregation behavior of Cr, a matrix strengthening contributor and corrosion inhibitor in high Cr F/M steels [7]. A review of fifteen publications indicated Cr can enrich or deplete at interfaces in F/M steels but only hypothesized an answer to why [8]. The studies reviewed and ones not reviewed were performed with a wide range of doses, temperatures and irradiation species. Some of the early quantitative analysis were conducted using Auger Electron Spectroscopy (AES), which has been demonstrated to overestimate average segregation levels due to fracture occurring at embrittled boundaries which tend have higher levels of segregation [9]. Other studies were conducted on early Scanning Transmission Electron Microscopes (STEM) with poor spatial resolution. More recent studies have utilized Field Emission Gun Scanning Transmission Electron Microscopy (FEG-STEM) coupled with Energy Dispersive X-Ray Spectroscopy (EDS) or Atom Probe Tomography (APT) to provide more quantitative information on the Cr behavior in irradiated F/M steels. Furthermore, observations were conducted on a wide range of microstructural features including prior austenite grain boundaries, martensite lath boundaries, across precipitate interfaces, dislocation loops, across voids or some failed to report the interface investigated. Models suffer from having limited experimental data to benchmark against and seem to lack sufficient detail to capture the complexity of RIS in F/M steels.

This work seeks to understand the primary mechanism of RIS in F/M steels at grain boundaries and makes the first steps towards removing the ambiguity of RIS in F/M steels. A systematic study was conducted using a model 9 wt. % Cr model F/M steel and a complex nano-featured oxide dispersion strengthened steel with modern materials characterization techniques to accomplish the goal of furthering the state of the field. Both microstructural variations and irradiation conditions were explored including influences on RIS from grain boundary structure, trends with irradiation temperature, trends with increasing irradiation dose, the influence of microstructure and the influence of alloying additions.

Ion irradiations have been demonstrated to simulate the RIS response created by neutrons [10]. Ion irradiations have the added benefit of being able to achieve significantly higher dose rates, precise temperature control, and leaves specimens with little to no residual activity following irradiation. Proton and heavy ion irradiations are an excellent method to fully characterize the RIS response over a wide range of irradiation conditions. Given this, a need still exists to confirm findings seen from ion irradiations with neutron irradiated F/M steel specimens. The result is an extensive study using ion irradiations which is compared with a select neutron irradiation experiment to assure the knowledge gained on ion induced RIS can be transferred for use in understanding neutron induced RIS in F/M steels.

Limited studies have been conducted on how grain boundary structure alters the capture and annihilation kinetics of radiation induced point defects and how this effects the solute segregation at grain boundaries in F/M steels. Investigating different grain boundary structures provides a method to determine how variations in the interfacial structure of grain boundaries alters the point defect kinetics at grain boundaries and ultimately how this affects the sink efficiency of the boundary. Within the irradiation campaigns, different grain boundary structures were observed to determine if structure is a significant factor in the RIS response of F/M steels.

A systematic proton irradiation campaign was conducted to determine the effects of dose (effective radiation damage accumulation) and temperature on the same model F/M steel heat. Increasing dose creates a higher concentration of point defects within the matrix, provides

more time for defect diffusion if the dose rate is held constant, and should increase the magnitude of segregation to grain boundaries given other irradiation induced microstructural features do not influence the point defect migration until steady state conditions are achieved. Varying the irradiation temperature alters the diffusion rate of point defect solute complexes migrating to the boundary and assists in determining if vacancy and/or interstitial mediated mechanisms are dominant for RIS in F/M steels. Comparing experiments with modeling results, where the model assumes a specific segregation mechanism, allows for the primary mechanism of RIS to be further confirmed. Here, the experimental observations are compared to recent theoretical work to expand the knowledge of RIS in F/M steels. All variables in the proton irradiations are compared including grain boundary structure, dose, and temperature. The same heat of the model F/M steel was also irradiated using neutrons at the Advanced Test Reactor National Scientific User Facility (ATR-NSUF) at similar doses and temperatures to extend the knowledge gained from ion irradiations to real world reactor environments.

The newest class of F/M steels includes nano-sized oxide particles embedded in the matrix which increase the high temperature creep strength of the material. Recent work was completed to understand the stability of these nanoclusters under irradiation [11] but the influence of nanoclusters on the RIS response has not been investigated. A systematic heavy ion irradiation campaign was conducted to determine the affects of nanoclusters on the RIS response in F/M steel, as well the temperature dependence of RIS in the NF-ODS steel. High doses and dose rates were utilized in an attempt to create unstable nanoclusters and understand the performance of the steel under extreme environments. The theoretical work conducted and the experimental studies on the two alloy systems serve as the critical first steps to a fully predictive model and thorough understanding of RIS in F/M steels.

In Chapter 2 F/M steel metallurgy, grain boundary structure, point defect interactions at grain boundaries, precipitate stability under irradiation and RIS in F/M steels, are reviewed. The proposed RIS models and experiments performed on F/M steels are presented and contrasted to the state of knowledge of RIS in austenitic stainless steels. Chapter 3 outlines the experimental

procedure used to irradiate the 9 wt. % Cr model F/M steel and the NF-ODS steel and how the measurement of RIS was performed. In Chapter 4 the results of RIS at grain boundaries in the both F/M steels are given. Chapter 5 discusses and analyzes the RIS data and relates the data to modeling work. Chapter 6 presents conclusions and future work needed to fully close the knowledge gap on F/M steels RIS response.

Table 1.1: Compositions of common commercial high Cr F/M steels for nuclear applications. Adapted from [3].

| Steel | C | Si | Mn | Cr | Mo | W | V | Nb | B | N | Other |
|---|---|---|---|---|---|---|---|---|---|---|---|
| 9Cr-1Mo (T9) | 0.12 | 0.6 | 0.45 | 9.0 | 1.0 | | | | | | |
| Mod 9Cr-1Mo (T91) | 0.10 | 0.4 | 0.40 | 9.0 | 1.0 | | 0.2 | 0.08 | | 0.05 | |
| E911 | 0.11 | 0.4 | 0.40 | 9.0 | 1.0 | 1.0 | 0.20 | 0.08 | | 0.07 | |
| NF616 (T92) | 0.07 | 0.06 | 0.45 | 9.0 | 0.50 | 1.8 | 0.20 | 0.05 | 0.004 | 0.06 | |
| 12Cr-1MoV (HT91) | 0.20 | 0.4 | 0.60 | 12.0 | 1.0 | | 0.25 | | | | 0.5 Ni |
| 12Cr-1MoWV (HT9) | 0.20 | 0.4 | 0.60 | 12.0 | 1.0 | 0.50 | 0.25 | | | | 0.5 Ni |
| HCM12 | 0.10 | 0.3 | 0.55 | 12.0 | 1.0 | 1.0 | 0.25 | 0.05 | | 0.03 | |
| TB12 | 0.10 | 0.06 | 0.50 | 12.0 | 0.50 | 1.8 | 0.20 | 0.05 | 0.004 | 0.06 | 0.1 Ni |
| TB12M | 0.13 | 0.25 | 0.50 | 11.0 | 0.50 | 1.8 | 0.20 | 0.06 | | 0.06 | 1.0 Ni |
| HCM12A (T122) | 0.11 | 0.1 | 0.60 | 12.0 | 0.40 | 2.0 | 0.25 | 0.05 | 0.003 | 0.06 | 1.0 Cu, 0.3 Ni |
| NF12 | 0.08 | 0.2 | 0.50 | 11.0 | 0.20 | 2.6 | 0.20 | 0.07 | 0.004 | 0.05 | 2.5 Co |

# Chapter 2

# Background

## 2.1 High Chromium Ferritic/Martensitic (F/M) Steels Basic Metallurgy

### 2.1.1 General Overview

High chromium F/M steels can be fully ferritic, fully martensitic, a duplex of $\delta$-ferrite and martensite, or a triplex of $\delta$-ferrite, martensite, and retained austenite. Altering the chemistry and/or the heat treatment of the steel results in the different microstructures. These microstructures can be custom tailored for a desired balance of strength, ductility, and toughness. The constitution of the steel after cooling can be predicted by knowing the composition and the use of a Schaeffler-Schneider diagram in Figure 2.1 [12]. Alloying elements are determined to be either Ni or Cr equivalents and assigned a biasing factor which is used to determine the final structure using the diagram [12]. Chemistry also controls the martensite start ($M_s$) and martensite finish ($M_f$) temperatures. For modern high Cr steels, the chemistry is controlled to maintain the $M_s$ temperature above room temperature to prevent the formation of retained austenite. A fully martensitic structure is desired as retained austenite decreases strength. The fully austenitic structure is cooled to form the martensitic structure. Upon quenching the parent austenite grain breaks down to several packets. These packets are further subdivided by laths which are characterized as being long narrow grains with widths in the sub-micrometer range and lengths several micrometers long [13]. Martensite laths are the finest grain structure in martensite and can easily be observed using transmission electron microscopy (TEM). Figure

2.2 is a schematic of the normal grain structure of a fully martensitic steel while Figure 2.3 is a bright field TEM micrograph of a fully martensitic lath structure. The crystallographic orientation difference between laths within the same packet boundary tend to be small due to their orientation relationship during the transformation of the parent austenite grain into the lath structure [14]. Lath structures contain dislocation networks, coarse $M_{23}C_6$ precipitates on prior austenite grain boundaries and finer precipitates intra-lath and on lath boundaries which is illustrated in Figure 2.2 as well [3]. $M_2X$ precipitates with elevated chromium content also precipitate out within the martensite laths. The morphology and distribution of precipitates and dislocations greatly affects the dislocation pinning characteristics during an applied stress. The result is a highly complex, highly engineered material where chemistry and heat treatments are optimized to obtain the desired constitution and structure, increase the stability of the martensite dislocation structure, and maximize the solid solution and precipitation hardening [13].

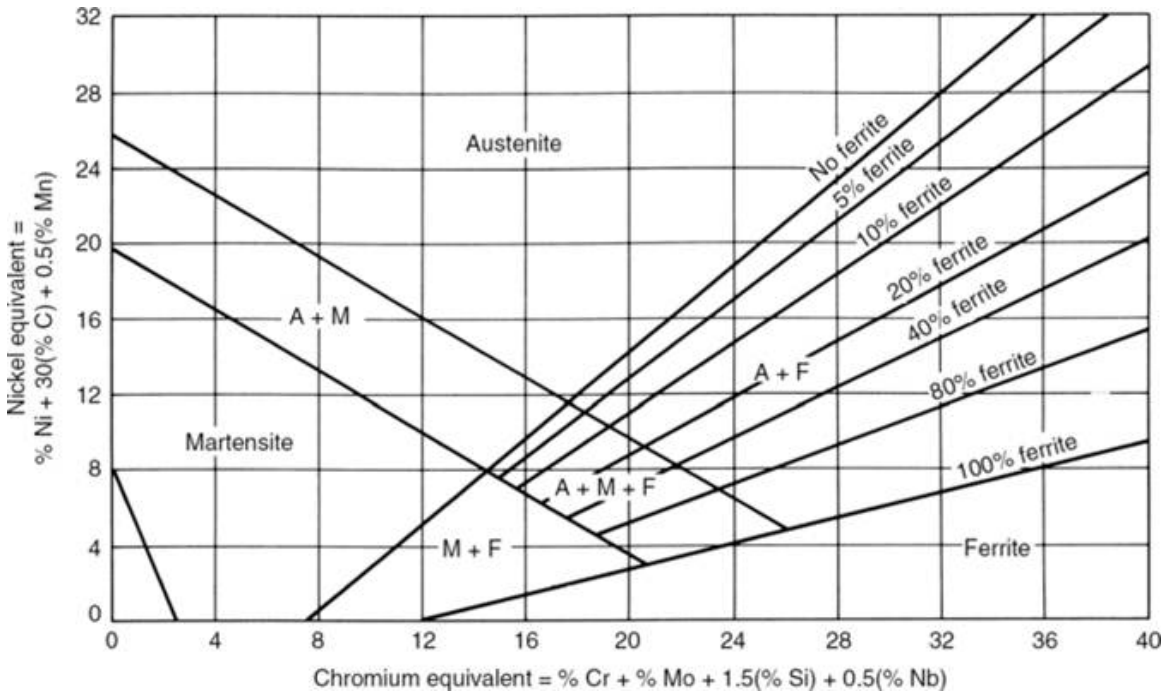


Figure 2.1: Schaeffler-Schneider diagram [12].

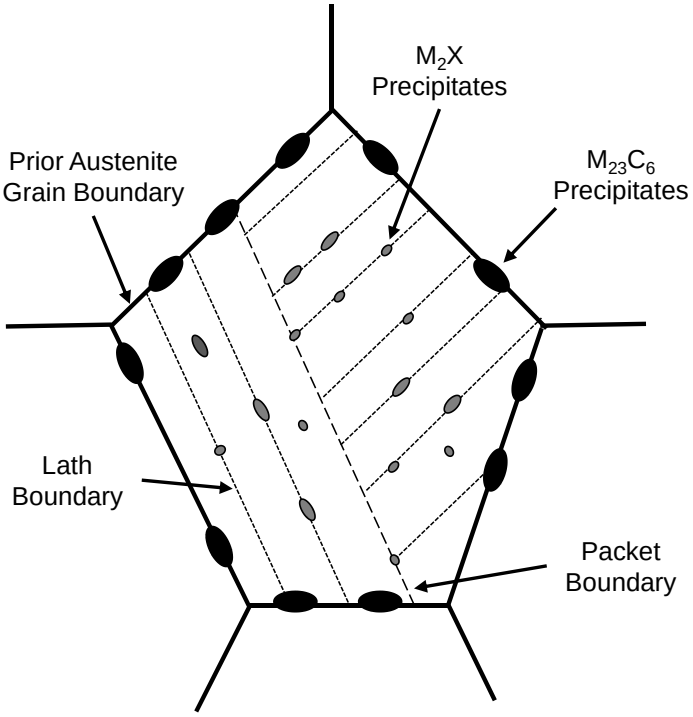


Figure 2.2: Typical microstructure of fully martensitic high chromium ferritic/martensitic steel. Microstructure contains different grain boundary types, multiple precipitate phases, and a high dislocation density. Schematic not to scale.

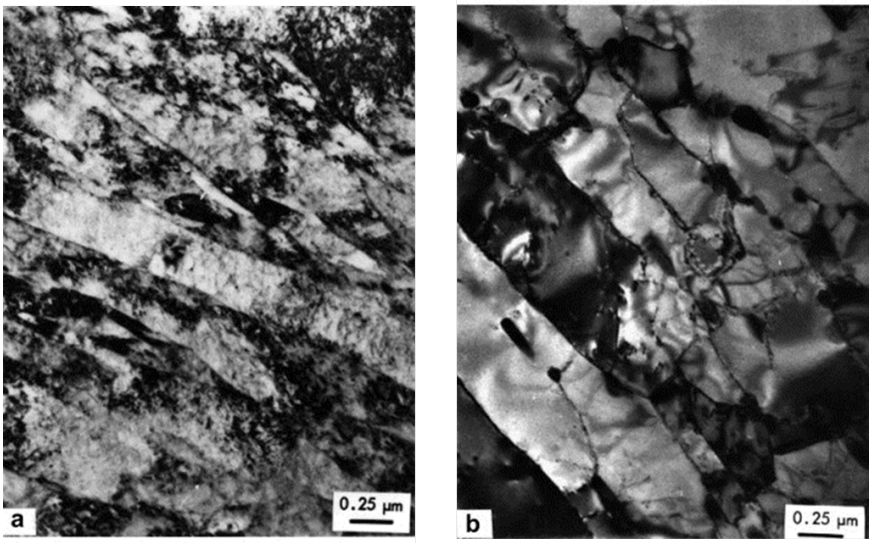


Figure 2.3: TEM bright image of HT9 (12Cr-1MoWV) in the a) normalized and b) normalized and tempered conditions [3].

### 2.1.2 Nano-featured Oxide Dispersion Strengthened (NF-ODS) F/M steel metallurgy

Nano-featured oxide dispersion strengthened (NF-ODS) steels are a complex alloy system which is typically fully ferritic or martensitic with a dispersion of nano-sized complex oxides within the matrix. These complex oxides are typically referred to as nanoclusters. These nanoclusters are a non-equilibrium phase in the BCC Fe matrix but remain stable even at high temperatures [15]. The fine dispersion of nanoclusters within the Fe-matrix serve as point defect annihilation sites and pinning sites for dislocation motion and serve to improve the high-temperature tensile and thermal creep properties over more traditional F/M steels [16–19]. An electron micrograph series, which shows the beneficial nanoclusters within the steel matrix, is presented in Figure 2.4 [20].

Most NF-ODS steels follow the same mechanical alloying fabrication route as seen in Figure 2.5 [21]. In the mechanical alloying step, the yttria is dissolved in the ferritic matrix to form new oxides during the subsequent processing steps. Ti additions reduce the cluster size and decreases cluster spacing within a NF-ODS steel. Y, Ti and O agglomerate during the hot extrusion processing step to form the small nanoclusters. The mechanical alloying and powder metallurgy technique lends to a fine grain ferritic microstructure as well as the dispersion of nanoclusters throughout the BCC Fe matrix.

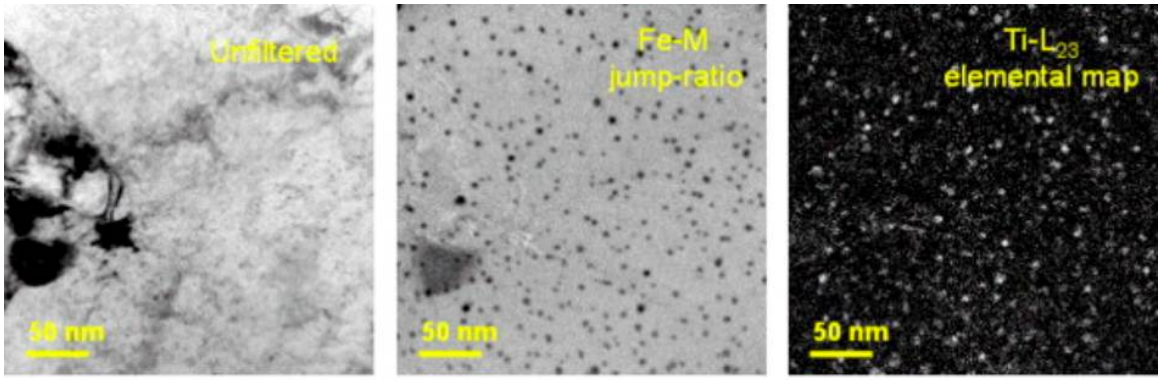


Figure 2.4: Energy filtered transmission electron micrograph (EFTEM) series where regions of Fe depletion (dark regions in Fe-M jump ratio map) and Ti enrichment (bright regions in $Ti - L_{23}$ element map) shows nanoclusters embedded in steel matrix (unfiltered map) [15].

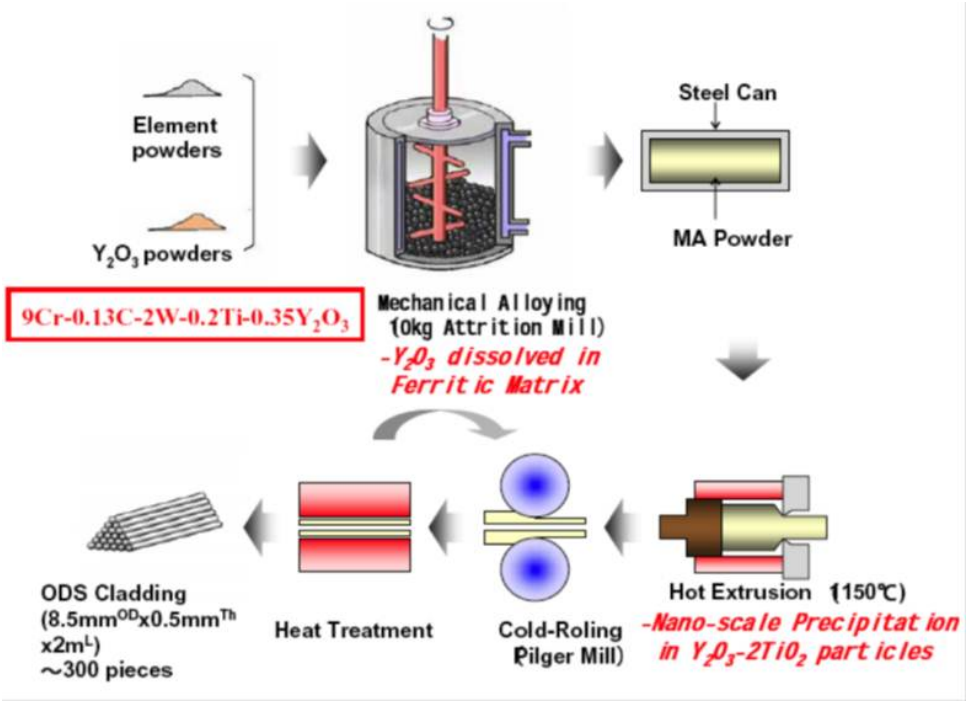


Figure 2.5: Standard fabrication process for nano-featured ODS steel cladding. Hot isostatic pressing (HIP) can be substituted for hot extrusion [21].

## 2.2 Atomic Structure and Properties of Grain Boundaries

Grain boundaries are a major microstructural feature in polycrystalline metals. Grain boundaries can dictate the properties of many polycrystalline metals including corrosion resistance, fracture, recrystallization, and diffusion behavior [22–24]. A grain boundary is the region where the atomic structure of a material is disordered due to the intersection of two grains. The structure, or the amount of atomic disorder, at the grain boundary is dependent on the crystal orientations of the grains which intersect to form the grain boundary.

Two general types of grain boundaries exist: a twist boundary and a tilt boundary. Figure 2.11 shows schematically a twist and tilt boundary. A twist boundary is described as when two grains are rotated about the normal to the boundary, resulting in only screw dislocations comprising the boundary. A tilt boundary is described by rotating the grains about an axis in the plane of the boundary, resulting in an array of edge dislocations, which comprise the boundary. Most grain boundaries have mixed characteristics and contain both twist and tilt characteristics. An arbitrary grain boundary can have five degrees of freedom. Two degrees of freedom arise from the plane of the boundary rotating in respect to the two grains, two more from the axis of rotation and one for the rotation angle for the second grain.

A full five parameter determination of a grain boundary requires knowledge of the boundary in 3-dimensions which requires techniques such as serial sectioning via focused ion beam or systematic polishing [25]. These techniques are time intensive and typically a one or three parameter characterization of the boundary is sufficient to characterize the boundary. A known exception is characterizing twins where grain boundary plane is needed to characterize the boundary. The misorientation axis and angle is a common classification scheme used to describe three out of the five parameters. Grain boundaries can be classified as low angle grain boundaries (LAGB), general high angle grain boundaries (HAGB), or a special grain boundaries by determining the misorientation angle and axis. A LAGB is typically classified as a boundary with a misorientation angle ($\theta$) less than ~15° while a general HAGB is classified

as having a misorientation higher than ~15º. A special grain boundary is a HAGB having a specific axis/angle pair identified to having higher than normal coherency at the boundary compared to general HAGBs and is typically identified using the coincident site lattice (CSL) convention. LAGB, general HAGB and special grain boundaries exhibit different behaviors, including grain boundary energy, due to variations in their local structure [26].

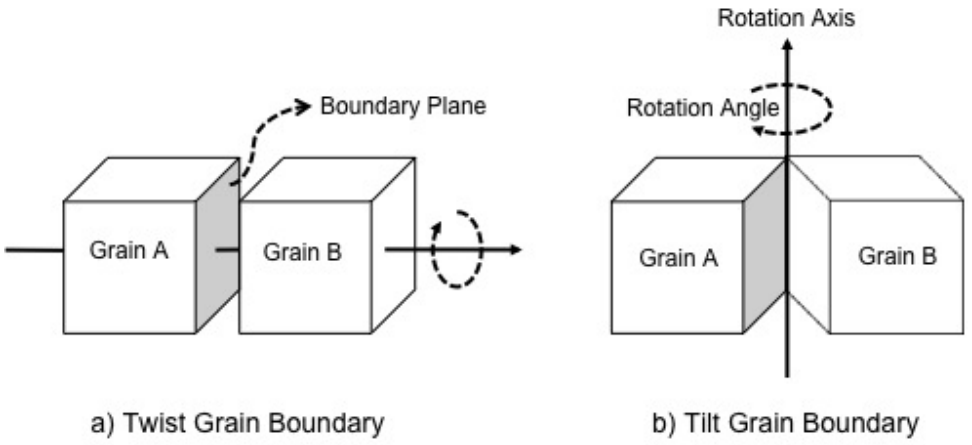


Figure 2.6: Schematic representation of a) twist boundary and b) tilt boundary.

### 2.2.1 Low Angle Grain Boundaries

A low angle grain boundary (LAGB) consists of an array of dislocations to accommodate the misfit between two grains with a misorientation below 15º. A LAGB can consist of a twist, tilt, or mixed character. The cores of the dislocations in a LAGB do not overlap. The dislocation spacing ($d$) at a grain boundary can be approximated by:

$$\frac{b}{d} = 2\sin\frac{\theta}{2} \simeq \theta \tag{2.1}$$

where $b$ is the Burgers vector and $\theta$ is the misorientation angle between two grains [27]. An increase in misorientation between the two grains results in an increased density of dislocations on the boundary. As the misorientation angle approaches 15º, the cores begin to overlap resulting in HAGBs. LAGBs have highly localized regions of disorder and are generally characterized as having a good degree of 'fit' or coherency at the boundary. Due to LAGB being modeled as an array of dislocations, the free energy of the LAGB can be determined using dislocation theory. The Read-Shockley model states the energy ($\gamma_b$) per unit area of a boundary varies with the misorientation angle ($\theta < 15º$) according to:

$$\gamma_b = \theta \left( \frac{E_c}{b} - \frac{\mu b}{4\pi (1-\nu)} \cdot \ln \theta \right) \tag{2.2}$$

where $\theta$ is the misorientation angle, $E_c$ is the energy of the dislocation core, $b$ is the Burgers vector, $\mu$ is the shear modulus, and $\nu$ is Poisson ratio [27]. The fit of the Read-Shockley model to experimental data is illustrated in Figure 2.7. The model only applies to boundaries where the dislocation cores are discrete. As the cores begin to overlap the model is insufficient and the boundaries begin to exhibit HAGB behavior. The transition between LAGBs and HAGBs exists at a misorientation angle between 10º to 15º.

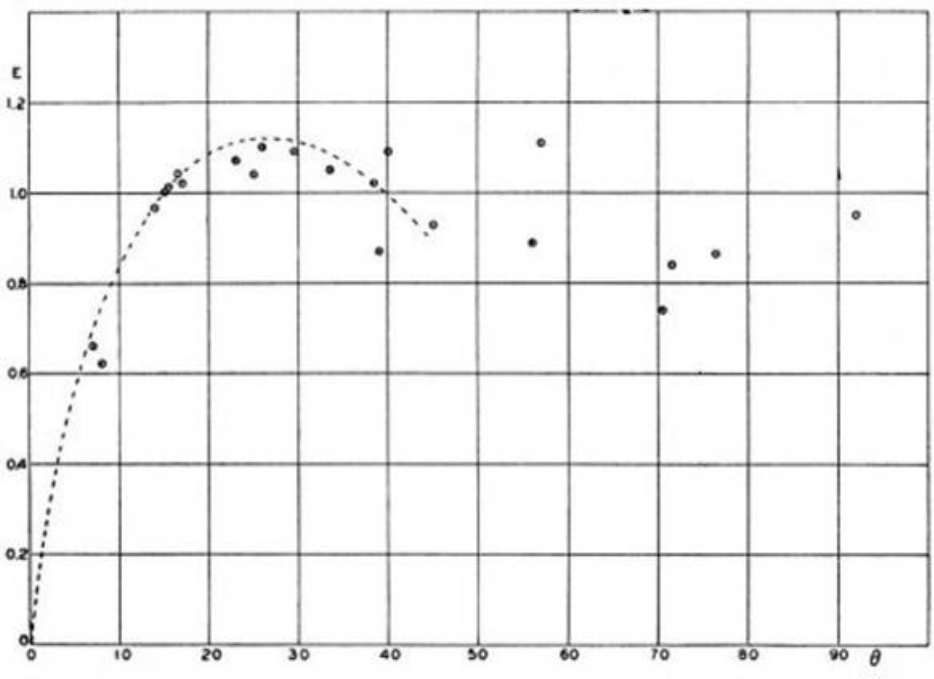


Figure 2.7: Comparison between model and experimental relative grain boundary energies of [100] tilt boundaries versus misorientation angle in Fe-Si [27].

## 2.2.2 High Angle Grain Boundaries

### 2.2.2.1 Coincident Site Lattice Grain Boundaries

A high angle grain boundary (HAGB) is classified as a boundary with a misorientation angle greater than 15º, and the dislocation cores in the grain boundary are no longer discrete. Overlapping of dislocation cores leads to Eq. 2.2 no longer being applicable. The current understanding of HAGB structure arises from geometrical concepts based on those laid out for LAGBs. For HAGBs it is assumed the material will maintain atomic positions across the grain boundary which coincides with ideal positions of both adjacent crystal lattice sites. This creates a new theoretical lattice, with the points which coincide called coincident sites and the

new lattice a coincidence site lattice or CSL. The concept of coincidence between two grains is illustrated in Figure 2.8. For cubic materials, the crystal lattice is periodic and therefore the CSL is also periodic. The unit cell for the CSL is larger than the unit cell of the crystal lattice. To quantify the density of coincidence sites we define [26]:

$$\Sigma = \frac{Number\ of\ coincidence\ sites\ in\ an\ elementary\ cell}{Total\ number\ of\ all\ lattice\ sites\ in\ an\ elementary\ cell}. \tag{2.3}$$

Grain boundaries where the grain orientations lead to a high density of coincidence sites are low $\Sigma$ CSL boundaries, also known as special boundaries. The axis/angle pairs which correspond to special grain boundaries for $\Sigma < 30$ is given in Table 2.1 [28]. It can be seen in Table 2.1 that the CSL occurs only at specific axis/angle pairs and is not continuous as a function of misorientation angle. Grain boundaries which do not fit specific CSL orientations within a certain degree of tolerance are considered a general HAGB. The most commonly used threshold for acceptable tolerance away from the CSL reference structure is the Brandon criterion [29]:

$$v_m = v_o \Sigma^{-\frac{1}{2}} \tag{2.4}$$

where $v_m$ is the maximum deviation from the exact CSL in degrees and $v_o$ is a proportionality constant based on the upper threshold misorientation for a low angle grain boundary, typically 15º. The Brandon criterion implies a low-angle grain boundary can be described as $\Sigma 1$. Use of the CSL convention, the Brandon criterion (Eq. 2.4), and the Read-Shockley relationship (Eq. 2.1) the highest possible density of dislocations in an exact CSL boundary can be calculated using:

$$\frac{b}{d} = v_m = v_o \Sigma^{-\frac{1}{2}}. \tag{2.5}$$

Therefore, the density of dislocations which can be accommodated in a CSL is directly related to its periodicity [25].

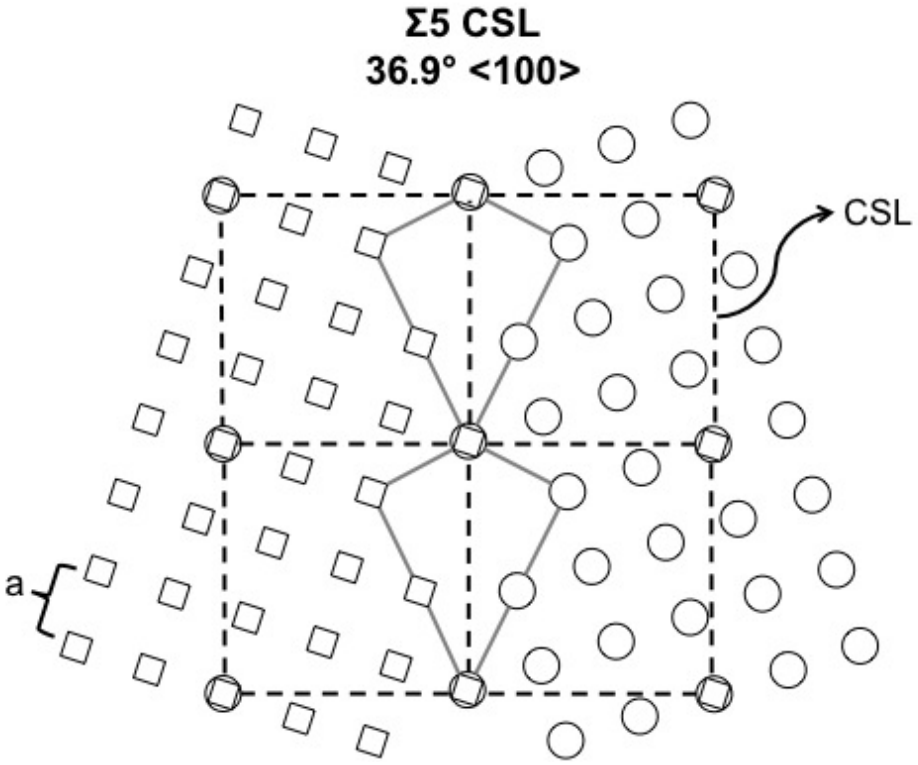


Figure 2.8: Schematic showing the coincidence site lattice (CSL) and structure of a $\Sigma = 5$ CSL grain boundary.

Table 2.1: Axis/Angle pair and twinning planes for cubic CSL up to $\Sigma \leq 30$ [29].

| $\Sigma$ | Twinning Planes | $\theta_{misorientation}$ | Axis | Distinct Forms |
|---|---|---|---|---|
| 1 | {100} and {110} | 0º | any | 1 |
| 3 | {111} and {211} | 60º | <111> | 4 |
| 5 | {210} and {310} | 36.87º | <100> | 6 |
| 7 | {321} | 38.21º | <111> | 8 |
| 9 | {221} and {411} | 38.94º | <110> | 12 |
| 11 | {311} and {332} | 50.48º | <110> | 12 |
| 13a | {320} and {510} | 22.62º | <100> | 6 |
| 13b | {431} | 27.80º | <111> | 8 |
| 15 | {521} | 48.19º | <210> | 24 |
| 17a | {410} and {530} | 28.07º | <100> | 6 |
| 17b | {322} and {433} | 61.93º | <221> | 12 |
| 19a | {331} and {611} | 26.53º | <110> | 12 |
| 19b | {532} | 46.83º | <111> | 8 |
| 21a | {541} | 21.79º | <111> | 8 |
| 21b | {421} | 44.40º | <211> | 24 |
| 23 | {631} | 40.45º | <311> | 24 |
| 25a | {430} and {710} | 16.25º | <100> | 6 |
| 25b | {543} | 51.68º | <331> | 24 |
| 27a | {511} and {552} | 31.58º | <110> | 12 |
| 27b | {721} | 35.42º | <210> | 24 |
| 29a | {520} and {730} | 43.61º | <100> | 6 |
| 29b | {432} | 46.39º | <221> | 24 |

#### 2.2.2.2 General High Angle Grain Boundaries

For general HAGBs the long range coincidence at the grain boundary is lost. To minimize the free energy at the boundary it is assumed crystals will utilize dislocations to try to maintain ideal fit at general HAGBs. These dislocations are called secondary grain boundary dislocations (SGBDs). The distinction between primary grain boundary dislocations and SGBDs is primary grain boundary dislocations are crystal lattice dislocations with periodic arrangement and a Burgers vector corresponding to the crystal lattice while SGBDs are confined to grain boundaries and have Burgers vectors corresponding to a shift in the local CSL. SGBDs have

Burgers vectors much smaller than that of primary grain boundary dislocations and displace the CSL. Just as primary dislocations serve to accommodate misorientation of a perfect crystal in a LAGB, SGBDs serve to compensate an orientation difference to the CSL while still conserving the CSL. Therefore, the larger the misorientation to an exact coincidence rotation, the higher density of SGBDs exists on the grain boundary as given by [27]:

$$d_{GB} = \frac{b_B}{\Delta\theta} \tag{2.6}$$

where $b_B$ is the SGBD Burgers vector which is much smaller than primary dislocation burgers vectors, $\Delta\theta$ is the change in misorientation angle to the reference CSL and $d_{GB}$ is the SGBD spacing on the grain boundary. Eq. 2.2 can be modified to accommodate the SGBD structure and the energy of a periodic SGBD arrangement is given as:

$$\gamma_b = \gamma_b^{CSL} + \Delta\theta \left( \frac{E_c^b}{b_B} - \frac{\mu b_B}{4\pi(1-\nu)} \cdot \ln\Delta\theta \right) \tag{2.7}$$

where $\gamma_b^{CSL}$ is the grain boundary energy of the reference CSL and $E_c^b$ is the energy of the SGBD core [22]. When the grain boundary reaches the exact orientation of a reference CSL structure Eq. 2.7 becomes $\gamma_b = \gamma_b^{CSL}$. When the grain boundary misorientation angle does not meet the exact CSL orientation the energy of the boundary increases depending on the distance away from the reference misorientation. The result is distinct cusps in the grain boundary energy plots at specific CSL orientations while maintaining the near asymptotic nature of the free energy of general HAGBs.

### 2.2.3 Determination of Misorientation Axis/Angle Pair

The determination of a grain boundary's misorientation axis and angle is based on the adjacent grain's orientation and crystal symmetry operators. For cubic materials there are 24 symmetry

elements due to any coincidence relationship being described by 24 equivalent axis/angle pairs [30]. Through the application of the appropriate symmetry operator the minimum rotation axis and angle can be calculated. To calculate the minimum rotation axis and angle the orientations of both adjacent grains must be determined. The crystal orientations of these grains, $g_A$ and $g_B$ are typically given in Euler angles. The Euler angles are converted into a 3 x 3 rotation matrix, $\mathbf{U}_A$ and $\mathbf{U}_B$ respectively. A 3 x 3 rotation matrix ($\mathbf{R}$) which describes rotation $\theta$ about an axis $u$ to bring the two rotation matrix into coincidence can be determined by [31]:

$$\mathbf{R} = \mathbf{U_A U_B^{-1}} \tag{2.8}$$

The rotation axis and angle can be calculated from the rotation matrix by:

$$u = [\mathbf{R}_{32} - \mathbf{R}_{23}, \mathbf{R}_{13} - \mathbf{R}_{31}, \mathbf{R}_{21} - \mathbf{R}_{12},] \tag{2.9}$$

and,

$$\theta = \cos^{-1}\left(\frac{\mathbf{R}_{11} + \mathbf{R}_{22} + \mathbf{R}_{33} - 1}{2}\right). \tag{2.10}$$

The orientation of each grain, and hence the axis/angle pair of a grain boundary can be readily determined with transmission electron microscopy (TEM). Kikuchi patterns generated by TEM have been used for orientation determination due to their high degree of accuracy and spatial resolution [32]. Kikuchi lines are formed when the electron beam from a TEM becomes divergent by inelastic scattering and then electrons in the exact Bragg diffraction conditions are elastically scattered on crystallographic planes. Knowledge of the crystallographic plane spacing and crystal structure allow one to utilize the Kikuchi lines in a pattern to index the pattern and determine the orientation of the crystal to the electron beam. The process for indexing and determining the orientation of a grain is analogous to the process utilized in electron back scatter diffraction (EBSD) patterns generated on a scanning electron microscope (SEM). Recent advances in software have automated the steps required to index patterns making the process of determining the crystal orientation via TEM routine.

## 2.3 Radiation Damage in Materials

Knowledge of the radiation damage event is critical to understanding the materials challenges of nuclear materials. A radiation damage event occurs when an energetic particle collides with atoms in a bulk material. If the incident particle has sufficient energy when it collides with a lattice atom it will displace the atom from its lattice site. This displaced atom is known as the primary knock-on atom (PKA). The PKA will come to rest within the crystalline lattice in an interstitial site and leave behind a vacancy site. A simplified schematic of the displacement process is illustrated in Figure 2.9. The vacancy and interstitial form a Frenkel defect pair. The displaced atom and incident particle can displace other lattice atoms creating a cascade of Frenkel defect pair production as they come to rest in the material. The cascade of defects is known as a damage cascade. Many of the point defects generated in a damage cascade recombine during the cascade quench but a small fraction do not, causing a higher concentration of point defects over the equilibrium concentration of point defects for the material at a given temperature. These point defects can become mobile and migrate throughout the material.

Radiation damage can be quantified by solving the damage rate equation ($R_d$):

$$R_D = N \int_{\check{E}}^{\hat{E}} \phi(E_i)\sigma_D(E_i)dE_i \tag{2.11}$$

where $N$ is the lattice atom density, $\phi(E_i)$is the energy-dependent particle flux and $\sigma_D(E_i)$ is the energy dependent displacement cross section. The probability for the displacement of a lattice atom by incident particles is determined by the displacement cross section:

$$\sigma_D(E_i) = \int_{\check{T}}^{\hat{T}} \sigma(E_i,T)\nu(T)dT \tag{2.12}$$

where $\sigma(E_i,T)$ is the probability that a particle of energy $E_i$ will impart a recoil energy $T$ to a struck lattice atom, and $\nu(T)$ is the number of displaced atoms from a collision of this

type [33]. The energy transfer cross section, and hence the damage rate, is dependent on the type of particle and the incident particle's energy. The hard-sphere approximation which treats the collisions as purely ballistic is used for neutron collisions. For ion-atom or atom-atom collisions, the hard-sphere model is invalid due to electron and nuclear interactions between an ion-atom or atom-atom collision. Depending on the minimum separation between particles during a collision, a Coulomb, screened Coulomb, or Born-Mayer potential can be utilized. The result is different ion types and energies lead to different cascade physics. Neutrons and heavy ions tend to produce large-scale and dense damage cascades that result in significant recombination during the cascade quench. Protons, due to the Coulomb interaction of the charged particle, tend to produce more localized and widely spaced cascades resulting in a higher number of freely migrating point defects. The variation in the cascade process can be seen schematically in Figure 2.10 for protons, heavy ions, and neutrons.

Quantification of radiation damage is inherently sophisticated. For experimental work, Eq. 2.11 and Eq. 2.12 are utilized to quantify damage in neutron irradiation environments. For ion irradiations, a program utilizing kinetic Monte Carlo calculations called Stopping Range of Ions in Matter (SRIM) is utilized to determine the damage rate in a material for a given experimental condition [34]. The program utilizes inputs such as material composition, incident particle, and incident particle energy to determine a value for the number of displaced lattice atoms per incident particle per unit length traveled ($D_{SRIM}$). Displacements per atom ($dpa$) is often used to describe radiation damage as it is a normalized unit. Dpa is defined as the average number of times an atom is displaced from a lattice site for a given fluence of energetic particles. One dpa means on average each lattice atom has been displaced from its lattice site once. The unit can be misleading, as even though each atom has been displaced once from its lattice site most atoms return to their original lattice site and a Frenkel defect pair is never created. $D_{SRIM}$ can be used to convert to the displacement rate ($K_o$) by:

$$\frac{dpa}{s} = K_o = \frac{\Phi \cdot D_{SRIM}}{N} \tag{2.13}$$

where $\Phi$ is the particle flux and $N$ is the lattice atom density of the irradiated material. The flux in Eq. 2.13 can easily be calculated knowing the current imparted into the samples and the irradiation area. For neutron-induced damage, a simplification to Eq. 2.11 can be made to provide a rough estimate of radiation damage. By assuming isotropic scattering and neglecting inelastic scattering, Eq. 2.11 becomes

$$R_D = N\sigma_s \left( \frac{\gamma \bar{E}_i}{4E_d} \right) \Phi \tag{2.14}$$

and

$$\gamma = \frac{4M_1M_2}{(M_1+M_2)^2} \tag{2.15}$$

where $E_i$ is the average neutron energy, $\Phi$ is the total neutron flux above energy $E_d/\gamma$, $E_d$ is the displacement energy for a lattice atom, $M$ is the particle mass and the bracketed term is the number of Frenkel pairs produced per neutron.

The elevated concentration of point defects caused by damage cascades can significantly change a material's properties over time. During irradiation the mobile defects can diffuse through the bulk lattice creating various extended defects within the crystalline material. Two-dimensional and three-dimensional extended defects can be created. These defects include but are not limited to dislocation lines, dislocation loops, stacking faults, voids and bubbles. The formation of this highly defective structure leads to many irradiation induced phenomena including: void swelling, irradiation growth, irradiation hardening, irradiation creep, and helium embrittlement. A generalized schematic of changes in material's properties due to extended defect formation from irradiation is in Figure 2.11.

The production of long-range defects is dependent on the materials structure. Point defects can be annihilated at microstructural features, such as grain boundaries, dislocations, precipitates and free surfaces. Capture and annihilation sites such as the ones described are known as

defect sinks. With the exception of radiation-induced segregation and precipitation, if point defects are annihilated at defect sinks, extended defects will not be produced in large quantities and the production of a highly defective structure will be arrested. Therefore, the creation of defects, and the resulting amount of damage imparted into a material from the radiation damage event, is an overall balance between the defect production, recombination kinetics, sink strength/efficiency and the density of defect sinks.

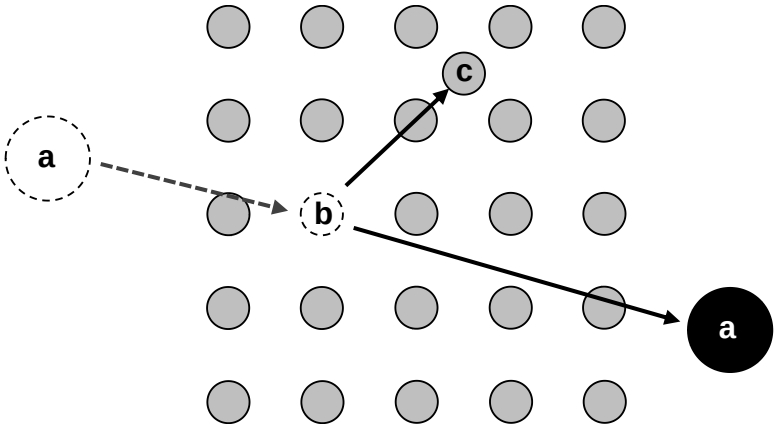


Figure 2.9: Production of a vacancy (b) and interstitial (c) due to a lattice atom being displaced by an energetic incident particle (a).

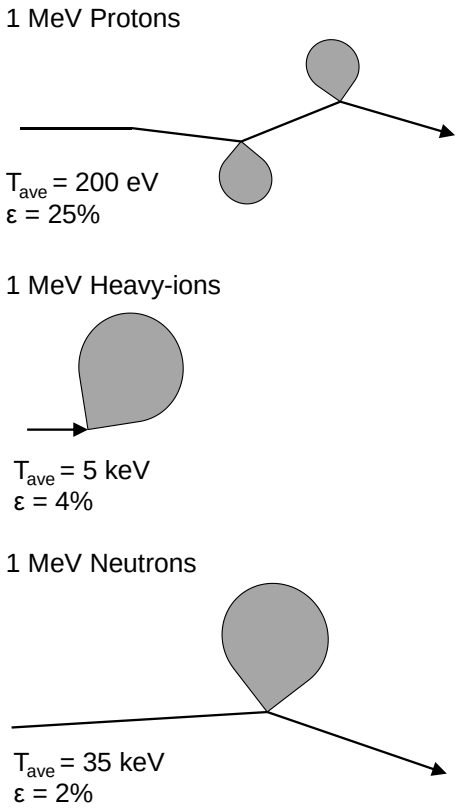


Figure 2.10: Schematic of damage cascade morphologies for different incident particles with the same incident energy. $T_{ave}$ is the average energy transferred per PKA and $\varepsilon$ is the production efficiency of freely migrating defects. Adapted from [35].

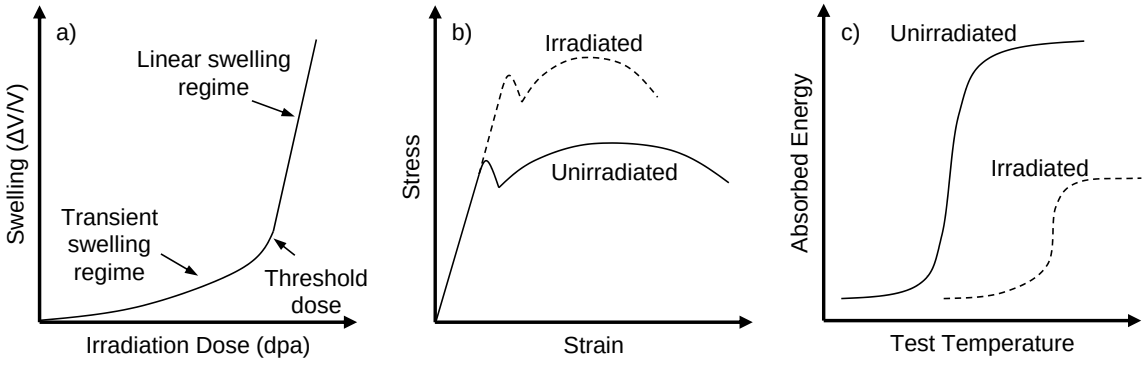


Figure 2.11: Schematic representation of radiation effects on material's properties: a) void swelling, b) irradiation induced hardening leading to reduced ductility and increased strength, c) irradiation embrittlement leading to decreased ductile to brittle transition temperature and reduction in upper shelf energy. Adapted from [13].

## 2.4 Grain Boundaries as Sites for Point Defect Annihilation

Grain boundaries are important sites for the destruction of point defects produced by irradiation. The annihilation of defects at grain boundaries is complex and may involve a sequence of mechanisms including the diffusion of defects to the sink and ultimately their destruction at the sink. Given this, two limiting types of sink action exist. Grain boundaries may destroy defects rapidly enough to maintain the point defect concentration at the thermal equilibrium near the grain boundary. In this case, the defects are destroyed at the maximum possible rate corresponding to the rate at which they are able to diffuse to the sinks. The grain boundaries operate as perfect sinks and the annihilation rate is bulk diffusion limited. Under other conditions grain boundaries may destroy point defects slowly, resulting in the defect concentration remaining uniform through the lattice and the grain boundary. In this case the grain boundary would not be operating as a perfect sink and the process becomes sink reaction limited [36]. Grain boundaries may also operate in an intermediate situation where the point defect annihilation mechanism is neither explicitly diffusion nor sink reaction limited but behaves with a mixed nature [37].

In general, point defects are annihilated at dislocation jogs, including primary grain boundary and secondary grain boundary dislocations, within the grain boundary. Point defects may reach these jogs by jumping into the dislocation core and then diffusing along the core to the jog or by direct jumps from the lattice to the jog. The mechanism is illustrated schematically for a low-angle symmetric tilt boundary in Figure 2.12. This results in the sink efficiency of a grain boundary to be determined by: (1) binding energy of point defect to grain boundary dislocation, (2) diffusivity of point defect along the grain boundary dislocation, (3) concentration of jogs, and (4) defect capture probability at the jog [38]. As there are many variables in determining the sink efficiency of a grain boundary wide variations are expected. The mechanisms for point

defect absorption at grain boundaries also show the importance of the grain boundary atomic structure. In particular, as discussed in Section 2.2 the grain boundary structure dictates the concentration of dislocations and hence jogs at the grain boundary.

The defect sink mechanism for grain boundaries has been observed either explicitly through high resolution transmission electron microscopy or inferred in a wide range of experiments on irradiated material systems. The direct climb of grain boundary dislocations as a result of point defect absorption in special grain boundaries was observed by Konem *et al.* in irradiated Au [39]. S. Zinkle has used defect denuded zones near grain boundaries to determine the interstitial diffusion coefficient in ion irradiated polycrystalline spinel and alumina [40]. More recently, dislocation loop denuded zones along grain boundaries in irradiated 316 and 304 stainless steel was observed by Bruemmer *et al.* indicating the grain boundaries in austenitic stainless steels act as efficient sinks for interstitials during irradiation [41]. Kaoumi *et al.* has observed similar results on the same heat of 9 wt. % Cr model F/M steel used in this study. Denuded zones were observed at grain boundaries irradiated with 1 MeV $Kr^{++}$ ions at specific crystallographic orientations [42]. Recent results are purely qualitative but indicate the mechanisms mentioned above are active for irradiated materials.

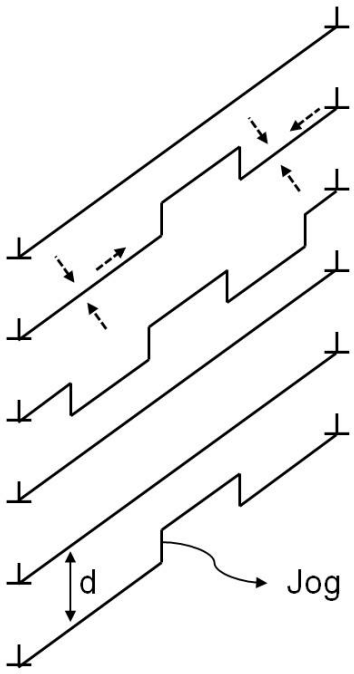


Figure 2.12: Low-angle symmetric tilt boundary, composed of parallel edge dislocations acting as a sink for point defects. Excess point defects are destroyed at jogs on the dislocations causing them to climb. Dashed lines indicate diffusion paths for point defects for destruction at the jogs [36].

## 2.5 Precipitate Stability Under Irradiation

### 2.5.1 Overview

A precipitate is considered to be in thermal equilibrium when there is no net flux between the diffusion of solute atoms to the precipitate and the migration of precipitate atoms into matrix. In the absence of irradiation, precipitates tend to dissolve into the matrix at high temperatures to maintain the bulk concentration, but at low temperatures coarse particles tend to grow at the expense of fine particles to reduce the interfacial energy between the particle and matrix. The growth of coarse particles is known as Ostwald ripening.

If a displacement cascade occurs within a precipitate it may eject atoms from the particle into the matrix. The atoms can then back-diffuse to rejoin the original precipitate, diffuse and join another particle, help to nucleate a new particle, or remain in solution within the matrix [43]. The first model which investigated particle resolution in the presence of irradiation was by Nelson *et al.* [44]. The model accounted for recoil and disordering dissolution, radiation enhanced diffusion, and equilibrium conditions. The model predicts coarsening of small particles and shrinking of large particles until a stable particle size is achieved. The process is known as inverse coarsening and shown in Figure 2.13.

The model presented by Nelson has limitations and a modified model which takes into account a gradient of solute atoms which exist until the particle reaches an equilibrium size or disappears completely was developed [43, 45, 46]. The modified model is represented schematically in Figure 2.14. The model assumes a particle under irradiation will have surface dissolution due to ballistic ejection of atoms from the precipitate. The dissolution causes a local solute supersaturation near the particle resulting in a continuous loss of solute atoms to the matrix down the outer concentration gradient seen in Figure 2.14b. The dissolution occurs until steady-state is reached where the dissolution is matched by back diffusion. If the precipitates are widely spaced, the matrix may not reach steady state and the precipitates will dissolve as in Figure 2.14e. If steady state is achieved and low solubility of solutes in the matrix exists, re-nucleation away from the original particle could occur. The re-nucleation process is shown in Figure 2.14d.

The modified model explains the need to study the original size and number density of precipitates as it will play a role in the growth or dissolution of the particle under irradiation. If coarse and widely dispersed particles are in equilibrium before irradiation, the model predicts they will shrink. Fine particles which are closely dispersed will tend to grow with increasing dose. The rearrangement of lattice atoms and enhanced diffusion caused by the radiation damage event can also cause the formation of incoherent and coherent precipitates to nucleate during the irradiation event. The evolution of precipitates under irradiation is governed by the rates of

re-solution, re-precipitation and the amount of radiation induced disordering.

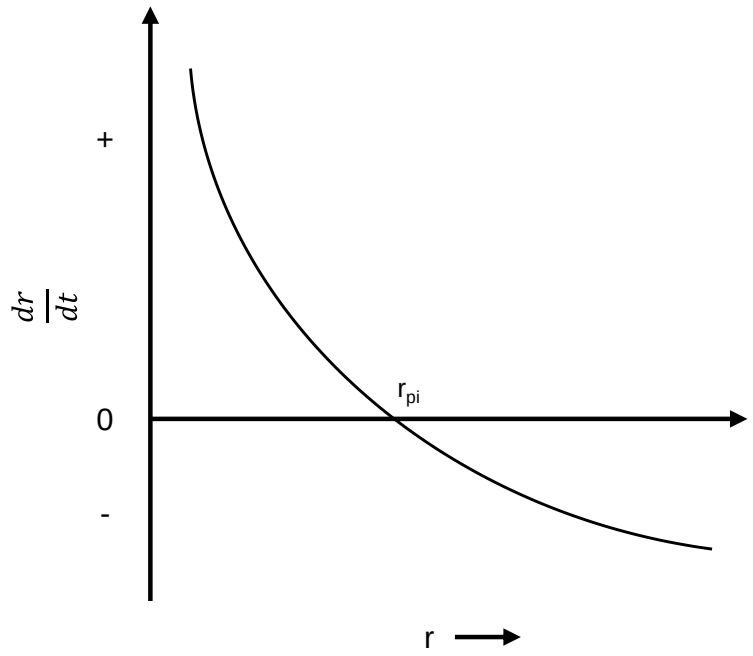


Figure 2.13: A schematic of the Nelson model for radiation-induced precipitate dissolution. Smaller particles coarsen at the expense of larger particles. After Ref. [44] .

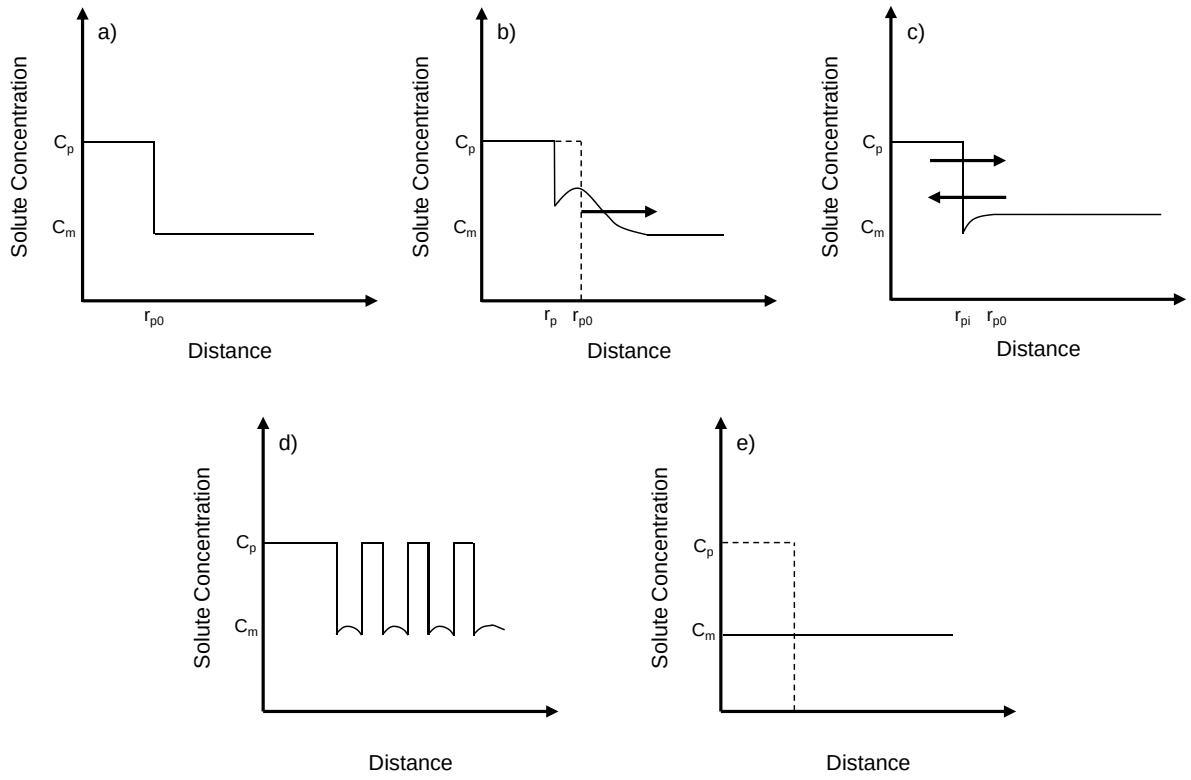


Figure 2.14: A schematic of a modified model for radiation-induced precipitate dissolution and precipitation as a function of dose where a) unirradiated equilibrium, b) surface dissolution at low doses, c) steady-state leading to d) nucleation of new precipitates because of matrix supersaturation, or e) precipitation continues to dissolve until it disappears. From Ref [45] .

### 2.5.2 Nanocluster Stability in NF-ODS F/M Steels

Nanocluster stability in NF-ODS steels has been investigated by a range of techniques including transmission electron microscopy, atom probe tomography, and scanning transmission electron microscopy [47–60]. Many of the studies were small in scope with only a limited dose and/or temperature range examined. These studies have been inconclusive in determining whether nanoclusters are stable under irradiation with reports of nanoclusters remaining stable, shrinking, or increasing in size after irradiation. Many of the studies were purely qualitative and

little information exists using quantitative analysis. A full literature review and discussion of nanocluster stability in NF-ODS steels can be found in Ref. [11].

Recent work was completed by A. Certain on studying nanoclusters in a quantitative manner over a wide range of temperatures and several doses [11]. The study was conducted on the 14YWT alloy system, which is used in this study. Results indicated at cryogenic temperatures nanoclusters were completely dissolved in the bulk matrix when irradiated to 100 dpa using heavy ions. At such low temperature and high dose rate, nanoclusters were unstable due to ballistic resolution and the reduced energy for back-diffusion of ejected atoms from the cluster. At intermediate temperatures, nanoclusters were present but many areas examined showed a highly reduced population of nanoclusters versus the unirradiated condition when using energy-filtered transmission electron microscopy (EFTEM). Atom probe tomography (APT), which is skewed towards studying small sized nanoclusters population, showed no change in the number density of nanoclusters from the unirradiated to irradiated state in the intermediate temperature range at 100 dpa. For heavy ion irradiations conducted at high temperatures (450-600 °C), no disconcernable change in the cluster population was observed using both EFTEM and APT indicating sufficient energy for back diffusion of ejected particles was in the system and aided in nanocluster stability. Figure 2.15 shows examples of the observed nanocluster population at each irradiation temperature by A. Certain while Table 2.2 summarizes the results for both the EFTEM and APT analysis of nanoclusters in irradiated 14YWT using heavy ions [11].

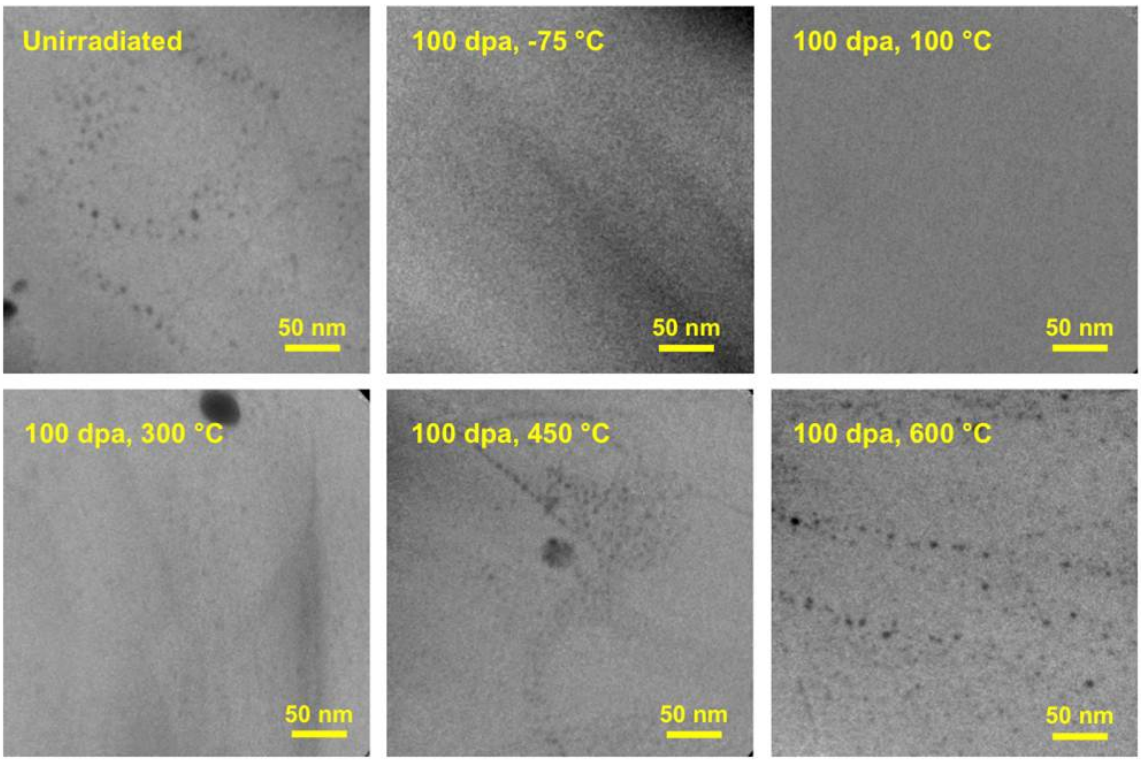


Figure 2.15: Fe-jump ratio images of 14YWT-SM10 with irradiation conditions indicated. Irradiations completed using $Ni^{2+}$ ions with a dose rate of ~$2x10^{-3}\,\frac{dpa}{s}$. Dark areas correspond to area of Fe depletion indicating the location of nanoclusters. Larger regions of Fe depletion correspond to titanium oxides or other precipitates. From Ref. [11].

Table 2.2: Summary of nanocluster stability in 14YWT irradiated using $Ni^{2+}$ ions. From Ref [11].

| Analysis Technique | Dose (dpa) | Temp. (°C) | Avg. Radius (nm) | St. Dev (nm) | Num. Density ($1/nm^3$) | St. Dev. ($1/nm^3$) |
|---|---|---|---|---|---|---|
| EFTEM | 100 | - | 1.3 | 0.7 | $4.0x10^{-5}$ | $2.0x10^{-5}$ |
| APT-Voltage | 100 | - | 1.0 | .4 | $5.0x10^{-4}$ | - |
| EFTEM | 100 | -75 | 2.0 | 0.7 | $1.0x10^{-7}$ | $3.0x10^{-7}$ |
| APT-Laser | 100 | -75 | - | - | - | - |
| EFTEM | 100 | 100 | 3.4 | 0.2 | $3.0x10^{-8}$ | $8.0x10^{-8}$ |
| APT-Laser | 100 | 100 | 0.8 | 0.3 | $7.0x10^{-4}$ | - |
| EFTEM | 100 | 300 | 1.5 | 0.6 | $2.0x10^{-5}$ | $1.0x10^{-5}$ |
| APT-Laser | 100 | 300 | 0.8 | 0.3 | $7.0x10^{-4}$ | - |
| EFTEM | 100 | 450 | 1.4 | 0.6 | $6.0x10^{-5}$ | $2.0x10^{-5}$ |
| APT-Laser | 100 | 450 | 0.9 | 0.3 | $7.0x10^{-4}$ | - |
| EFTEM | 100 | 600 | 1.4 | 0.6 | $3.0x10^{-5}$ | $2.0x10^{-5}$ |
| APT-Laser | 100 | 600 | 1.0 | 0.4 | $7.0x10^{-4}$ | - |

## 2.6 Radiation Induced Segregation (RIS)

### 2.6.1 Overview

RIS is a non-equilibrium process of alloying elements in a material segregating to or away from defect sinks during irradiation. RIS occurs when the mobile point defects created by a radiation damage event migrate towards defect sinks within the material. When a particular type of point defect (vacancy or interstitial) is associated more strongly with various chemical elements, these elements will redistribute within the bulk material as the point defects migrate towards a defect sink. This process is illustrated schematically in Figure 2.16 for a simple 50% A atoms - 50% B atoms binary alloy system. Figure 2.16a shows the vacancy concentration gradient near a sink, such as a grain boundary, where the net flux of vacancies towards the boundary is counteracted by the flux of A and B atoms away from the boundary. Here, the

A atoms are preferentially coupled to the vacancy flux resulting in the enrichment of B atoms at the sink interface. In Figure 2.16b, the interstitial concentration gradient is plotted near a sink. The B atoms are preferentially coupled to the interstitial flux resulting in enrichment of B atoms to the sink. RIS is therefore dependent on both the vacancy and interstitial flux to the defect sink and the net balance between them determines the RIS response. The result of RIS can be a significant change in the material's overall properties, including the material's corrosion resistance and fracture properties.

RIS is dependent on the irradiation environment, the material composition, and the microstructure of the material of interest. At low temperatures, the point defects created by the damage cascade have low mobility due to insufficient energy for long-range diffusion. At intermediate temperatures, the diffusion is fast enough that point defects generated by radiation diffuse to defect sinks. Intermediate temperatures are typically described as temperatures ranging between 30-50% of the melting temperature of the material [6]. If there is preferential diffusion of defects of certain atoms to sinks, depletion or enrichment of alloying elements at a sink may occur due to the coupling of the motion between atoms and defects and hence atom fluxes being associated with defect fluxes. At very high temperatures, the equilibrium thermal defect concentrations are sufficiently large and the back diffusion of vacancies tends to prevent the development of RIS. Temperature can also change the RIS response by modifying which point defect-solute complex migrates faster for a given system.

Dose rate is also a significant factor in determining the RIS response of materials. Typically, increasing the dose rate will shift the temperature dependence of RIS to higher temperatures. The generalized regime for RIS as a function of temperature and dose rate is depicted in Figure 2.17. The dose rate dependence is due to the competition between the recombination rate of point defects and the probability of defects finding sinks. Lower point defect generation rates ($K_o$) results in point defects being generated more slowly in the matrix. If temperature is held constant, than the thermal mobility of the point defects is not modified and therefore the probability of the point defect finding a defect sink over finding another point defect to

recombine is increased. The result is at low dose rates the probability of a defect finding a sink dominates resulting in an increased RIS response as seen in modeling results presented in Figure 2.18.

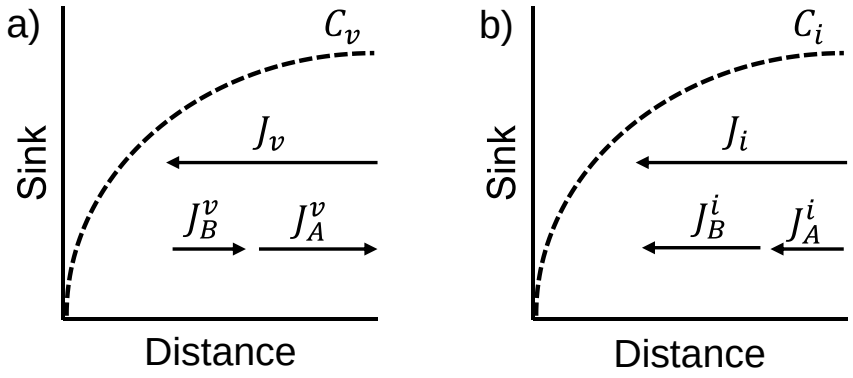


Figure 2.16: Mechanisms for radiation-induced segregation due to point defect and solute coupling in a binary alloy where a) enrichment of B occurs if $d_B^v < d_A^v$ and b) enrichment of B occurs if $d_B^i > d_A^i$ . Arrows represent the magnitude of the flux.

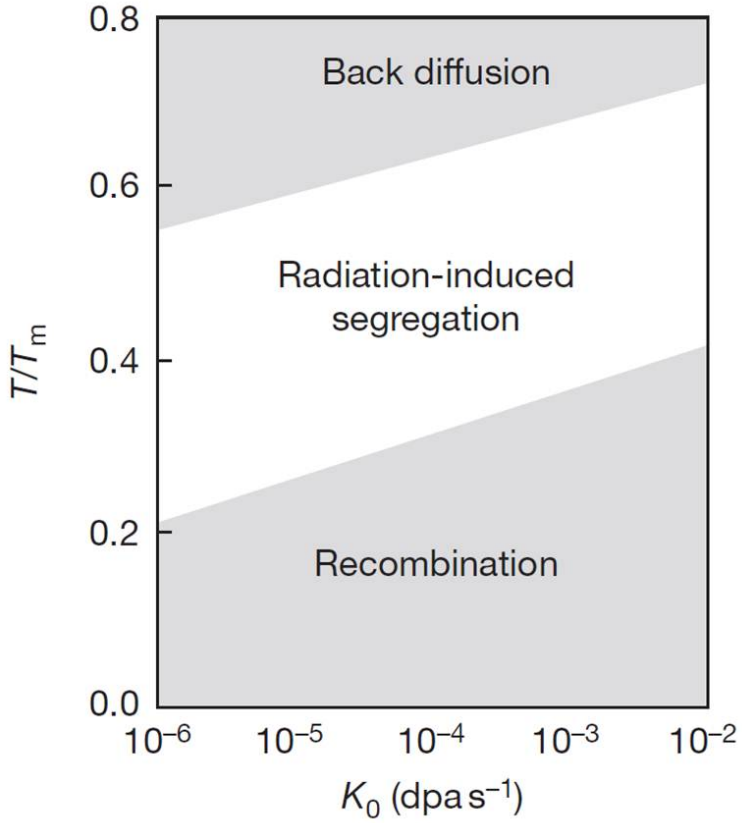


Figure 2.17: Temperature and dose rate effect on radiation induced segregation [61].

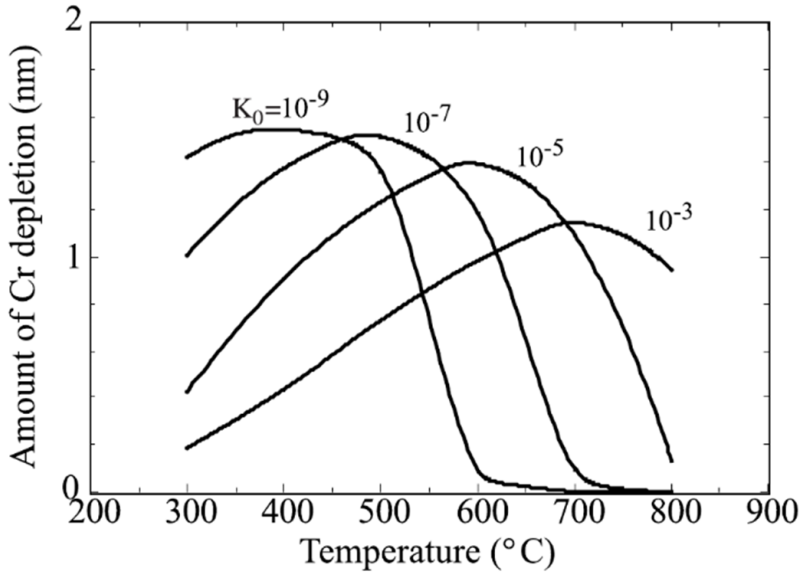


Figure 2.18: Dose rate dependence on chromium depletion at grain boundaries as predicted by modified inverse Kirkendall (MIK) model. Modified from [35].

### 2.6.2 Radiation Induced Segregation in Steels

RIS has been most prominently studied in austenitic stainless (FCC) steels. In these FCC alloys it has been shown that Cr is depleted near grain boundaries under irradiation. The depletion of Cr at boundaries leads to reduced corrosion resistance at the boundary. The result is an increased susceptibility to irradiation-assisted stress corrosion cracking [62]. Substantial work has been conducted to develop a predictive model of RIS in austenitic stainless steels to predict and therefore limit failure while in-service. Initially, the Perks model [63] was used to model RIS at grain boundaries. The Perks model assumes the segregation is based on the differences in the atom-vacancy jump rates of the solute atoms. This mechanism is the inverse Kirkendall effect. The Perks model was later refined resulting in the development of the modified inverse Kirkendall model (MIK). The MIK model includes effects of local composition on the diffusivities of alloy species and concluded the RIS response in FCC steels can be modeled using only the vacancy flux. The result is the most widely accepted model for RIS in FCC steels is the modified inverse Kirkendall (MIK) model as it captures the composition, dose, and temperature dependence of RIS in a wide range of FCC steels. A representative diagram of the fit between the Perks and MIK model and experimental findings in an irradiated FCC steel is given in Figure 2.19 and 2.20 [5]. Recent first principles based modeling has demonstrated both the vacancy mediated and the interstitial mediated mechanisms could be active in austenitic alloys although the contribution from interstitials can be significantly smaller than the vacancy contribution [64]. Given this, these models still predict Cr depletion near grain boundaries in FCC alloys.

For F/M steels, no conclusive trends or dependencies have been drawn. Experiments have shown that Cr can enrich, deplete, or not segregate to grain boundaries and internal interfaces in F/M steels [65–83]. Cr enrichment has been seen in neutron irradiated HT9 [71] and FV448 [68, 74, 75], and in carbon ion irradiated Fe-Cr-Si alloy while a Fe-Cr-Ti alloy in the same

experiment showed Cr depletion [66]. Electron irradiations and Ni ion irradiations have shown enrichment or depletion can occur on a wide range of alloy systems [68, 72]. Recent, more systematic work by Wharry *et al.* using protons and Fe ion irradiations have shown Cr enrichment is observed in T91 up to a ~530 °C and then depletion occurs while the magnitude of segregation increases with dose [82]. Marquis *et al.* have shown Cr enrichment or depletion can occur at different boundaries within the same Fe ion irradiated model oxide dispersion strengthened steel specimen [80]. A summary of experimental literature on the Cr behavior in F/M steels at internal interfaces can be seen in Figure 2.21. It is important to note that much of the experimental results on RIS in F/M steels is fragmented with only Wharry *et al.* completing systematic ion irradiation studies [81, 83]. The result is broad conclusions can not be made on RIS behavior using solely the experimental data.

Little work has been completed on modeling RIS in F/M steels and the well established theories for FCC systems appear to not directly transfer to the BCC system. Recent *ab-initio* and molecular dynamics studies of Cr in BCC-Fe have shown the RIS behavior in F/M steels to be complex, with both the interstitial-Cr and vacancy-Cr complexes diffusing faster than BCC-Fe under typical reactor conditions [84–87]. Figure 2.22 shows a plot of the diffusivity ratios for these complexes as functions of temperature as calculated using first principles by Choudhury *et al.* [86]. Work by Terentyev *et al.* have shown the interstitial diffusion could be strongly dependent on Cr composition in concentrated Fe-Cr alloys [87]. Wharry *et al.* has had success applying the MIK model to capture the experimental composition and temperature dependance for RIS in T91 with interstitial contributions included [82] but the model lacks sufficient details to predict the dose dependence. The lack of modeling work benchmarked against experimental findings has also made it difficult to conclude the primary mechanism for RIS in F/M.

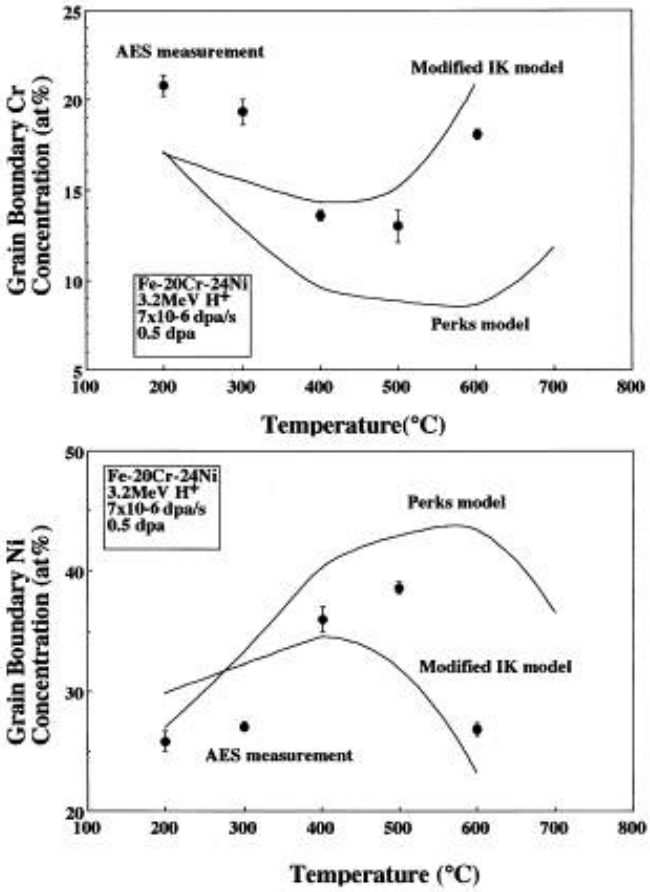


Figure 2.19: Comparison of model calculations using the Perks and the MIK model to experimental measurements using AES as a function of temperature for a Fe-20Cr-24Ni FCC alloy [5].

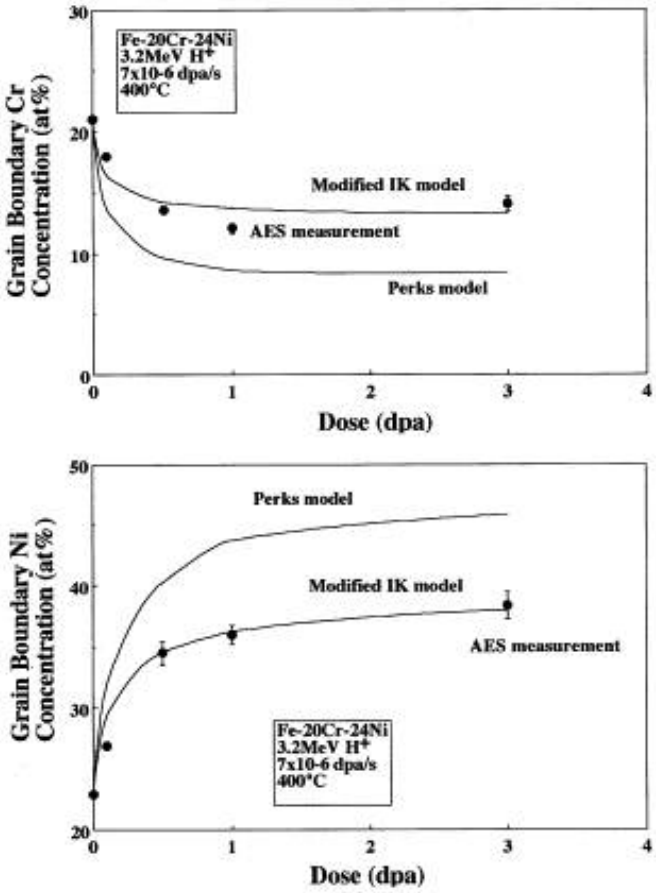


Figure 2.20: Comparison of model calculations using the Perks and the MIK model to experimental measurements using AES as a function of dose for a Fe-20Cr-24Ni FCC alloy [5].

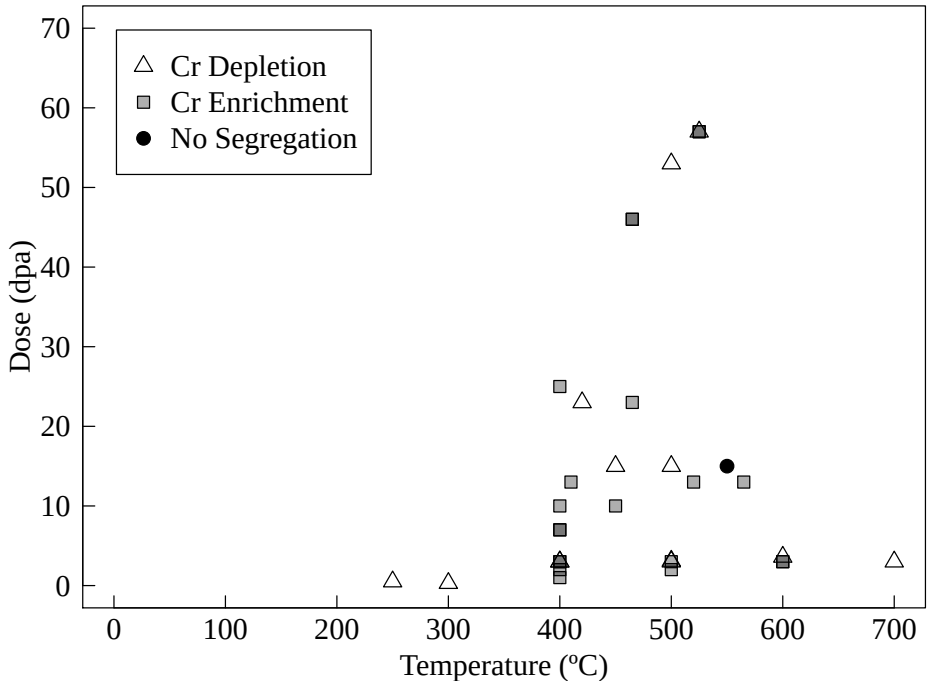


Figure 2.21: Summary of published research on RIS in F/M steels up to 70 dpa and 700 °C.

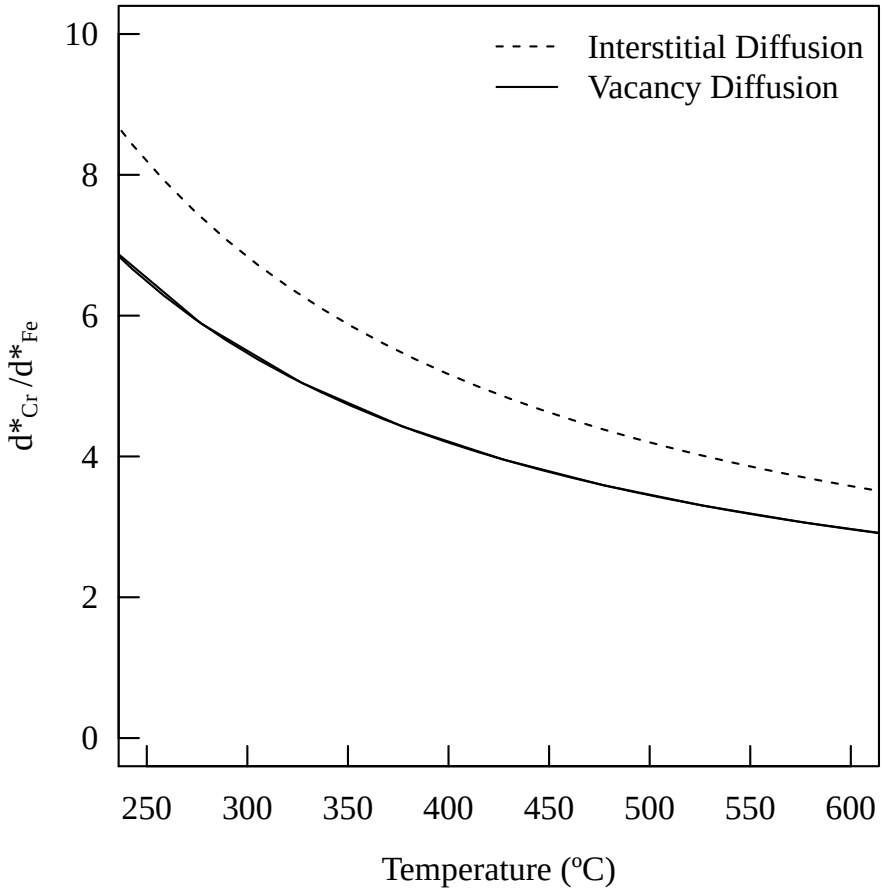


Figure 2.22: Cr and Fe diffusivity ratios for interstitial and vacancy mechanisms as determined from first principles by Choudhury *et al.* [86].

### 2.6.3 Model for Radiation Induced Segregation and Grain Boundary Structure

Recently, more systematic experimental studies have shown variation in the RIS response of different grain boundaries within the same sample for BCC steels [80, 81]. Similar behavior has also been observed in FCC systems and has been suggested the variation could be attributed to

differences in grain boundary structure [6, 88–90]. These results suggest that not only does dependencies on composition, dose, dose rate, and other experimental conditions exist for RIS in F/M steels, but a dependence on the fundamental differences between specific grain boundaries and more generally different interfaces may also exist.

Most models for RIS treats grain boundaries as a perfect sink, or a sink which can capture and absorb every point defect which migrates to the boundary. The result of this assumption is every grain boundary with the same irradiation history should have identical RIS behavior. A perfect sink would also exhibit the largest possible RIS response. Significant variability within a material for constant irradiation conditions in both austenitic and F/M steels indicate the assumption that every boundary acts as a perfect sink is possibly invalid. Recent theoretical and experimental studies on austenitic stainless steels has demonstrated the perfect sink condition is not universally applicable [88, 90, 91]. The magnitude of the RIS response at the grain boundaries in austenitic stainless steels was shown to change as a function of the grain boundary structure as seen in Figure 2.23. The findings predict the grain boundary structure alters the defect flux behavior, and hence the solute flux behavior at the grain boundary.

The work of Duh *et al.* and Sakaguchi *et al.* was extended by L. Barnard[1] in concert with the efforts presented in this text to determine the primary mechanisms for RIS in F/M steels including grain boundary structure dependence. The model is modified from a version of a model used to study RIS in Ni-Cr model alloys by Barnard *et al.* [92]. The theories of Wiedersich *et al.* are employed to develop a rate theory model which solves the coupled diffusion equations for defects and alloy components as the defects diffuse toward the sink [93]. A complete model description and derivation for the boundary conditions are provided in Appendix A. The model is detailed briefly in this section for clarity.

The following coupled equations are used to obtain one dimensional concentration profiles of elemental species and single vacancies and single interstitials near a grain boundary for a model system [93],

[1]Results courtesy of Leland Barnard, Computational Materials Group, University of Wisconsin - Madison (lmbarnard@wisc.edu)

$$\frac{\partial C_j}{\partial t} = -\frac{\partial J_j}{\partial x} \tag{2.16}$$

$$\frac{\partial C_v}{\partial t} = \varepsilon K_o - R_R C_v C_i - R_{VD} C_V - \frac{\partial J_v}{\partial x} \tag{2.17}$$

$$\frac{\partial C_i}{\partial t} = \varepsilon K_o - R_R C_v C_i - R_{ID} C_I - \frac{\partial J_i}{\partial x} \tag{2.18}$$

where $C_j$ is the site fraction of species $j$, $J_j$ is the flux of species $j$,$R_R$ is the rate coefficient for recombination of vacancies and interstitials, $R_{VD}$ and $R_{ID}$ are the rate of vacancies and interstitials loss to dislocations respectively, $K_o$ is the dose rate in dpa/s and ε is the damage efficiency which is dependent on the radiation species. Typically used damage efficiencies are provided in Figure 2.10. The rate of vacancy and interstitial loss to dislocations, $R_{VD}$ and $R_{ID}$, can be determined using the following equation (where $d$ = vacancy or interstitial) [4]:

$$R_d = Z_{dD} 4\pi r_{rD} \frac{\rho_D}{\delta} D_d \tag{2.19}$$

where $Z_{dD}$ is the bias factor, $r_{rD}$ is the radius of capture for defect species $d$, $\rho_D$ is the dislocation density, $\delta$ is the interplanar distance, and $D_d$ is the diffusivity of defect species d. The dislocations are assumed to be unbiased and $Z_{dD}$ is set equal to 1.

The modified boundary conditions for point defect migration established by Duh *et al.* are included within the model. The boundary condition alters the sink efficiency and hence the flux of point defects at the grain boundary. The model assumes boundaries with high interfacial coherency, such as low angle and low Σ CSL boundaries, have a low point defect capture efficiency under irradiation. The result is the concentrations of point defects near a grain boundary are not constrained to the thermodynamic equilibrium.

The theory predicts the grain boundary efficiency and hence the resulting RIS response is highly dependent on both the diffusion of point defects to and along a grain boundary and the number of point defect annihilation sites. Using classical grain boundary structure and energetic theories these concepts have been applied based on grain boundary misorientation angle. The work of Duh *et al.* only applied the modified boundary conditions towards the vacancy migration as it assumes the mechanisms in the MIK model. For F/M steels, the boundary conditions are applied for both the vacancy and the interstitial migration. Therefore, the flux of defects into the grain boundary is determined by the grain boundary diffusion coefficient for point defects defined by (where d denotes a vacancy or an interstitial) [91]:

$$d_d^{GB} = g_d a^2 Z f_d^{GB} \nu_o \sum_k C_k \exp\left(-\frac{\left(E_a^{k,d} - a^2\gamma\right)}{k_b T}\right) \tag{2.20}$$

where $g_d$ is a dimensionless constant based on the structure which is taken to be equal to 1 for F/M steels, $a$ is the lattice parameter, $Z$ is the BCC coordination number, $f_d^{GB}$ is the correlation factor for defect type $d$ in the grain boundary, $\nu_o$ is the attempt frequency, and $\gamma$ is the specific grain boundary energy. For a multicomponent system, $C_k$ is the fraction of component $k$ near the boundary and $E_a^{k,d}$ is the migration activation energy of component $k$ for defect type $d$. In Equation 2.20, the structure dependence of the grain boundary diffusion coefficient is captured in the grain boundary energy term. The theory assumes the dislocations contained within grain boundaries play the primary role in the point defect interactions. The result is the classical grain boundary energy equations based on the dislocation model of point defects from Section 2.2 can be applied and Equation 2.20 can be cast in terms of the grain boundary misorientation. The model predicts grain boundaries which have very high energy due to large misorientations, such as general high angle grain boundaries, will have diffusion fast enough that the boundary will act as an ideal sink. For boundaries with high coherency and hence low energy, the grain boundary will have slower diffusion of point defects to point defect annihilation sites at the boundary. In similar fashion, the number of point defect annihilation sites for a given grain boundary can be determined by the misorientation angle as given in the following expressions:

$$\rho_{HAGB} = \frac{4\delta}{b} \sin\left(\frac{\Delta\theta}{2}\right) \tag{2.21}$$

for high angle grain boundaries where $\Delta\theta$ is $\Delta\theta = \theta - \theta_{CSL}$ and $\delta$ is the thickness of the boundary which is assumed to be one atomic layer and the density for low angle grain boundaries is given by:

$$\rho_{LAGB} = \frac{\theta}{b}. \tag{2.22}$$

From Eqs. 2.21 and 2.22 it can be seen the model predicts that low angle grain boundaries will have a lower density of annihilation sites compared to general high angle boundaries due to differences in structure. The resulting predicted concentration gradient of point defects at a grain boundary using modified boundary conditions for a F/M steel can been seen in Figure 2.24 [94].

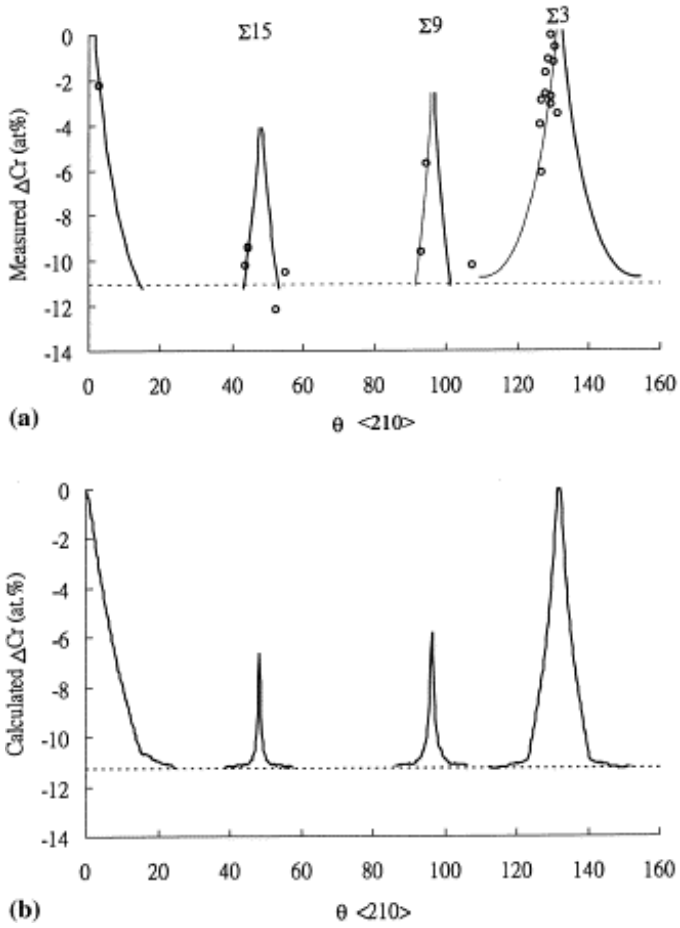


Figure 2.23: Variation in Cr segregation at grain boundaries as a function of misorientation angles for a 304 irradiated stainless steel, where a) is the measured and b) is calculated results [91].

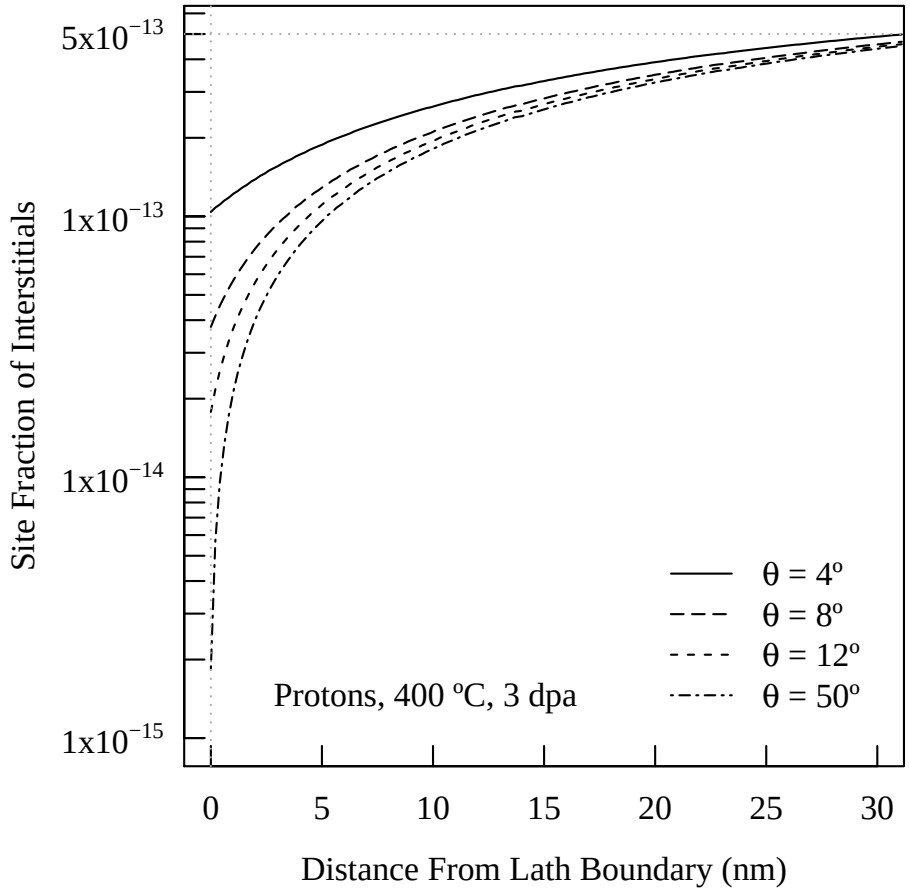


Figure 2.24: Interstitial concentration gradient near an irradiated lath boundary for several grain boundary misorientations as determined by the rate theory model for a model Fe-Cr BCC system [94].

## 2.7 STEM-EDS Measurements for Solute Segregation to Interfaces

Scanning transmission electron microscopy coupled with electron dispersive spectroscopy (STEM-EDS) has been widely used to study segregation of solute atoms to grain boundaries. STEM-EDS is widely used as it provides concentration profiles along a grain boundary, or more recently 2D concentration maps within reasonable time frames. Recent advances in EDS detectors and STEM systems has significantly reduced the time required to investigate a boundary making it possible to study several boundaries within a typical microscopy session. The small volume of sample needed to do STEM-EDS investigations also lends itself to work on activated samples as a smaller and hence lower activity sample can be used. Another advantage is STEM-EDS data interpretation is fairly straightforward compared to other techniques such as APT.

Several considerations must be made when using STEM-EDS to investigate segregation. The measured segregation profile is sensitive to many experimental factors including: accelerating voltage, STEM probe diameter, specimen thickness, specimen tilt, sample drift, surface contamination and specimen composition [95]. Thickness of the specimen is a significant contributing factor to the measured segregation profile. As the electron beam passes through the specimen it will broaden resulting in the interaction volume of the beam with the specimen being larger than the incident probe width and effectively reduce the measured boundary concentration. This phenomena is shown schematically in Figure 2.25. The interaction volume also increases for heavier specimens and lower accelerating voltages. Reducing the specimen thickness reduces beam broaden effects driving the measurement closer to the actual composition value but results in fewer X-rays produced resulting in reduced statistical precision in the composition quantification. Increasing the specimen thickness also increases the sensitivity of the measurement to the grain boundary misorientation to the electron beam. A specimen 100 nm thick requires a misorientation of ~20° to see a 50% reduction in the relative measured

intensity in the segregant EDS peak where a specimen 300 nm requires only a misorientation of ~5° of the grain boundary to the incident probe to have the same reduction in measured intensity [96]. Reducing the electron probe results in increased spatial resolution but also degrades sensitivity to the measurement and increases the sensitivity of the measurement to grain boundary inclination to the probe. Overall, the acceleration voltage is the least significant factor affecting the measured composition for interfacial segregation. Recent advances in control and data acquisition software has allowed for advanced drift correction and drift prediction algorithms which compensate for drift of specimens during long acquisition times. These advances have reduced the contributions of drift in the error of the STEM-EDS measurement. The result is for interfacial segregation, where the solute is confined to the first few atomic layers to the grain boundary, STEM-EDS experimental factors typically combine to reduce the measured segregation compared to the actual interfacial segregation and the reduction can be fairly significant if the measurements are not executed with care.

The result of the experimental factors contributing to the reduced measured segregation profile means STEM-EDS is most effective in measuring relative changes in segregation due to processing such as thermal mechanical treatments or irradiation than absolute segregation within one condition, especially when STEM conditions such as accelerating voltage and probe size are held constant. The ideal experiment would involve conducting all STEM-EDS experiments within one session on one specimen to limit variations in the measured segregation profiles due to changes in probe size and specimen thickness. In practice, for a large scale experiment with multiple specimens, the ideal experiment can not be conducted. Therefore, some error will be introduced into the experiment due to session to session STEM condition variations and specimen to specimen thickness variations which manifests itself as experimental scatter.

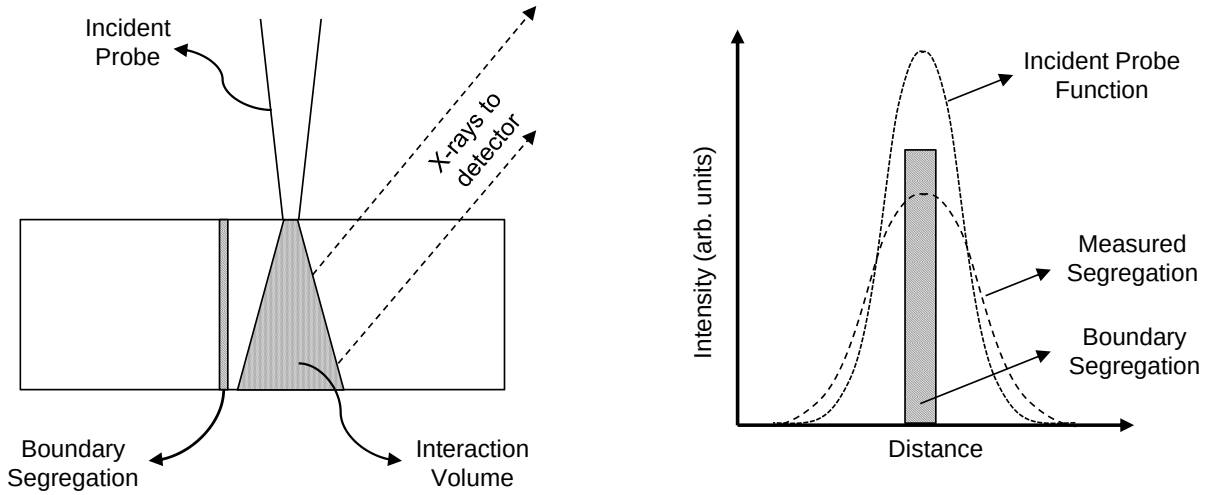


Figure 2.25: Schematic showing the the beam broadening and sampling effects due to the resolution of typical STEM/EDS systems.

# Chapter 3

# Experimental

## 3.1 Specimens

### 3.1.1 Model F/M Steel

A 9 wt. % Cr model steel designed to approximate the microstructure of commercially available F/M steels, such as T91 and NF616, was utilized to study general segregation trends and affects of grain boundary structure. A model steel was used due to the simplified chemistry and low precipitate density which facilitated both experimental and modeling investigations. The composition of the steel is 0.015 wt. % O, 0.72 wt. % C, 8.68 wt. % Cr, and balance Fe. The model steel was austenitized at 950 °C for 60 minutes in an argon atmosphere and cooled to room temperature. The steel was then tempered at 750 °C for ~60 minutes and air-cooled to room temperature. The steel was received as 1 mm plate. The resulting microstructure consisted of tempered martensite with inter-dispersed ferrite throughout the matrix. This study focused only on the martensite phase of the model steel. The as-received martensite phase of the steel has a complicated microstructure including prior-austenite grain boundaries, packet boundaries, lath boundaries, Cr-rich carbides, and dislocation networks. A bright field TEM micrograph of the as-received microstructure is presented in Figure 3.1. This study focused on the segregation of Cr to lath boundaries, as the high density of lath boundaries compared to other internal interfaces ensured numerous boundaries for investigations.

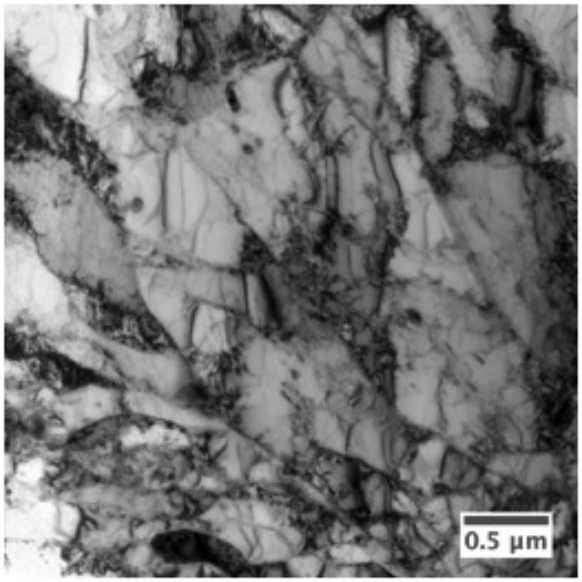


Figure 3.1: Bright field transmission electron microscopy (TEM) micrograph of the as-received microstructure of the 9 wt. % Cr model F/M steel

### 3.1.2 NF-ODS F/M Steel

A 14 at. % Cr nano-featured oxide dispersion strengthened (NF-ODS) F/M steel was used to investigate the relationship between nanocluster stability and radiation induced segregation. Twelve specimens of 14YWT-SM10 ferritic steel were provided by Oak Ridge National Laboratory (ORNL). Specimens had a nominal dimension of 10 x 3 x 1 mm and a nominal composition of 14 at. % Cr, 3 at. % W, 0.4 at. % Ti, 0.35 at. % $Y_2O_3$, and balance Fe. 14YWT variants are manufactured using powder metallurgy. The precursor powders were ball milled for 40 hours and transferred to a mild steel can, degassed in a vacuum of ~$10^{-2}$ mbar at 400 °C and sealed. The can containing the powder was then extruded at 850 °C. The as-received specimens had a complex microstructure with a fully ferritic structure and Y-Ti-O nanocluster dispersions within the grains and on grain boundaries.

## 3.2 Proton Irradiations

Protons were utilized due to their higher damage rates, relative low cost, and simplicity of logistics over neutron irradiated samples [10]. The 2.0 MeV protons used in this study created an almost flat damage profile up to ~15 $\mu m$ deep from the sample surface within the 9 wt. % Cr model F/M steel specimens as seen in Figure 3.2. Damage rates were calculated using SRIM 2006, stopping power version - 2003 [34]. Electron microscopy samples were fabricated from the flat damage profile region. Samples irradiated to 400 °C were irradiated at the University of Wisconsin Ion Beam Laboratory (UW-IBL) while the 500 °C specimens were irradiated at the University of Michigan Ion Beam Laboratory (MIBL). Table 3.1 summarizes the resulting dose, dose rate, and temperature for each condition irradiated.

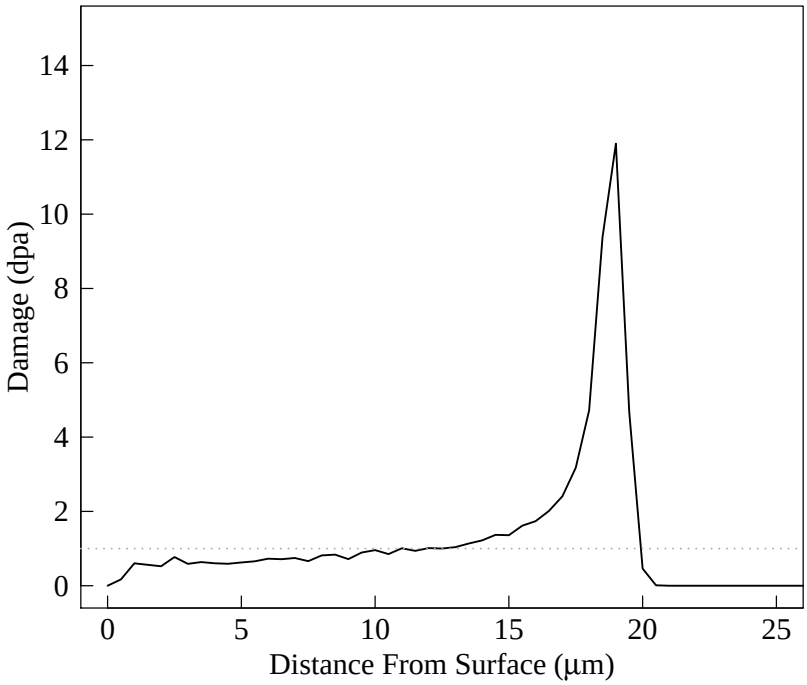


Figure 3.2: Damage profile for a binary homogeneous Fe-9Cr alloy using 2.0 MeV protons with a fluence of $1.1\times10^{19}\ \frac{protons}{cm^2}$.

Table 3.1: Summary of irradiation conditions for proton irradiated samples

| Temperature °C | Dose (dpa) | Dose Rate (dpa/s) |
|---|---|---|
| 400 | 1 | $5.9x10^{-6}$ |
| 400 | 2 | $4.4x10^{-6}$ |
| 400 | 3 | $4.8x10^{-6}$ |
| 500 | 1 | $1.2x10^{-5}$ |
| 500 | 2 | $1.2x10^{-5}$ |
| 500 | 3 | $1.2x10^{-5}$ |

### 3.2.1 400 °C Irradiations of a Model F/M Steel

Samples for irradiation were fabricated from the as-received 9 wt. % Cr model F/M steel bulk material. Electrical discharge machining (EDM) was utilized to create 1 x 3 x 20 mm bar specimens. All samples were mirror polished using standard metallographic techniques prior to irradiation. Samples were mounted to the irradiation stage using strapping bars. Care was taken to minimize the stress applied to the samples from the retention device. The irradiation temperature was controlled by controlling the stage temperature using heating and cooling elements. The stage can be heated using a resistively heated cartridge heater and/or cooled using air cooling lines which run near the surface of the irradiation stage. Sample temperatures were monitored with both thermocouples and thermal imaging equipment. Three k-type thermocouples were spot welded to the surface of sacrificial samples to determine the irradiation temperature. An infrared pyrometer, which was calibrated for the temperature range of the irradiation and the emissivity of the material, was used to measure temperature uniformity across the samples during irradiation. The stage surface is constructed of molybdenum due to its high thermal conductivity and sputtering resistance. Indium was placed between the samples and stage to provide efficient heat transfer between the samples and stage and provide precise temperature control. The temperature was maintained within $\pm$20 °C during the experiment by controlling the back heating and cooling elements.

An aperture system was placed in front of the irradiation stage to define the irradiation area and determine the beam distribution. The full stage configuration including the aperture system is shown in Figure 3.3. The ion beam is rastered across the irradiation area and aperture system to assure uniform beam distribution. The stage is electrically isolated to calculate the beam current as a function of time. A National Instruments LabVIEW system was developed which monitored the beam current and temperature while calculating the total fluence in the material. The system allowed for continuous monitoring during the experiment while providing a history of the irradiation. Alarms were also built in to alert the operator when experimental parameters were outside of predefined acceptable limits. From the experiment history the dose, dose rate, and temperature distribution were calculated which is provided in Table 3.1 .

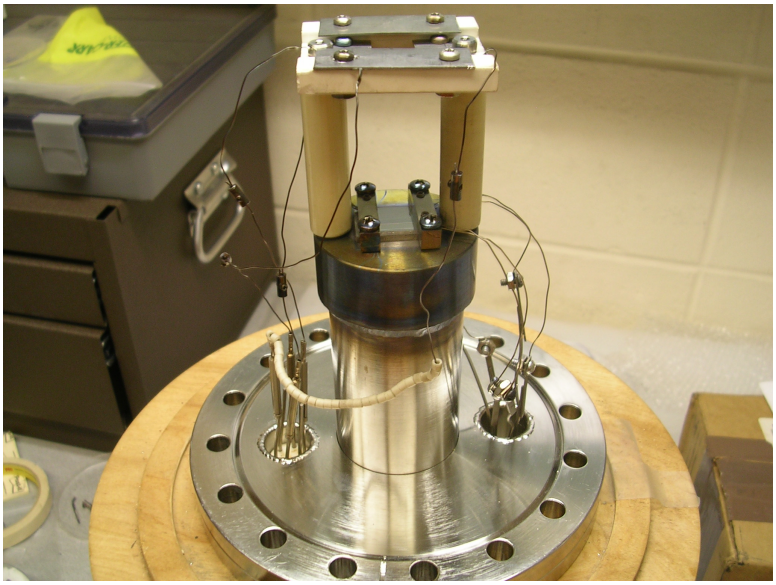

Figure 3.3: Fully assembled sample stage for proton irradiations.

### 3.2.2 500 °C Irradiations of a Model F/M Steel

Sample preparation and experimental configuration for the 500 °C was almost identical to the 400 °C samples. Specimens were 1 x 1 x 20 mm bar specimens fabricated using EDM from

the same heat of the 9 wt. % Cr model steel specimens used in the 400 °C proton irradiations. Samples were mirror polished using standard metallographic techniques. Both k-type thermocouples and an infrared pyrometer where used to monitor temperature. Specimens were maintained at 500 ±10 °C during the experiment. The configuration of the ion source at the MIBL at the time of this study allowed for a higher current of protons to be placed on the stage and for the flux to be more accurately controlled over long exposures. The result is a slightly elevated dose rate over the 400 °C specimens and a nearly uniform dose rate over all doses as seen in Table 3.1 .

## 3.3 Neutron Irradiations of a Model F/M Steel

The same heat of the 9 wt. % Cr model steel specimens used in the proton irradiations were irradiated to 3 dpa at a nominal temperature of 500 ºC in the Advanced Test Reactor (ATR) at the Idaho National Laboratory (INL). Specimens were loaded into a non-instrument lead, inert gas filled rodlet-capsule enclosure and placed in ATR East Flux Trap where the maximum fast flux is $9.7x10^{13}\ \frac{neutrons}{s \cdot cm^2}$ (E > 1 MeV). Dose calculations assumed a dose of 3 dpa in a stainless steel is approximately equivalent to a neutron fluence of $2.1x10^{21}\ \frac{neutrons}{cm^2}$. Based on this assumption, the average dose rate was $1.0x10^{-7}\ \frac{dpa}{s}$ with the reactor operating for 250 Effective Full Power Days (EFPD). The rodlet containing the samples did not have instrument leads or passive temperature monitors and therefore the exact average temperature cannot be determined. Simulations calculated the average temperature to be expected between 523-526 ºC, but an adjacent rodlet during the irradiation campaign was determined to be ~100 ºC lower than the simulated temperature as determined by passive SiC temperature monitors. Another adjacent rodlet did show excellent agreement between predicted and observed temperatures [97].

The SiC temperature monitors have several limitations in determining the irradiation temperature. The SiC monitors work on the principle that neutron irradiation induces a lattice expansion

of the SiC and the expansion can be annealed out when the post-irradiation annealing temperature exceeds the irradiation temperature. Errors in determining the irradiation temperature in SiC monitors has been quoted to be as low as 12 ºC and as high as 100 ºC [98, 99]. SiC temperature monitors work best when the monitors are irradiated at a constant temperature. Errors are introduced when the monitors are irradiated at variable temperatures during the irradiation. If the irradiation temperature rises during the end of an irradiation the early onset defects will be annealed out resulting in the quoted temperature to be skewed towards the higher end irradiation temperature. If the temperature decreases during irradiation the higher temperature defects will be frozen-in while still accumulating lower temperature defects resulting in the quoted temperature indicating the lowest irradiation temperature [100]. The lack of SiC temperatures in the exact rodlet where the samples used for this irradiation and the relative uncertainty in the exact average irradiation temperature quoted by the adjacent SiC temperature monitors results in the large uncertainty of the average irradiation temperature for the neutron irradiated samples.

## 3.4 Heavy Ion Irradiations of a NF-ODS Steel

Heat SM10 of the 14YWT bulk specimens were irradiated using $Ni^{2+}$ ions. The heat of the 14YWT alloy is important as heat to heat variations in the nanocluster distribution exist. Heavy ion irradiations were used due to their high dose rate compared to proton or neutron irradiations. High dose rates were needed to drive the system towards unstable nanoclusters to determine the effect of nanoclusters on RIS is NF-ODS steels [11]. Heavy ion irradiations have the disadvantage of shallow irradiation depth, typically on the order of 1-2 $\mu m$ and requires focused ion beam (FIB) lift out TEM samples for post irradiation examination. Specimens were irradiated at the Environmental Molecular Sciences Laboratory (EMSL) at Pacific Northwest National Laboratory (PNNL). $Ni^{2+}$ ions were produced using a source of negative ions via cesium sputtering (SNICS) ions source and accelerated to 5.0 MeV using a NEC Pelletron tandem accelerator. The beam was rastered across the sample for uniform beam distribution

and irradiation temperature was maintained through beam heating and/or coupled with a rear mounted filament heater or liquid nitrogen cooling. Specimens were irradiated to 100 dpa at -75 ºC, 100 ºC, 300 ºC, 450 ºC, and 600 ºC. The dose and dose rate for the 14YWT specimens were calculated using SRIM2006. The damage rate was calculated to be ~$2x10^{-3}\ \frac{dpa}{s}$. The SRIM damage profile as well as the implanted Ni atomic percent profile can be seen in Figure 3.4.

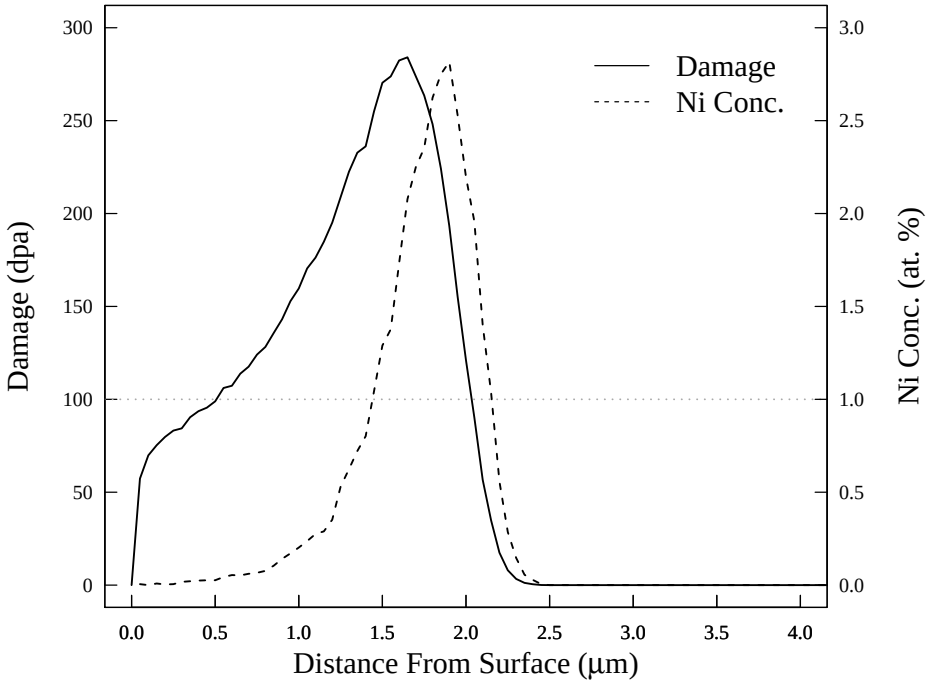


Figure 3.4: Damage profile for a binary homogeneous Fe-14Cr alloy using 5.0 MeV $Ni^{2+}$ with a fluence of $1.5\times10^{17}\ \frac{ions}{cm^2}$.

# 3.5 Scanning Transmission Electron Microscopy (STEM)

## 3.5.1 Sample Preparation

### 3.5.1.1 As-Received and Proton Irradiated Samples

Samples for scanning transmission electron microscopy (STEM) investigations were fabricated using FIB lift-out techniques. Magnetism of F/M steels creates electron beam aberrations during STEM investigations. FIB lift-out samples were needed to reduce the volume size of the samples to minimize these effects. The majority of cross sectional FIB lift-out samples were fabricated using a Hitachi NB-5000 FIB/SEM at Oak Ridge National Laboratory. A small subset of samples were fabricated on a Zeiss 1540XB Crossbeam FIB/SEM at the University of Wisconsin – Madison or a FEI Quanta 3D FEG DualBeam FIB/SEM housed at the Center for Advanced Energy Studies (CAES) at the Idaho National Laboratory.

As-received samples were lifted out from a mirror polished surface in cross section. Irradiated FIB lift-out samples were extracted less than 20 $\mu m$ deep from the irradiated sample surface to maintain a relatively even dose throughout the FIB lift-out foil. The use of FIB lift-out samples eliminated all noticeable aberrations caused by the magnetism of the samples during STEM investigations. The lift-out procedure followed the standard procedures for specimen fabrication except for a few alterations that improved the fabrication process and aided the alignment of the transmission electron microscope.

The first departure from standard sample fabrication techniques was to mount the lifted out lamella within a chevron instead of the normal ‘flag’ mount. Figure 3.5 shows a schematic of the two different mounting configurations on commercially available Omniprobe FIB TEM specimen grids. Locking the lamella on both sides of the sample prior to thinning prevented the sample from warping or bending during thinning. Bending, particularly as the samples reach thicknesses below 200 nm, is prominent in F/M steels due to the residual stress in the sample.

Preventing the sample from relieving this stress resulted in uniform thickness throughout the entirety of the FIB lift-out and minimized FIB induced damage.

Another unique aspect utilized in the FIB lift out procedure was a two-step deposition in the protective top cap of lamella before the 'hog' or bulk cutting process. Typically, only a one step deposition of either C or Pt is deposited which provides a protective cap and minimizes the FIB damage. C caps have the benefit of quick deposition rates and the ability to be applied using an electron beam deposition while Pt caps are more resistant to damage from the Ga ion beam. Samples for this study were first capped using C followed by a subsequent Pt cap on top of the C cap. This provided the benefit of both types of protective caps while also giving an excellent amorphous area of electron transparent C after thinning to perform alignment procedures during TEM and STEM investigations. The C cap assisted in using a fast Fourier transform (FFT) method for objective lens stigmation and the use of a Ronchigram for condenser lens stigmation and condenser aperture centering while in STEM mode. All FIB lift-outs were finished using a low energy (keV), low current (pA) beam to remove Ga contamination from the surface and reduce the observable FIB induced damage during STEM investigations. An SEM micrograph of a finished FIB lift-out is provided in Figure 3.6.

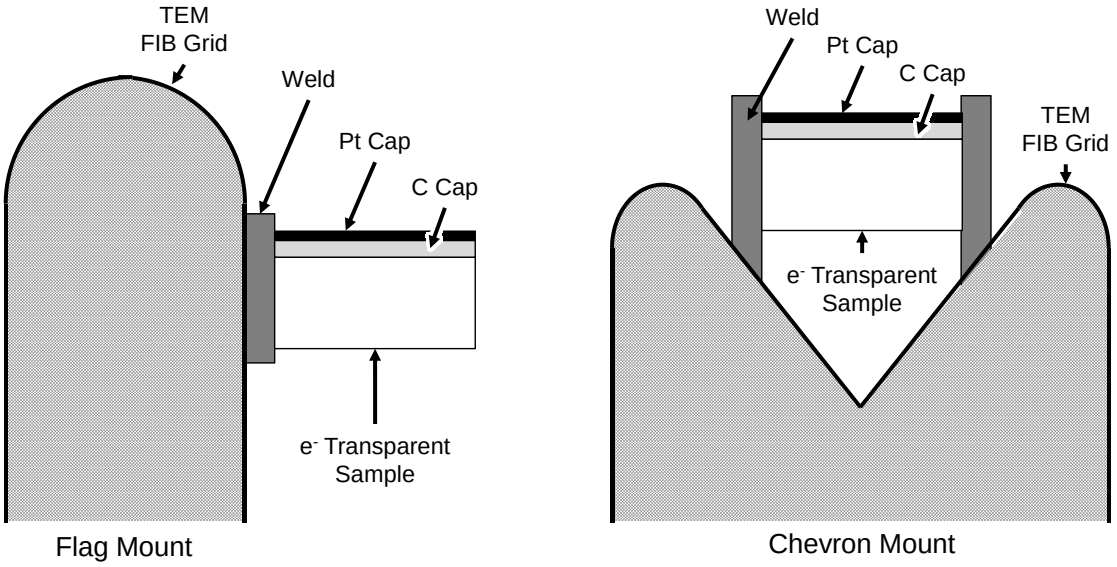


Figure 3.5: Schematic of FIB lift out sample mounting and preparation technique. Chevron mounting prevented sample warping during the thinning process.

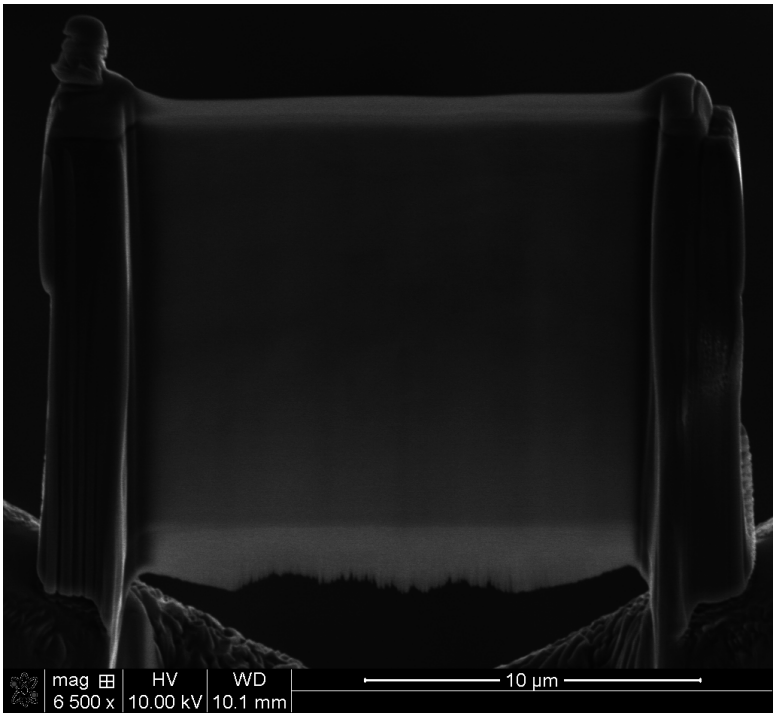


Figure 3.6: SEM micrograph of an electron transparent FIB lift-out 9 wt. % Cr model as-received specimen for STEM investigations. Specimen mounted using the chevron mounting technique.

#### 3.5.1.2 Neutron Irradiated Samples

The same process for the proton-irradiated samples was used for the neutron irradiated samples. The FIB lift-out techniques had the added advantage of significantly reducing the activity level of the neutron irradiated specimens. A FEI Quanta 3D FEG DualBeam FIB/SEM housed at the Center for Advanced Energy Studies (CAES) at Idaho National Laboratory was used. The CAES facility was used as it is only one of a few laboratories equipped to handle radioactive samples available to university researchers. Standard procedures for handling radioactive samples were followed during the specimen fabrication process.

#### 3.5.1.3 Heavy Ion Irradiated Samples

The same TEM specimens used by A. Certain for EFTEM studies [11] was used here for STEM investigations. The shallow damage region in the heavy ion irradiated samples required planar focused ion beam lift out samples. A Hitachi NB-5000 FIB/SEM at Oak Ridge National Laboratory was used to perform the focused ion beam lift out procedure. A 12 x 5 $\mu m$ Pt deposition was performed on the irradiated surface. The sample was then milled around the platinum cap and undercut to release the specimen from the bulk sample. The sample was then lifted out and mounted to the chevron posts on Omniprobe FIB TEM specimen grids. The mounting procedure was identical to the chevron mount in Figure 3.5. Mounted lift-outs were then thinned using the same thinning techniques for neutron and proton irradiated specimens.

### 3.5.2 Microchemical Mapping

#### 3.5.2.1 As-Received and Proton Irradiated Samples

Specimens of interest were investigated using a Philips CM200-FEG operated in scanning transmission electron microscopy (STEM) mode with an accelerating voltage of 197 kV and equipped with an EDAX energy dispersive X-ray spectroscopy (EDS) detector. The Philips CM200-FEG is housed within the Shared Research Equipment User Facility (ShaRE) at Oak Ridge National Laboratory (ORNL). Acquisition was accomplished using Gatan DigiScan software. 2D EDS spectrum imaging techniques were used as it provides a detailed map of the microchemical inhomogeneities at lath boundaries and limits sample integrity loss compared to more traditional 1D profile line scans [101]. A few lath boundaries where investigated using both spectrum images and profile line scans. The resulting quantification for spectrum images and profile line scans from the same region of interest were equivalent within the experimental error.

STEM investigations were performed using annular dark field (ADF) imaging. The predominantly diffraction contrast image formation of ADF over the mass contrast dominated imaging provided by high angle annular dark field imaging resulted in clear imaging of the lath boundaries of interest and gave enough features near the boundary for drift correction. 48 x 96 nm drift corrected spectrum images were acquired from lath boundaries that were orientated edge-on to the electron beam and free of nearby on-boundary precipitates. Spectrum images contained 32 x 64 pixels, an incident probe size of ~1.5 nm at FWHM, a 1 second dwell time per pixel, and ~1 nA incident probe current. Spectrum images were drift corrected every 32 pixels during acquisition. Drift was minimized to lower than the 1.5 nm pixel spacing per drift correction to limit position errors during scans. The ADF signal was also recorded at each pixel simultaneously with the EDS signal. Total acquisition time was approximately 40 minutes for a typical spectrum image.

Spectrum images were saved in Gatan's Digital Micrograph DigiScan raw format (*.dat) and proprietary *.dm3 format after acquisition. The raw *.dat format records the number of x-ray counts per channel at each x-y position during acquisition while the *.dm3 format records tagging information, such as magnification, time constant, and energy per channel, along with the raw spectrum image. The raw *.dat format is also easily importable into other software, including the MATLAB programming environment. ADF images were saved in uncompressed *.dm3, *.tiff, and *.dat formats. Contrast images in the raw *.dat format record the detector intensity at each x-y position during acquisition and is importable into standard programming environments.

#### 3.5.2.2 Neutron Irradiated Samples

A FEI Tecnai F30-FEG S-TWIN operated in STEM mode with an accelerating voltage of 300 kV and equipped with an EDAX energy dispersive X-ray spectroscopy (EDS) detector housed at Center for Advanced Energy Studies (CAES) at Idaho National Laboratory was utilized in this study to investigate microchemical variations within the neutron irradiated specimens.

Spectrum image acquisition was handled using FEI's TEM Imaging and Analysis software (TIA). Spectrum images were acquired using ADF imaging. Lath boundaries were investigated using 2D EDS spectrum imaging. Spectrum images used similar settings to the proton irradiated samples with a region of interest size of 48 x 96 nm containing 32 x 64 pixels, an incident probes size of ~1-2 nm at FWHM, a 1 second dwell time per pixel, and drift correction after every 32 pixels. The probe current was not directly measured. Spectrum images were drift corrected every 32 pixels during acquisition. Drift was minimized to lower than the 1.5 nm pixel spacing per drift correction to limit position errors during scans. The ADF signal was also recorded at each pixel simultaneously with the EDS signal acquisition. Total acquisition time was approximately 40 minutes for a typical spectrum image. Spectrum images were saved in TIA's tagged *.emi format and raw *.ser format. The raw *.ser format is easily importable into other software and programming environments for data analysis. The ADF signal was saved in TIA's tagged *.emi format and in the uncompressed *.tiff format.

#### 3.5.2.3 Heavy Ion Irradiated Samples

Heavy ion irradiated and as-received 14YWT-SM10 specimens were investigated using a FEI Titan S-Twin D2080 CEOS Cs corrected (S)TEM operated in STEM mode with an accelerating voltage of 200 kV housed at the Materials Science Center (MSC) at the University of Wisconsin - Madison. The FEI Titan is equipped with an EDAX energy dispersive X-ray spectroscopy (EDS) detector and spectrum image acquisition is handled using FEI's TEM Imaging and Analysis software (TIA). The CEOS probe aberration corrector was not utilized during acquisition as high resolution imaging was not required for microchemical analysis. Edge on ferritic grain boundaries were investigated for microchemical variations using spectrum imaging techniques. 2D EDS spectrum images were acquired with a region of interest size of 50 nm x 50 nm containing 50 x 50 pixels, a 500 ms dwell time per pixel, drift corrected every 50 pixels, and with simultaneous ADF signal acquisition turned on. Drift was minimized to reduce position error over the duration of the scan. Total time for a typical acquisition was

approximately 25 minutes. Spectrum images were saved in TIA's tagged *.emi format and raw *.ser format. The ADF signal was saved in TIA's tagged *.emi format and in the uncompressed *.tiff format.

### 3.5.3 Spectrum Imaging Data Analysis

#### 3.5.3.1 Model F/M Steel

The same quantification algorithm was used for data generated from the as-received, proton and neutron irradiated samples in the 9 wt. % Cr model F/M steel. The algorithm was built using the MATLAB programming platform. Raw data files from TIA and Digiscan were imported and processed to determine the microchemical composition at each pixel resulting from the spectrum imaging technique. Samples were assumed to adhere to the thin film criterion during elemental quantification. The script assumes a normalized Fe-Cr binary alloy system. The script calculates the integrated characteristic X-ray intensities at each pixel for the Cr $K_\alpha$ and Fe $K_\alpha$ peaks. Once the integrated X-ray intensities are known the composition is quantified at each pixel using the Cliff-Lorimer equation [102]:

$$\frac{C_{Cr}}{C_{Fe}} = k_{CrFe}\frac{I_{Cr}}{I_{Fe}} \tag{3.1}$$

and

$$C_{Cr} + C_{Fe} = 1 \tag{3.2}$$

where $C$ is the concentration of Cr and Fe, $I$ is the integrated characteristic X-ray intensities and $k_{CrFe}$ is the correlation factor between $C$ and $I$. The correlation factor, or k-factor, was calculated experimentally by measuring the concentration far away from the grain boundary

segregation. Once the composition of Cr and Fe was calculated, quantitative 2D concentration maps can be generated. Figure 3.7 shows a representative concentration map generated using the custom script and the ADF image acquired during the EDS acquisition. Concentration maps revealed the general microchemistry around the boundary. Several boundaries investigated exhibited small Cr-rich precipitates which were not revealed using standard TEM or STEM contrast imaging. Boundaries which contained these low-contrast precipitates were removed from the overall analysis as it is hypothesized the precipitates may change the mechanism for RIS at the boundary.

2D concentration maps are difficult to interpret for quantitative data analysis including the width and magnitude of the Cr segregation to grain boundaries. To overcome this deficiency, spectrum images were also post processed to generate 1D concentration profiles. Each spectrum image was binned 32 pixels along the boundary direction. The total counts in the Cr $K_\alpha$ and Fe $K_\alpha$ were summed over the 32 pixels resulting in increased total counts in each peak over the pixel by pixel quantification used in the concentration maps. The Cliff-Lorimer equation, Eq. 3.1, was used to calculate the concentration of each binned pixel in weight percent. The error at each point in the 1D concentration profiles was calculated based on the total counts in each binned x-ray peak and the error associated with the k-factor calculation. It is assumed the majority of the error in the quantification is based on the counting statistics of the EDS technique and it obeys Gaussian statistics [103]. The relative error is calculated for the summed x-ray intensity by:

$$Rel.\,Error = \frac{3\sqrt{N}}{N} \times 100\% \tag{3.3}$$

where the error is based on 99.7% confidence and $N$ is the number of counts in the peak above background. Error in the k-factor measurement is calculated using the student's t distribution as it is assumed the measurements are made in a single phase region. The k-factor error is given by,

$$Rel.\,Error = \frac{t_{99}^{n-1} S}{\sqrt{N}} / \overline{N} \tag{3.4}$$

where $t_{99}^{n-1}$ is the Student T value, $S$ is the standard deviation, $N$ is the number of measurements made to determine the k-factor value. The total error at each binned pixel is calculated summing the errors in quadrature. From Eq. 3.3 and Eq. 3.4, it can be seen the best way to minimize the total error in the measurement is by increasing the number of counts in each peak and increasing the number of measurements made for each k-factor calculation. Practically, the best way to increase the number of counts while still using the same microscopy instrumentation and spectrum imaging conditions is to increase the thickness of the sample. Increasing the thickness of the sample increases the count rate but has the disadvantage of making measurements more prone to boundary inclination and beam broadening effects as discussed in Section 2.7. Therefore, a delicate balance must be struck to increase count rate but limit other sample-induced errors during the measurements.

1D concentration profiles were fitted using a non-linear optimization algorithm to fit a single Gaussian peak function to the profiles. From the calculated Gaussian peak function the peak Cr and Fe content at the boundary, the full-width at half maximum, and area under the segregation profile were calculated. Figure 3.8 shows the 1D concentration profile for Cr calculated from the raw data presented in Figure 3.7 and the resulting fit using the Gaussian peak function.

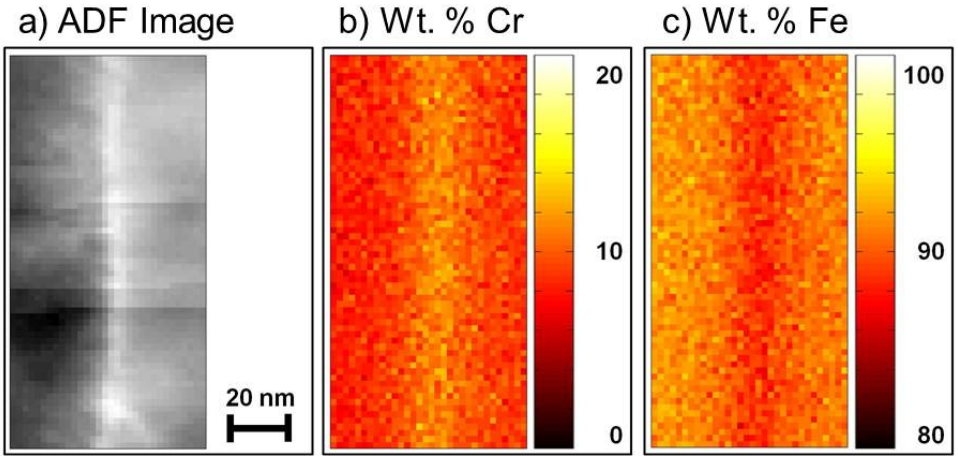


Figure 3.7: Quantitative concentration maps from a LAGB ($\theta$ = 3.7° <$\bar{2}\,\bar{1}\,\bar{6}$>) irradiated to 3 dpa at 400 °C. The ADF STEM image (a); Cr map (b); Fe map (c).

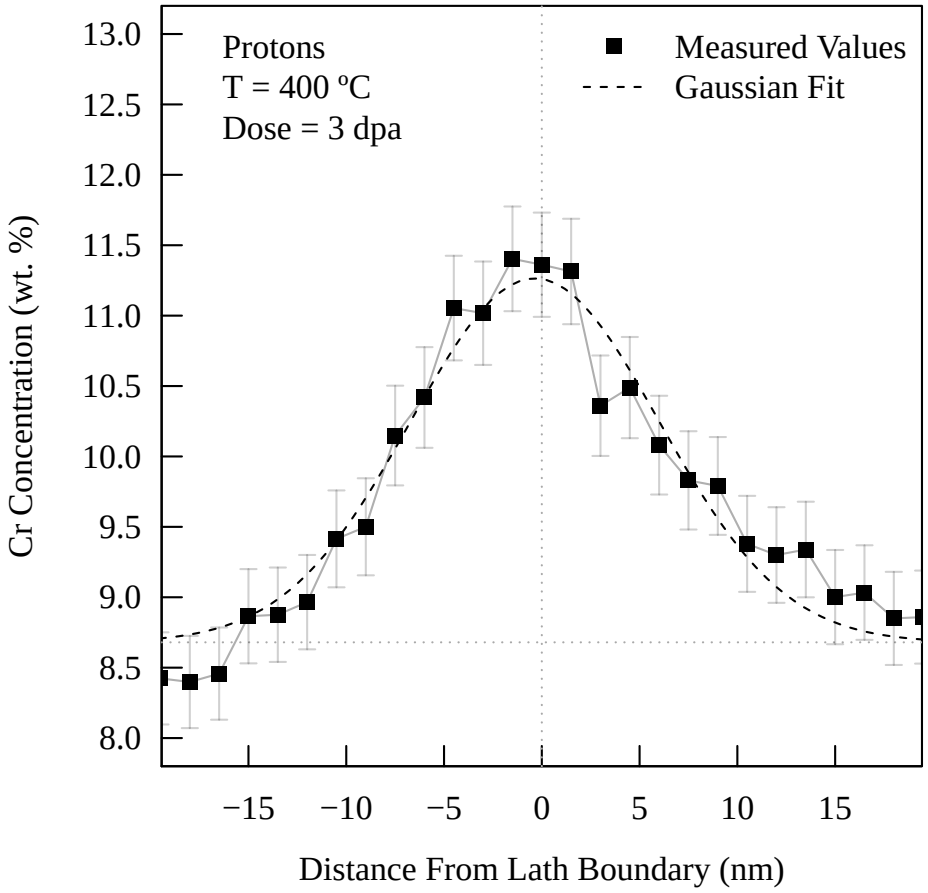


Figure 3.8: 1D Cr concentration profile from a LAGB ($\theta$ = 3.7° <$\bar{2}\,\bar{1}\,\bar{6}$>) irradiated to 3 dpa at 400 °C. The measured on-boundary Cr concentration was 11.4 wt. % while the Gaussian fit calculated a Cr concentration of 11.3 wt. %. Segregation peak FWHM calculated as 15.0 nm with an area of 41.2 $nm \cdot wt.\%$.

#### 3.5.3.2 NF-ODS Steel

The complicated microchemical nature of the 14YWT-SM10 alloy required a more complex data analysis algorithm for determining microchemical variations near grain boundaries compared to the model F/M steel. The analysis algorithm for the model F/M steel was expanded to include microchemical species not observed in the model F/M steel including Ni, W, Y and

Ti. Raw data files from TIA were imported and processed to determine the qualitative and semi-quantitative composition at each pixel. The script calculated the integrated characteristic X-ray intensities at each pixel for the Fe $K_\alpha$, Cr $K_\alpha$, Ni $K_\alpha$, W $L_\alpha$, Y $K_\alpha$, and Ti $K_\alpha$ peaks. From the integrated X-ray intensities, qualitative concentration maps were generated. Contrast in the maps were normalized. Figure 3.9 shows representative concentration maps generated using the custom script. Qualitative concentration maps revealed the spatial dependence and relative concentrations of alloying species near the grain boundary. To further examine the relationship between microchemistry and microstructure, a RGB color overlay map was used to determine the relative concentration of Fe, Cr, and Ti at the boundary. Fe and Cr serve as markers for matrix contributions while the Ti overlay serves as a marker for nanocluster distribution near and on the boundary. An example of the RGB color overlay map is in Figure 3.10 where Cr, Fe, and Ti are depicted in red, blue, and green respectively.

The script assumes Ti, Y, and O are solely contained within the nanoclusters and do not contribute to the matrix or grain boundary EDS signal. This assumption is supported by APT results [11]. The result of the assumption is the bulk and grain boundary composition can be computed assuming a normalized ternary system of Fe, Cr, and W, but the results are only semi-quantitative as mixing of other solutes within the matrix and the addition of Ni atoms within the matrix could be present. The composition of nanoclusters was not calculated due to limitations in deconvoluting the chemistry of embedded particles from the matrix signal. The k-factors used in quantification using the Cliff-Lorimer equation were calculated experimentally by measuring the concentration far away from the grain boundary. Semi-quantitative 2D concentration maps were generated from the calculated compositions at each pixel using the Cliff-Lorimer equation in atomic percent. 1D concentration profiles were also generated by binning the entire 50 pixel map along the boundary direction. An example of a concentration profile is in Figure 3.11. Error was calculated based on the counting statistics of the EDS technique with a 68% confidence. 1D concentration profiles were fitted using a non-linear optimization algorithm to fit a single Gaussian peak function to the profiles. From the peak function, the peak Cr and Fe concentration at the boundary and the FWHM at the boundary

was calculated. For profiles exhibiting 'w-shaped' concentration profiles, an example of which is in Figure 3.11, the on-boundary Cr concentration was determined from the experimental data at the boundary and not from the peak fitting function.

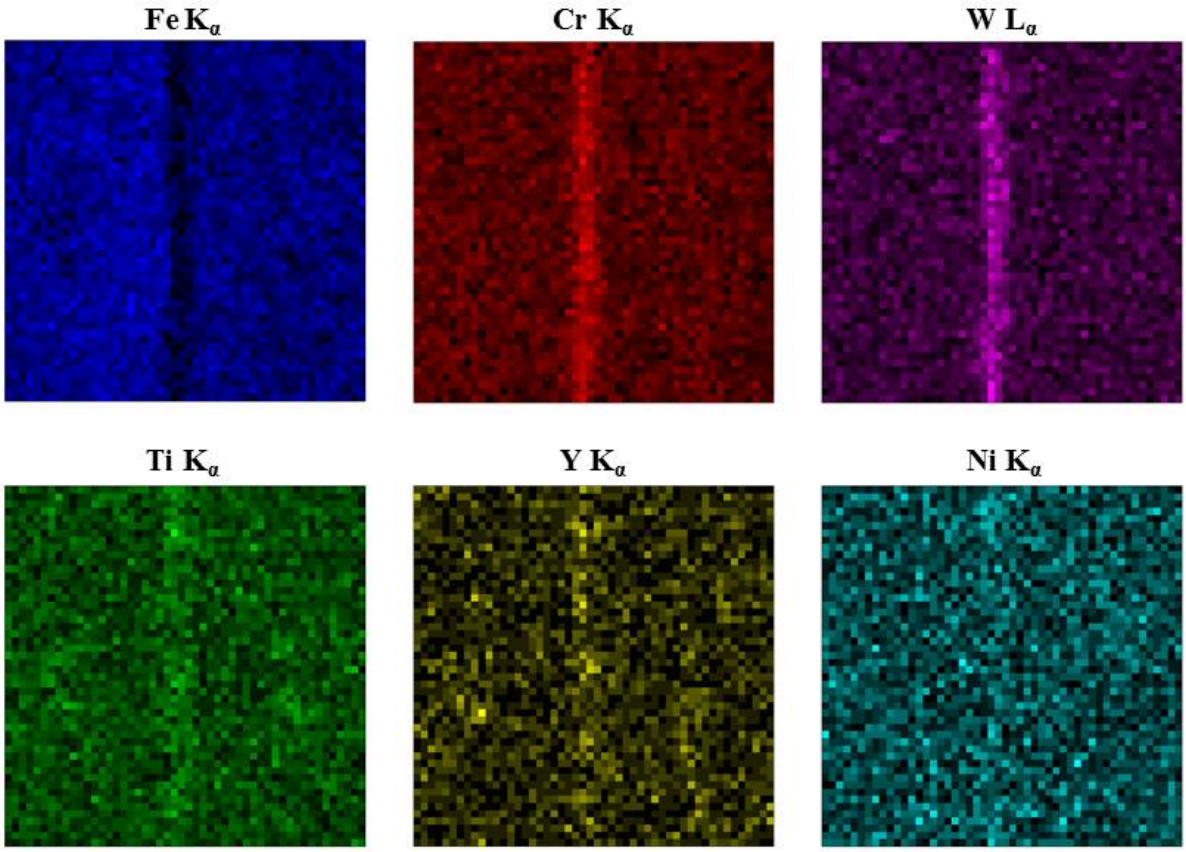


Figure 3.9: Qualitative concentration maps from an as-received grain boundary in 14YWT. Each map is 50 x 50 pixels corresponding to a region of interest of 250 $nm^2$.

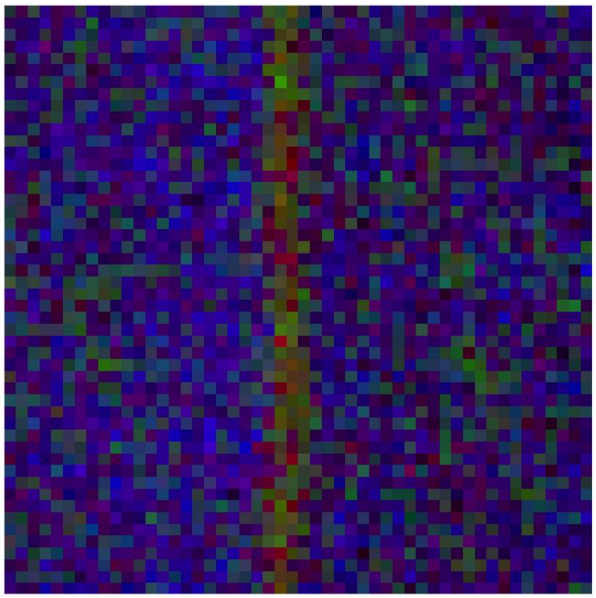

Figure 3.10: Qualitative RBG overlay map of Fe, Cr, and Ti from an as-received grain boundary in 14YWT. Overlay generated from maps calculated and shown in Figure 3.9. Cr, Fe, and Ti are depicted in red, blue, and green respectively. Map is 50 x 50 pixels corresponding to a region of interest of 250 $nm^2$.

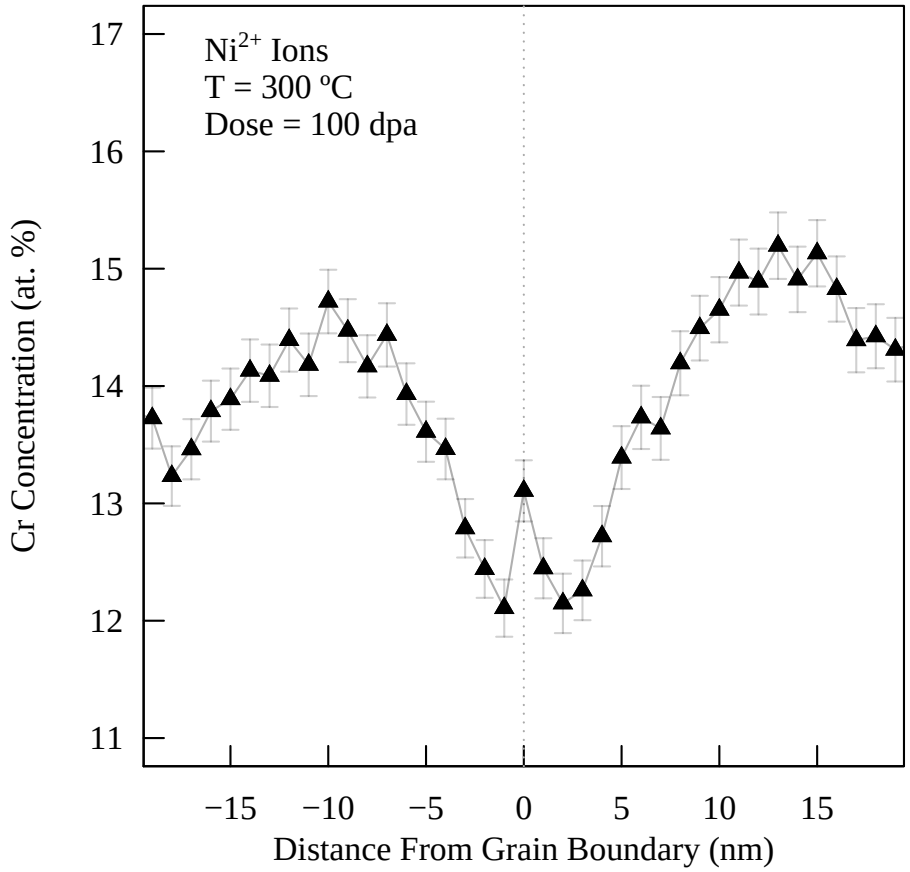


Figure 3.11: 1D Cr concentration profile from general high angle grain boundary in 14YWT irradiated to 100 dpa at 300 °C. The profile shows a typical 'w-shaped' profile observed at lower irradiation temperatures in 14YWT.

### 3.5.4 Kikuchi Pattern Analysis

Lath boundary misorientation axis/angle pairs were determined in STEM mode immediately following the acquisition of each spectrum image for all specimens and irradiation conditions. Diffracted Kikuchi patterns were captured for each lath that comprised a lath boundary using a post column CCD camera. Patterns were post processed using a logarithmic filter to improve the contrast of the Kikuchi lines with the background signal. An example of a Kikuchi pattern

with a logarithmic filter applied obtained from an as-received 9 wt. % Cr model sample is presented in Figure 3.12. Laths were considered to have a body-centered cubic (BCC) crystallography. Diffracted Kikuchi patterns were indexed using a specialized software program, Euclid's Phantasies v1.1 (EP v1.1), developed by J.J. Fundenberger *et al.* [104]. The program can quickly index Kikuchi pattern orientations with minimal user input and output lath orientations in Euler's angles. Kikuchi patterns were indexed in EP v1.1 by manually selecting Kikuchi bands. The indexed output from EP v1.1 of Figure 3.12 is presented in Figure 3.13 as an example. Calculated lath orientations from EP v1.1 were then used to calculate the axis/angle pair of each lath boundary investigated. A freeware program, TexTools v3.3, was utilized to calculate the grain boundary axis/angle pair [105]. Calculated axis/angle pairs where compared with tabulated values of the axis/angle pairs for all possible low Σ-CSL boundaries for cubic systems.

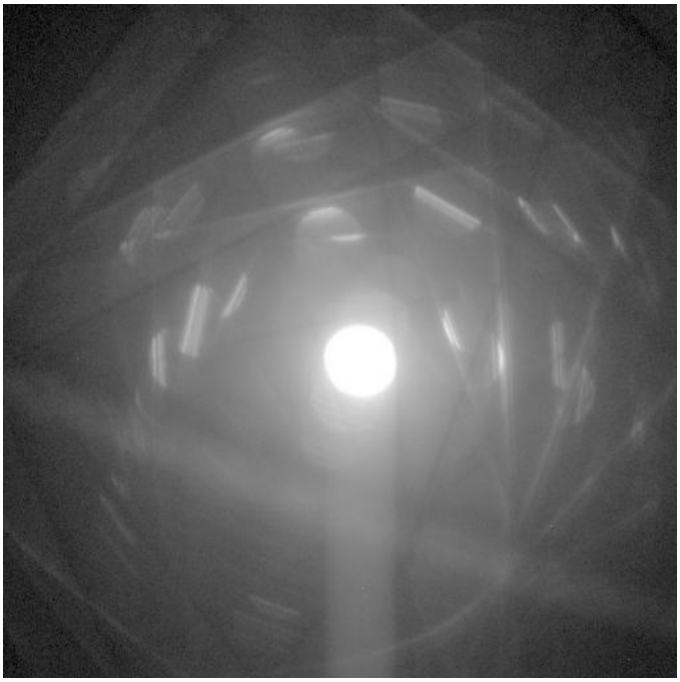

Figure 3.12: Example diffracted Kikuchi pattern from an as-received 9 wt. % Cr F/M model steel lath. The vertical band extending from the undiffracted beam is an artifact due to over saturation in the CCD camera. The calibrated camera length is 119 mm.

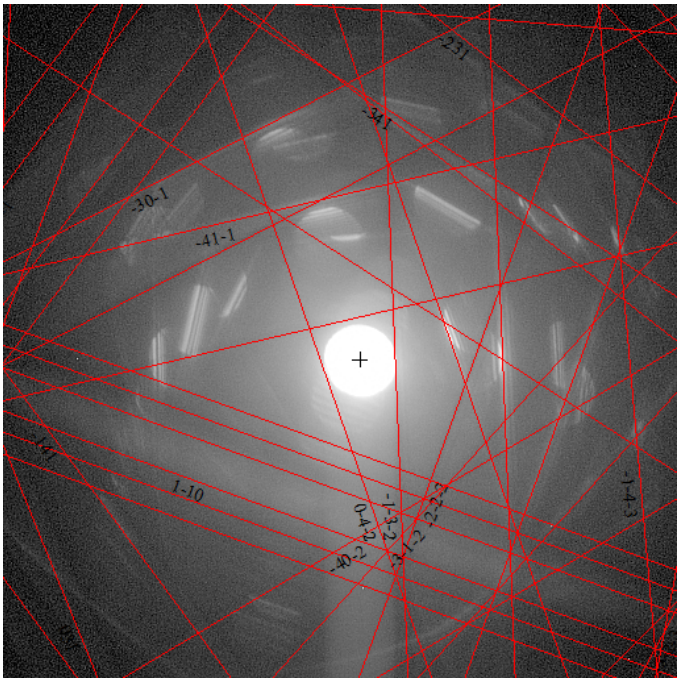


Figure 3.13: Example of fully a indexed Kikuchi pattern of the Kikuchi pattern presented in Figure 3.12 using EP v1.1. The lath orientation was determined to be $\varphi_1$: 283.02, $\Phi$: 32.6, $\varphi_2$: 220.12.

# Chapter 4

# Results

## 4.1 Model F/M steel

A complete database of all lath boundaries investigated including the on-boundary Cr content, the misorientation angle, misorientation axis, calculated full-width at half maximum (FWHM) of the segregation profile, and the integrated area under the segregation peak is found in Appendix B for the 9 wt. % Cr model F/M steel. Table 4.1 summarizes the number of observations made for each boundary type at each irradiation condition. The misorientation angles of the investigated lath boundaries provides insight into the general grain boundary character distribution of lath boundaries in the model F/M steel. Figure 4.1 is a grain boundary character distribution plot generated from Table 4.1. Figure 4.1 includes only eighty eight lath boundaries in the total analysis, which is statistically too low to provide confidence in the overall bulk lath boundary character distribution, but does indicate the majority of lath boundaries in the 9 wt.% Cr model steel are high coherency boundaries with either a low angle or $\Sigma 3$ grain boundary structure. This is an expected result as the orientation relationship during the transformation of the parent austenite grain into lath martensite constrains the laths into specific orientations preventing the formation of a large fraction of low coherency boundaries [14].

The as-received material was investigated for prior Cr segregation at lath boundaries. No Cr or Fe segregation was detected at all lath boundaries investigated in the as-received condition. Figure 4.2 shows a representative quantitative concentration map of Cr and Fe and the corresponding ADF STEM image. 1D concentration profiles of the as-received lath boundaries showed no variance in the microchemistry near the boundaries within the error of the experiment. All lath boundaries investigated in the as-received condition, as seen in Table 4.1 and

Figure 4.1, were determined to be low-angle grain boundaries. No information exists on the Cr and Fe distribution at lath boundaries at general high angle or special grain boundaries in the observed samples in the as-received state; however, it is assumed no prior segregation exists at these boundaries. This assumption is supported by Wharry *et al.* who found no prior segregation to grain boundaries in T91 on prior austenite grain boundaries which are preferentially general high angle grain boundaries [81]. A wide range of RIS responses were observed at lath boundaries in the model F/M steel. The overwhelming qualitative response observed, as seen in Appendix B, is Cr enrichment and corresponding Fe depletion. Due to the assumption of a binary Fe-Cr system in the quantification algorithm and the inability of standard EDS techniques to accurately detect low-Z elements, no information on the C behavior after irradiation is known.

The database generated on the RIS response revealed a large amount of experimental scatter at all conditions observed. A detailed discussion of the accuracy and efficiency of using STEM-EDS to measure interfacial/planar segregation is provided in Section 2.7. Experimental scatter in trends where the misorientation angle is the independent variable was expected due to the random nature in the selection of the grain boundaries which allows for all five degrees of freedom to be available for grain boundaries while the present results use only a three parameter representation to determine the grain boundary structure. Some concentration profiles revealed non-symmetric Cr enrichment around the lath boundary origin which also contributes to the experimental scatter observed. An example of a non-symmetric profile is provided in Figure 4.3. Tailing of the profile can be the result of several factors including boundary inclination to the beam during acquisition, grain boundary motion during irradiation due to point defect capture, or due to the differences in diffusivity of defects and solutes along close packed or more open planes due to non-symmetric misorientation of grains [90, 106–108]. Deconvolution of which factor(s) contributed to the asymmetric concentration profiles would require knowledge of the experimental system not available during this investigation. Other experimental factors, including the sample thickness and probe size variation from session to session only serve to increase the observed scatter in the experimental database. The scatter in the data dictated the

large data set summarized in Table 4.1 and Appendix B to verify overall trends in the RIS response.

Given the experimental scatter, the largest variation in the Cr segregation after proton irradiation was due to variances in the grain boundary structure. The proton irradiation parameters, including dose and temperature, also altered the RIS response but the grain boundary structure was the most significant contributing factor to the RIS response. On-average, grain boundary structure resulted in variances up to ~3 wt. % in the on-boundary Cr concentration for boundaries irradiated under the same conditions while changes in dose or temperature for the same grain boundary type were on the order of 1-2 wt. %. The variations seen in the RIS response due to grain boundary structure were also reflected in the neutron irradiated samples. Three distinct regimes were identified based on grain boundary structure and energetics described in Section 2.2. The three regimes were: low angle grain boundaries (LAGBs), special (low-$\Sigma$ CSL) grain boundaries, and general high angle grain boundaries. Grain boundaries adhered to the same trends within these three regimes over all irradiation conditions including dose, temperature, and incident particle except trends in the segregation width for neutron irradiated samples.

Table 4.1: Irradiation conditions and grain boundaries observed in each experimentally determined regime. Average on-boundary Cr content is not provided as it varies greatly for low angle and special grain boundaries.

| Temperature (°C) | Incident Particle | Dose (dpa) | Dose Rate (dpa/s) | # of LAGBs Meas. | # of Σ3 GBs Meas. | # of Gen. HAGBs Meas. |
|---|---|---|---|---|---|---|
| - | - | - | - | 5 | 0 | 0 |
| 400 | Protons | 1 | $5.9x10^{-6}$ | 15 | 2 | 2 |
| 400 | Protons | 2 | $4.4x10^{-6}$ | 14 | 0 | 2 |
| 400 | Protons | 3 | $4.8x10^{-6}$ | 9 | 4 | 1 |
| 500 | Protons | 1 | $1.2x10^{-5}$ | 4 | 1 | 1 |
| 500 | Protons | 2 | $1.2x10^{-5}$ | 8 | 1 | 0 |
| 500 | Protons | 3 | $1.2x10^{-5}$ | 5 | 1 | 2 |
| 500 | Neutrons | 3 | $1.0x10^{-7}$ | 3 | 4 | 4 |

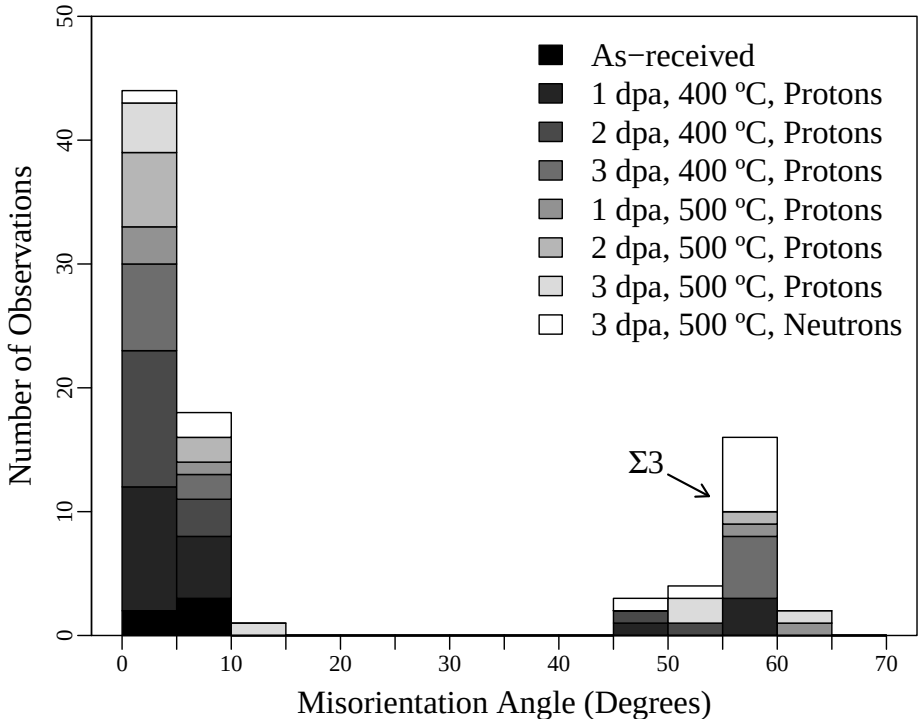


Figure 4.1: Grain boundary misorientation distributions for all lath boundaries observed in the model F/M steel. A significant portion of boundaries where high coherency boundaries including very low angle grain boundaries and Σ3 grain boundaries.

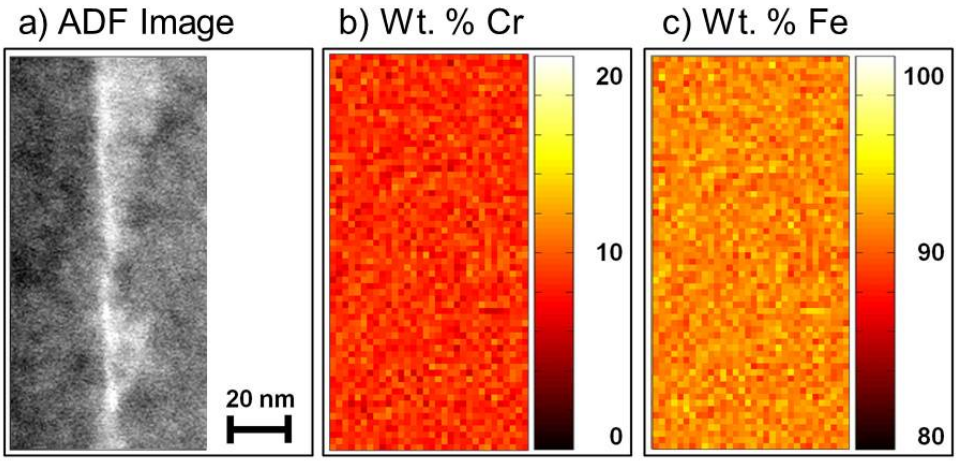


Figure 4.2: Quantitative concentration maps showing no segregation to the lath boundary in an as-received LAGB ($\theta$ = 8.9° <6 $\bar{1}$ $\bar{2}$>). The ADF STEM image (a); Cr map (b); Fe map (c).

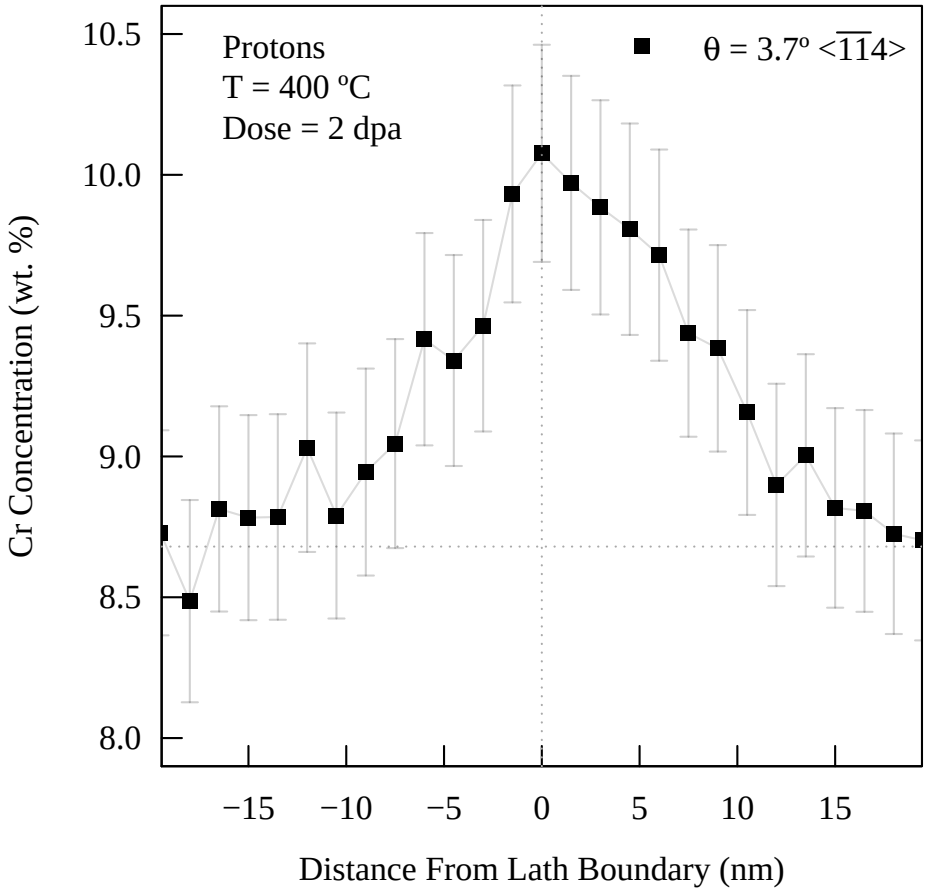


Figure 4.3: 1D Cr concentration profile from a LAGB ($\theta$ = 3.7° <$\bar{1}\,\bar{1}\,4$>) irradiated to 2 dpa at 400 °C. The profile shows asymmetry around the origin with tailing of the profile for positive distances from the boundary origin.

### 4.1.1 Low Angle Grain Boundary RIS Response

LAGBs exhibited the largest variation in the maximum on-boundary Cr content and width of the segregation profile from boundary to boundary. Cr enrichment increased with increasing misorientation angle with very low angles ($\theta \lesssim 5°$) showing almost no segregation to the boundary and larger angle low angle grain boundaries having Cr enrichment of several weight percent to the boundary. Figure 4.4 shows 1D concentration profiles for select grain boundaries in the

LAGB regime irradiated using protons to 2 dpa at 400 °C. The increase in the Cr enrichment is consistent with the increase in the primary grain boundary dislocations and grain boundary energy increasing with misorientation. The scatter in the calculated on-boundary Cr content resulted in difficulties in determining the exact relationship between the misorientation angle and peak segregation as both a linear or logarithmic regression fit to the data showed similar coefficients of determination; although, both fits did indicate the trend of increasing segregation with misorientation. The width of the segregation profiles in the LAGB regime decreased with misorientation angle for proton irradiated boundaries in the low angle grain boundary regime. Typical segregation profiles were quite broad in proton irradiated specimens with the FWHM being on the order of tens of nanometers and decreased with increasing misorientation angle. This behavior is seen for LAGBs irradiated using protons to 2 dpa at 400 °C in Figure 4.5. Neutron irradiated lath boundaries had lower FWHM values compared to the proton irradiated specimens. The limited observations of LAGBs in the neutron irradiated specimen prevents the determination in trends as a function of misorientation in the LAGB for the neutron irradiated specimen.

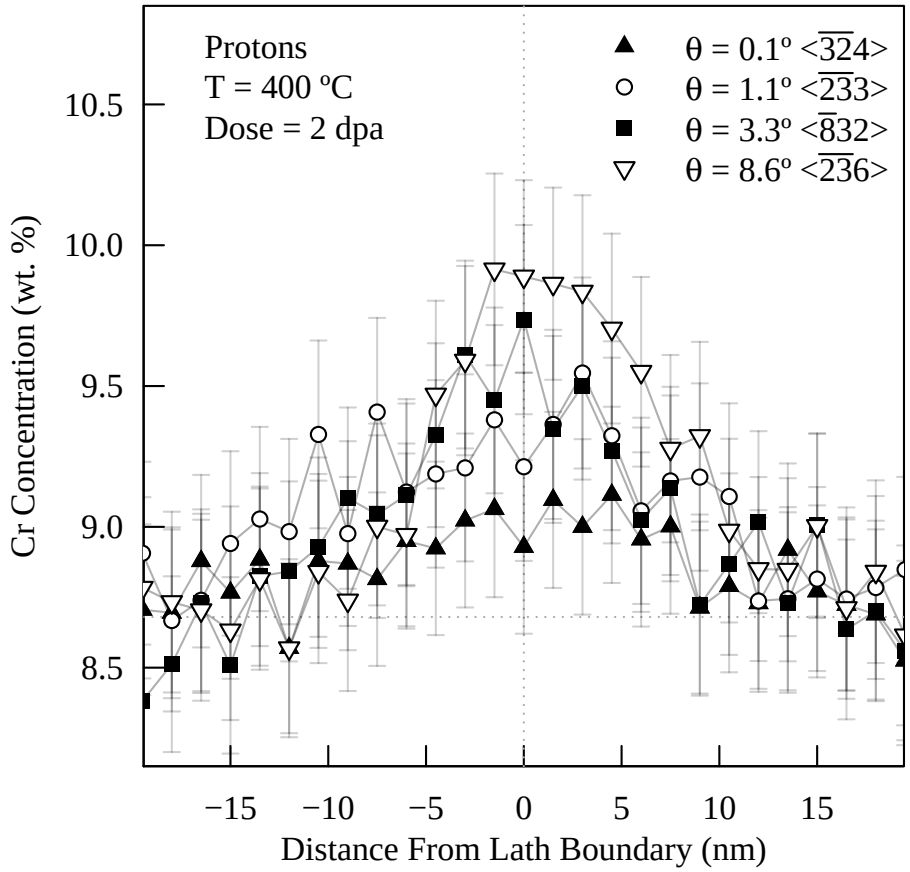


Figure 4.4: 1D Cr concentration profile for select LAGBs irradiated to 2 dpa at 400 °C using protons. The measured on-boundary Cr concentration increases with increasing misorientation.

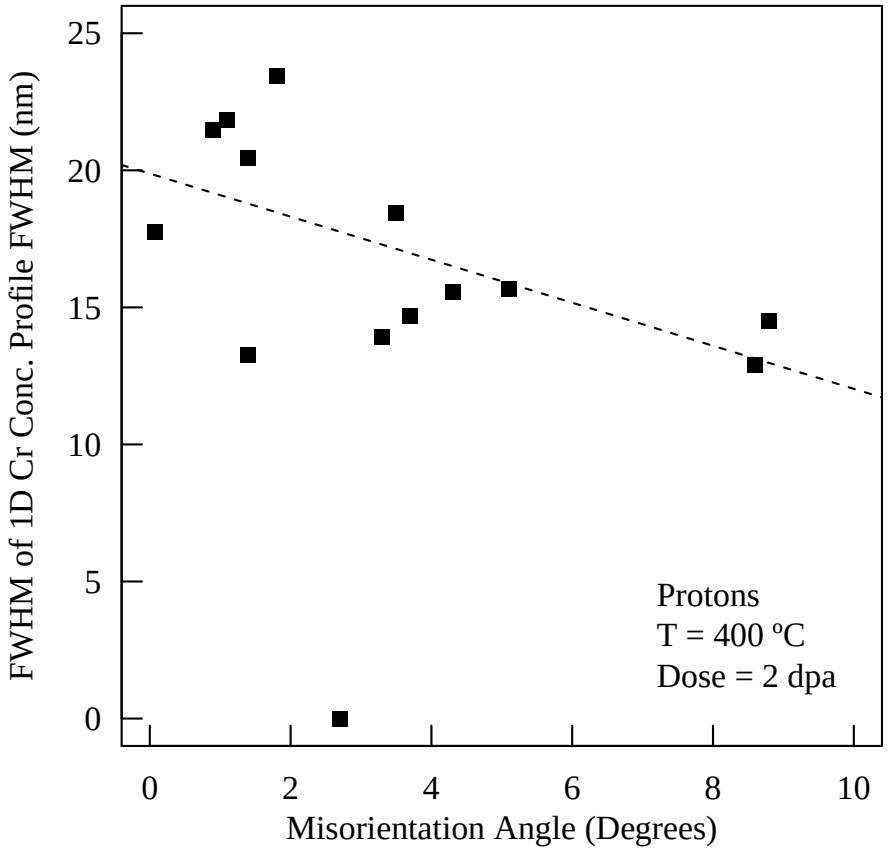


Figure 4.5: Calculated FWHM of 1D Cr concentration profiles for LAGBs irradiated to 2 dpa at 400 °C using protons. Dashed line indicates linear regression with the outlier at $\theta = 2.7°$ removed from the regression analysis.

## 4.1.2 High Angle Grain Boundary RIS Response

### 4.1.2.1 Coincident Site Lattice Grain Boundaries

The only CSL boundaries observed in the data set were $\Sigma 3$ or near $\Sigma 3$ grain boundaries in both the proton and neutron irradiated samples. The $\Sigma 3$-CSL boundaries in the proton irradiated condition exhibited similar amounts of Cr segregation including the amount and width to the

boundary as LAGBs. A comparison between a proton irradiated LAGB and a $\Sigma 3$ grain boundary is presented in Figure 4.6. $\Sigma 3$ boundaries have boundary coherency similar to LAGBs which can be described as $\Sigma 1$ boundaries. The similar coherency between LAGBs and $\Sigma 3$ boundaries supports the RIS response observed between the two boundary types. Distinct cusps in the on-boundary Cr enrichment as a function of misorientation were observed near the $\Sigma 3$ criterion. The minimum Cr segregation was seen at the exact $\Sigma 3$ $\theta = 60°$ <1 1 1> condition. This behavior can be seen for neutron-irradiated boundaries in Figure 5.3. Similar responses were observed in the proton-irradiated boundaries but were not as well defined as seen in Figure 4.8. The cusps seen in the RIS response as a function of misorientation are similar to the cusps seen in grain boundary energy plots due to a loss in boundary coherency the further a grain boundary structure deviates from the reference $\Sigma 3$ structure. Several boundaries that fit the criterion of being a $\Sigma 3$ or near a $\Sigma 3$ did not trend with the majority of the data. $\Sigma 3$ boundaries can be classified as twin boundaries. Twin boundaries have been shown to change significantly depending on if the boundary is symmetric or non-symmetric where the symmetry is determined by the grain boundary plane [109]. Determination of the grain boundary plane using transmission electron microscopy can be determined by considering directions of grain boundary traces and specimen surface using trace analysis, obtaining the specimen thickness, and measuring the width of the projected grain boundary plane, followed by an angle between specimen surface and grain boundary plane to obtain the grain boundary plane normal direction [110]. Specimen thickness can be determined several ways including convergent beam electron diffraction (CBED) and energy filtered transmission electron microscopy (EFTEM) for the grain boundary plane determination but was not conducted as the process is prohibitively time consuming for large data sets and the analysis can have errors on the order of several percent which propagate through the grain boundary plane calculation.

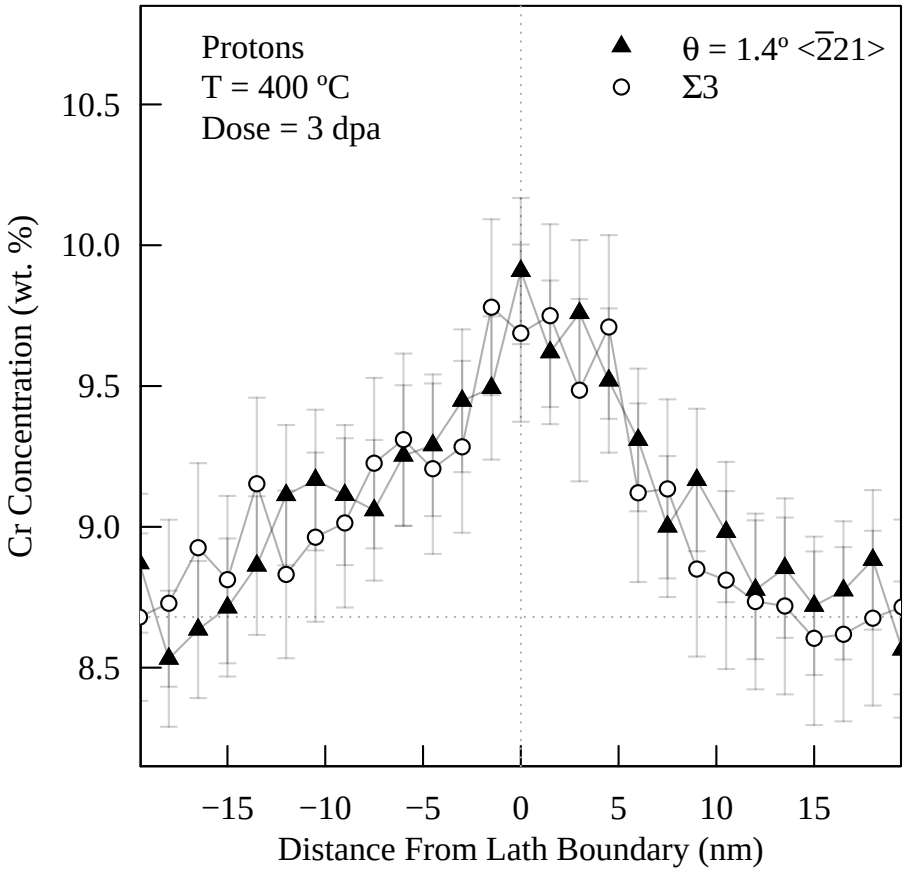


Figure 4.6: 1D Cr concentration profile for a select LAGB ($\theta$ = 1.4° <$\bar{2}$ 2 1>) and $\Sigma$3 lath boundary irradiated to 3 dpa at 400 °C using protons.

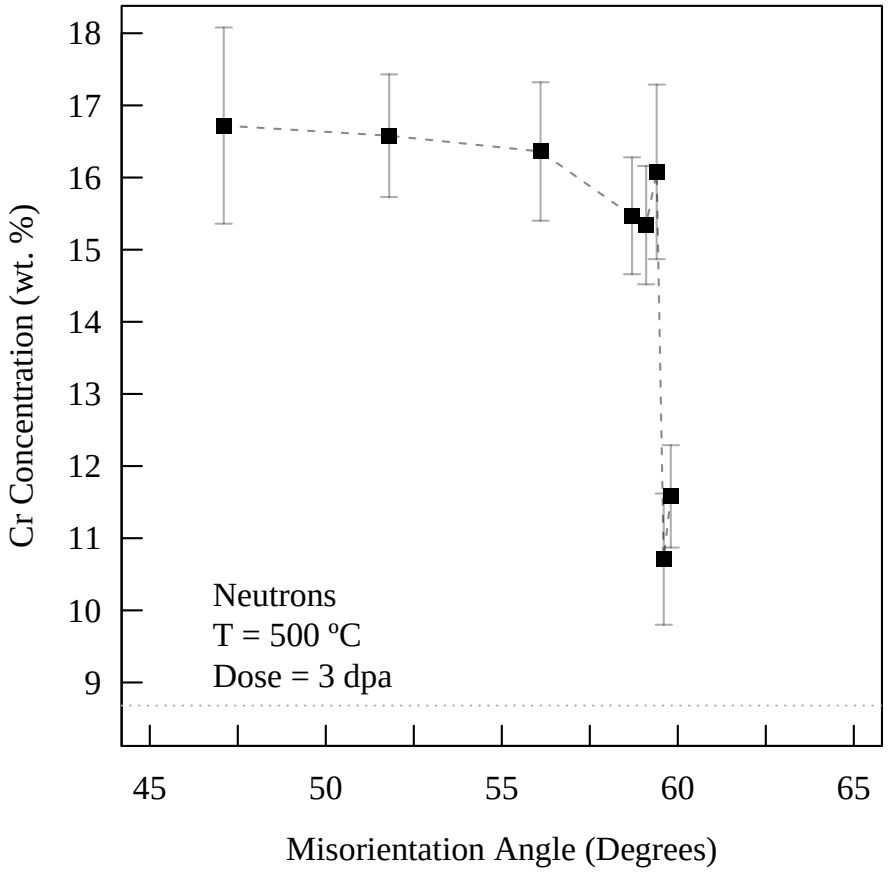


Figure 4.7: On-boundary Cr concentration as a function of misorientation for high angle grain boundaries near the Σ3 orientation irradiated to 3 dpa at 500 °C using neutrons.

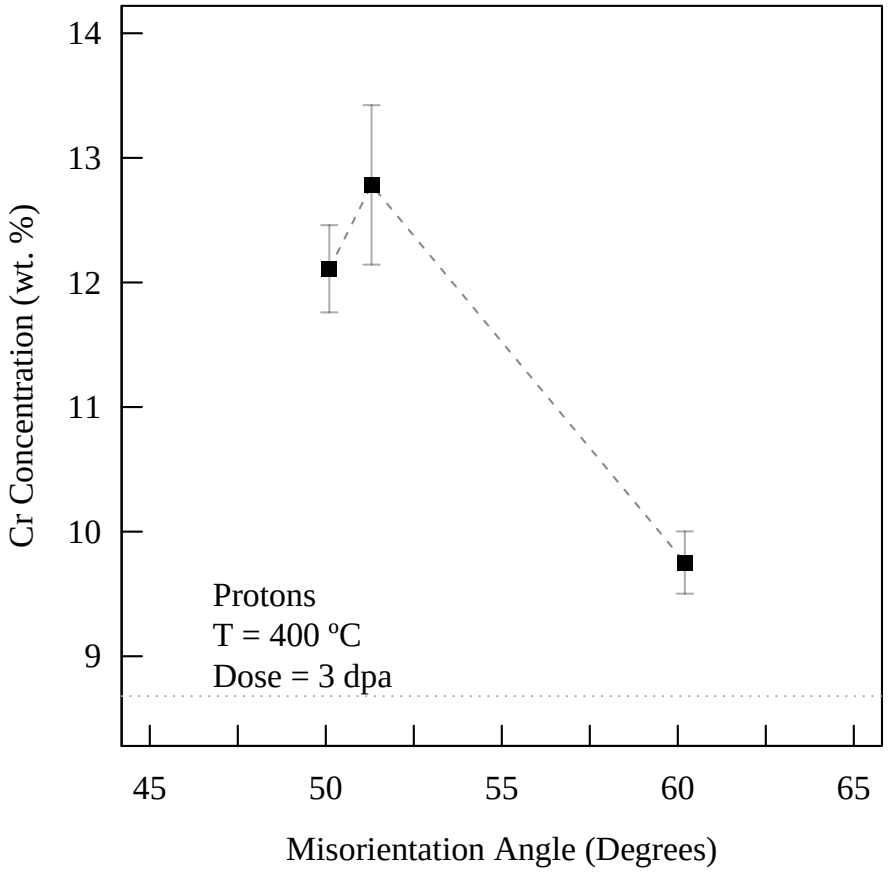


Figure 4.8: On-boundary Cr concentration as a function of misorientation for high angle grain boundaries near the Σ3 orientation irradiated to 3 dpa at 500 °C using protons.

#### 4.1.2.2 General High Angle Grain Boundaries

General HAGBs exhibited the highest magnitude of Cr enrichment and narrow segregation profiles compared to LAGBs and special grain boundaries. Concentration profiles for HAGBs were sharp with the average FWHM below 7 nm for both the proton and neutron irradiated lath boundaries. The low number of general HAGBs observed in the proton irradiated conditions, as seen in Table 4.1, makes it difficult to present trends on Cr enrichment versus misorientation angle in the proton irradiated conditions. Conversely, sufficient observations where made for

general HAGBs in the neutron irradiated material. Neutron irradiated general HAGBs in the misorientation range of 45° - 58° showed a gradual linear decrease in on-boundary Cr content as the misorientation approached the Σ3 condition. The overall trend of the Cr enrichment as a function of misorientation was presented in Figure 4.7 and Figure 4.8, while Figure 4.9 shows the concentration profiles of select boundaries in the general HAGB regime for neutron irradiated boundaries. Figure 4.10 shows concentration profiles for general HAGBs irradiated to 2 dpa at 400 °C for protons which shows a similar FWHM value as the neutron irradiated general HAGBs.

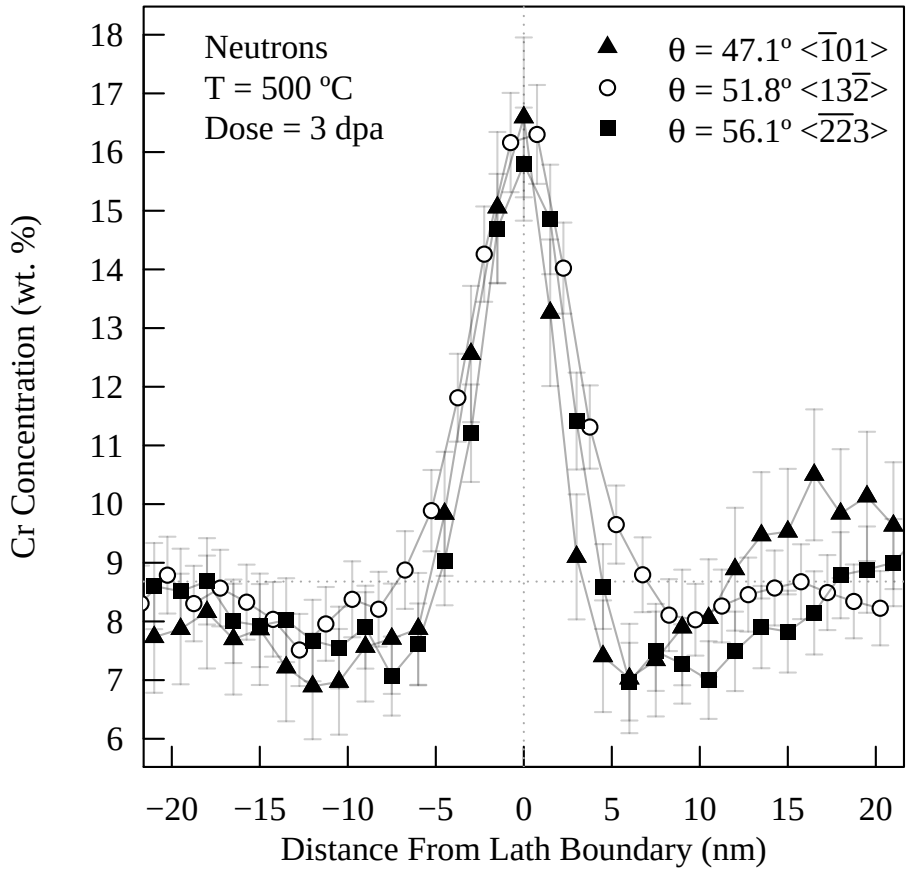


Figure 4.9: 1D Cr concentration profile for general HAGBs irradiated to 3 dpa at 500 °C using neutrons.

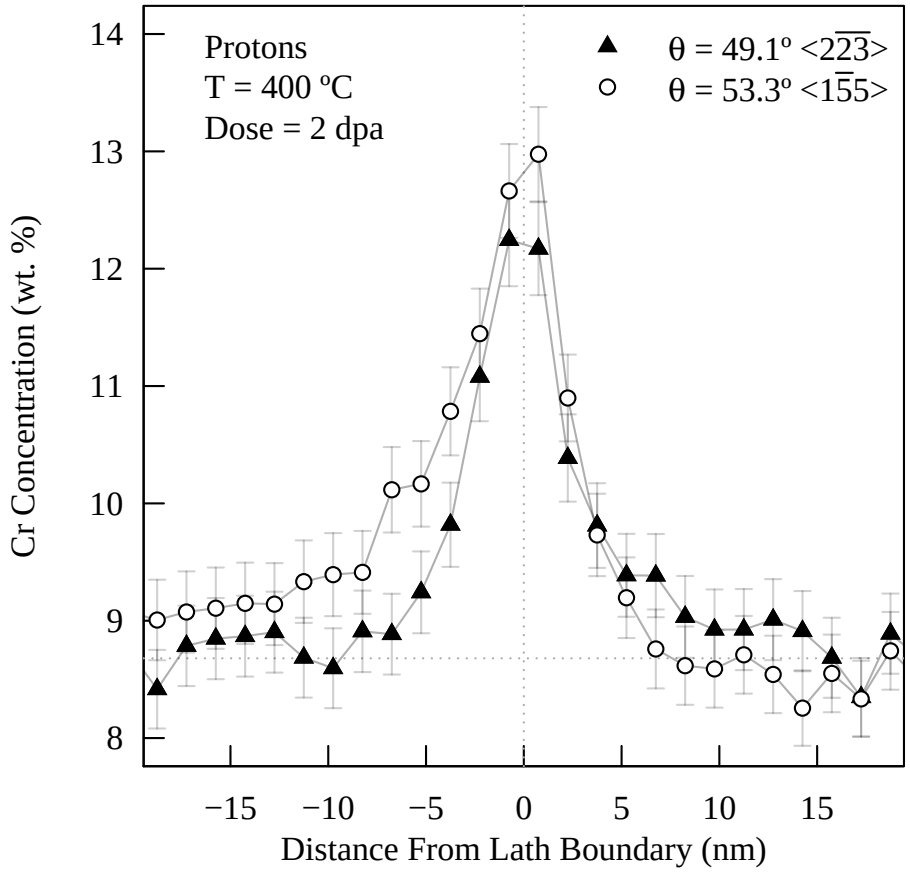


Figure 4.10: 1D Cr concentration profile for general HAGBs irradiated to 2 dpa at 400 °C using protons.

### 4.1.3 RIS Response with Irradiation Dose

Another contributing factor to variation in the RIS response of the 9 wt. % Cr model steel was irradiation dose. The dose dependence is only determined from proton irradiated specimens as neutron irradiations were only conducted at one irradiation condition. Low angle grain boundaries with misorientation angles below 5 degrees proton irradiated to 1 dpa at 400 ºC and several in the 1 dpa at 500 ºC condition showed no segregation of Cr or Fe. The magnitude

of the Cr response increased with dose at boundaries with similar structure and irradiated to the same temperature. Select segregation profiles of low angle grain boundaries with similar structure and irradiated to the same temperature, but different dose are in Figure 4.11. The dose sensitivity of the proton induced RIS response over the entire LAGB regime is illustrated in Figure 4.12. The significant amount of scatter in the FWHM data prevents any conclusions to be drawn on the influence of dose on the width of segregation profiles. Qualitatively, no evidence of extended radiation induced defects influencing the RIS response were observed up to 3 dpa.

Several specimens were investigated to determine more quantitatively if dislocation loop and defect cluster denuded zones were present near grain boundaries to determine if radiation induced defects influenced the RIS response. Weak beam dark field imaging techniques were used to image the dislocation loops and defect clusters. An example of a resulting bright field and weak beam dark field transmission electron microscopy micrograph is shown in Figure 4.13. The 'black dot' damage seen in Figure 4.13 is indicative of small defect clusters developed under ion irradiation [111]. Given this, the results can be misleading as FIB sample preparation has been shown to produce similar defect contrast as ion induced radiation damage [112, 113]. FIB sample preparation was needed to mitigate magnetic aberrations caused by the magnetic samples during STEM investigations. To fully support the observation of radiation induced defects at low doses not influencing the RIS response a more quantitative characterization of radiation induced defects on electropolished foils would be needed.

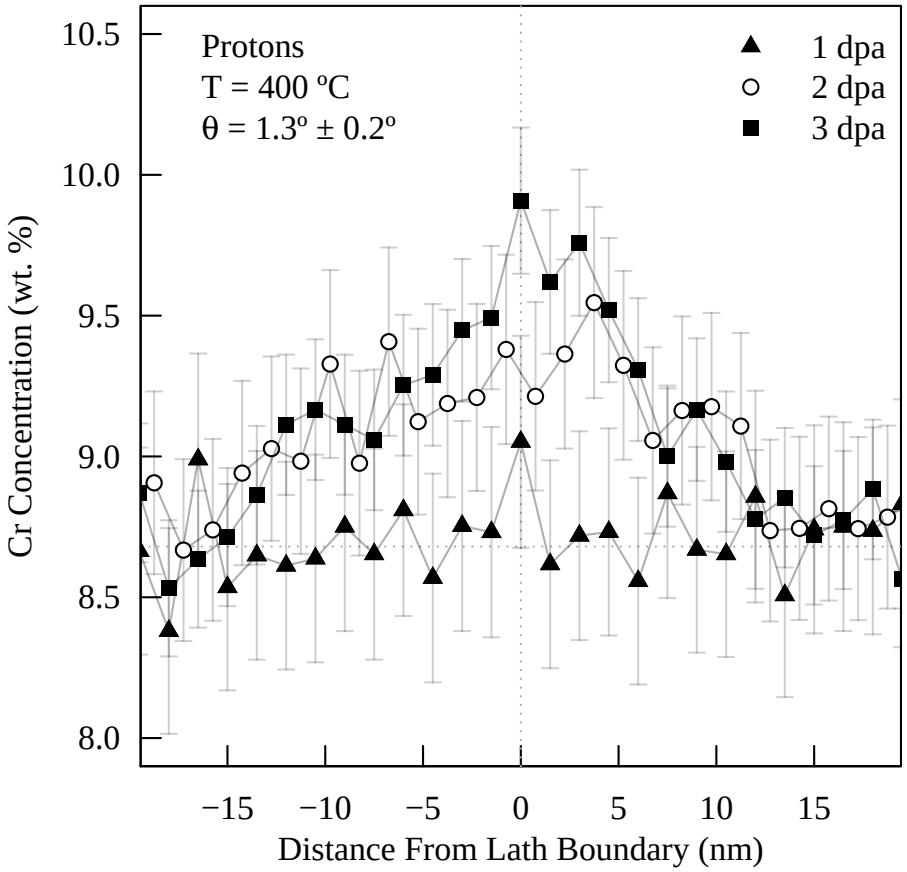


Figure 4.11: 1D Cr concentration profiles for low angle lath boundaries with similar structure showing the dose sensitivity of the RIS response for the irradiated model steel at a temperature of 400 °C using protons.

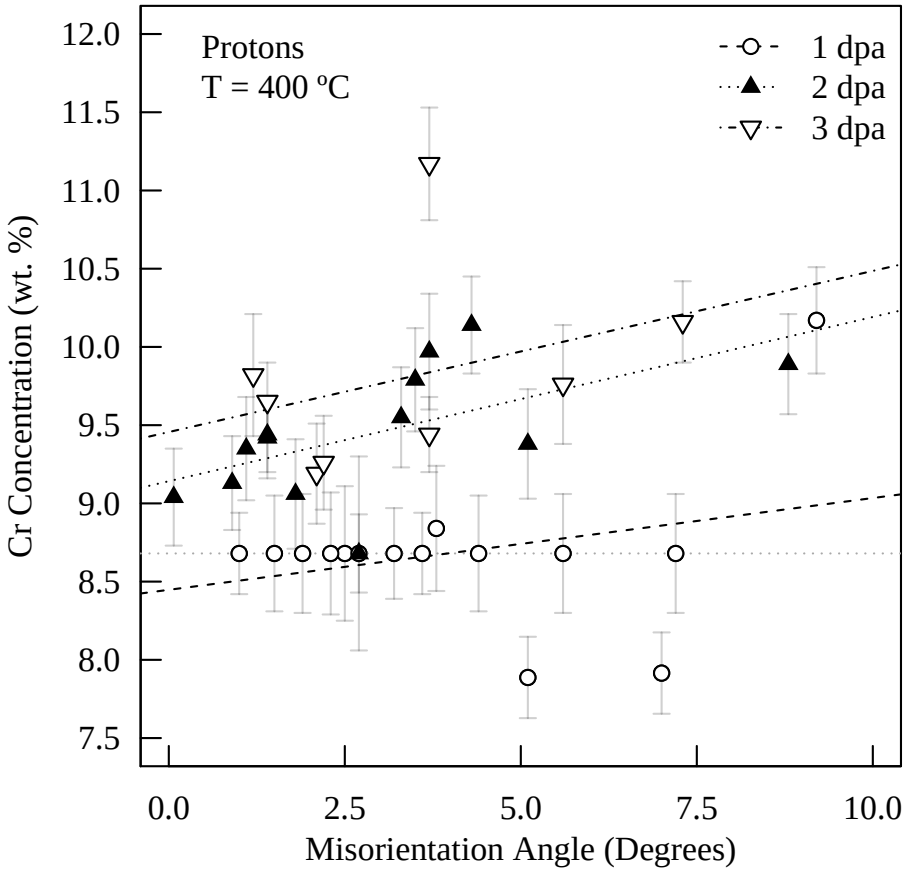


Figure 4.12: On-boundary Cr concentration as a function of misorientation angle for low angle lath boundaries showing the dose sensitivity of the RIS response for the irradiated model steel at a temperature of 400 ºC using protons. Dashed lines indicate linear regression calculated from each data group. Positive slope in 1 dpa condition due to data point at $\theta = 9.2^{\circ}$. Significant scatter is the result of experimental factors.

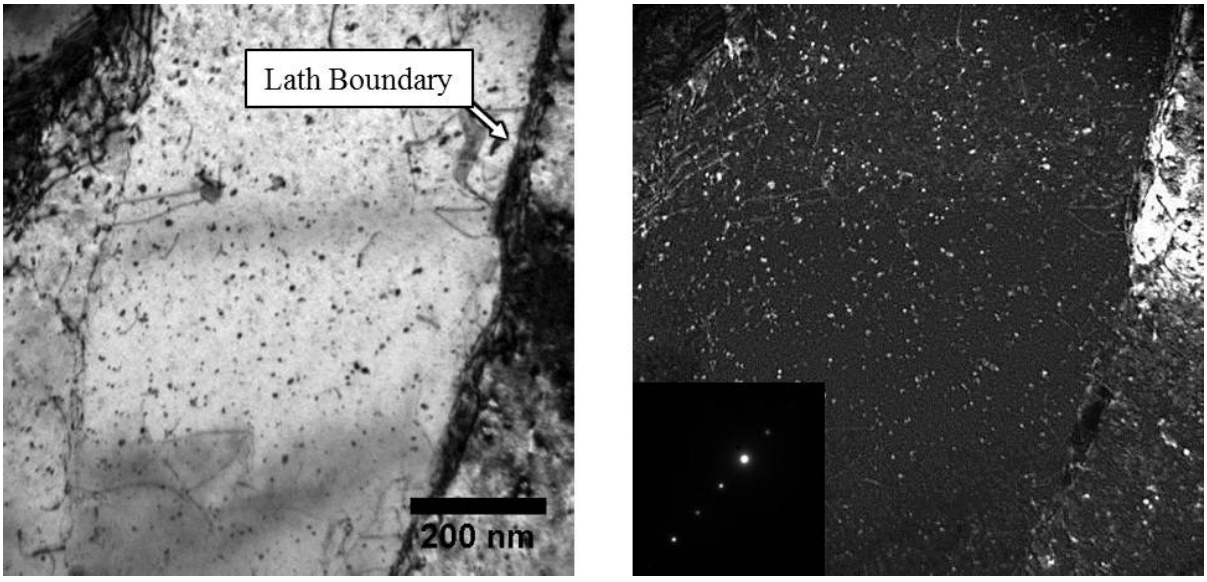


Figure 4.13: Bright field and Weak Beam Dark Field (WBDF) image of a lath and lath boundary showing the defect structure in a FIB lift-out specimen irradiated to 1 dpa at 400 ºC. Micrographs taken in the (g,3g) condition near the [113] zone axis imaged using $g_{110}$.

### 4.1.4 RIS Response with Irradiation Temperature

The RIS response also varied with temperature when dose and structure were held constant in the proton irradiated samples. The magnitude of the Cr RIS response decreased with increasing temperature between 400 ºC and 500 ºC. The FWHM did not significantly change for RIS induced at different temperatures. Figure 4.14 illustrates the typical experimentally measured RIS profiles from low angle grain boundaries irradiated to the two temperature set points. Figure 4.15 shows the reduced RIS response in the LAGB regime due to the increase in irradiation temperature. The reduced RIS response was also seen for the special grain boundary regime. The limited data in the HAGB regime prevents any conclusions on the temperature response within this regime.

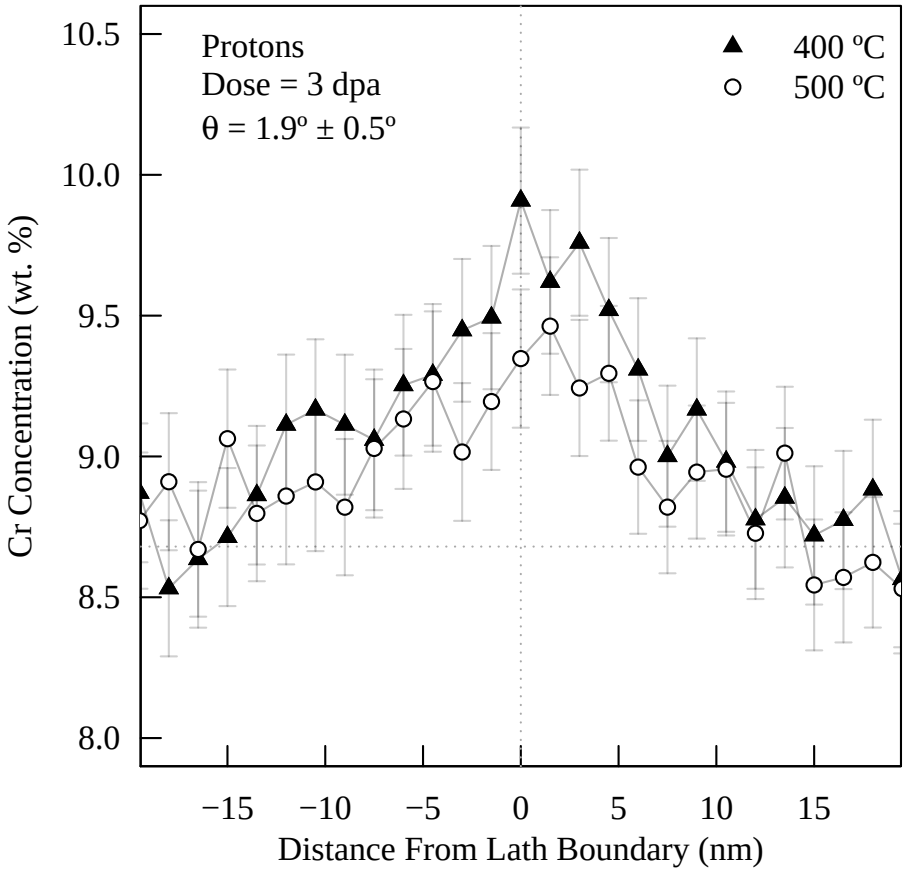


Figure 4.14: 1D Cr concentration profiles for low angle lath boundaries with similar structure showing the temperature sensitivity of the RIS response for the irradiated model steel at a dose of 3 dpa using protons for the 400 ºC and 500 ºC conditions.

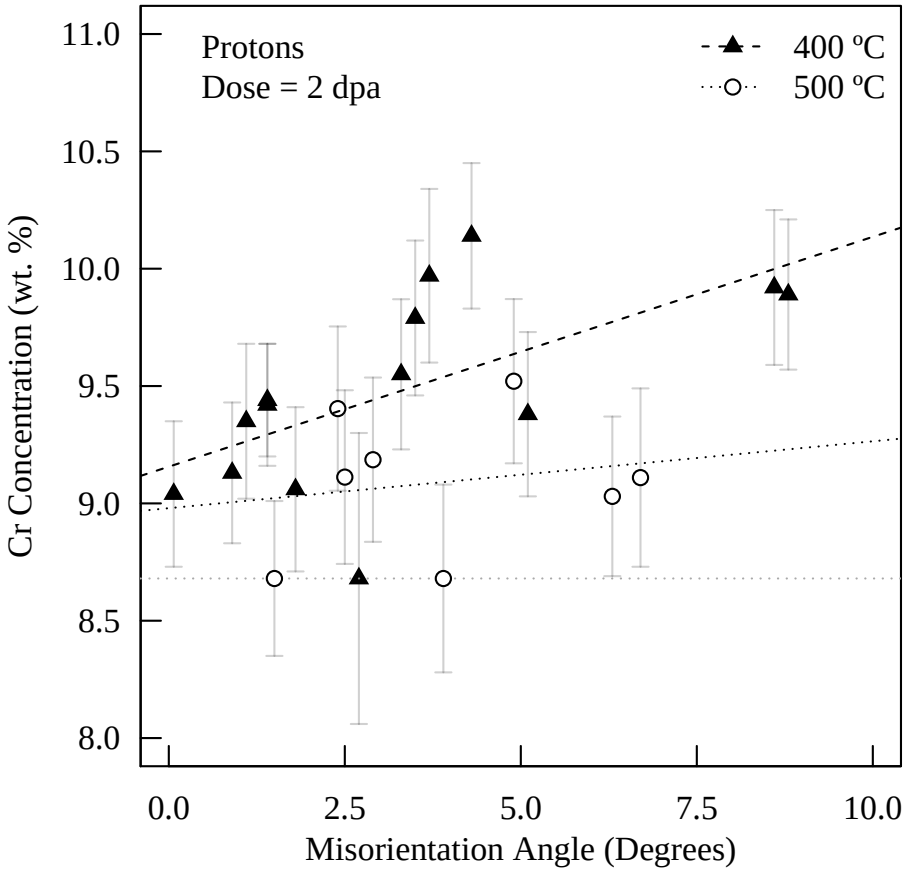


Figure 4.15: On-boundary Cr concentration as a function of misorientation angle for low angle lath boundaries showing the temperature sensitivity of the RIS response for the irradiated model steel at a dose of 2 dpa using protons for the 400 ºC and 500 ºC conditions. Dashed lines indicate linear regression calculated from each data group. Significant scatter is the result of experimental factors.

### 4.1.5 RIS Response with Incident Particle

A variation in the RIS response for neutron and proton irradiated grain boundaries was observed. Neutron irradiated grain boundaries had sharp profiles over all grain boundary regimes

as seen in Figure 4.16, while proton irradiated boundaries varied depending on the grain boundary type. Neutron irradiation also resulted in a significant increase in the Cr enrichment observed at all grain boundary types. Figure 4.17 shows a comparison between Cr concentration profiles of proton and neutron irradiated boundaries with similar structure with the same irradiation temperature while Figure 4.18 shows a comparison of profiles between a boundary irradiated to 400 ºC using protons versus a boundary with similar structure which was neutron irradiated. The proton data at 400 ºC is presented against the neutron data due to the uncertainty in the neutron irradiation temperature. Figures 4.17 and 4.18 also shows distinct regions of Cr depletion near the enrichment peak in the neutron irradiated boundaries. These regions were not observed in proton irradiated boundaries but this could be the result of the resolution limit of the experimental analysis techniques. Figure 4.19 summarizes the differences in the measured on boundary Cr content between proton and neutron irradiated boundaries at a dose limit of 3 dpa.

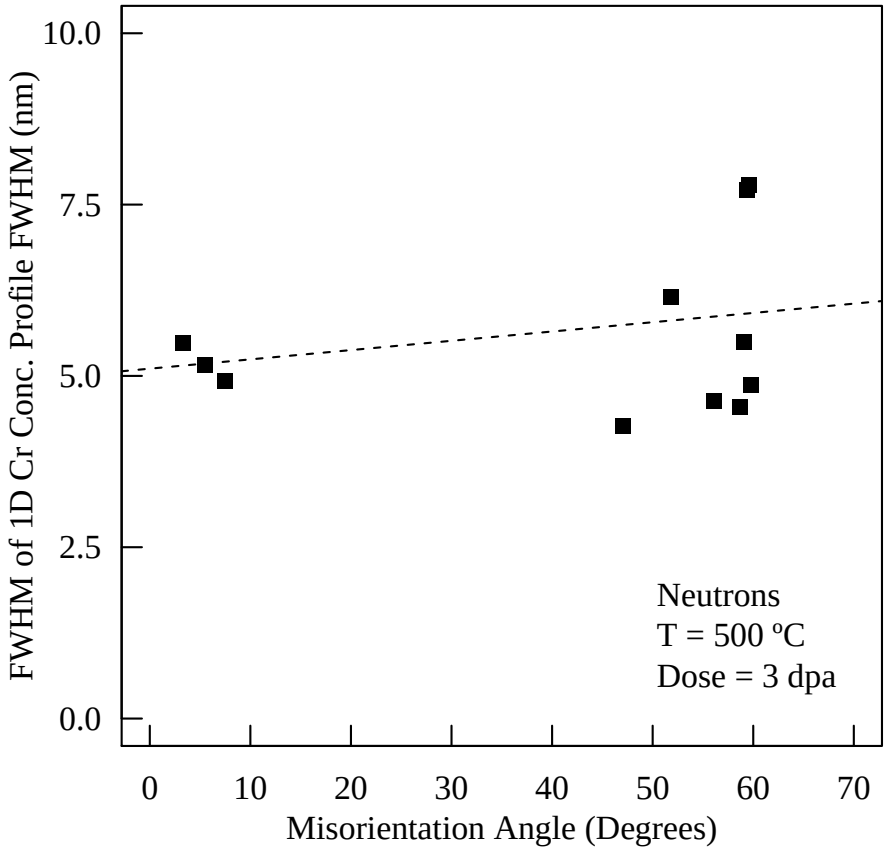


Figure 4.16: Calculated FWHM of 1D Cr concentration profiles for lath boundaries irradiated to 3 dpa at 500 °C using neutrons. Dashed line indicates linear regression.

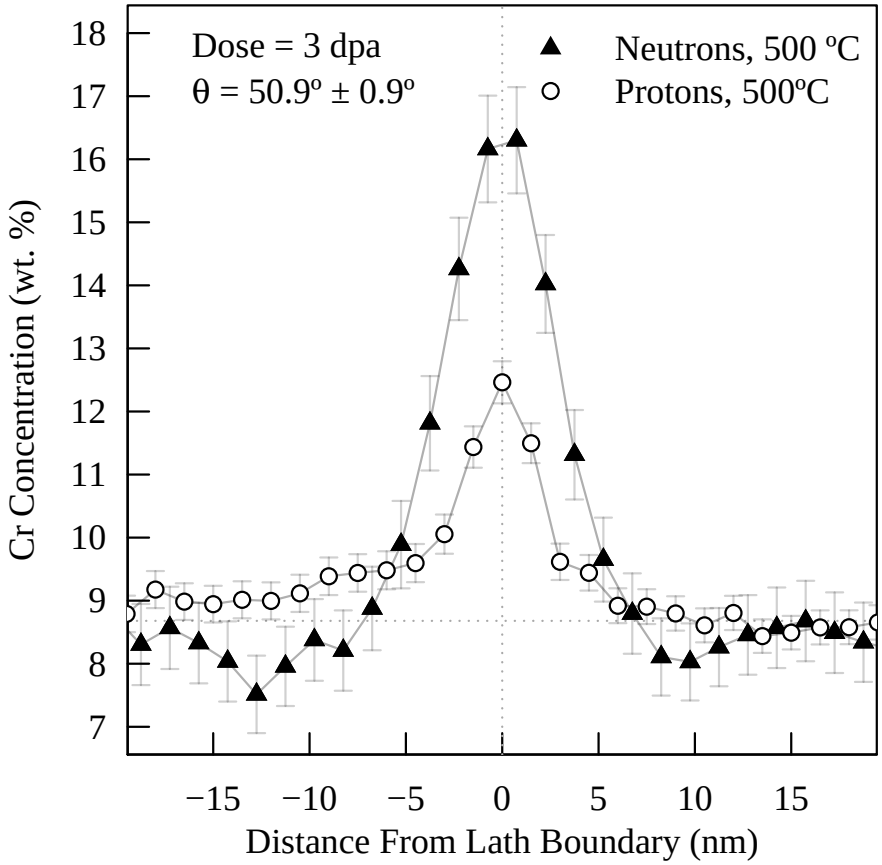


Figure 4.17: 1D Cr concentration profile for LAGBs with similar structure ($\theta = 50.9º \pm 0.9º$) irradiated to 3 dpa at 500 ºC using protons and neutrons. Proton irradiation resulted in a reduced Cr enrichment over neutron irradiation.

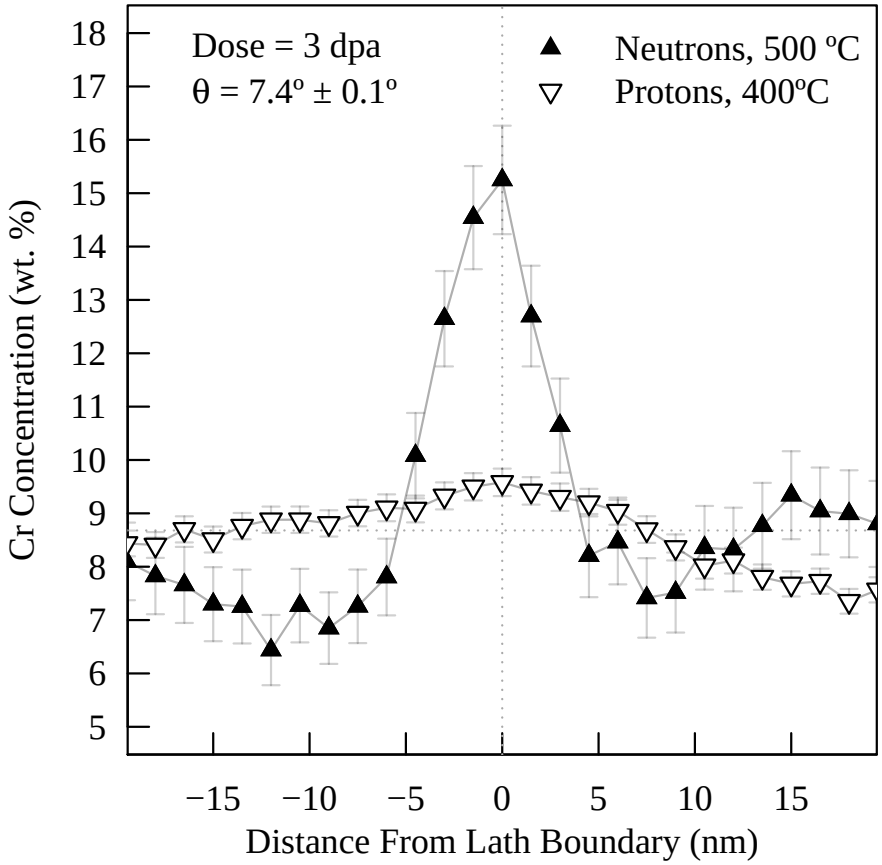


Figure 4.18: 1D Cr concentration profile for LAGBs with similar structure ($\theta = 7.4º \pm 0.1º$) irradiated to 3 dpa at 400 ºC using protons and 3 dpa at 500 ºC using neutrons. Proton irradiation resulted in a reduced Cr enrichment over neutron irradiation.

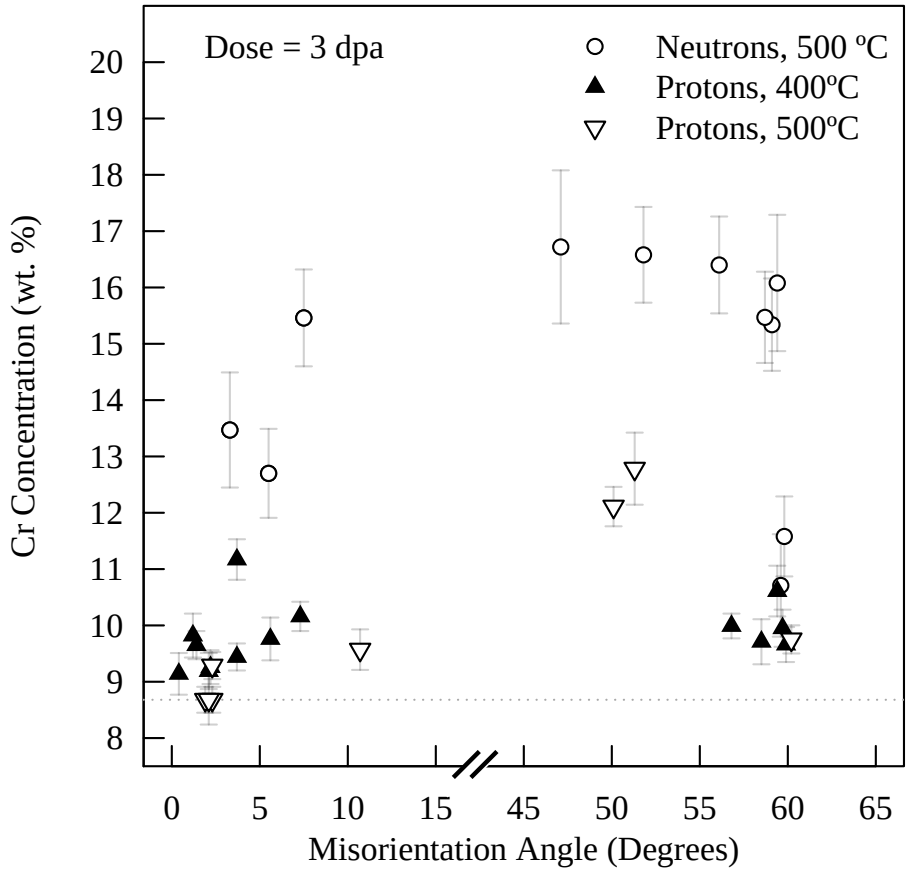


Figure 4.19: On-boundary Cr concentration as a function of misorientation angle for lath boundaries showing the incident particle RIS response for the irradiated model steel at a dose of 3 dpa.

## 4.2 NF-ODS F/M steel

A complete database of all grain boundaries investigated including the on-boundary Cr content, the misorientation angle, misorientation axis, calculated FWHM of the segregation profile, and the shape of the segregation profile is found in Appendix C for the 14YWT-SM10 alloy. Table 4.2 summarizes Appendix C and indicates the number of grain boundaries observed at each irradiation condition. The majority of all grain boundaries observed in 14YWT were low coherency, high energy, general high angle grain boundaries. The as-received material showed prior enrichment of Cr and W to the grain boundaries with Fe depleting. Nanoclusters were also detected near and on grain boundaries in the 14YWT as-received specimens using STEM-EDS. Figure 4.20 shows a representative overlay map showing the microchemical distribution near grain boundaries in the as-received material. The presence of nanoclusters on grain boundaries is supported by EFTEM and APT results on the same NF-ODS steel alloy [11]. The average on-boundary Cr enrichment in the as-received state was significant with the average Cr concentration at 21.1 $\pm$ 1.1 at. % with the width of the segregation profiles being less than 3 nm. As-received concentration profiles had an inverted 'v-shape' as seen in Figure 4.21.

Table 4.2: Irradiation conditions and grain boundaries observed in each experimentally determined regime.

| Temperature (°C) | Dose (dpa) | Dose Rate (dpa/s) | # of GBs Meas. |
|---|---|---|---|
| - | - | - | 5 |
| -75 | 100 | $2.3x10^{-3}$ | 2 |
| 100 | 100 | $2.3x10^{-3}$ | 4 |
| 300 | 100 | $2.3x10^{-3}$ | 5 |
| 450 | 100 | $2.3x10^{-3}$ | 5 |
| 600 | 100 | $2.3x10^{-3}$ | 4 |

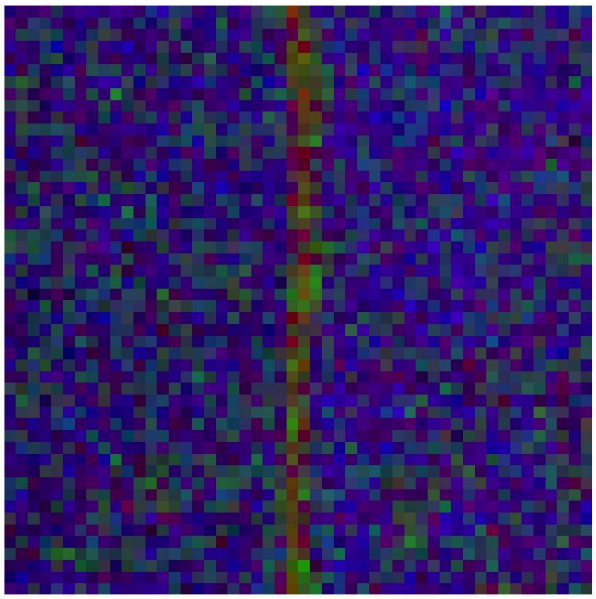

Figure 4.20: Qualitative RBG overlay map of Fe, Cr, and Ti from an as-received grain boundary in 14YWT. Cr, Fe, and Ti are depicted in red, blue, and green respectively. Map is 50 x 50 pixels corresponding to a region of interest of 250 $nm^2$.

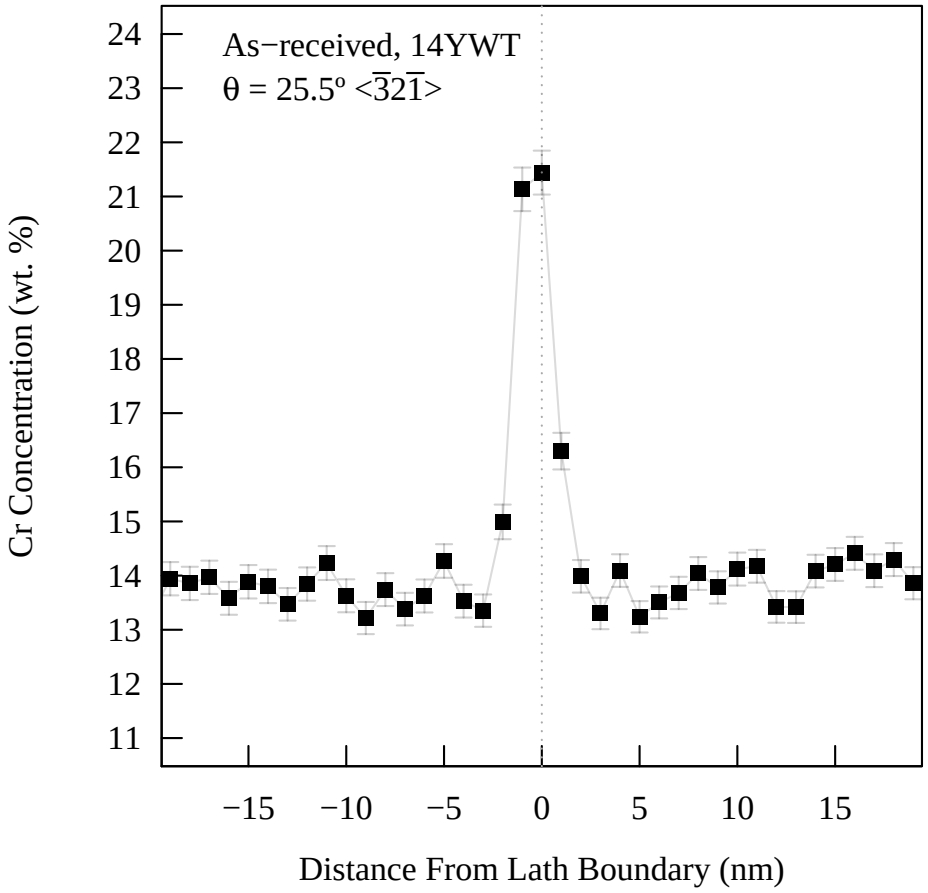


Figure 4.21: 1D semi-quantitative Cr concentration profile from a general high angle grain boundary in the as-received 14YWT alloy. The profile indicates significant Cr enrichment in the as-received state to grain boundaries.

### 4.2.1 Low Temperature RIS Response

Heavy ion irradiation resulted in a wide response in the segregation behavior to grain boundaries in 14YWT at different temperatures. Spectrum imaging revealed an almost homogenous distribution of solute and solvent within the matrix in the 100 dpa, -75 ºC $Ni^{2+}$ irradiated samples as seen in Figure 4.22. Overlay maps and concentration maps revealed no detectable

nanoclusters distributed within the matrix in the 100 dpa, -75 ºC irradiated samples which corresponds with the nanocluster distributions presented in Table 2.2. Segregation was observed in the 100 ºC irradiated samples, with both Cr and Fe depleting at the grain boundary. The enriching species to the grain boundary was revealed to be Ni through the qualitative concentration maps as seen in Figure 4.23. 1D concentration profiles along 100 ºC irradiated grain boundaries revealed a complex Cr segregation profile with a defined depleted region around the grain boundary and possible enrichment at the exact grain boundary location. The change in Cr concentration between the area around the boundary and the boundary itself is quite small and within the error of the experiment but was present in two out of the four boundaries observed. The two boundaries which exhibited minor 'w-shaped' profiles were near high coherency, Σ3 and Σ11 special grain boundary orientations indicating a possible grain boundary structure dependance for boundaries irradiated to 100 ºC although more boundaries would be need to be investigated to verify this conclusion. Figure 4.24 is an example of the one of the boundaries indicating the minor 'w-shaped' profile observed in the 100 dpa, 100 ºC condition. Nanoclusters were not detected on or near grain boundaries using spectrum imaging in the 100 ºC samples, although exceedingly small nanoclusters ($\lesssim$ 3 nm) could be under the detection limits of the experiment.

Similar responses were observed in the 100 dpa, 300 ºC irradiated specimens compared to the 100 ºC irradiated specimens. Both Cr and Fe were depleted and Ni enriched after irradiation to 100 dpa at 300 ºC. Figure 4.25 shows representative concentration maps from a grain boundary irradiated at 300 ºC. As seen in Figure 4.25, no clearly detectable nanoclusters were observed within the spectrum images obtained from the 300 ºC samples. The 300 ºC samples clearly indicated a region of depletion around the boundary with retention of the prior Cr enrichment on the grain boundary resulting in a pronounced 'w-shaped' segregation profile as seen in Figure 4.26. The average on-boundary Cr concentration for the 300 ºC grain boundaries was higher than the 100 ºC samples, with the segregation in the 300 ºC samples being 12.9 $\pm$ 0.5 at. % and the 100 ºC at 11.2 $\pm$ 0.5 at. %. The higher concentration is due to the pronounced 'w-shaped' profiles observed in the 300 ºC samples.

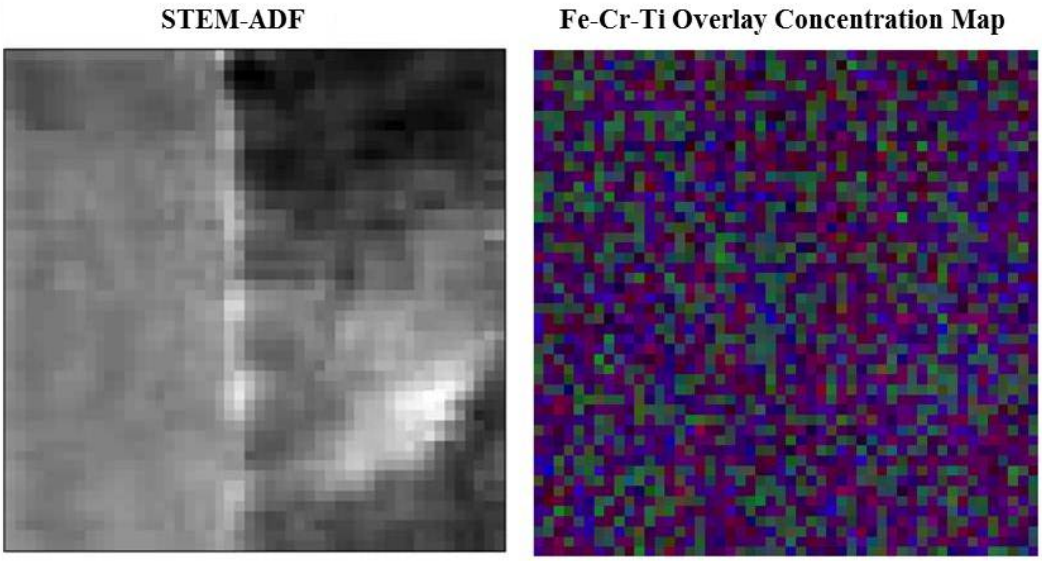


Figure 4.22: STEM-ADF image and qualitative RBG overlay map of Fe, Cr, and Ti from a grain boundary irradiated to 100 dpa at -75 ℃ using $Ni^{2+}$ ions in 14YWT. Cr, Fe, and Ti are depicted in red, blue, and green respectively. Grain boundary runs top to bottom in the map. Map is 50 x 50 pixels corresponding to a region of interest of 250 $nm^2$. Map indicates a homogenous microchemistry near the grain boundary.

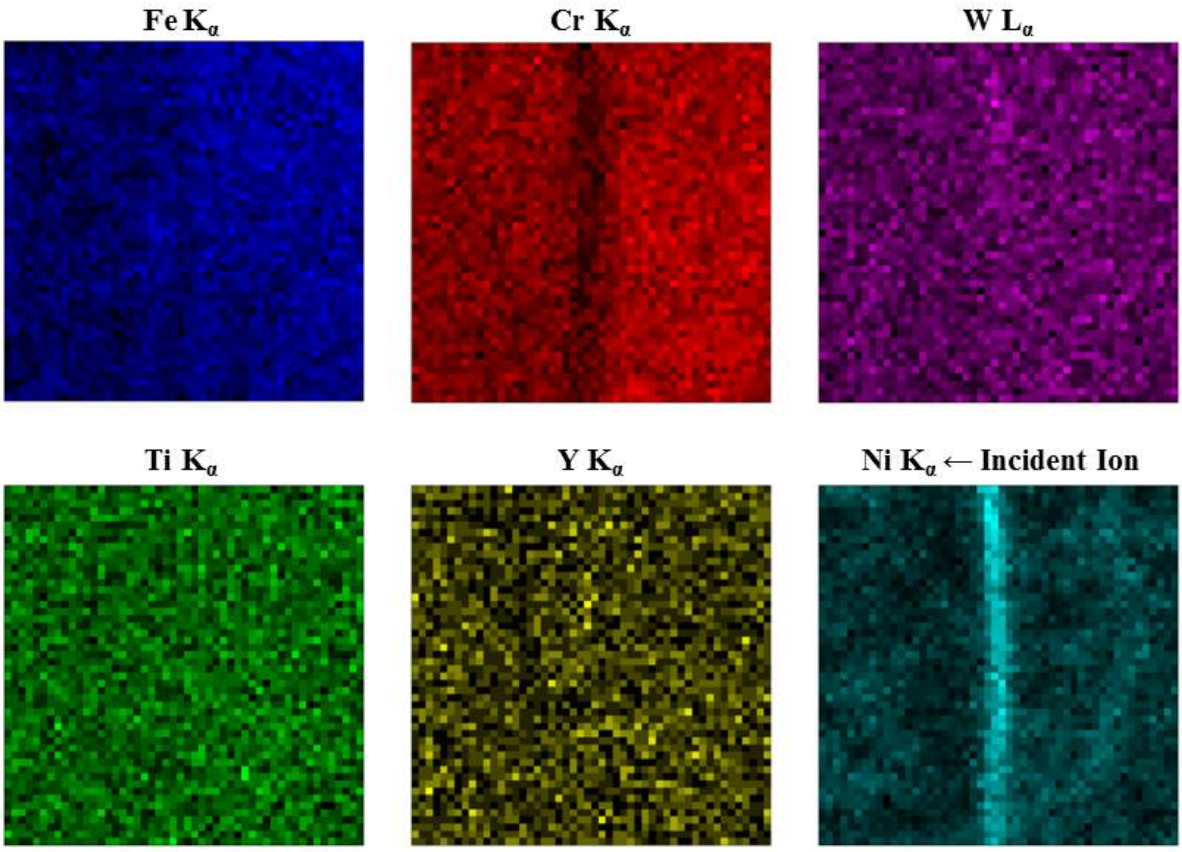


Figure 4.23: Qualitative concentration maps from a grain boundary irradiated to 100 dpa at 100 ºC in 14YWT. Each map is 50 x 50 pixels corresponding to a region of interest of 250 $nm^2$.

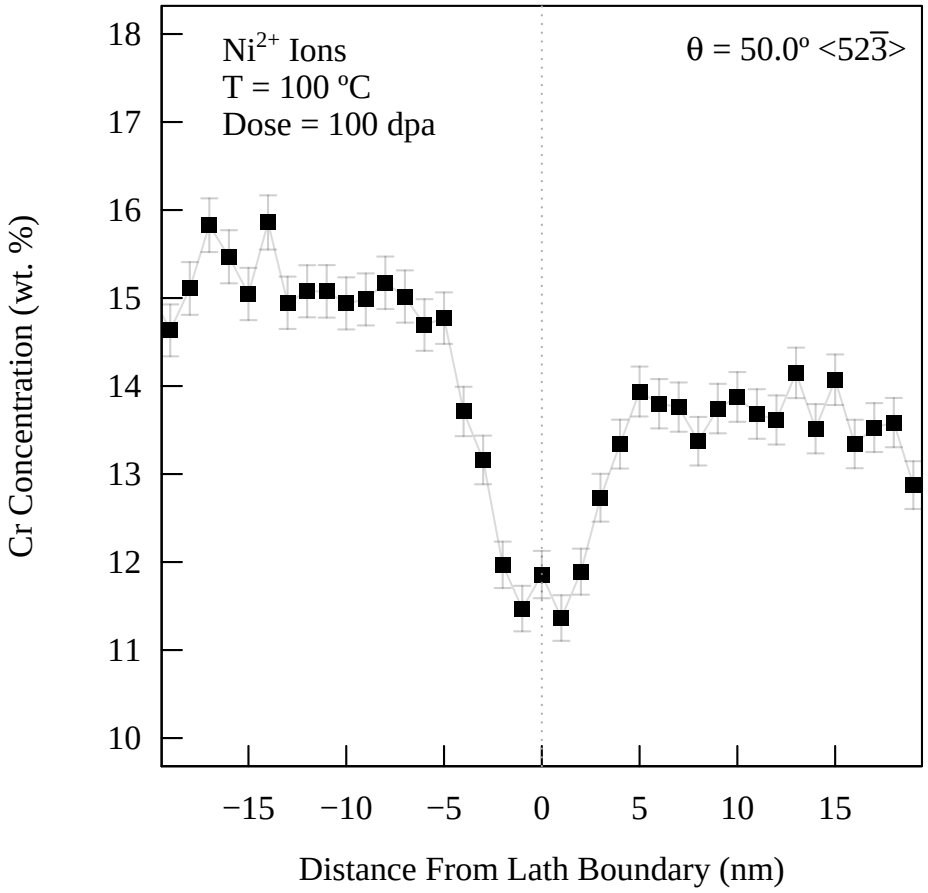


Figure 4.24: 1D semi-quantitative Cr concentration profile from a grain boundary irradiated to 100 dpa at 100 ºC using $Ni^{2+}$ ions in the 14YWT alloy.

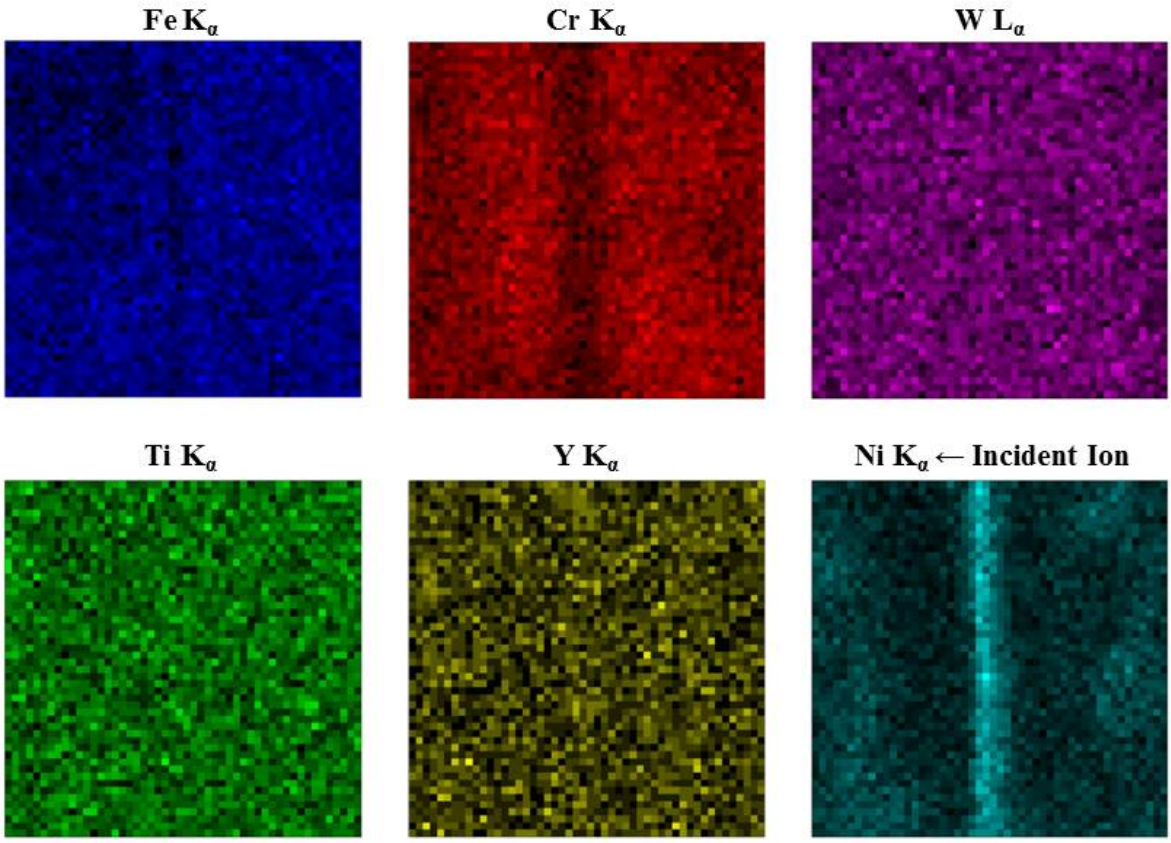


Figure 4.25: Qualitative concentration maps from a grain boundary irradiated to 100 dpa at 300 ºC using $Ni^{2+}$ ions in 14YWT. Each map is 50 x 50 pixels corresponding to a region of interest of 250 $nm^2$.

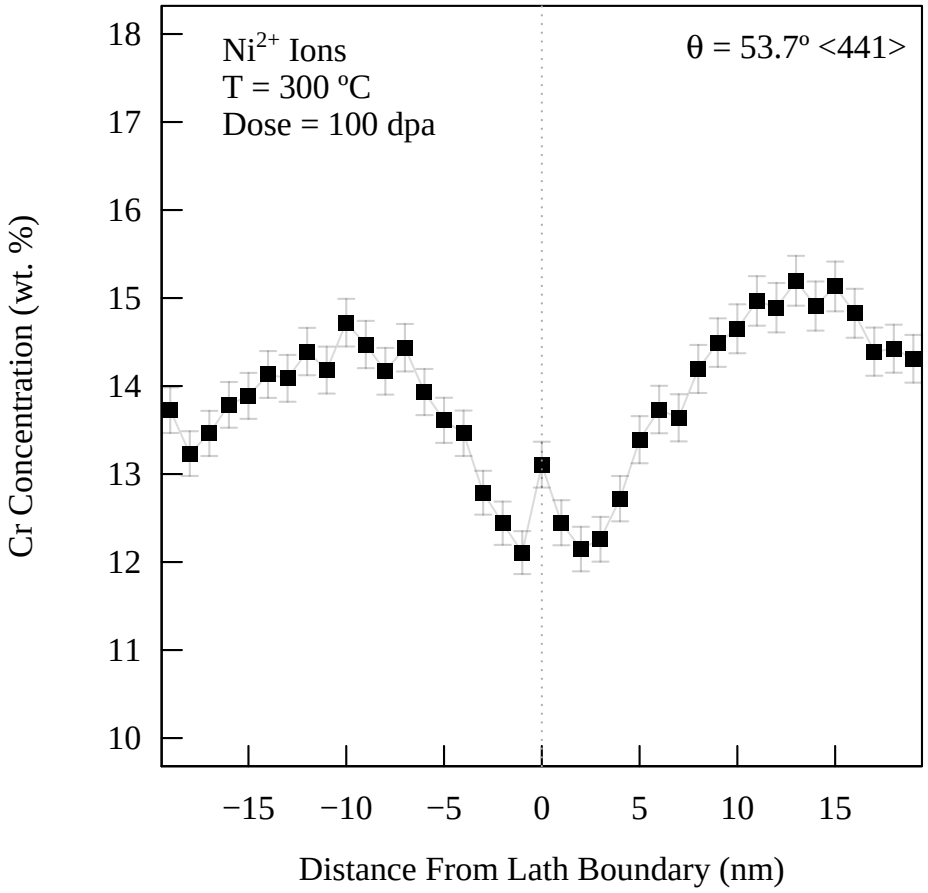


Figure 4.26: 1D semi-quantitative Cr concentration profiles from a grain boundary irradiated to 100 dpa at 300 ºC using $Ni^{2+}$ ions in the 14YWT alloy. The profiles show a 'w' profile shape.

### 4.2.2 High Temperature RIS Response

14YWT specimens irradiated to 450 ºC and 600 ºC showed a distinctly different segregation response compared to the low and intermediate irradiation temperatures. Both irradiation conditions showed limited variation in the segregation response compared to the as-received condition with Cr and W enriching to the boundary and Fe depleting. Ni segregation was less pronounced at higher temperatures. Figure 4.27 shows qualitative concentration maps of a

grain boundary from a specimen irradiated to 100 dpa at 600 ºC, showing the typical high temperature segregation response of grain boundaries. Segregation was constrained to only several nanometers compared to wider profiles observed at intermediate irradiation temperatures. Profiles were also less complex, with the Cr, W, and Fe profiles exhibiting an inverted 'v' shape profile. Figure 4.28 shows the typical Cr segregation profiles observed from the high temperature regime. The average on-boundary concentration in the 450 ºC condition was 19.3 $\pm$ 1.5 at. % and 18.3 $\pm$ 0.9 at. % in the 600 ºC condition. Both conditions had detectable nanoclusters near and on-grain boundaries as seen in the overlay maps in Figure 4.29 for a grain boundary irradiated to 100 dpa at 450 ºC and another boundary irradiated at 600 ºC. The limited number of grain boundaries observed in each condition prevented fully investigating segregation response as a function of grain boundary structure in the 14YWT specimens.

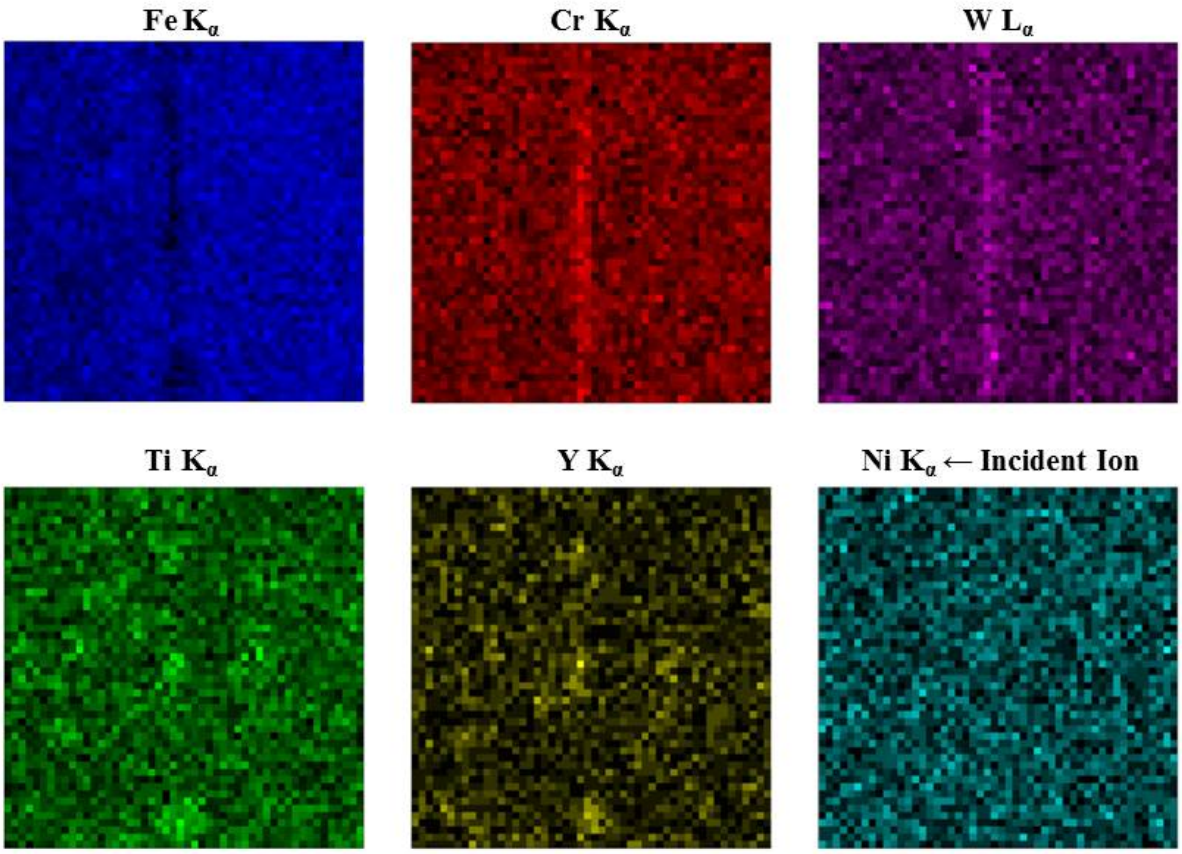


Figure 4.27: Qualitative concentration maps from a grain boundary irradiated to 100 dpa at 600 ºC using $Ni^{2+}$ ions in 14YWT. Each map is 50 x 50 pixels corresponding to a region of interest of 250 $nm^2$. Clusters on and near the grain boundary as indicated by the concentrated regions in the Ti and Y maps.

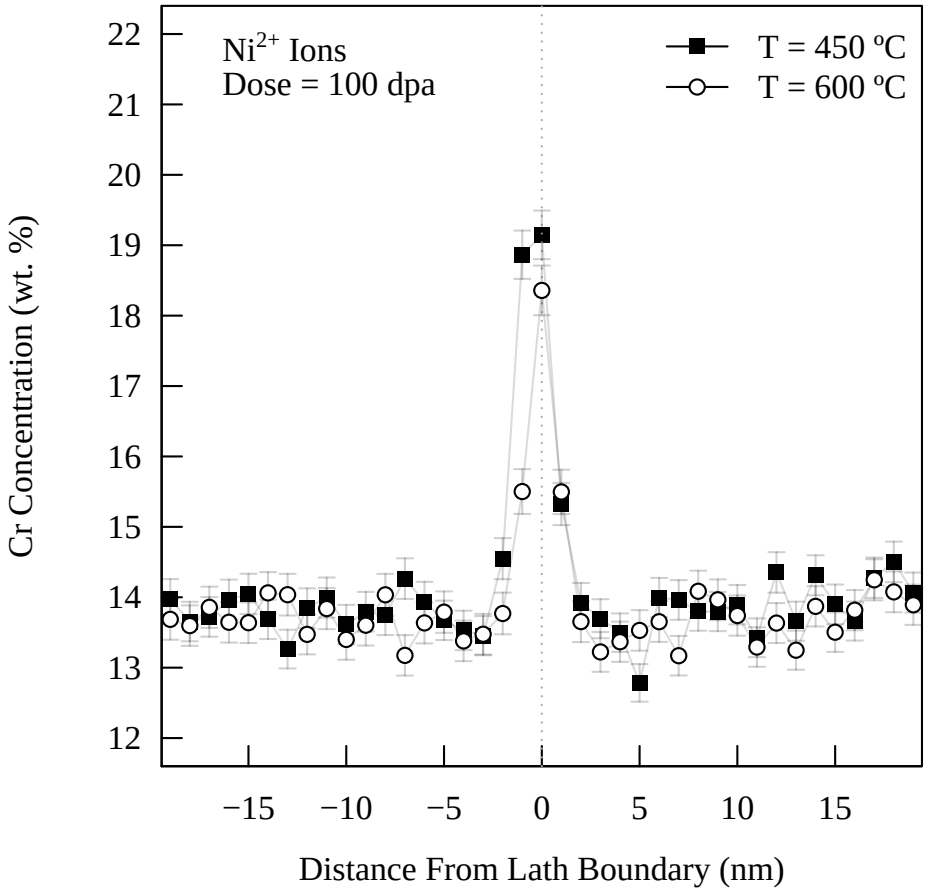


Figure 4.28: 1D semi-quantitative Cr concentration profiles from grain boundaries irradiated to 100 dpa using $Ni^{2+}$ ions in the 14YWT alloy. The profiles indicates significant Cr enrichment in grain boundaries irradiated to 450-600 ºC.

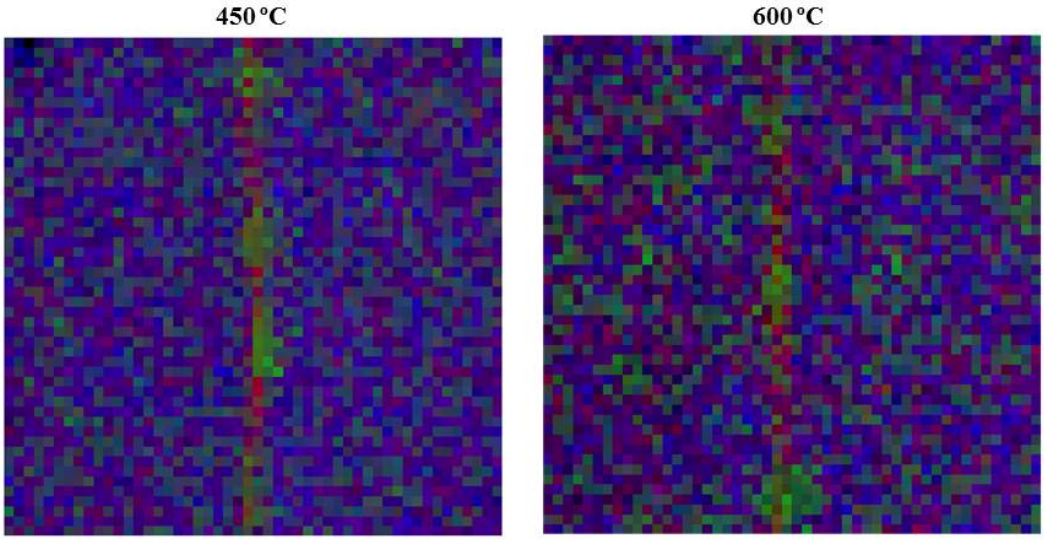


Figure 4.29: Qualitative RBG overlay maps of Fe, Cr, and Ti from a grain boundary irradiated to 100 dpa at 450 ºC and 600 ºC using $Ni^{2+}$ ions in 14YWT. Cr, Fe, and Ti are depicted in red, blue, and green respectively. Grain boundary runs top to bottom in the map. Map is 50 x 50 pixels corresponding to a region of interest of 250 $nm^2$.

# Chapter 5

# Discussion

## 5.1 Radiation Induced Segregation (RIS) in Traditional F/M Steels

### 5.1.1 *Ab-initio* Based Rate Theory Model to Predict RIS at Different Grain Boundary Structures in F/M Steels

The *ab-initio* based rate theory model with modified boundary conditions developed by L. Barnard and described in Section 2.6.3, Appendix A, and Refs. [86, 94] was used to simulate radiation induced segregation in the 9 wt. % Cr model F/M steel investigated experimentally in this study. The rate theory model calculations were conducted by L. Barnard[1]. The ambiguity in the experimental conditions, including the dose, dose rate, temperature, and defect production efficiency of free migrating point defects in the neutron irradiated specimen prevented creditable comparisons between the experiment and the rate theory model. The complex microstructure and chemistry due to nanocluster inclusions in the 14YWT specimens also prevented a direct comparison to the simple rate theory model. The proton-irradiated specimens were irradiated at a much higher degree of control compared to the neutron irradiation and the simplified chemistry allows for an accurate comparison between the experimental results and the simulation results in the proton irradiated model F/M steel.

[1]Results courtesy of Leland Barnard, Computational Materials Group, University of Wisconsin - Madison (lmbarnard@wisc.edu)

#### 5.1.1.1 RIS Modeling Parameters and Electron Probe-Concentration Profile Convolution Model

The dose, dose rate, and temperature were selected based on the experimental conditions in Table 3.1 while the defect damage production efficiency, $\varepsilon$, was selected as 20% which is consistent with 2.0 MeV incident protons into Ni and widely used for rate theory models on RIS for proton irradiated steels [114]. The model assumed a binary BCC Fe-Cr system which results in the effect of C content on the system not being captured within the model. The relevant species dependent diffusivities for both vacancy and interstitial mechanisms were determined using first principles by Choudhury *et al.* for the dilute Fe-Cr system and provided in Table 5.1 [86]. It is recognized the diffusivities could be dependent on composition and could be different in the concentrated BCC Fe-Cr system. The dilute case was selected due to simplicity in the *ab-initio* calculations and provides an initial starting point for understanding diffusion and RIS in BCC Fe-Cr alloys. A plot of the ratios $d^{v}_{Cr}/d^{v}_{Fe}$ and $d^{i}_{Cr}/d^{i}_{Fe}$ as functions of temperature were depicted in Figure 2.22. The first principle study by Choudhury suggests Cr should be enriched at defect sinks as interstitial-Cr diffusion is dominant in the temperature regime investigated [86]. The necessary physical constants to use the modified boundary conditions are also provided in Table 5.1.

The spatial resolution of the STEM-EDS acquisition system used within this study prevents a direct correlation between the outputted 1D concentration profiles of the rate theory model and the experimental results as discussed in Section 2.7. The large detection probe compared to the narrow predicted concentration profiles results in 'smearing' or exaggerating the width and under-estimating the magnitude of 1D concentration profiles and 2D concentration maps. To better correlate experimental results to simulation a simple convolution model was used [115, 116]. Doig *et al.* showed an electron probe of a STEM-EDS system can be assumed to maintain Gaussian behavior and be defined as:

$$I(x,t) = \frac{I_o}{\pi\sigma^2 + \beta t^3} exp\left(-\frac{x^2}{(2\sigma^2 + \beta t^3)}\right) \tag{5.1}$$

where,

$$\beta = 500\frac{\rho}{A}\left(\frac{4Z}{E}\right)^2 \tag{5.2}$$

and

$$\sigma = \frac{r}{2.35} \tag{5.3}$$

and $I$ is the total electron flux, $r$ is the measured FWHM of the incident electron probe size in nm, $t$ is the specimen thickness in nm, $Z$ and $A$ are the mean atomic number and weight of the specimen, $\rho$ is the specimen density, and $E$ is the electron accelerating voltage in volts. Here, the experimental STEM conditions were utilized as inputs. The electron probe function was then convolved with the concentration profile to determine the estimated observed concentration profiles based on the modeling results using:

$$I = \int_{-\infty}^{\infty}\int_{0}^{t} C_x \cdot I(x,t)\, dt\, dx \tag{5.4}$$

where $C_x$ is the solute concentration as a function of distance from the grain boundary and $I(x,t)$ is the electron probe function in Eq. 5.1. Section 2.7 indicated experimental STEM conditions tend to reduce the measured segregation compared to the real grain boundary segregation. The convolution model captured this affect as seen in Figure 5.1 for two different segregation profiles using the same STEM conditions within the model. Figure 5.1 also illustrates the effect of beam broadening on the predicted STEM-EDS profile measurement is more significant for sharp segregation profiles such as those measured in the general HAGB regime experimentally.

Table 5.1: Physical parameters used in the Fe-Cr RIS model. Diffusion parameters obtained from an Arrhenius fit to the values calculated by Choudhury *et al.* [86] from first principles. Table from [94].

| Basic RIS model parameters | | |
|---|---|---|
| Parameter | Notation | Value |
| Pre-exponential factor for Fe interstitial diffusivity | $d_{0,Fe}^{Int}$ | $6.59x10^{-7}\ \frac{m^2}{s}$ |
| Pre-exponential factor for Cr interstitial diffusivity | $d_{0,Cr}^{Int}$ | $6.85x10^{-7}\ \frac{m^2}{s}$ |
| Pre-exponential factor for Fe vacancy diffusivity | $d_{0,Fe}^{Vac}$ | $5.92x10^{-6}\ \frac{m^2}{s}$ |
| Pre-exponential factor for Cr vacancy diffusivity | $d_{0,Cr}^{Vac}$ | $5.46x10^{-6}\ \frac{m^2}{s}$ |
| Activation energy for Fe interstitial diffusivity | $E_a^{Fe,Int}$ | $0.36\ eV$ |
| Activation energy for Cr interstitial diffusivity | $E_a^{Cr,Int}$ | $0.27\ eV$ |
| Activation energy for Fe vacancy diffusivity | $E_a^{Fe,Vac}$ | $0.77\ eV$ |
| Activation energy for Cr vacancy diffusivity | $E_a^{Cr,Vac}$ | $0.68\ eV$ |
| Dislocation density | $\rho_d$ | $5x10^{13}\ m^{-2}$ |
| Grain boundary model parameters | | |
| Grain boundary attempt frequency | $\nu_o$ | $5x10^{12}\ sec^{-1}$ |
| Burgers vector | $b$ | $2.48x10^{-10}\ m$ |
| Shear Strength | $\mu$ | $86.0\ GPa$ |
| Poisson's ratio | $\nu$ | 0.3 |
| Grain boundary correlation factor | $f_{Int}^{gb}, f_{Vac}^{gb}$ | 0.5 |

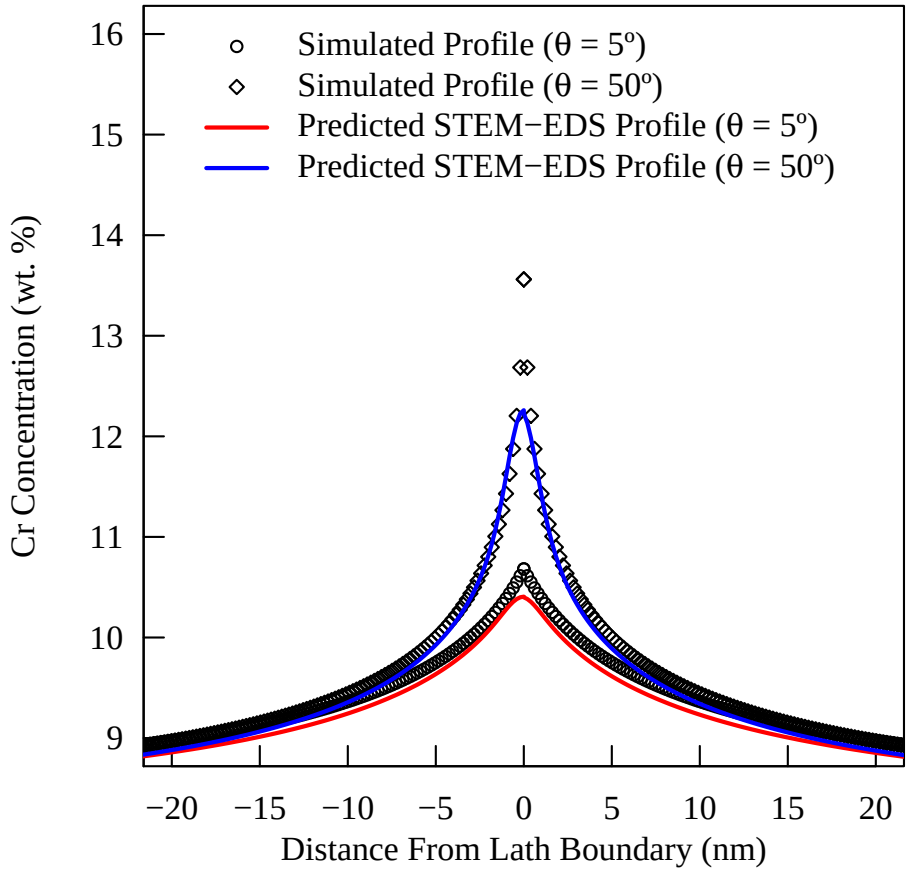


Figure 5.1: Simulated 1D Cr concentration profiles using rate theory modeling and predicted STEM-EDS measurement based on the simulated profiles assuming a specimen thickness of 75 nm for two different grain boundary types. Rate theory model used a dose of 3 dpa and temperature of 400 ºC to determine the amount of Cr segregation.

#### 5.1.1.2 Sensitivity of Electron Probe-Concentration Profile Convolution Model

As discussed in Section 2.7, experimental variables including specimen thickness, incident probe FWHM, and boundary tilt to the incident probe ($\alpha_{tilt}$) affect the measured segregation profile using STEM-EDS. These factors must be taken into account when using the convolution model in Section 5.1.1.1 to compare experimental results to the simulated profiles. The

sensitivity of the electron-probe-concentration profile convolution model can be determined using sensitivity analysis. The model sensitivities, $\partial X/\partial P_{input}$ (where $X$ is the model-calculated output and $P_{input}$ is the model input variable), are calculated assuming a reference STEM condition based on the experimental studies. Here, only the specimen thickness, electron probe size, and grain boundary tilt are assumed to vary from measurement to measurement with the reference case considered to be $t = 75\,nm$, $r = 1.5\,nm$, and $\alpha_{tilt} = 0°$. The model sensitivity can be approximated by,

$$\frac{\partial X}{\partial P_{input}} \cong \frac{\Delta X}{\Delta P} = \frac{X' - X_{reference}}{P'_{input} - P_{reference}} \tag{5.5}$$

where $X'$ is either the model calculated on-boundary Cr concentration or the model calculated FWHM. The input parameter $P'_{input}$ was assumed to vary by $+30\%$ of the reference case for $t$ and $r$ while the grain boundary tilt was assumed to vary 5° from edge on. The normalized significance of each input parameter ($S_X^P$) can be determined from the calculation in Eq. 5.5 by,

$$S_X^P = \frac{X' - X_{reference}}{P' - P_{reference}} \cdot \frac{P_{reference}}{X_{reference}} \tag{5.6}$$

Calculations were performed using the outputted concentration profiles from the rate theory model assuming an irradiation at 400 ºC to 3 dpa for a general high angle grain boundary with a misorientation angle of 50°. The resulting calculations of the significance analysis is provided in Figure 5.2.

Changing the input parameters had the largest affect in changing the simulated FWHM of the segregation profiles compared to the calculated on-boundary Cr concentration. The analysis shows the convolution model is most sensitive to the grain boundary tilt to the electron beam. The specimen thickness and electron probe size are also significant but had very little influence on the measured on-boundary Cr concentration where a 30% change in thickness or probe size resulted in a change of less than 0.5 wt. % at the boundary which is within the error of typical

spectrum imaging analysis techniques. The thickness and electron probe size become even more insignificant as the concentration profiles calculated via the rate theory model become broader with reduced intensity, such as the simulated profiles in the low angle grain boundary regime. This is due to the resolution of the electron probe function closely approaching the resolution of the concentration profile providing a more accurate, direct representation of the concentration profile.

The sensitivity analysis of the idealized system also reveals a potential cause for a portion of the scatter in observed experimental results. The large variance in the measured concentration profile due to very small inclinations of the grain boundary to the electron probe could be contributing to the observed scatter. The determination of the grain boundary inclination to the beam during STEM-ADF imaging is non-trivial and some misalignment could occur in the experimental setup. Other scatter in the experimental data could arise from variations in the specimen thickness and electron probe. Care was taken during the microscopy sessions to utilize the same imaging conditions for each spectrum image, but other factors such as hysteresis in the lenses or the quality of the electron beam focus could vary the probe size from specimen to specimen. The FIB specimens most likely reduced the variation in the specimen thickness from sample to sample compared to wedge polishing or electropolishing techniques. Given this, some variation in the specimen thickness was still present. The analysis of the comparison of the rate theory model to the experimental results assumed the model adhered to the reference case in the sensitivity analysis but with a lower and upper bound in specimen thickness of 25 nm to 125 nm respectively. The input parameters could be modified on a case by case basis to develop a better fit between the experimental results and the rate theory model but this process was not conducted as it would introduce undue bias to the analysis.

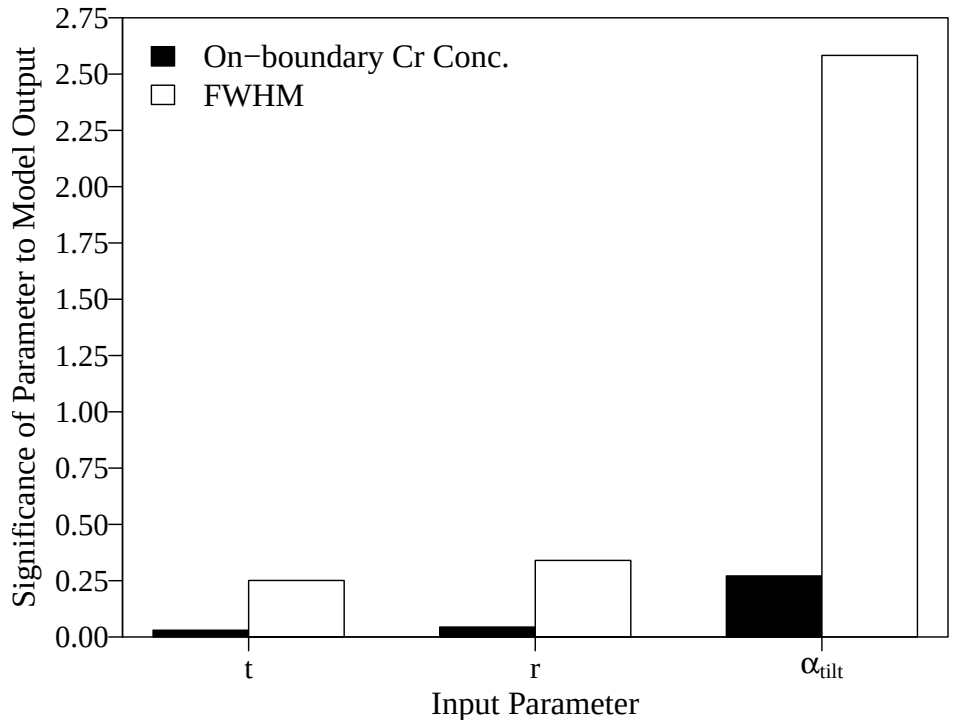


Figure 5.2: Significance of different input parameters into the electron-probe-concentration profile convolution model used to compare simulated profiles using rate theory to experimental results on the 9 wt. % Cr model alloy. Analysis based on a 400 ºC to 3 dpa irradiated general HAGB with a misorientation angle of 50º.

#### 5.1.1.3 Comparison of Proton Irradiation Results to RIS Modeling

Overall, the model showed reasonable agreement with the measured segregation profiles of proton irradiated grain boundaries in the model F/M steel. The general, qualitative trends in the RIS response due to changes in grain boundary structure, dose, and temperature were captured. The model predicted the Cr enrichment coupled with Fe depletion seen in the experimental results. This response has also been observed experimentally and accurately predicted using a similar rate theory model in the more complex T91 F/M steel at prior austenite grain boundaries by Wharry *et al.* [81, 83]. These results indicated both the vacancy and interstitial mediated mechanisms are significant with the interstitial diffusion dominant in F/M steels.

Figure 5.3 plots the segregation in the model F/M steel as a function of misorientation in the low angle grain boundary regime for the 400 ºC, 2 dpa condition. The model accurately predicts the trend of increasing Cr segregation with increasing misorientation in the low angle grain boundary regime. Figure 5.4 plots the segregation width as function of misorientation in the low angle grain boundary regime. The model shows good agreement with the trends observed in the experiment for the measured segregation profiles, especially when considering the width of the measured profile is significantly impacted by the convolution model input factors as well as experimental factors.

Figure 5.5 plots the segregation as a function of misorientation for $\Sigma 3$ grain boundaries in the F/M model alloy for the 400 ºC, 3 dpa condition. The reduced RIS response observed near the $\Sigma 3$ grain boundary condition was captured by the rate theory model. The boundary conditions within the model utilized a simplified view of the grain boundary structure. The result is the model assumed all boundaries are symmetric and therefore the effect of grain boundary plane is not explicitly determined. The addition of grain boundary plane could be included into the rate theory model in the grain boundary energy term for the low $\Sigma$ grain boundaries as grain boundary plane has been well established to modify the grain boundary energy. Inclusion of the grain boundary plane might confirm the experimental outliers observed in Figure 5.5 are the result of variances in the grain boundary plane without directly determining the plane experimentally.

Figure 5.6 plots the segregation profiles for general high angle grain boundaries in the 400 ºC, 2 dpa condition. The model captured the reduced profile width and increased magnitude of the Cr segregation profiles for general high angle grain boundaries when compared to the other grain boundary regimes. The agreement for general high angle grain boundaries was not as good as those in the low angle and special grain boundary regimes. As discussed in Section 5.1.1.2, the calculated segregation profiles using the convolution model are more sensitive to the model input parameters for sharp concentration profiles such as those in Figure 5.6. For example, adjusting the convolution model to assume a specimen thickness of 40 nm and an electron

probe width of 1.1 nm brings the model within the error of the experimentally determined segregation profiles in Figure 5.6. These adjustments are not outside of reasonable values for the experiment. In contrast, the adjustment in values results in a 0.1 wt. % in the Cr concentration and 0.8 nm difference in the profile width for a low angle grain boundary ($\theta = 5$º).

Figure 5.7 plots the segregation in the model F/M steel as a function of dose and misorientation angle in the low angle grain boundary regime. The low angle grain boundary regime is selected for dose and temperature comparisons due to the limited sensitivity in the input parameters for the convolution model. The model captured the experimental response of increasing segregation with dose although the agreement is not accurate in predicting the magnitude. The model showed better agreement at higher doses and fails to predict the negligible RIS response at low angle boundaries in the 1 dpa condition. The discrepancies observed based on irradiation dose indicate the model lacks sufficient detail to capture the experimentally determined low dose response of the alloy such as early on-set irradiation induced defects.

The segregation in the model F/M steel as a function of temperature and misorientation angle in the low angle grain boundary regime is plotted in Figure 5.8. The model accurately predicted the qualitative reduced RIS response with increasing irradiation temperature. On average, the model showed the best agreement to experimental data at the 400 ºC. At 500 ºC, the model over predicted the magnitude of the Cr enrichment to the boundary by several weight percent which can be seen in Figure 5.8. The poor agreement indicates a refinement is needed in the temperature contributions within the rate theory model. Refinements could include both the pre-exponential factor and activation energy used to calculate the diffusivity of each species as these values were derived in the dilute limit and the modeling values are benchmarked against experiments conducted on a concentrated alloy.

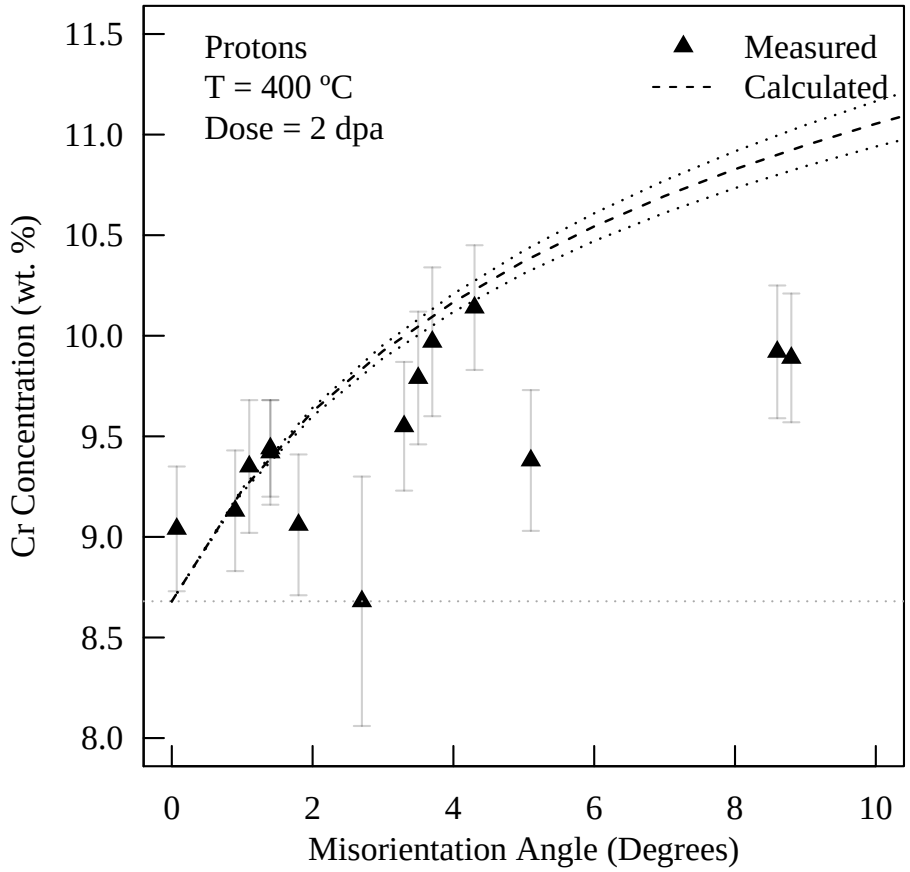


Figure 5.3: On-boundary Cr concentration as a function of misorientation angle for low angle lath boundaries for the irradiated model steel at a temperature of 400 ºC and a dose of 2 dpa using protons. Dashed line indicates calculated values from the *ab-initio* based rate theory model with the center line indicating a specimen thickness of 75 nm bounded by $\pm$50 nm.

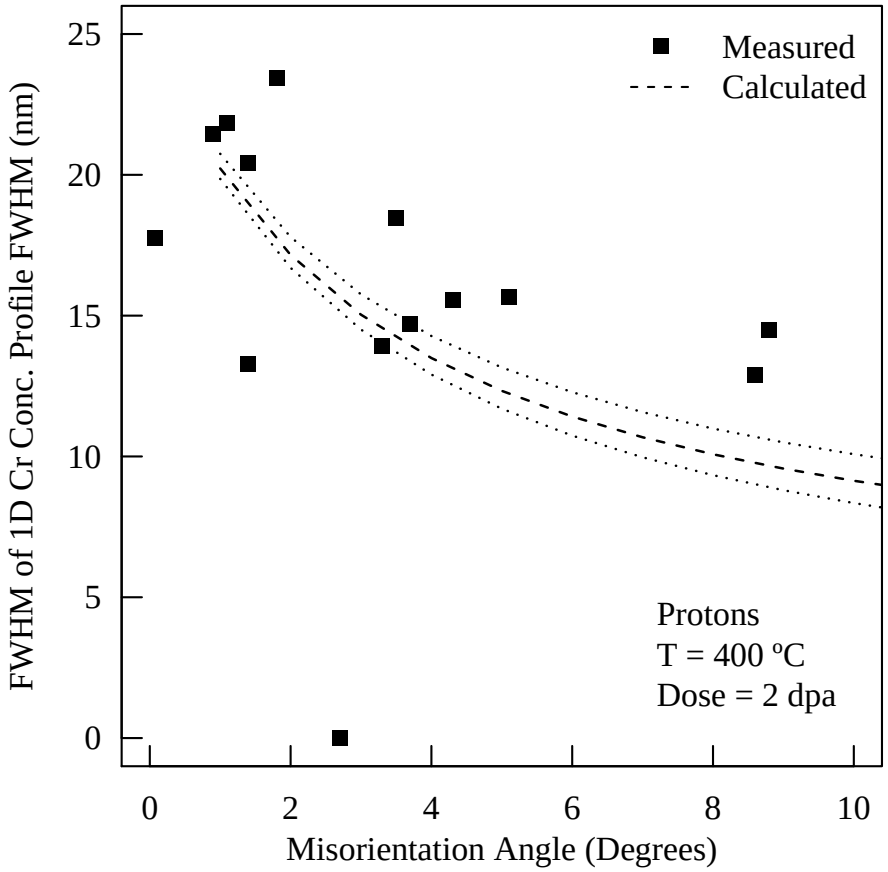


Figure 5.4: Calculated and measured FWHM of 1D Cr concentration profiles for LAGBs irradiated to 2 dpa at 400 °C using protons. Dashed line indicates calculated values from the *ab-initio* based rate theory model with the center line indicating a specimen thickness of 75 nm bounded by $\pm$50 nm.

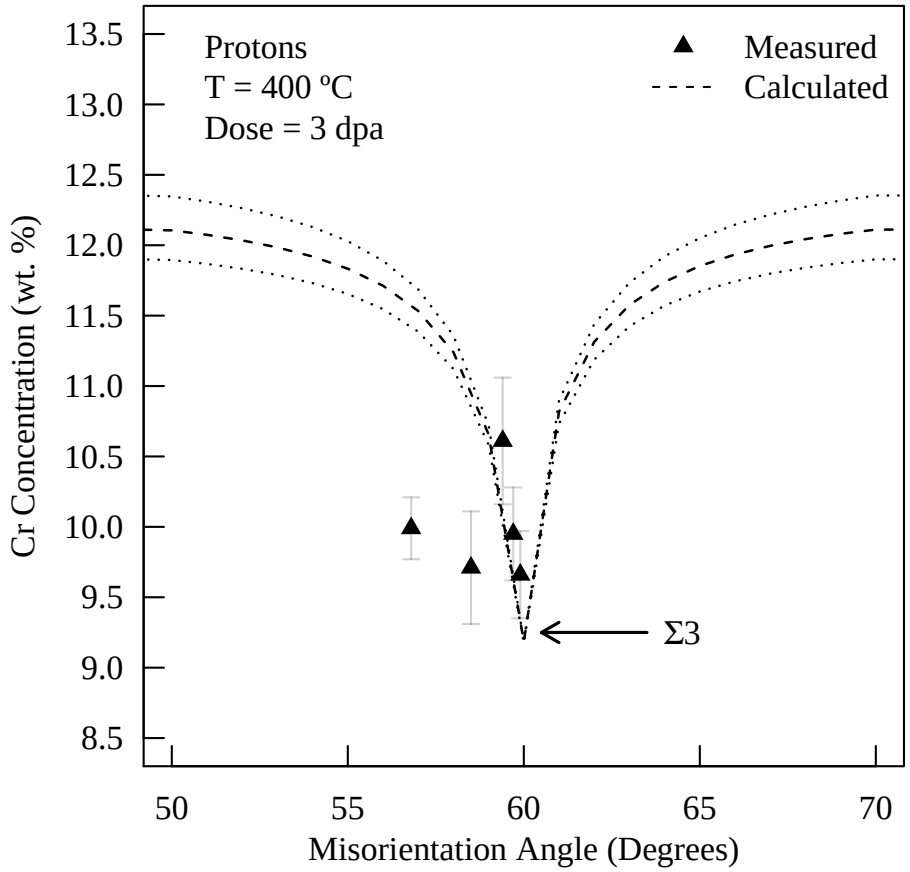


Figure 5.5: On-boundary Cr concentration as a function of misorientation angle for lath boundaries near the Σ3 condition for the irradiated model steel at a temperature of 400 ºC and a dose of 3 dpa using protons. Dashed line indicates calculated values from the *ab-initio* based rate theory model with the center line indicating a specimen thickness of 75 nm bounded by ±50 nm.

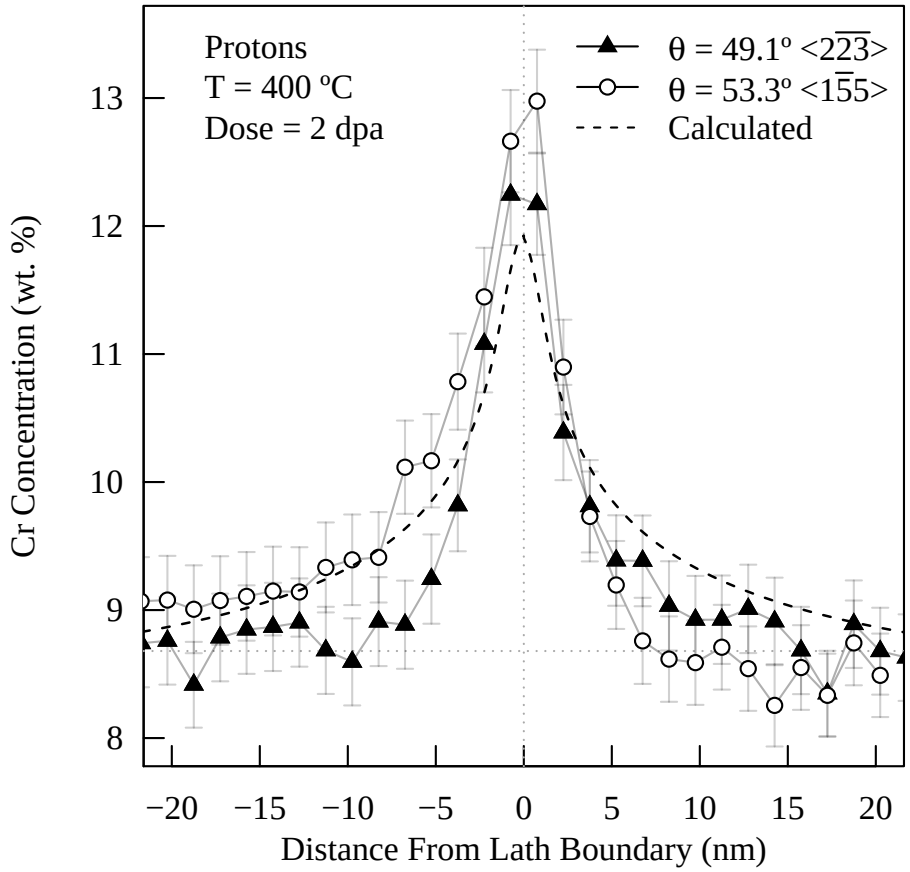


Figure 5.6: Measured and calculated 1D Cr concentration profiles for general HAGBs irradiated to 2 dpa at 400 °C using protons. Calculated boundary assumed $\theta = 50^{\circ}$ and a specimen thickness of 75 nm.

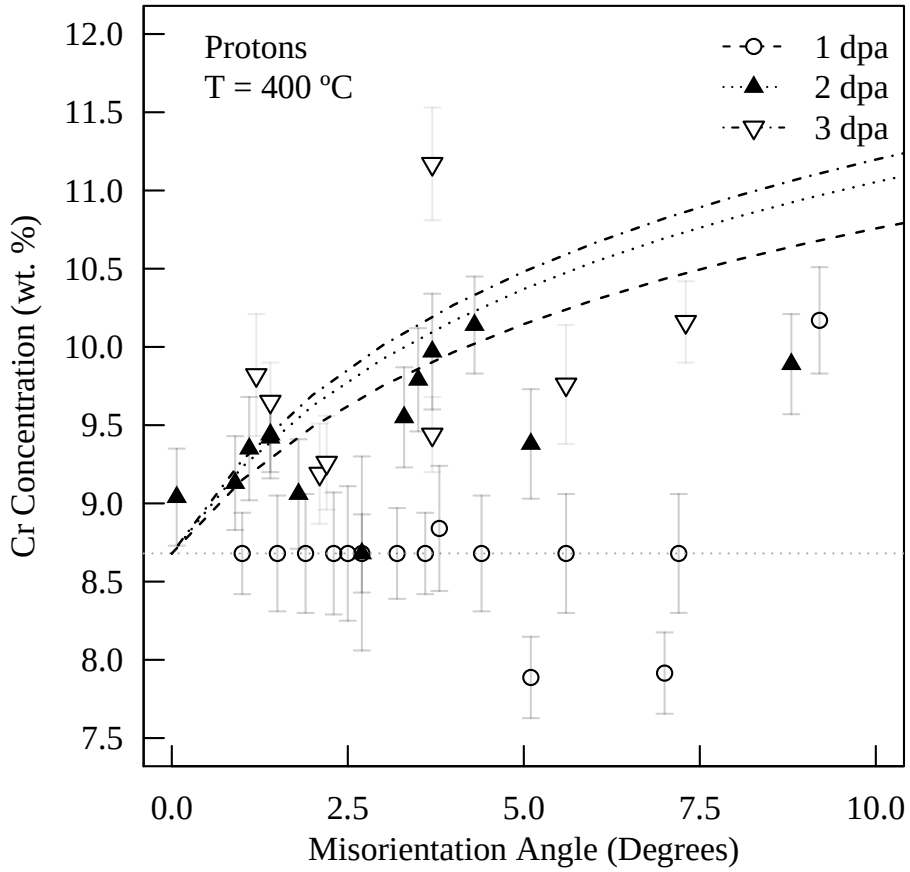


Figure 5.7: On-boundary Cr concentration as a function of misorientation angle for low angle lath boundaries showing the dose sensitivity of the RIS response for the irradiated model steel at a temperature of 400 ºC using protons. Dashed line indicates calculated values from the *ab-initio* based rate theory model with an assumed specimen thickness of 75 nm.

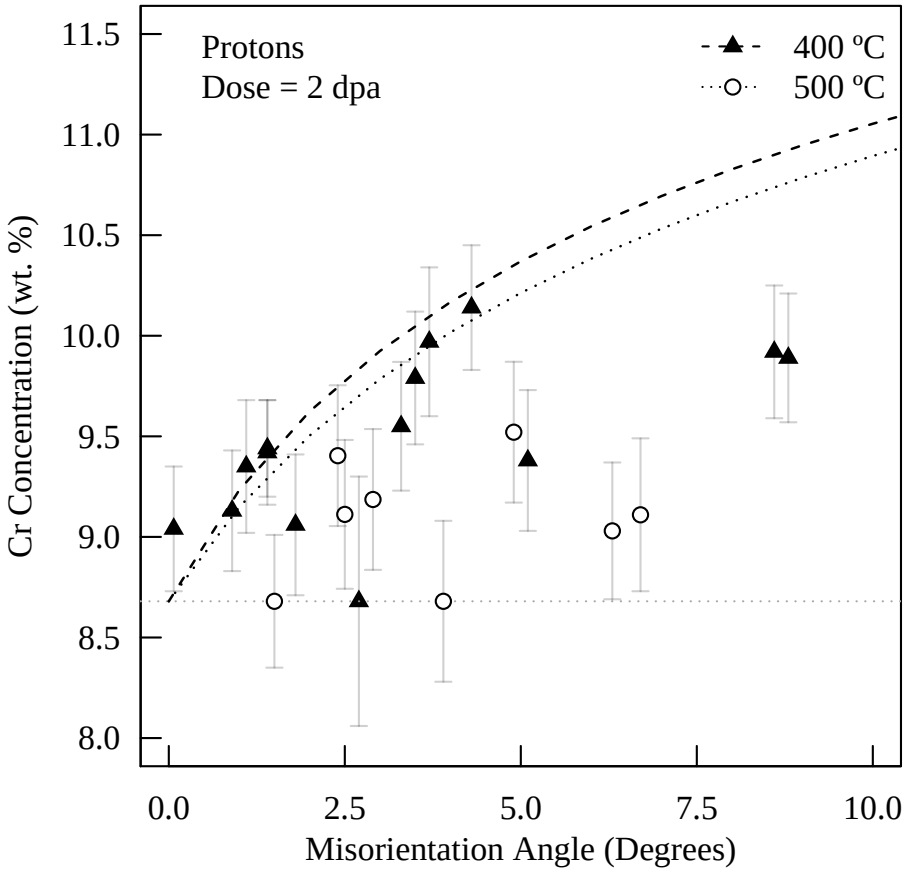


Figure 5.8: On-boundary Cr concentration as a function of misorientation angle for low angle lath boundaries showing the temperature sensitivity of the RIS response for the irradiated model steel at a dose of 2 dpa using protons. Dashed line indicates calculated values from the *ab-initio* based rate theory model with an assumed specimen thickness of 75 nm.

#### 5.1.1.4 Limitations of Predicting RIS Using an *Ab-Initio* Based Rate Theory Model

The *ab-initio* based rate theory model showed reasonable agreement with the experimentally determined RIS response across different grain boundary structures. The qualitative trends with dose and temperature were also captured by the model. The agreement between the model and the experiment in this work as well as the similar rate theory model proposed by Wharry *et*

*al. [82]* indicates rate theory models can be utilized to simulate RIS in F/M steels. The modified boundary conditions in the model presented here which accounts for differences in grain boundary structure is an improvement over previously proposed RIS models which assume an ideal sink behavior. Given this, further refinements are needed to improve the model.

In the low angle grain boundary regime the model consistently predicted the upper limit in the magnitude of the segregation profiles. The model assumes an idealized symmetric 1D diffusion directly normal to the close packed planes within the F/M steel. The idealized nature of the rate theory model could be a contributing factor to the upper limit prediction as non-symmetric or diffusion along other plane directions could alter the rate of migration of point defects to the boundary. A more accurate prediction would account for differences in the grain orientations to the grain boundary plane providing a better alignment between the experiment and the model. Inclusion of this parameter would also better determine if the non-symmetric profiles observed experimentally, such as the one provided in Figure 4.3, is the result of non-symmetric diffusion, grain boundary inclination, and/or grain boundary migration under irradiation.

The experimental data suggests a delayed on-set of RIS as a function of dose which was not captured by the model. One possible explanation is at low doses the radiation induced microstructure is still evolving and has not reached steady-state. Changes in the irradiation-induced microstructural evolution could alter the flux of point defects to the grain boundary resulting in a delayed RIS response. Topbasi *et al.* has shown defect cluster density increases with dose with a saturation point around 6 dpa at low temperatures in NF616 [117]. Wharry *et al.* have shown coarsen of precipitates and increased coverage of precipitates to grain boundaries with increasing dose up to 3 dpa in T91 [81]. These complex responses are not captured by the model as it assumes a constant dislocation density over all doses based on limited experimental data in the 9 wt. % Cr model alloy and would not account for any early on-set matrix sinks. The experimentally determined dislocation density was based on determining the specimen thickness using EFTEM techniques and weak beam dark field imaging in focused ion beam lift-out specimens, resulting in a non-idealized semi-quantitative assessment of the dislocation density.

The precipitate evolution was not studied as surface contamination after irradiation and long term storage prevented standard TEM replica sample preparation; a technique typically used for precipitate studies in F/M steels. A more rigorous analysis of the dislocation density and precipitate evolution could lead to better parameterization of the model and greater agreement between the model and the experiment. A more detailed study in the irradiation-induced microstructure evolution may also serve to improve the predicted magnitude of the segregation profile. Increased in-matrix sink density results in more point defects lost to matrix sinks reducing the RIS response at the boundary and could push the predicted magnitudes closer to the average measured on-boundary concentration.

The rate theory model determines the rate of segregation of each species can be described by a diffusivity in an Arrhenius form of:

$$d_{Cr}^{x} = d_{0,Cr}^{x} exp\left(\frac{-E_a^{Cr,x}}{kT}\right) \tag{5.7}$$

$$d_{Fe}^{x} = d_{0,Fe}^{x} exp\left(\frac{-E_a^{Fe,x}}{kT}\right) \tag{5.8}$$

where $d$ is the diffusivity of each element, $d_0$ is the pre-exponential factor, and $E_a$ is the activation energy for either Cr or Fe, $k$ is the Boltzmann factor, and $T$ is the temperature. The pre-exponential factor and activation energy are calculated based on *ab-initio* calculations where the activation energy is determined using the multi-frequency framework developed by LeClaire [118]. The activation energies are calculated based on the jump events of a point defect in close proximity to a solute. For Fe-Cr vacancy activation energies, these values were calculated to range from .62 eV to .69 eV by Choudhury *et al.* and .57 to .66 eV by *Wong et al.* [85, 86]. These calculations were completed in the dilute limit and therefore can only be used as guidelines and not definitive values for modeling RIS in non-dilute alloys such as the work presented here. Similar variations in calculated values for the interstitial migration have been reported in literature [86, 119–121]. Allen [6] showed rate theory models including the modified Inverse

Kirkendall and Perks model are significantly impacted by the migration energies utilized compared to model inputs such as the pre-exponential factor. As an example, a change of the BCC Cr vacancy activation energy by .01 eV lowers the diffusion coefficient by a factor of .84 at 400 °C and .86 at 500 °C.

The sensitivity of these models to the inputted activation energy indicates the possible explanation for the limited agreement between the model and the experiment as a function of temperature. Changing the activation energy within the rate theory model can significantly impact the calculated output, especially when considering temperature variations. The model and activation energies utilized have only been compared to experimentally determined segregation data within a very small temperature window. A reasonable test of the activation energies utilized in this study would be to compare the model against a larger temperature regime and determine if the small adjustments in the activation energy, within the variance in the reported literature, provides better agreement over a large temperature window.

The model assumed a simplified Fe-Cr system. Impurities and minor alloying elements which are present in commercial and NF-ODS steels, such as T91 or 14YWT, are not considered within the model. Minor alloying elements could interact with the point defect flux resulting in an altered RIS response in complex alloy systems. Further development would be needed to understand the role of minor alloying elements on the Cr segregation response to utilize the model for commercial F/M steels.

The *ab-initio* based rate theory model was consistent with the experimental results on the model F/M steel. Specifically, the general trends in the grain boundary structure were demonstrated to accurately predict both the magnitude and the width of Cr enrichment to irradiated grain boundaries further strengthened the observation that RIS is affected by the interfacial structure of grain boundaries. The model demonstrated some limitations, specifically in determining the magnitude of dose and temperature effects, but it is the first step towards developing a model to predict RIS at different interfacial structures in F/M steel alloys over a wide range of irradiation conditions.

### 5.1.2 Vacancy and Interstitial Diffusivity

The direction of radiation induced segregation is dependent on the relative magnitude of the vacancy and interstitial diffusivities. Choudhury *et al.* predicted that Cr enrichment at the temperature ranges investigated should be the prominent RIS response due to $d^{i}_{Cr}/d^{i}_{Fe} > 1$ and $d^{v}_{Cr}/d^{v}_{Fe} < d^{i}_{Cr}/d^{i}_{Fe}$ [86]. This finding is supported by recent work on commercial alloys [81], and was the prominent response of the results presented here for the model F/M steel. Furthermore, the values for the diffusivity ratios used in the rate theory model benchmarked to the results used here were derived from the study of Choudhury *et al.* The agreement between experiment and theory presented in Section 2.6.3, as well as in recent literature, suggests both the vacancy and interstitial mediated mechanisms are significant for RIS in F/M steels. The strong contribution of the vacancy and interstitial flux in F/M steels could be a possible explanation for the observation of both Cr enrichment and depletion to the boundary within the reported literature. The balance of vacancies and interstitials migrating to grain boundaries could be altered by a complex microstructural evolution under irradiation or minor alloying elements preferentially interacting with a specific defect flux.

### 5.1.3 Temperature and Dose Rate Dependence

In this study, both the temperature and dose rate changed between the 400 °C and 500 °C proton irradiated samples. The variation in dose rate is due to differences in the equipment used to irradiate the samples at 400 °C and 500 °C. The largest variation in the dose rate was between the 400 °C and 500 °C, 2 dpa proton irradiations. The reported dose rate was nearly 2.75 times faster for the 500 °C condition. RIS is sensitive to changes in both dose rate and temperature. Lower dose rates lead to more RIS at a fixed temperature due to reduced recombination effects. For F/M steels, reducing the irradiation temperature increases the Cr-interstitial contribution leading to more RIS as determined by the *ab-initio* rate theory model. Both affects combine to lead to the reduction in the RIS response in the specimens irradiated at 500 °C versus 400 °C.

The reduced RIS response seen in the model alloy at 500 °C is similar to results on T91 [83] shown in Figure 5.9. The T91 irradiations were conducted with a fixed dose rate and the dose rate was identical to the 500 °C model F/M samples used in the this study. The similar RIS response in the model alloy to T91 indicates the dominant effect in the variation of the RIS response was most likely due to changes in irradiation temperature. To fully deconvolute what mechanism is dominant in the reduction of the RIS response with increasing temperature further irradiations and analysis would be needed. Specifically, irradiations conducted over a wide temperature window with a fixed dose rate would provide sufficient information on the temperature contributions to the RIS response.

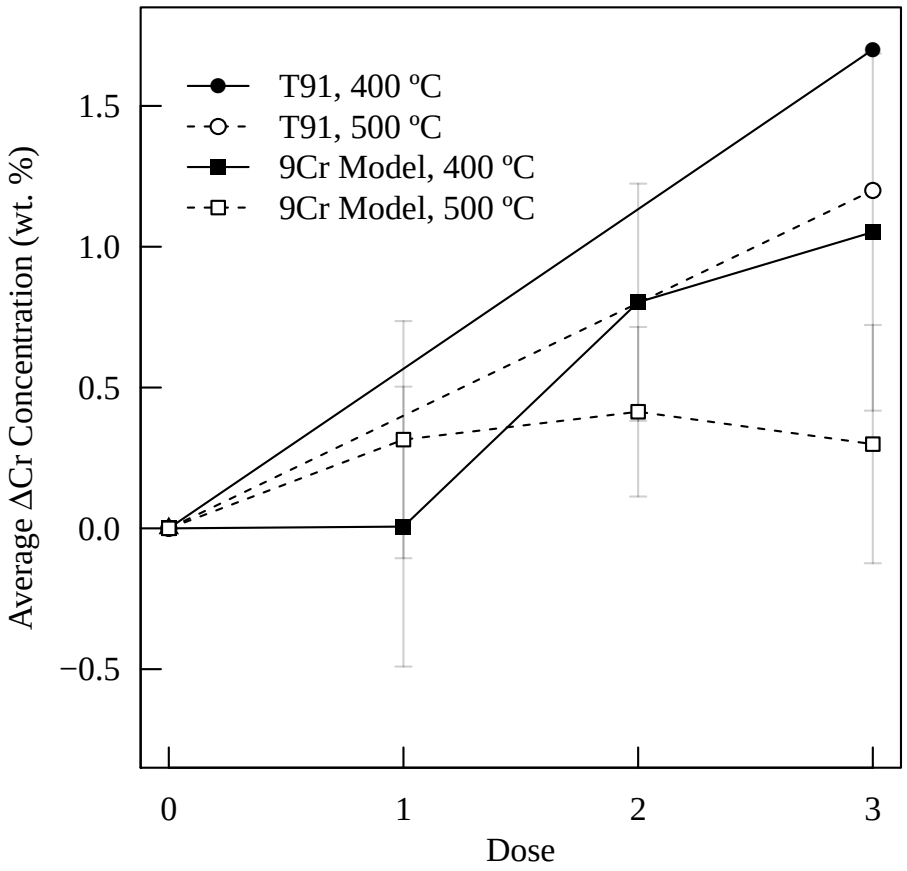


Figure 5.9: On-boundary Cr concentration as a function of dose for T91 and the 9 wt. % Cr model steel. T91 measurements obtained from prior austenite grain boundaries while the model steel measurements acquired from low angle lath boundaries. All specimens irradiated using 2.0 MeV protons. From [81].

### 5.1.4 Dose Dependence

The experimental results in the model F/M steel indicates the segregation at the grain boundaries are increasing with dose at the low doses observed as illustrated in Figure 5.9. This response has been observed in T91 at similar doses irradiated using protons [83]. The results presented here and on T91 are consistent with RIS seen in austenitic alloys at lose dose [122]. The continuous increase in the model F/M steel at low doses indicates the attainment of steady state conditions was not met. The decreasing segregation rate with increasing dose, which is also predicted via the rate theory model, suggests the system is approaching saturation. Higher dose irradiations are needed to verify the dose to steady-state for the model F/M steel.

### 5.1.5 Comparison of Neutron to Proton Irradiation Experiments

Neutron irradiated grain boundaries at a nominal temperature of 500 °C had Cr segregation to the boundary on the order of 1.25-1.5 times higher than proton irradiated grain boundaries at either 400 °C or 500 °C at the same dose and similar misorientation angles. The change in the magnitude in segregation is consistent with trends seen in austenitic stainless steels where neutron irradiations with significantly lower dose rates irradiated at the same temperature typically resulted in higher segregation levels compared to proton irradiations, even when the efficiency of freely migrating defects between the two incident particles are taken into consideration [123]. Although the magnitude of the segregation changed between the neutron and proton irradiations, the trends with segregation and misorientation angle were similar between the two experiments. Figure 5.10 shows the RIS response as a function of misorientation for the two irradiation conditions in the high angle grain boundary regime. The reduced segregation at $\Sigma 3$ grain boundaries compared to general high angle grain boundaries in both conditions suggests the mechanisms which affects the sink efficiencies of grain boundaries is independent

of the incident particle. Given this, the measured difference between the two incident particle irradiation indicates incident particle does affect other processes which leads to RIS at grain boundaries.

Proton and neutron irradiations have fundamentally different damage processes which affect the damage cascade and the dose rate. Was *et al.* have shown the differences in the damage process can be accounted for by using a higher irradiation temperature for proton irradiations to achieve similar freely migrating point defect migration processes [10]. Was *et al.* showed an 85 °C higher irradiation temperature for protons reasonably matched the complex RIS response of neutrons where the proton irradiation dose rate was $7.0x10^{-6}$ dpa/s and the neutron dose rate was estimated at $7.6 - 10.0x10^{-8}$ dpa/s in two 300 series austenitic stainless steels. The results presented here did not show the same type of agreement between neutrons and protons seen in austenitic stainless steels for the irradiations conducted at 3 dpa. The dose rate for the F/M steel was two orders of magnitude higher when comparing the 500 °C condition and half that for the 400 °C proton irradiation. The direct comparison between the neutron and proton irradiations conducted on F/M steels is complicated because of the ambiguity in the determination of the neutron irradiation temperature [100]. It is probable the correct proton irradiation temperature to capture the dose rate-temperature-incident ion correlation was not observed and better agreement between proton and neutron experiments could be developed.

The comparison of the proton and neutron irradiations is further complicated when considering dose equivalence between the two irradiations. Light ions are typically considered to be more effective in producing the freely migrating defects which contribute to RIS compared to neutrons. Protons have been quoted to have a production efficiency of ~20% while neutrons are significantly lower at ~2% [114]. The dose equivalence is further complicated when considering neutron irradiations as the nuclear reactors have a range of incident neutron energies while ion irradiations are typically highly mono-energetic. The dose of the neutron experiments was calculated assuming an average neutron energy and the damage processes of the entire neutron energy spectrum was not explicitly determined. The proton irradiations were conducted

by rastering the proton beam which results in the beam only interacting with the specimen for very short fractions of time which results in a high local displacement rate and hence greater point defect recombination [10]. Neutrons will also cause transmutation of alloying elements in the irradiated model steel which could interact with the point defect fluxes to grain boundaries, an effect which cannot be simulated using solely protons [10]. The ambiguity in the dose rate, temperature, as well as defect production kinetics makes drawing any conclusions on comparing neutron irradiations to proton irradiations difficult. The clear indication is more controlled neutron experiments are needed, such as those which utilize temperature instrument lead capsules to provide greater information on the specimen temperature history.

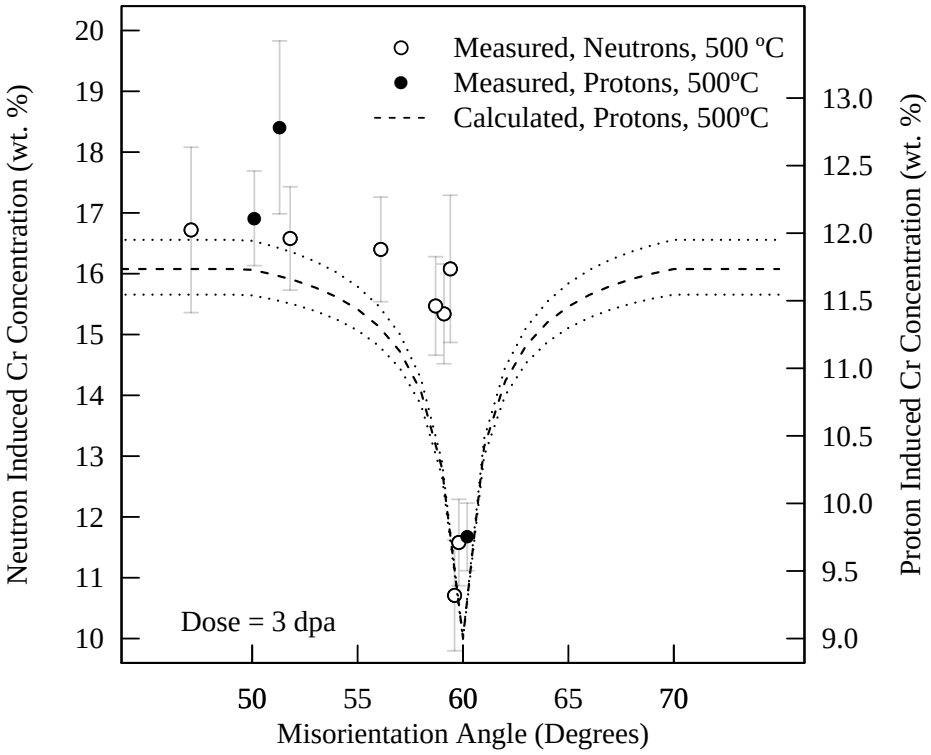


Figure 5.10: On-boundary Cr concentration as a function of misorientation angle for lath boundaries showing the incident particle RIS response for the irradiated model steel at a dose of 3 dpa. Dashed line indicates calculated values from the *ab-initio* based rate theory model with the center line indicating a specimen thickness of 75 nm bounded by $\pm$50 nm.

### 5.1.6 Role of Grain Boundary Structure on RIS

RIS at grain boundaries is directly related to the flux of point defects to grain boundary, the capture of the point defect flux by the boundary, and ultimately their destruction. RIS can be used to imply the grain boundary point defect sink efficiency and mechanisms related to the efficiency. The experimental RIS results show the grain boundary point defect sink efficiency changes depending on the grain boundary misorientation angle, with three distinct regimes: low angle grain boundaries, special grain boundaries, and general high angle grain boundaries. The *ab-initio* based rate theory model agreed with the trends observed in the experimental results based on the misorientation angle. The modified boundary conditions within the model indicate the grain boundary annihilation mechanisms outlined in Section 2.4 are active, specifically the density of annihilation sites at the grain boundary and the diffusion of point defects to the annihilation site. The result is the structure or coherency of the boundary is directly related to the sink efficiency of the boundary and the RIS response at the boundary.

Results indicate the Cr enrichment at the lath boundary rapidly increases with increasing misorientation angle for LAGBs for all doses investigated. Therefore, assuming no mechanistic change as a function of local composition, the total number of vacancy and/or interstitials absorbed at the grain boundary at a fixed dose must also increase with increasing misorientation angle in the LAGB regime. As discussed in Section 2.2.1, LAGBs are comprised of an array of primary grain boundary dislocations and the dislocation density increases with increasing misorientation. The increased density of dislocations provides a higher concentration of dislocation jogs where point defects can diffuse through the lattice and be absorbed. The observed trends indicates the probable mechanism for point defects annihilation rates at the boundary is either a sink reaction or mixed behavior of sink and bulk diffusion reaction limited. A sink reaction limited or mixed behavior mechanism would result in the concentration of point defects to be uniform or near uniform across grain boundaries during irradiation, driving the limited RIS response observed experimentally over the wide range of irradiation conditions. The higher

RIS at higher misorientation angles in the LAGB regime indicates a possible shift towards a stronger bulk diffusion reaction limited process and the grain boundaries approaching the perfect sink condition, although the limited data in the range of 10°-15° prevents any concrete conclusions to be made.

The high coherency across the interface at Σ3 grain boundaries resulting in low grain boundary energy suppresses the RIS response in traditional F/M steels. The higher coherency at the boundary lends to a structure similar to those of low angle grain boundaries which can be classified as Σ1 grain boundaries. Therefore, a large portion of the grain boundary exhibits bulk like behavior with limited fast diffusion paths along the boundary and minimum point defect annihilation sites. The result is the sink efficiency at very low sigma grain boundaries is lower than general high angle grain boundaries and the point defect concentrations are higher at the boundary for special grain boundaries. The results presented here were for Σ3 grain boundaries but the theory for special grain boundaries in F/M steels could be extended to other high coherency CSL grain boundaries, such as Σ9 or Σ11. The cusps observed in the RIS response when the boundary structure deviates from the exact CSL reference structure is due to the increase in the density of secondary grain boundary dislocations as given in Eq. 2.6 to accommodate the misfit from the exact CSL structure ($\Delta\theta = \theta - \theta_{CSL}$). Distinct cusps in the RIS response at Σ3 grain boundaries have also been observed in 304L stainless steels irradiated with protons at 450 °C to 1 dpa by Duh *et al.* [88]. The special grain boundary RIS response is similar to that of low angle grain boundaries where with an increase in misorientation a increase in primary grain boundary dislocations is needed to accommodate the minor misfit between the two grains as given in Eq. 2.1. The similar RIS response between low angle grain boundaries and low Σ boundaries supports the theories on the point defect capture and annihilation rates for both boundary types.

The enrichment of Cr at general HAGBs was significantly higher than boundaries in the LAGBs or for Σ3 boundaries over all irradiation conditions. This result suggests that the destruction of defects at general HAGB is unrestricted. The ease at which a general HAGB can absorb

point defects is due to the SGBDs and high density of dislocations at the boundary [37]. As in the low angle grain boundary case, point defects are annihilated at jogs on dislocations. The difference between HAGBs and LAGBs is the method for which point defects can diffuse at the boundary and the density of dislocations at the grain boundary. For general HAGBs, diffusion of lattice point defects to SGBD can occur via bulk diffusion through the adjoining grains as in the LAGB case for primary grain boundary dislocations but can also diffuse to SGBDs through rapid short-circuit diffusion along the boundary [37]. The faster diffusion path coupled with the higher density of dislocation jogs for general HAGBs leads to the boundary acting in the near perfect sink condition. HAGBs which act as a perfect sink should exhibit the largest RIS response when compared to LAGBs or special grain boundaries, as supported in the results for the HAGBs presented here.

The results presented here with coupling to the rate theory modeling indicates a direct relationship between interfacial coherency, interfacial energy, point defect annihilation rates at the interface, and the resulting RIS response of the interface. The inter-relationship between these factors has been proven to be quite complex. Given this, a generalized-simplified view of the mechanisms can be made. A simplified schematic of the role of coherency at grain boundaries in the point defect flux is presented in Figure 5.11. The difference in the structure and resulting grain boundary point defect concentration gradients is illustrated schematically in Figure 5.12. The simplified view of the RIS-interface structure based on the results in lath boundaries for F/M steels could possibly transfer to other defect sinks and internal interfaces, including matrix-precipitate interfaces.

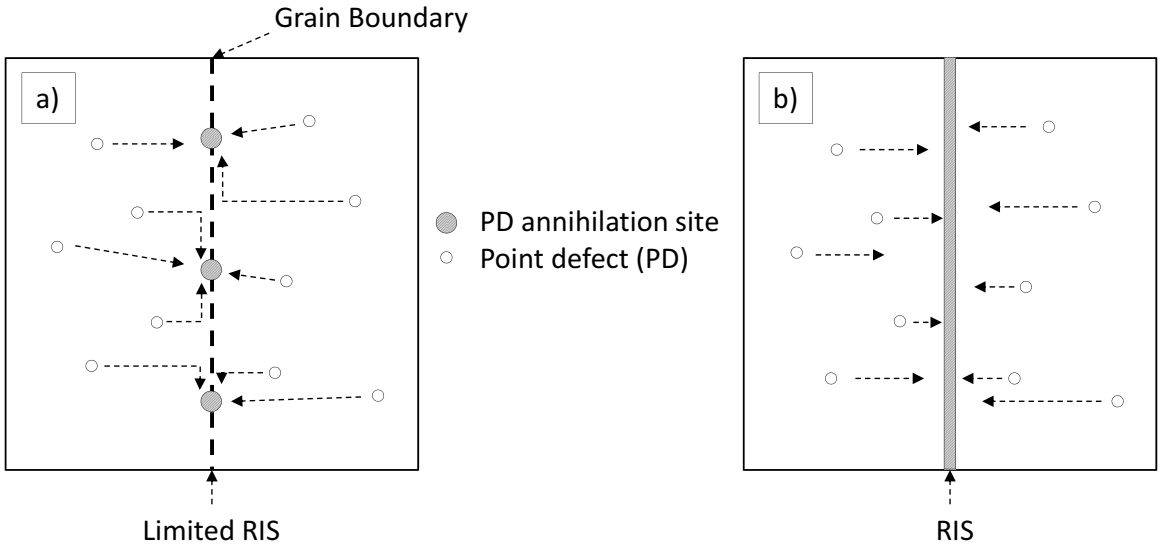


Figure 5.11: Schematic of point defect interactions with relationship to different grain boundary structures and RIS: a) high coherency; point defect diffusion along the boundary is near bulk diffusion values and the annihilation sites are discrete and limited resulting in low sink efficiency and b) low coherency; point defect diffusion along the boundary is rapid and the annihilation sites are non-discrete resulting in high sink efficiency.

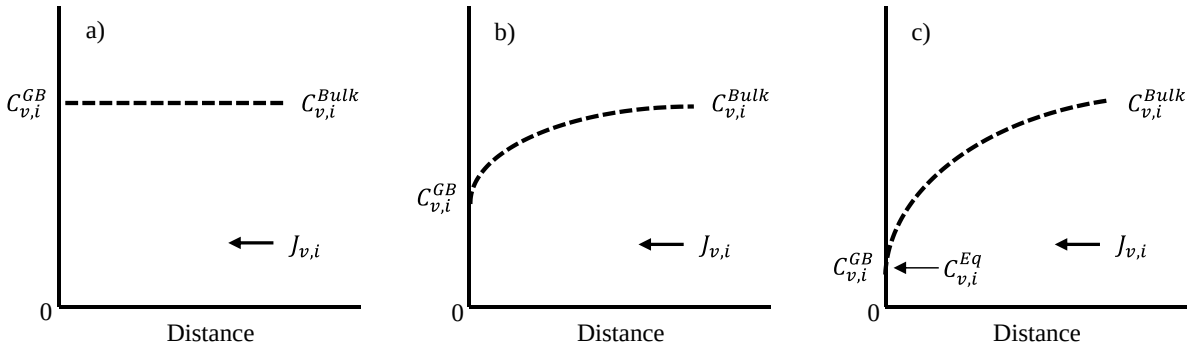


Figure 5.12: Point defect concentration gradients for radiation-induced segregation where a) an interface has a high coherency leading to low sink efficiency resulting in the boundary being a poor sink for point defects, b) an interface has moderate coherency leading to a moderate sink efficiency and an effective sink for point defects and c) the interface has low coherency leading to the perfect sink condition and $C_{v,i}^{GB} \approx C_{v,i}^{Eq}$.

## 5.2 Radiation Induced Segregation (RIS) in NF-ODS F/M Steels

The model F/M steel had predictable RIS responses based on standard theory for RIS in Fe-based systems. The NF-ODS steel exhibited a complex and unexpected response over the wide temperature range observed. The model F/M steel is a simple ternary Fe-Cr-C system with no minor alloying elements influencing the irradiated grain boundary chemistry. The NF-ODS steel contains minor alloying elements with some not typical in F/M steel systems as well as the presence of nanoclusters within the matrix. These microchemical and microstructural features compound to generate the atypical RIS response in the 14YWT NF-ODS steel. The RIS response and the role of microstructure and microchemistry are discussed in the following sections.

### 5.2.1 Evolution of Segregation Profiles

The Cr segregation profiles exhibited a large variation in the shape and sign of the segregation as a function of temperature in the irradiated 14YWT specimens. At cryogenic temperatures no segregation of Cr was detected. Other alloying elements including W and Fe did not have detectable segregation after cryogenic irradiations as well. At such low temperatures, the solute atoms are placed into solid solution due to ballistic mixing and there is insufficient energy for back-diffusion of solute atoms to diffuse back to grain boundaries. The ballistic resolution of solute atoms at grain boundaries is similar to ballistic resolution of nanoclusters under cryogenic irradiation temperatures at high doses [11]. At high temperature (450-600 °C), Cr and W were enriched at the boundary and Fe depleted and profiles exhibited an inverted 'v-shape' profile. The magnitude and width of segregation remains nearly unchanged from the as-received state. The difference between an irradiated grain boundary at 450 °C and an unirradiated grain boundary is presented in Figure 5.13. This RIS behavior is different than the 9 wt. % Cr model steel where a change in the grain boundary chemistry was observed at both 400 °C and 500 °C

after proton irradiation. The arrested RIS responses suggests a reduced flux of point defects at the grain boundary in NF-ODS steels compared to the more traditional model F/M steel.

At low to intermediate temperatures (100-300 °C), the Cr segregation profile showed the formation of 'w-shaped' profiles while W and Fe enriched with typical inverted 'v-shaped' profiles. At 100 °C, the 'w-shaped' Cr profile had almost completely transformed to a 'v-shaped' profile and significant Cr depletion was observed. Even at low temperatures first principle modeling suggests Cr interstitials should be a fast diffuser and qualitatively Cr enrichment at the boundary should occur after irradiation. The retention of pre-segregation of Cr at grain boundaries irradiated to high temperature and the formation of 'w-shaped' profiles and eventual depletion of Cr at the boundary at low to intermediate temperatures indicates the mechanisms proposed for the model F/M steel are an over simplification for complex alloy systems and segregation behavior must be driven by either prior segregation to the grain boundary, binding of Cr to minor alloying elements, the high density of nanoclusters in the NF-ODS steel or the a combination of several factors.

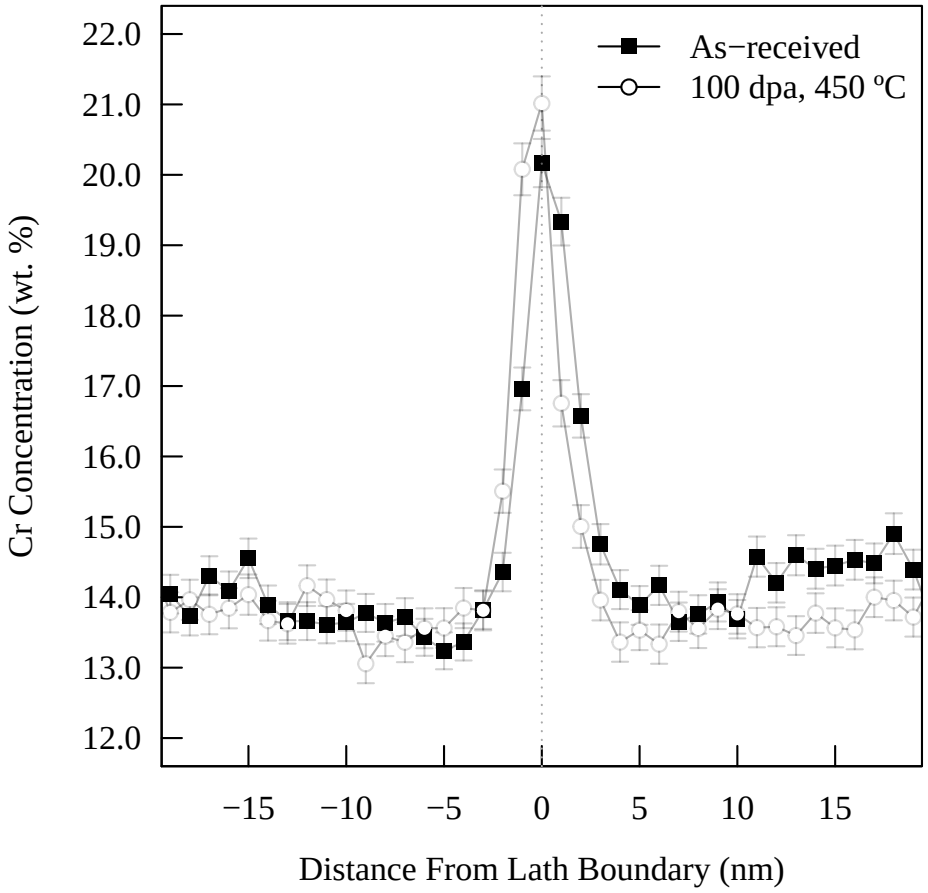


Figure 5.13: 1D semi-quantitative Cr concentration profiles from an as-received grain boundary and a grain boundary irradiated to 100 dpa using $Ni^{2+}$ ions at 450 °C in the 14YWT alloy. The profiles indicates little change in the microchemistry of grain boundaries after irradiation at 450 °C.

### 5.2.2 Cr Vacancy and Interstitial Diffusivity

The NF-ODS alloy showed a driving force for Cr depletion at grain boundaries when irradiated to 100-300 °C. Several factors could be contributing to Cr depletion at grain boundaries in the NF-ODS steel. One factor would be a crossover in the Cr-Fe diffusion coefficient ratios, $d^{v}_{Cr}/d^{v}_{Fe}$ and $d^{i}_{Cr}/d^{i}_{Fe}$, at low temperature. If the vacancy diffusion dominates over the interstitial

diffusion, $d^{v}_{Cr}/d^{v}_{Fe} > d^{i}_{Cr}/d^{i}_{Fe}$, Cr would deplete at the boundary. According to the calculated ratios in Figure 2.22, a crossover in the diffusion coefficient ratios is not observed at the irradiation temperatures performed experimentally. The reasonable agreement between the model F/M steel and the rate theory model which utilizes the diffusion coefficient ratios in Figure 2.22 suggests the calculated values are within reason, at least in the temperature range of 400-500 °C. On the other hand, Wharry *et al.* suggested a cross over at 530 °C, where vacancy diffusion is predicted to dominate resulting in Cr depletion above 530 °C using the inverse Kirkendall (IK) model for 9 wt. % Cr steels [82]. The significant depletion even at 100 °C in the 14YWT alloy indicates the study of Wharry *et al.* is not in agreement with the findings here. Both studies were focused on RIS in 9 wt. % Cr steels. Terentyev *et al.* investigated the migration of single self-interstitial Cr atoms based on composition in BCC Fe-Cr alloys and suggested above ~10 wt. % Cr, Cr cannot diffuse via interstitial mechanisms due to trapping and therefore the vacancy diffusion would dominate leading to Cr depletion at the grain boundary [87]. The possibility of an insignificant interstitial diffusion to the grain boundary due to the significantly higher Cr content in 14YWT is further supported by Wharry *et al.* as reasonable agreement between experiment and the IK model for several F/M steels with varying Cr concentration was only achieved when a composition-dependent interstitial migration energy was used. Given this, Ohnuki *et al.* found Fe-13 wt. % Cr ferritic alloys irradiated using $C^{+}$ ions up to 118 dpa at 525 °C showed Cr enrichment to the grain boundary indicating other factors not accounted for via modeling can contribute to the sign of the segregation. The complexity of the 14YWT alloy system and idealized nature of typical RIS models and first principle simulations combine to make it difficult to determine if the key driving force behind Cr depletion at 100-300 °C is due to a crossover in the Cr-Fe diffusion coefficient ratios. The results on 14YWT, comparison to the model steel, and literature does indicate both the interstitial and vacancies play a significant role and the dominating mechanism can be easily changed based on both the irradiation condition and alloy.

### 5.2.3 Role of Nanoclusters on the RIS response

The NF-ODS alloy showed a limited RIS response in specimens irradiated to 450-600 °C while boundaries at low and intermediate temperatures showed significant variation in the microchemistry at boundaries as compared to the as-received state. At 450-600 °C, back diffusion or point defect recombination effects should be limited and segregation would be anticipated at high doses and temperatures, particularly based on the results presented for the model F/M steel alloy and those within the literature. The limited RIS response at high temperature could be the result of a reduced flux of point defects to the boundaries. Wharry *et al.* showed the RIS response is highly dependent on the sink density within the material in F/M steels where the change of Cr at the boundary changes by several atomic percent depending on the density of sinks within the material using the IK model [82]. The inclusion of nanoclusters within the matrix could serve as point defect sinks and the very high density within the material in the as-received state could significantly reduce the total net flux of point defects to grain boundaries. The nanocluster density, typically on the order of $10^{21} - 10^{23}\ m^{-2}$, in 14YWT is significantly higher than the dislocation density typically quoted at $10^{13} - 10^{14}\ m^{-2}$ suggesting the nanoclusters are the dominate sink compared to dislocations within the matrix [124, 125].

At low temperature the nanoclusters are unstable due to ballistic resolution, but the motion of Cr and other solutes within the matrix are still high enough for migration to grain boundaries resulting in the segregation seen in the 100-300 °C samples. At cryogenic temperatures migration of all species is effectively frozen out creating the flat segregation profiles observed. The APT and EFTEM data provided in Table 2.2 presented conflicting results on the number density of clusters as a function of temperature where APT showed no change and EFTEM analysis showed significant change. Three mechanisms are proposed which includes the discrepancies in the number density but links the behavior of nanoclusters to RIS: 1) coherent nanoclusters remain stable under irradiation at low temperature but are less effective sinks than unstable, semi-coherent or incoherent clusters which are more stable at high temperature, 2) small nanoclusters act as biased sinks and are the dominant nanocluster population at low temperature

and 3) the RIS behavior is dependent on the effective average surface area of nanoclusters per unit volume which reduces as clusters become unstable at low temperature.

14YWT alloys have two populations of nanoclusters of interest which could be effective sinks for point defect capture. The first is particles on the size of ~10-20 nm which are semi-coherent or coherent precipitates while the other is much smaller particles on the size of ~2 - 4 nm which have been hypothesized to be highly coherent with the matrix [59, 125–128]. The first population of particles is easily detectable using energy filtered transmission electron microscopy (EFTEM) while the clusters with the size of 2-4 nm can be detected using APT. The skewness in the sampled particle size population can be seen in Table 2.2. Based on the results presented on the model F/M steel, the coherency of an interface strongly determines the sink efficiency of said interface. Therefore, any population of precipitate which is incoherent or semi-coherent with the matrix would interact more strongly with point defects than a coherent precipitate. Figure 5.14 plots the change in Cr concentration as a function of temperature with the change in number density of nanoclusters for the two populations sampled using EFTEM and APT from Table 2.2. Figure 5.14 reveals a strong correlation between the number density of particles within the matrix as detected by EFTEM to on-boundary Cr concentration change as a function of temperature. The relationship between number density and Cr concentration at the boundary seen at 600 °C is of particular interest. The reduction in the number density could be the result of coarsening of larger particles at the expense of smaller ones which reduces the number of nanoclusters and hence the number defect sink sites which limit RIS to the grain boundary. The data only suggest this mechanism at higher temperature but further work would be needed, particularly observing the relationship at even higher temperatures as the number density may remain stable at high temperature and the effect observed in the data here is due to experimental error. APT did not show any correlation as the nanocluster number density remained constant over all temperatures while the Cr concentration varied. The strong dependence between the EFTEM nanocluster stability results and the RIS results suggests the larger particles could be acting as more efficient sinks for point defects compared to very small nanoclusters within the matrix due to their potential difference in coherency with the matrix.

Another way the nanoclusters could be altering the RIS response is by altering the balance of vacancy and interstitial fluxes to the grain boundary. If the small nanoclusters sampled by the APT technique were to exhibit a biased nature, for example an infinity for Cr-interstitials, it could reduce the overall flux of Cr-interstitials reaching the boundary and result in the Cr depletion observed at the boundary in the 100 - 300 °C irradiated samples. At higher temperatures the larger nanoclusters could be the dominate sink for point defects limiting the biased sink effect of the small nanoclusters seen at lower temperatures. Other sinks have been observed as biased sinks such as dislocations preferentially absorbing and annihilating interstitials while voids tend to absorb vacancies [129–131]. It is unclear whether the size of nanoclusters is a factor in the affinity of the nanocluster to absorb one defect species versus another. The proposed biased sink mechanism for nanocluster-RIS relationship would also be predicated on the observation that on average APT is sampling only one type of nanocluster population while EFTEM is sampling another, similar to the number density theory proposed prior.

The coherency of nanoclusters within the matrix as a function of their size is still highly debatable with only a few studies conducted and very few of them being in agreement with each other and the nature of the nanoclusters interacting with the defect flux is yet to be determined. Furthermore, EFTEM and APT may sample from both populations limiting the validity of the analysis of the results. The coherency of the nanoclusters and their stability within the matrix after irradiation and the biased sink affect are only proposed as two potential mechanisms for limiting the RIS response at high temperature. Another possibility is the change in available effective surface area of nanoclusters under irradiation at the different temperature set points. A reduction in the total surface area available for point defects to interact with could alter the total defect flux which reaches grain boundaries and contributes to RIS. Using the information from Table 2.2, Figure 5.15 plots the effective average surface area of nanoclusters per unit volume of area as a function of irradiation temperature for both the EFTEM and APT determined nanocluster populations as well as the average change in Cr concentration at the boundary. Figure 5.15 shows similar trends in the effective surface area of nanoclusters as a function of temperature where the average surface area per unit volume of nanoclusters is significantly increased

at high temperature compared to low and intermediate temperatures. If EFTEM and APT were sampling both coherent and incoherent nanoclusters populations, which is very likely, or nanoclusters do not exhibit a interfacial coherency dependency with size, the available surface area hypothesis could be likely.

To fully deconvolute what mechanism plays a significant role further analysis would be needed, particularly using APT where 3D reconstructions can determine the exact effective surface area of nanoclusters using isoconcentration surfaces, to provide fully conclusive evidence on the relationship between nanocluster effective surface area and the RIS response in NF-ODS alloys. Also, further work would be needed using high resolution transmission electron microscopy to determine the coherency of different nanoclusters after irradiation to different temperatures. Finally, in-situ experiments would be needed to be determined if different sized nanoclusters exhibit a biased defect nature. It could also be plausible that several mechanisms combine to determine an effective sink efficiency for the particle and hence the RIS response. Independent of whether the change in surface area, the biased nature of the nanoclusters, or the loss of incoherent particles influences the RIS response, the results indicate a very strong dependence on nanoclusters and RIS. A simplified cartoon of this proposed interaction is seen in Figure 5.16.

The interaction of nanoclusters with the defect flux would also suggest segregation should be observed at the nanocluster interface (core-shell) or a change in the bulk chemistry of the nanocluster irradiated at 450 °C or higher. Several attempts were made to investigate the chemistry of the nanoclusters using STEM-EDS to determine if the irradiated nanoclusters exhibited a core-shell microchemical morphology without success. The unknown thickness of the matrix material above and below a nanocluster which contributes to the EDS signal prevents a simplified deconvolution technique to determine the exact chemistry of the interface and nanocluster. Advanced data processing techniques, including principle component analysis were also inconclusive in examining core-shell morphologies. Furthermore, particles under ~5-10 nm were investigated in very thin areas of the TEM specimen to limit matrix contributions to the EDS

signal but limited Cr, Ti, and Y counts could be observed and using longer dwell times to increase counts only created significant beam damage during acquisition. Use of APT to investigate the RIS at the interface currently includes pitfalls which prevents the determination of a core-shell morphology as well. The main concern using APT is the difference in evaporation rate between the matrix and the nanoclusters leading to non-uniform evaporation of the matrix and nanoclusters and generates overlap between the matrix and cluster during standard APT reconstruction techniques. The overlap prevents an accurate determination if RIS is occurring at the interface of the nanoclusters.

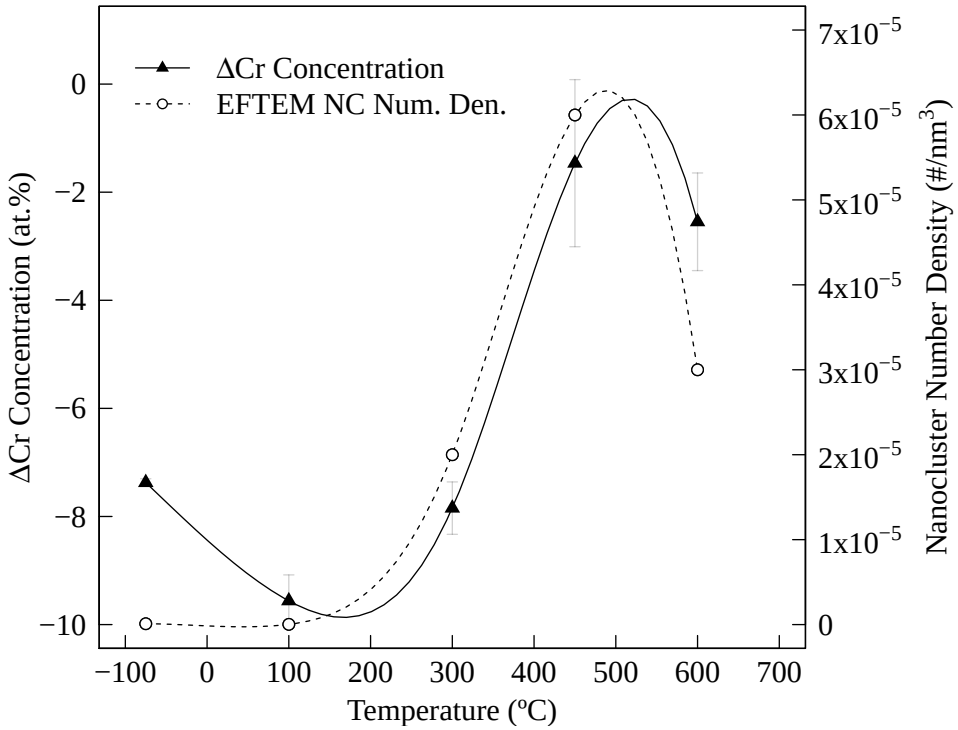


Figure 5.14: Change in on-boundary Cr concentration and EFTEM determined nanocluster number density as a function of temperature after 100 dpa irradiation using $Ni^{2+}$ ions. APT determined number density not plotted as it remains constant at ~$7x10^{-4}\ \frac{\#}{nm^3}$.

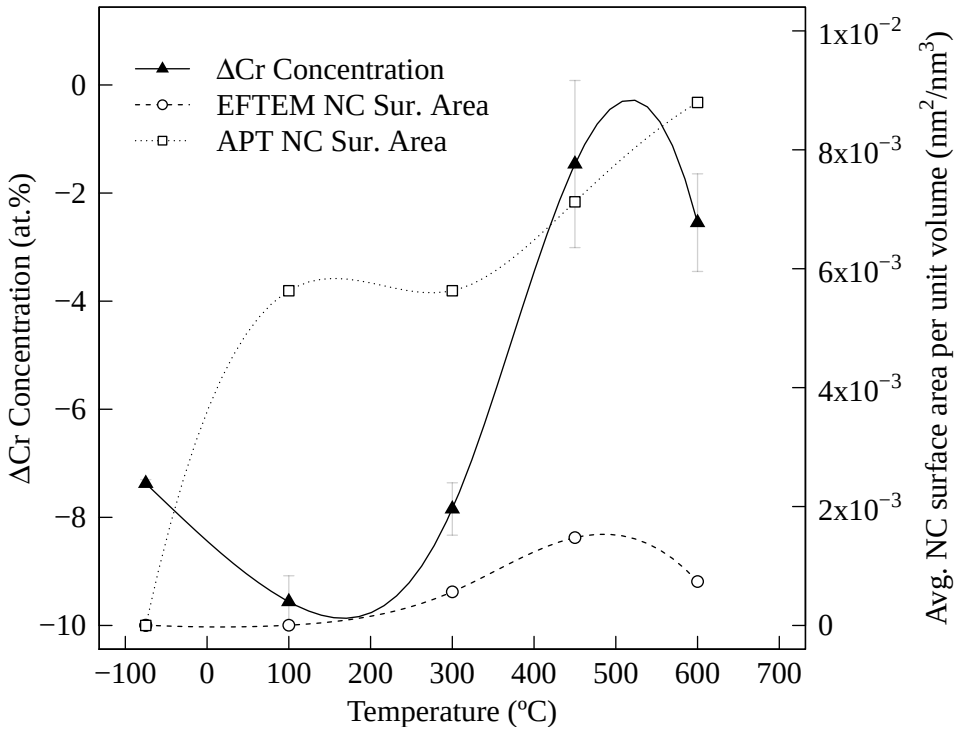


Figure 5.15: Change in on-boundary Cr concentration and EFTEM and APT determined average nanocluster surface area assuming a perfect sphere as a function of temperature after 100 dpa irradiation using $Ni^{2+}$ ions.

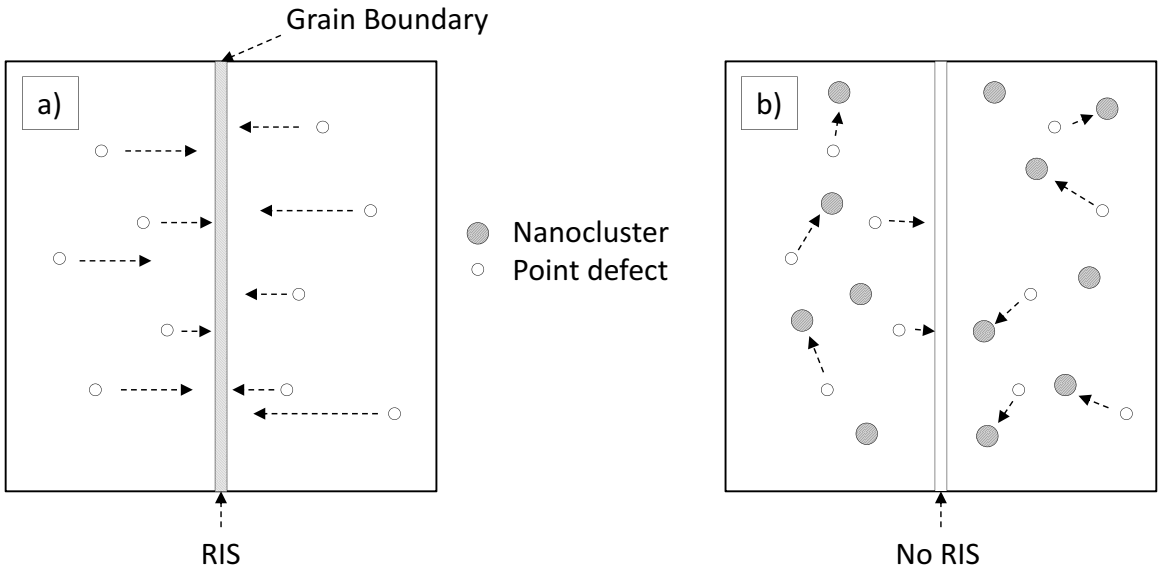


Figure 5.16: Schematic of nanocluster and point defect interactions with relationship to grain boundaries and RIS: a) low temperature; nanoclusters become unstable and have limited interactions with point defect migration to grain boundaries and b) high temperature; nanoclusters remain stable during irradiation and interact with point defect flux preventing significant RIS to the grain boundary.

### 5.2.4 Influence of Minor Alloying Elements on RIS

Minor solute atoms may interact with the flux of major solute atoms near the grain boundary altering the RIS response of the 14YWT specimens. Ti could be contributing to the depletion at low temperatures. At low temperature the nanoclusters become unstable and a small fraction of the Ti originally retrained within the nanocluster could go into solution due to ballistic mixing near the precipitates. Parish *et al.* found evidence of Ti being injected into the matrix around nanoclusters in 14YWT irradiated using $Pt^{3+}$ ions irradiated to a temperature of -100 °C indicating Ti could sit within the matrix when nanoclusters become unstable [132]. As discussed in Section 5.2.2, Ohnuki *et al.* found Cr enriched to grain boundaries in an irradiated Fe-13 wt. % Cr ferritic alloy [66]. When the composition of the alloy was modified to include 1 wt. %

Ti, Cr depletion was observed at grain boundaries irradiated to 118 dpa at 525 °C. The study also found a reduction in void swelling in the Fe-Cr-Ti alloy over the Fe-Cr binary alloy. The difference in the RIS response as well as void swelling rate in ferritic alloys with Ti addition suggest the migration behavior of Fe and Cr can be affected by the presence of Ti in the matrix. The complex nature of the Cr-Fe vacancy and interstitial diffusivity, as well as the limited data on how Ti is altering the Cr migration near defects sinks prevents verifying if the depletion seen near grain boundaries in the 14YWT specimens is due to the Cr-Fe diffusion coefficient ratio changes as a function of temperature discussed previously or the presence of Ti within the matrix.

The development of 'w-shaped' profiles in the NF-ODS at low temperature and very high dose indicates a strong binding of Cr within the grain boundary plane preventing diffusion of Cr out of the boundary into the matrix during the defect flux under irradiation. The formation of 'w-shaped' profiles have been observed in FCC steels with pre-segregation of Cr to the boundary at low doses [133]. J. Busby demonstrated the 'w-shape' profile in FCC steels could not be fully accounted by the pre-irradiation Cr enrichment seen in several 300 series austenitic stainless steels [134]. The work indicated the modified inverse Kirkendall model for FCC alloys over estimated the rate of transition from fully enriched to 'w' profiles to fully depleted profiles with increasing dpa with experimentally determined depletion rates. Similar work was demonstrated by Simonen and Bruemmer in neutron-irradiated FCC steels [135]. These findings suggests the delayed onset of depletion in the experiment was the result of binding of the Cr and Mo within the boundary plane and possible interactions of Cr with co-segregating elements during irradiation. With the significant pre-irradiation enrichment of W to grain boundaries in 14YWT a Cr-W interaction at the grain boundary causing the 'w' profile could be feasible. Cr-W binding is supported by the Cr and W concentrations at the grain boundary following the same trends as a function of temperature as seen in Figure 5.17. It is recognized the measured segregation profiles are only semi-quantitative due to the quantification algorithm used. To overcome this

deficiency several grain boundaries were analyzed using atom-probe tomography (APT)[2]. Select segregation profiles of Cr and W are provided in Figures 5.18-5.20. APT showed good agreement with profiles determined using STEM-EDS. Atom probe measurements further supports Cr-W interactions. At 100 °C, APT revealed full depletion of Cr to the grain boundary which corresponds to depletion of W at the boundary. At 300 °C, W was enriched while Cr displayed the 'w-shaped' profiles, inline with results obtained using STEM-EDS. At 450 °C and 600 °C, W and Cr were both fully enriched in the boundary as determined using both STEM-EDS and APT. The relationship between Cr and W as determined using both STEM-EDS and APT strongly suggests a Cr-W interaction retarding the RIS response at low temperatures and very high doses at the grain boundary plane which results in the observed 'w-shaped' profiles in the NF-ODS steel.

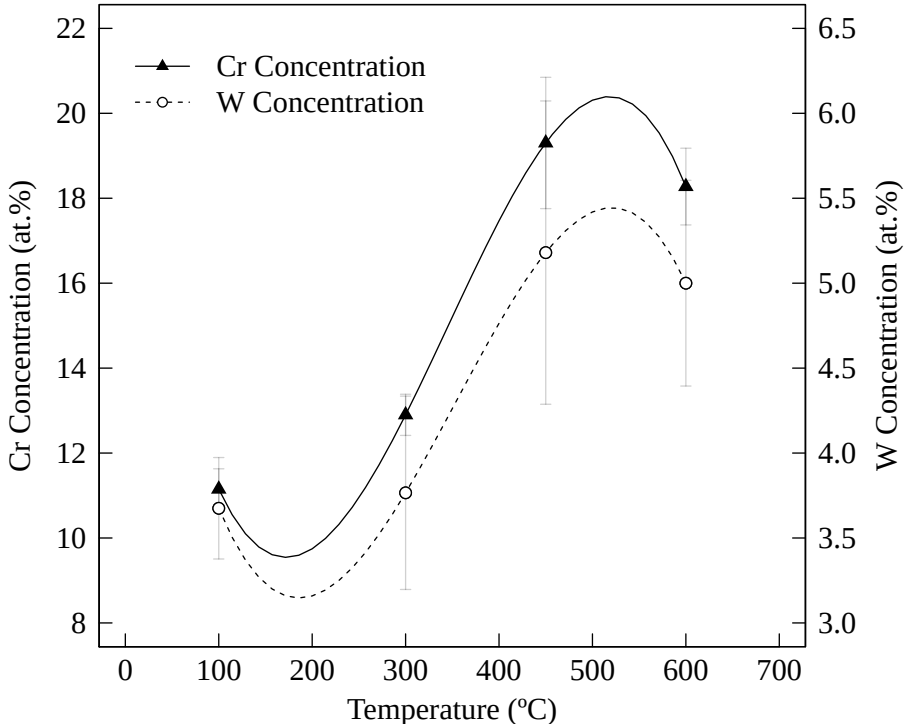


Figure 5.17: Change in on-boundary W and Cr concentration as a function of temperature after 100 dpa irradiation using $Ni^{2+}$ ions.

[2]Results courtesy of Alicia Certain, Pacific Northwest National Laboratory (Alicia.Certain@pnnl.gov). Results to be published.

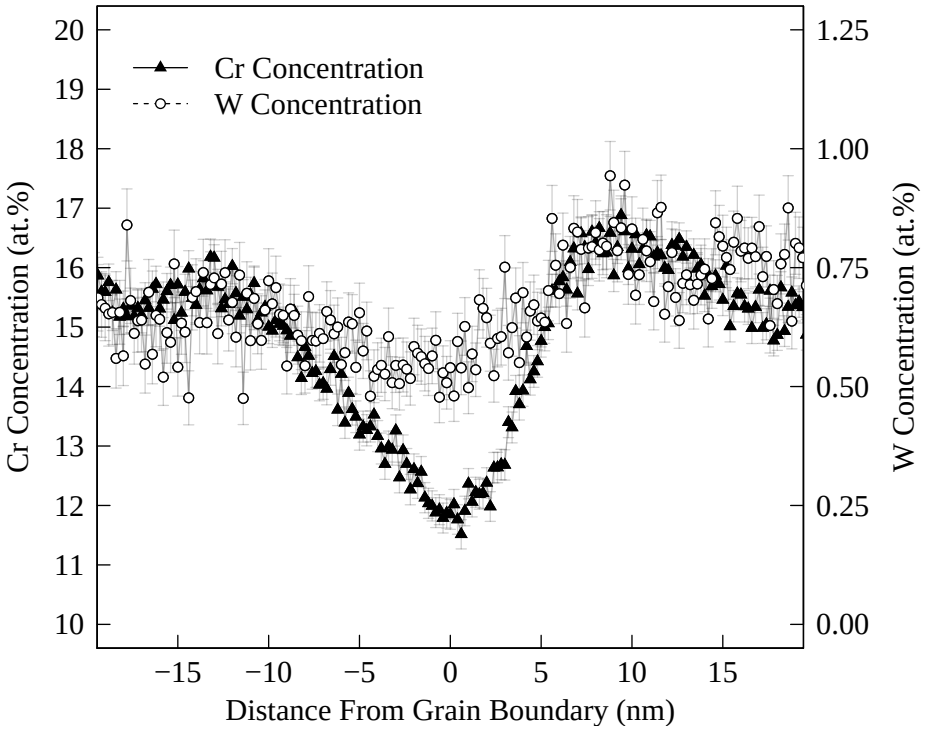


Figure 5.18: 1D Concentration profiles of Cr and W determined using APT from a grain boundary irradiated to 100 dpa at 100 °C using $Ni^{2+}$ ions.

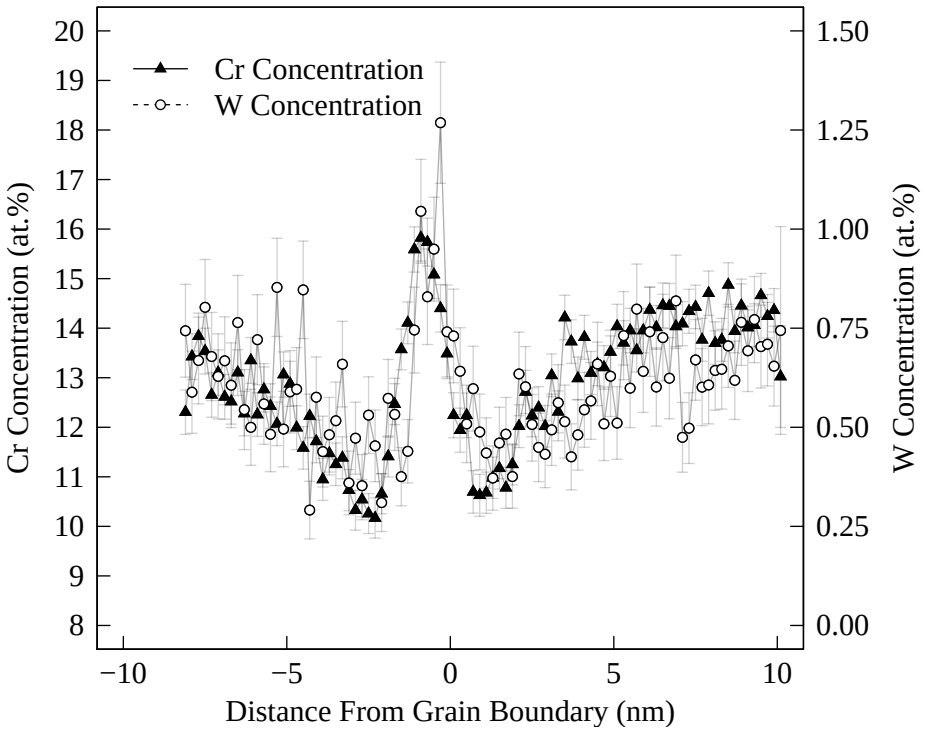


Figure 5.19: 1D Concentration profiles of Cr and W determined using APT from a grain boundary irradiated to 100 dpa at 300 °C using $Ni^{2+}$ ions.

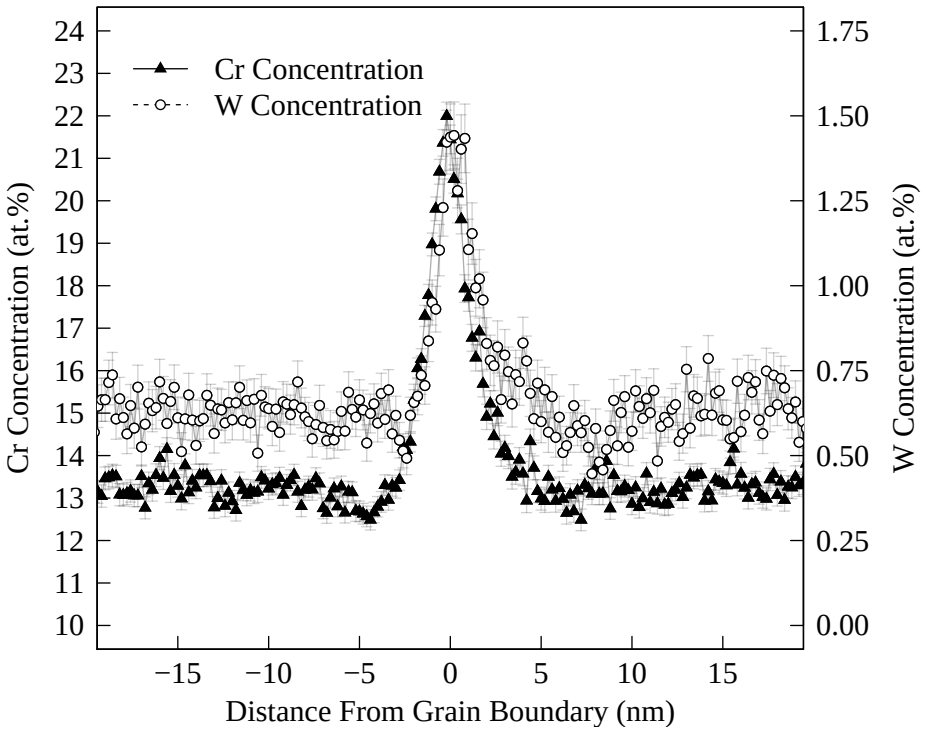


Figure 5.20: 1D Concentration profiles of Cr and W determined using APT from a grain boundary irradiated to 100 dpa at 450 °C using $Ni^{2+}$ ions.

### 5.2.5 Influence of Implanted Ni Ions on RIS

Ion irradiation introduces a small concentration of implanted ions into the specimen and their concentration profiles are dependent on the irradiation conditions and target material. Figure 3.4 showed the depth and concentration of Ni ions implanted in the 14YWT specimens with a max concentration around ~2.75 at. % at the end of the ion range. These implanted Ni ions are at a high enough concentration to be detected using standard STEM-EDS analysis. The results showed Ni ions were observed to diffuse to grain boundaries after irradiation and qualitatively the highest at 100-300 °C. The exact concentration is difficult to determine as the extraction depth of the TEM specimens after final thinning and hence the exact bulk concentration of Ni

ions is unknown after TEM specimen fabrication. The depth would be needed to determine the exact bulk concentration of Ni ion to use experimentally determined k-factors which is used in the quantification algorithm. APT is capable of quantify the amount of Ni in the system as correlation factors are not needed for reconstruction. APT has the capability to quantify the Ni concentration, but the volume analyzed is large enough that signification variations in the local dose can occur along the specimen axis or parallel to the specimen axis depending on the sample preparation technique and significant variations in the local Ni concentration are possible [136].

The small concentration of Ni implanted into the system could alter the RIS response especially when compared to neutron irradiations. In the results presented here, Ni was implanted to the same concentration over all irradiation temperatures and therefore the mechanisms for nanoclusters and minor alloying elements affecting the RIS response as a function of temperature is most likely not affected by the Ni ions. Given this, Ni has been shown to be a slower diffuser interstitially compared to Cr and Fe while slower than Cr and faster than Fe under vacancy mechanisms in a BCC dilute limited system [86]. The result is the Ni ions could be affecting the sign of the Cr segregation when compared to neutron or proton irradiations.

# Chapter 6

# Conclusions

## 6.1 Summary

Radiation induced segregation is a complex process which occurs in F/M steels. Several underlying mechanisms for RIS in F/M steels were investigated. A model F/M steel and advanced NF-ODS steel were investigated using a variety of irradiation parameters to determine the RIS response under different conditions. Experimental results were compared with recent modeling work to further develop the current understanding of RIS in F/M steels.

The RIS response in F/M steels was shown to be an intricate process with many variables responsible for determining the sign and magnitude of the segregation at grain boundaries. Enrichment of Cr to the grain boundary in the model F/M steel indicated the conclusions of recent modeling work that predicted interstitial and vacancy fluxes to grain boundaries are both significant under irradiation with Cr enrichment occurring due to Cr interstitials being the fastest diffuser within the matrix are within reason. The observed Cr depletion in the NF-ODS indicates the ratio of point defect fluxes could be altered by either interstitial trapping due to the high Cr matrix concentration or the addition of minor alloying elements interacting with the point defect flux. The complex nature of the point defect flux and close balance of the vacancy and interstitial flux to grain boundaries could be a reasonable explanation to the inconsistent observations within the open literature.

The dose dependence within the model F/M steel indicated that F/M steels have a traditional dose response with non-steady state conditions occurring at the low doses observed in the study.

Results indicated the RIS response is also dependent on the temperature and the dose rate especially when comparing segregation across different incident particles. Comparisons between ion and neutron irradiations was difficult due to the limited amount of temperature control provided for neutron irradiation. Other factors including the differences in damage processes further complicate the matter. The large variation within the results indicates a strong need to complete highly systematic studies to verify trends with F/M steels due to high sensitivity to factors such as dose, dose rate, temperature, and irradiation ion.

Results of the investigation found the RIS response was dependent on the local structure present at the grain boundary. The RIS behavior at different grain boundary types can be attributed to how the point defects generated via radiation damage migrate to and annihilate at grain boundaries. Grain boundaries in the low angle regime performed as inefficient sinks for point defects due to highly localized regions of disorder which can annihilate point defects along the boundary. The RIS behavior at LAGB is therefore determined by the rate at which the atoms can be absorbed at the sinks. Special grain boundaries showed similar responses to LAGBs indicating the RIS response is also driven by the slow rate at which defects are annihilated at the boundary due to the high coherency and low energy at the boundary. Grain boundaries in the general HAGB regime have a high distribution of dislocations and dislocation jogs at the boundary. The high density of dislocation jogs resulted in the HAGBs ability to perform as efficient sinks for point defects leading to a higher RIS response over LAGBs. HAGBs seems to be controlled by how rapidly the atoms can diffuse to the local interface region resulting in the RIS response to be rate limited by the point defect diffusion to the boundary, therefore performing in the near perfect sink condition.

The RIS response in NF-ODS steels is impacted by the presence of nanoclusters under irradiation. At low temperatures the nanoclusters are unstable and a significant change in the grain boundary chemistry was observed. At high temperature the nanoclusters remained stable under irradiation leading to an arrested RIS response. The nanoclusters act as sites for point defect trapping which reduces the point defect flux to grain boundaries under irradiation. The exact

property of the nanoclusters which drives the point defect capture including number density, available surface area, interface coherency, or biased sink capture of point defects remains to be determined. Given this, the unstable clusters at low temperature indicate a loss of effective sink density resulting in significantly higher RIS at low temperature.

The dependence of the RIS response on the structure and density of internal interfaces establishes important concepts for RIS in F/M steels. Recent advances in grain boundary engineering techniques which alter the grain boundary character distribution of a material through different thermal and mechanical treatments may provide an avenue to make F/M steels which are highly resistant to RIS. Processing the steels to avoid the production of a high fraction of general HAGB will lead to steels which are more resistant to RIS. Also, the observation made here that the RIS response is reduced in the presence of high density point defect annihilation sites, such as the nanoclusters in the 14YWT specimens, shows the benefits of nanoclusters within the the F/M steel matrix. Further development of NF-ODS steels might lead to the development of steels which are RIS resistant over a broad temperature range.

## 6.2 Future Work

The work presented here has established the first steps towards understanding the fundamental mechanisms for RIS in F/M steel. A solid foundation has been formed, but gaps still exist to fully understand RIS in F/M steels. RIS in F/M steels has been proven to be highly complex and no one body of work will fully capture all aspects of RIS in F/M steel. Given this, there are some clear extensions of the work presented here.

This study showed a dependence on both the dose rate and temperature of RIS in F/M steels. The behavior over a wide range of dose rates and temperatures was not fully explored. Further work into investigating RIS over a wide range of temperatures, particularly for the model F/M steel would be highly beneficial. A large temperature window will allow for the determination if the modeling input values used are applicable over a wide temperature range. It will also

provide insight into whether there is a cross-over temperature which results in Cr depletion to grain boundaries, a possible effect observed in the NF-ODS steel.

A systematic study of dose rate would further develop the understanding of RIS in F/M steels. Dose rate is widely known to influence the RIS response but very few studies exist which vary dose rate while keeping other conditions constant. Recent developments in ion beam systems allows for orders of magnitude differences in achievable dose rates using the same ion which could be utilized to complete the proposed work. Coupling of dose rate and temperature studies would also be advantageous to further the knowledge of how different incident particle irradiations influence the RIS response in F/M steels. By understanding the dose rate and temperature effects, a more focused analysis on the differences in the damage processes of incident ions could be studied, particularly the production of free migrating defects after a damage cascade quench.

Structure played a large role in determining the RIS response at grain boundaries. An extension of this work would be to investigate other interfaces. Precipitates can be coherent, semi-coherent, and incoherent each with a unique interfacial structure. Research could be completed investigating whether the coherency-RIS dependency observed at grain boundaries can be transferred to precipitate-matrix interfaces. This study would significantly impact the development of using nanoclusters dispersions with different interfacial structures in F/M steels.

APT can provide 3D microchemical maps of different structures. APT could be potentially leveraged to obtain information on not only the segregation across the grain boundary but within the grain boundary plane. The theories proposed in this work indicate the dislocations and dislocation jogs within the grain boundary plane act as preferential sites for point defect absorption. APT might reveal the distribution of segregates within the plane is non-uniform with solute atoms sitting on the grain boundary dislocations. The homogeneity of the segregation within the plane could be studied over all three grain boundary regimes.

The structure was shown to influence the concentration gradient of points defects. An annealing study of the RIS at these different structures would provide more information about the rate

of point defect annihilation at the boundary. A very high dose irradiation at different grain boundary structures would assist in determining if there is different RIS saturation limits at low angle versus high angle grain boundaries. Both these experiments could be linked to further understand the relationship between grain boundary structure and point defects.

The Ti additions or high Cr content was speculated to interact with the point defect fluxes resulting in the depletion at the grain boundary. The composition dependence of Cr to point defect mobility is still not well understood. A study using irradiated model alloys with varying Cr content, along with Ti additions within solution could be conducted. Varying the Cr concentration would help determine if the proposed interstitial trapping mechanism is reasonable. Ti additions would indicate if composition refinements could be made to reduce the RIS behavior at F/M steel grain boundaries.

Only one neutron irradiation condition was observed at the time of this study for the model F/M steel. Further work in understanding the RIS process under neutron irradiation would be beneficial to verify the trends observed with ion irradiation experiments. With this, the effects of ion beam scanning have only be speculated. Experimental investigations into the effects of rastered versus non-rastered irradiations would assist in bridging the gap between neutron and ion irradiation experiments.

# Bibliography

[1] U.S. DOE Nuclear Energy, *Light Water Reactor Sustainability Program: Intergrated Program Plan*, 2012. https://inlportal.inl.gov/portal/server.pt/document/105278/inl-ext-11-23452_lwrs_program_plan_pdf.

[2] U.S. DOE Nuclear Energy Research Advisory Committee & the Generation IV International Forum, *A Technology Roadmap for Generation IV Nuclear Energy Systems*, 2002. http://www.gen-4.org/PDFs/GenIVRoadmap.pdf.

[3] R. Klueh, D. Harries, *High-chromium ferritic and martensitic steels for nuclear applications*, of *Monograph (American Society for Testing and Materials)*, ASTM, 2001.

[4] G. Was, *Fundamentals of radiation materials science: metals and alloys*, Springer, 2007.

[5] T. Allen, G. Was, *Acta Materialia*, 1998, **46**, 3679 – 3691.

[6] T. R. Allen, Ph.D. thesis, University of Michigan, 1997.

[7] E. Bain, H. Paxton, *Alloying elements in steel*, American Society for Metals, 1966.

[8] Z. Lu, R. Faulkner, G. Was, B. Wirth, *Scripta Materialia*, 2008, **58**, 878–881.

[9] V. J. Keast, D. B. Williams, *Acta Materialia*, 1999, **47**, 3999 – 4008.

[10] G. S. Was, J. T. Busby, T. Allen, E. A. Kenik, A. Jensson, S. M. Bruemmer, J. Gan, A. D. Edwards, P. M. Scott, P. L. Andreson, *Journal of Nuclear Materials*, 2002, **300**, 198 – 216.

[11] A. G. Certain, Ph.D. thesis, University of Wisconsin, 2012.

[12] H. Schneider, *Foundary Trade J*, 1960, **108**, 562.

[13] B. Raj, M. Vijayalakshmi in *Comprehensive Nuclear Materials*, E. in Chief: Rudy J.M. Konings (Ed.), Elsevier, Oxford, 2012, pp. 97 – 121.

[14] S. Morito, X. Huang, T. Furuhara, T. Maki, N. Hansen, *Acta Materialia*, 2006, **54**, 5323–5331.

[15] D. T. Hoelzer, J. Bentley, M. A. Sokolov, M. K. Miller, G. R. Odette, M. J. Alinger, *Journal of Nuclear Materials*, 2007, **367-370, Part A**, 166–172.

[16] S. Ohtsuka, S. Uaki, M. Fujiwara, T. Kaito, T. Narita, *Materials Transactions*, 2005, **46**, 487–492.

[17] H. Sakasegawa, S. Ukai, M. Tamura, S. Ohtsuka, H. Tanigawa, H. Ogiwara, A. Kohyama, M. Fujiwara, *Journal of Nuclear Materials*, 2008, **373**, 82–89.

[18] S. Ukai, T. Okuda, M. Fujiwara, T. Kobayashi, S. Mizuta, H. Nakashima, *Journal of Nuclear Science and Technology*, 2002, **39**, 872–879.

[19] T. Yamamoto, G. R. Odette, P. Miao, D. T. Hoelzer, J. Bentley, N. Hashimoto, H. Tanigawa, R. J. Kurtz, *Journal of Nuclear Materials*, 2007, **367-370, Part A**, 399–410.

[20] A. G. Certain, K. G. Field, T. R. Allen, M. K. Miller, J. Bentley, J. T. Busby, *Journal of Nuclear Materials*, 2010, **407**, 2–9.

[21] S. Ukai in *TMS 2005*.

[22] G. Gottstein, L. S. Shvindlerman, *Grain boundary migration in metals: thermodynamics, kinetics, applications*, CRC Press, 1999.

[23] I. A. Harris, P. Jones, *Grain boundaries: their character, characterisation and influence on properties*, IOM Communications, London, 2001.

[24] V. Randle, *The role of the coincidence site lattice in grain boundary engineering*, Institute of Materials, 1996, 1996.

[25] O. Engler, V. Randle, *Introduction to texture analysis: macrotexture, microtexture, and orientation mapping*, CRC Press, 2009.

[26] P. Lejcek, *Grain Boundary Segregation in Metals*, Springer, 2010.

[27] W. T. Read, W. Shockley, *Phys. Rev.*, 1950, **78**, 275–289.

[28] A. S. for Metals. Materials Science Division. Seminar Committee, M. S. of AIME., *Grain-boundary structure and kinetics: papers*, American Society for Metals, 1980.

[29] D. Brandon, *Acta Metallurgica*, 1966, **14**, 1479 – 1484.

[30] C. Goux, *Mem. scient. Rev. Metall.*, 1961, **58**, 661.

[31] C. T. Forwood, L. Clarebrough, *Electron microscopy of interfaces in metals and alloys*, of *Electron microscopy in materials science series*, A. Hilger, 1991.

[32] D. Williams, C. Carter, *Transmission electron microscopy: a textbook for materials science. Basics*, Springer, 2009.

[33] D. Olander, *Fundamental aspects of nuclear reactor fuel elements: prepared for the Division of Reactor Development and Demonstration, Energy Research and Development Administration*, of *Tid 26711 P1*, Technical Information Center, Office of Public Affairs, Energy Research and Development Administration, 1976.

[34] J. Ziegler, J. Biersack, *SRIM 2006*, 2006. `http://www.srim.org/`.

[35] G. Was, T. Allen, *Journal of Nuclear Materials*, 1993, **205**, 332 – 338.

[36] R. W. Balluffi in *Presented at the Intern. Conf. on Fundamental Aspects of Radiation Damage in Metals, Gatlinburg, Tenn., 6-10 Oct. 1975*, pp. 6–10.

[37] A. Sutton, R. Balluffi, *Interfaces in crystalline materials*, of *Monographs on the physics and chemistry of materials*, Clarendon Press, 1996.

[38] R. W. Balluffi, *physica status solidi (b)*, 1969, **31**, 443–463.

[39] Y. Komen, P. Petroff, R. Balluffi, *Phil. Mag.*, 1972, **26**, 239.

[40] S. Zinkle, *Effects of radiation on materials: 15th international symposium*, of *ASTM special technical publication 1125*, R. Stoller, A. Kumar, D. Gelles (Eds.), ASTM, 1992.

[41] S. M. Bruemmer, D. J. Edwards, V. Y. Guertsman, E. P. Simonen in *Microstructural Processes in Irradiated Materials, 2000 MRS Proceedings*.

[42] D. Kaoumi, J. Adamson, A. Motta, M. Kirk, R. Birtcher, T. Faney, B. Wirth, J. Bentley in *Microscopy and Microanalysis Conference 2010*.

[43] H. J. Frost, K. C. Russell, *Journal of Nuclear Materials*, 1981, **103 & 104**, 1427–1432.

[44] R. S. Nelson, J. A. Hudson, D. J. Mazey, *Journal of Nuclear Materials*, 1972, **44**, 318–330.

[45] P. Wilkes, *Journal of Nuclear Materials*, 1979, **83**.

[46] A. D. Brailsford, *Journal of Nuclear Materials*, 1980, **91**, 221–222.

[47] K. Asano, Y. Kohno, A. Kohyama, T. Suzuki, H. Kusanagi, *Journal of Nuclear Materials*, 1988, **155-157, Part 2**, 928 – 934.

[48] H. Kinoshita, N. Akasaka, H. Takahashi, I. Shibahara, S. Onose, *Journal of Nuclear Materials*, 1992, **191-194, Part B**, 874 – 878.

[49] E. Little, *Effects of Radiation on Materials: 17th International Symposium*, D. Gelles, N. R., A. Kumar, E. Little (Eds.), ASTM, 1996.

[50] J. Saito, T. Suda, S. Yamashita, S. Ohnuki, H. Takahashi, N. Akasaka, M. Nishida, S. Ukai, *Journal of Nuclear Materials*, 1998, **258-263, Part 2**, 1264 – 1268.

[51] P. Dubuisson, R. Schill, G. I. Hugon, M.-P., J.-L. Seran, *Effects of Radiation on Materials: 18th International Symposium*, N. R., M. Hamilton, F. Garner, Kum (Eds.), ASTM, 1999.

[52] N. Akasaka, S. Yamashita, T. Yoshitake, S. Ukai, A. Kimura, *Journal of Nuclear Materials*, 2004, **329-333, Part B**, 1053 – 1056.

[53] I. Monnet, P. Dubuisson, Y. Serruys, M. Ruault, O. Katasov, B. Jouffrey, *Journal of Nuclear Materials*, 2004, **335**, 311 – 321.

[54] A. Kimura, H. Cho, N. Toda, R. Kasada, K. Yutani, H. Kishimoto, N. Iwata, S. Ukai, M. Fujiwara, *Journal of Nuclear Science and Technology*, 2007, **44**, 323–328.

[55] P. Pareige, M. Miller, R. Stoller, D. Hoelzer, E. Cadel, B. Radiguet, *Journal of Nuclear Materials*, 2007, **360**, 136 – 142.

[56] H. Kishimoto, K. Yutani, R. Kasada, O. Hashitomi, A. Kimura, *Journal of Nuclear Materials*, 2007, **367-370, Part A**, 179 – 184.

[57] H. Kishimoto, R. Kasada, O. Hashitomi, A. Kimura, *Journal of Nuclear Materials*, 2009, **386-388**, 533 – 536.

[58] S. Yamashita, K. Oka, S. Ohnuki, N. Akasaka, S. Ukai, *Journal of Nuclear Materials*, 2002, **307-311, Part 1**, 283 – 288.

[59] K. Oka, S. Ohnuki, S. Yamaguchi, N. Akasaka, S. Ohtsuka, H. Tanigawa, *Materials Transactions (Japan)*, 2007, **48**, 2563–2566.

[60] T. R. Allen, J. Gan, J. I. Cole, M. K. Miller, J. T. Busby, S. Shutthanandan, S. Thevuthasan, *Journal of Nuclear Materials*, 2008, **375**, 26–37.

[61] M. Nastar, F. Soisson, *1.18 - Radiation-Induced Segregation*, of *Comprehensive Nuclear Materials*, E. in Chief: Rudy J.M. Konings (Ed.), Elsevier, Oxford, 2012, pp. 471–496.

[62] P. Scott, *Journal of Nuclear Materials*, 1994, **211**, 101 – 122.

[63] J. Perks, A. Marwick, C. English, *Computer code to calculate radiation induced segregation in concentrated ternary alloys*, AERE-R-12121, 1986, p. 48.

[64] J. D. Tucker, R. Najafabadi, T. R. Allen, D. Morgan, *Journal of Nuclear Materials*, 2010, **405**, 216–234.

[65] E. Little, D. Stow, *Journal of Nuclear Materials*, 1979, **87**, 25 – 39.

[66] S. Ohnuki, H. Takahashi, T. Takeyama, *Journal of Nuclear Materials*, 1981, **104**, 1121 – 1125.

[67] H. Takahashi, S. Ohnuki, T. Takeyama, *Journal of Nuclear Materials*, 1981, **104**, 1415 – 1419.

[68] H. Takahashi, K. Shiba, S. Nakahigashi, S. Ohnuki, H. Kinoshita, F. Garner, *Reduced activation materials for fusion reactors*, of *ASTM special technical publication*, R. Klueh, N. Packan, D. Gelles, M. Okada (Eds.), ASTM, 1990.

[69] J. Brimhall, D. Baer, R. Jones, *Journal of Nuclear Materials*, 1983, **117**, 218 – 223.

[70] J. Brimhall, D. Baer, R. Jones, *Journal of Nuclear Materials*, 1984, **122**, 196 – 200.

[71] R. Clausing, L. Heatherly, R. Faulkner, A. Rowcliffe, K. Farrell, *Journal of Nuclear Materials*, 1986, **141-143**, 978 – 981.

[72] T. Muroga, A. Yamaguchi, N. Yoshida, *Effects of radiation on materials*, *Vol. ASTM STP 1046*, N. Packan, R. Stoller, A. Kumar (Eds.), Philadelphia, PA (USA); ASTM, Philadelphia, PA, 1989.

[73] T. Kato, H. Takahashi, S. Ohnuki, K. Nakata, J. Kuniya, *Journal of Nuclear Materials*, 1991, **179-181**, 623 – 625.

[74] E. Little, T. Morgan, R.G, *Materials Science Forum*, 1992, **97-99**, 323–328.

[75] T. Morgan, E. Little, R. Faulkner, J. Titchmarsh, *Effects of radiation on materials: 15th international symposium*, of *ASTM special technical publication 1125*, R. Stoller, A. Kumar, D. Gelles (Eds.), ASTM, 1992.

[76] I. Neklyudov, V. Voyevodin, *Journal of Nuclear Materials*, 1994, **212-215**, 39 – 44.

[77] R. Schäublin, P. Spätig, M. Victoria, *Journal of Nuclear Materials*, 1998, **258-263**, 1350 – 1355.

[78] Z. Lu, R. Faulkner, N. Sakaguchi, H. Kinoshita, H. Takahashi, P. Flewitt, *Journal of Nuclear Materials*, 2006, **351**, 155 – 161.

[79] G. Gupta, Z. Jiao, A. Ham, J. Busby, G. Was, *Journal of Nuclear Materials*, 2006, **351**, 162 – 173.

[80] E. A. Marquis, S. Lozano-Perez, V. de Castro, *Journal of Nuclear Materials*, 2011, **417**, 257–261.

[81] J. P. Wharry, Z. Jiao, V. Shankar, J. T. Busby, G. S. Was, *Journal of Nuclear Materials*, 2011, **417**, 140–144.

[82] J. P. Wharry, Z. Jiao, G. S. Was, *Journal of Nuclear Materials*, 2012, **425**, 117–124.

[83] G. S. Was, J. P. Wharry, B. Frisbie, B. D. Wirth, D. Morgan, J. D. Tucker, T. R. Allen, *Journal of Nuclear Materials*, 2011, **411**, 41 – 50.

[84] K. Wong, J. Shim, B. Wirth, *Journal of Nuclear Materials*, 2007, **367-370**, 276 – 281.

[85] K. L. Wong, H.-J. Lee, J.-H. Shim, B. Sadigh, B. D. Wirth, *Journal of Nuclear Materials*, 2009, **386-388**, 227 – 230.

[86] S. Choudhury, L. Barnard, J. Tucker, T. Allen, B. Wirth, M. Asta, D. Morgan, *Journal of Nuclear Materials*, 2011, **411**, 1 – 14.

[87] D. Terentyev, P. Olsson, T. Klaver, L. Malerba, *Computational Materials Science*, 2008, **43**, 1183 – 1192.

[88] T. Duh, J. Kai, F. Chen, *Journal of Nuclear Materials*, 2000, **283-287**, 198 – 204, 9th Int. Conf. on Fusion Reactor Materials.

[89] S. Watanabe, Y. Takamatsu, N. Sakaguchi, H. Takahashi, *Journal of Nuclear Materials*, 2000, **283-287, Part 1**, 152 – 156.

[90] N. Sakaguchi, S. Watanabe, H. Takahashi, R. G. Faulkner, *Journal of Nuclear Materials*, 2004, **329-333**, 1166 – 1169.

[91] T. S. Duh, J. J. Kai, F. R. Chen, L. H. Wang, *Journal of Nuclear Materials*, 2001, **294**, 267 – 273.

[92] L. Barnard, J. D. Tucker, S. Choudhury, T. R. Allen, D. Morgan, *Journal of Nuclear Materials*, 2012, **425**, 8–15.

[93] H. Wiedersich, P. Okamoto, N. Lam, *Journal of Nuclear Materials*, 1979, **83**, 98 – 108.

[94] K. G. Field, L. Barnard, C. Parish, J. Busby, D. Morgan, T. Allen, *J. Nucl. Mater.*, 2012, **Submitted**.

[95] R. Keyse, A. Garratt-Reed, P. Goodhew, G. Lorimer, *Introduction to Scanning Transmission Electron Microsco*, BIOS Scientific Publishers Limited, 1998.

[96] P. Doig, Fl, *The influence of electron probe size and grain boundary orientation in the STEM-EDS X-ray microanalysis of grain boundary segregation*, P. Doig (Ed.), The Institute of Physics, 1983, chapter Chapter 3: X-ray analysis, pp. 87–90.

[97] K. L. Davis, B. M. Chase, T. Unruh, D. L. Knudson, J. L. Rempe, *Evaluations of University of Wisconsin Silicon Carbide Temperature Monitors 300 LO and 400 LO B*, Tech. Rep. INL/EXT-11-24226, 2011.

[98] L. L. Snead, A. M. Williams, A. L. Qualls, *Revisiting the use of SiC as a Post Irradiation Temperature Monitor*, M. Grossbeck (Ed.), ASTM STP 1447, 2003.

[99] L. L. Snead in *Presented at the International Symposium on Materials Test Reactors*.

[100] J. L. Rempe, K. Condie, D. L. Knudson, L. L. Snead, *Silicon Carbide Temperature Monitor Measurements at the High Temperature Test Laboratory*, Tech. Rep., Idaho National Labratory (INL/EXT-10-17608), 2010.

[101] V. J. Keast, D. B. Williams, *Current Opinion in Solid State and Materials Science*, 2001, **5**, 23 – 30.

[102] G. Cliff, G. Lorimer, *Journal Of Microscopy-Oxford*, 1975, **103**, 203–207.

[103] J. Goldstein, D. Williams, G. Cliff, *Principles of Analytical Electron Microscopy*, D. Joy, A. Romig, J. Goldstein (Eds.), Ple, 1986.

[104] J. J. Fundenberger, A. Morawiec, E. Bouzy, J. S. Lecomte, *Ultramicroscopy*, 2003, **96**, 127 – 137.

[105] ResMat, *HTextTools Version 3.3*, 2000. `http://www.resmat.com/download/TexTools.ZIP`.

[106] I. A. Vatter, J. M. Titchmarsh, *Ultramicroscopy*, 1989, **28**, 236–239.

[107] A. J. Ardell, *Radiation-Induced Solute Segregation in Alloys*, of *Materials Issues for Generation IV Systems*, V. Ghetta, D. Gorse, D. Maziere, V. Pontikis (Eds.), Springer,

2008, pp. 285–310.

[108] M. Laws, P. Goodhew, *Acta Metallurgica et Materialia*, 1991, **39**, 1525 – 1533.

[109] V. Randle, *Acta Materialia*, 1998, **46**, 1459–1480.

[110] H. Jang, D. Farkas, J. De Hosson, *J. Mater. Res*, 1992, **7**, 1707–1717.

[111] M. Jenkins, Kirk, *Characterization of Radiation Damage by Transmission Electron Microscopy*, Taylor & Francis, 2000.

[112] H.-H. Jin, *Journal of Electron Microscopy*, 2010, **59**, 463–468.

[113] B. D. Miller, J. Gan, J. Madden, J. F. Jue, A. Robinson, D. D. K. Jr., *Journal of Nuclear Materials*, 2012, **424**, 38–42.

[114] V. Naundorf, M.-P. Macht, H. Wollenberger, *Journal of Nuclear Materials*, 1992, **186**, 227 – 236.

[115] P. Doig, D. Lonsdale, P. Flewitt, *Quantitative microanalysis with high spatial resolution*, of *Book (Metals Society)*, The Metals Society, London, 1981.

[116] P. Doig, D. Lonsdale, P. E. J. Flewitt, *Philosophical Magazine A*, 1980, **41**, 761–775.

[117] C. Topbasi, A. T. Motta, M. A. Kirk, *Journal of Nuclear Materials*, 2012, **425**, 48 – 53.

[118] A. D. Le Claire, *Philosophical Magazine*, 1970, **21**, 819–832.

[119] R. A. Johnson, *Phys. Rev.*, 1964, **134**, A1329–A1336.

[120] C.-C. Fu, F. Willaime, P. Ordejón, *Phys. Rev. Lett.*, 2004, **92**, 175503.

[121] P. Olsson, *Journal of Nuclear Materials*, 2009, **386-388**, 86 – 89.

[122] G. S. Was, P. L. Andersen, *Corrosion*, 1997, **63**, 19–45.

[123] T. Allen, J. Cole, E. Kenik, G. Was, *Journal of Nuclear Materials*, 2008, **376**, 169 – 173.

[124] J. Bentley, D. Hoelzer, *Microscopy and Microanalysis*, 2008, **14**, 1416–1417.

[125] M. Brandes, L. Kovarik, M. Miller, M. Mills, *Journal of Materials Science*, 2012, **47**, 3913–3923.

[126] C. Cayron, A. Montani, D. Venet, Y. de Carlan, *Journal of Nuclear Materials*, 2010, **399**, 219 – 224.

[127] D. Bhattacharyya, P. Dickerson, S. Maloy, G. Odette, M. Nastasi, A. Misra in *TMS 2011*.

[128] V. de Castro, E. Marquis, S. Lozano-Perez, R. Pareja, M. Jenkins, *Acta Materialia*, 2011, **59**, 3927 – 3936.

[129] W. Wolfer, L. Mansur, *Journal of Nuclear Materials*, 1980, **91**, 265 – 276.

[130] T. Okita, W. G. Wolfer, *Journal of Nuclear Materials*, 2004, **327**, 130 – 139.

[131] G. Odette, M. Alinger, B. Wirth, *Annual Review of Materials Research*, 2008, **38**, 471–503.

[132] C. Parish, P. Edmondson, Y. Zhang, M. Miller, *Journal of Nuclear Materials*, 2011, **418**, 106 – 109.

[133] S. Bruemmer, E. Simonen, P. Scott, P. Andresen, G. Was, J. Nelson, *Journal of Nuclear Materials*, 1999, **274**, 299 – 314.

[134] J. T. Busby, Ph.D. thesis, University of Michigan, 2001.

[135] E. P. Simonen, S. M. Bruemmer in *Corrosion 98*.

[136] M. Miller, Y. Zhang, *Ultramicroscopy*, 2011, **111**, 672 – 675.

[137] R. Balluffi, A. King, *Phase Transformations During Irradiation*, F. Nolfi (Ed.), Applied Science Publication, 1983.

[138] Y. Mishin, C. Herzig, *Materials Science and Engineering: A*, 1999, **260**, 55 – 71.

[139] A. N. Aleshin, V. Y. Aristov, B. S. Bokshtein, L. S. Shvindlerman, *physica status solidi (a)*, 1978, **45**, 359–366.

# Appendix A

The RIS model for a binary Fe-Cr system with modified boundary conditions is based on the Wiedersich *et al.* model for RIS in a binary alloy [93] and Duh *et al.* [91] derived boundary conditions. In the Wiedersich model the segregation is due to the diffusion of point defects and their rate equations are:

$$\frac{\partial C_{Fe}}{\partial t} = -\frac{\partial J_{Fe}}{\partial x} \tag{A-1}$$

$$\frac{\partial C_{Cr}}{\partial t} = -\frac{\partial J_{Cr}}{\partial x} \tag{A-2}$$

$$\frac{\partial C_v}{\partial t} = \varepsilon K_o - R_R C_v C_i - R_{VD} C_V - \frac{\partial J_v}{\partial x} \tag{A-3}$$

$$\frac{\partial C_i}{\partial t} = \varepsilon K_o - R_R C_v C_i - R_{ID} C_I - \frac{\partial J_i}{\partial x} \tag{A-4}$$

where $C$ is the site fraction, $J$ is the flux of the species of interest, $R_R$ is the rate coefficient for recombination of vacancies and interstitials, $R_{VD}$ and $R_{ID}$ are the rate of vacancies and interstitials loss to dislocations respectively, $K_o$ is the dose rate in dpa/s and $\varepsilon$ is the damage efficiency which is dependent on the incident particle. The rate of vacancy and interstitial loss to dislocations, $R_{VD}$ and $R_{ID}$, can be determined using the following equation (where $d$ = vacancy or interstitial):

$$R_d = Z_{dD} 4\pi r_{rD} \frac{\rho_D}{\delta} D_d \tag{A-5}$$

where $Z_{dD}$ is the bias factor, $r_{rD}$ is the radius of capture for defect species $d$, $\rho_D$ is the dislocation density, $\delta$ is the interplanar distance, and $D_d$ is the diffusivity of defect species d. The dislocations are assumed to be unbiased and $Z_{dD}$ is set equal to 1.

The conservation equations for alloying elements Fe and Cr are:

$$\frac{\partial C_{Fe}}{\partial t} = -\nabla J_{Fe} \tag{A-6}$$

$$\frac{\partial C_{Cr}}{\partial t} = -\nabla J_{Cr} \tag{A-7}$$

The model assumes all diffusion of vacancies and interstitials occurs with Fe and Cr atoms and the fluxes of defects and atoms to the grain boundary can be written as:

$$J_i = J^i_{Fe} + J^i_{Cr} \tag{A-8}$$

$$J_v = -\left(J^v_{Fe} + J^v_{Cr}\right) \tag{A-9}$$

$$J_{Fe} = J^v_{Fe} + J^i_{Fe} \tag{A-10}$$

$$J_{Cr} = J^v_{Cr} + J^i_{Cr}. \tag{A-11}$$

Knowing the partial diffusion coefficients for each species the fluxes can be rewritten as:

$$J_{Fe} = -(d^v_{Fe}N_{Fe} + d^i_{Fe}N_{Fe})\alpha\nabla C_{Fe} + d^v_{Fe}N_{Fe}\nabla C_v - d^i_{Fe}N_{Fe}\nabla C_i \tag{A-12}$$

$$J_{Cr} = -(d^v_{Cr}N_{Cr} + d^i_{Cr}N_{Cr})\alpha\nabla C_{Cr} + d^v_{Cr}N_{Cr}\nabla C_v - d^i_{Cr}N_{Cr}\nabla C_i \tag{A-13}$$

$$J_v = d^v_{Fe}N_v\alpha\nabla C_{Fe} + d^v_{Cr}N_v\alpha\nabla C_{Cr} - (d^v_{Fe}N_{Fe} + d^v_{Cr}N_{Cr})\nabla C_v \tag{A-14}$$

$$J_i = -d^i_{Fe}N_i\alpha\nabla C_{Fe} - d^i_{Cr}N_i\alpha\nabla C_{Cr} - (d^i_{Fe}N_{Fe} + d^i_{Cr}N_{Cr})\nabla C_i \tag{A-15}$$

where $d^v_{Fe}$, $d^i_{Fe}$, $d^v_{Cr}$, and $d^i_{Cr}$ are the partial diffusion coefficients, $N$ is the number density of each species, and $\alpha = (1 + \partial ln\,\gamma_{Fe}/\partial lnN_{Fe}) = (1 + \partial ln\,\gamma_{Cr}/\partial lnN_{Cr})$ is the thermodynamic factor which accounts for the difference between the chemical potential gradient and the concentration gradient. The terms $\gamma_{Fe}$ and $\gamma_{Cr}$ are the activity coefficients for Fe and Cr, respectively. Only three of the four flux equations in Eqs. A-12 - A-15 are independent according to:

$$J_i - J_v = J_{Fe} + J_{Cr} \tag{A-16}$$

because the atom and defect fluxes must balance. Eqs. A-12 - A-15 can then be used in the original concentration rate equations obtaining:

$$\frac{\partial C_v}{\partial t} = \varepsilon K_o - RC_vC_i - \nabla\left[d^v_{Fe}N_v\alpha\nabla C_{Fe} + d^v_{Cr}N_v\alpha\nabla C_{Cr} - (d^v_{Fe}N_{Fe} + d^v_{Cr}N_{Cr})\nabla C_v\right] \quad \text{(A-17)}$$

$$\frac{\partial C_i}{\partial t} = \varepsilon K_o - RC_vC_i - \nabla\left[d^i_{Fe}N_i\alpha\nabla C_{Fe} - d^i_{Cr}N_i\alpha\nabla C_{Cr} - (d^i_{Fe}N_{Fe} + d^i_{Cr}N_{Cr})\nabla C_i\right] \quad \text{(A-18)}$$

$$\frac{\partial C_{Cr}}{\partial t} = \nabla\left[-(d^v_{Cr}N_{Cr} + d^i_{Cr}N_{Cr})\alpha\nabla C_{Cr} + d^v_{Cr}N_{Cr}\nabla C_v - d^i_{Cr}N_{Cr}\nabla C_i\right] \quad \text{(A-19)}$$

and the concentration of Fe can be found by $C_{Fe} = 1 - C_{Cr}$. Typical applications of the model assume the grain boundary acts as a perfect sink and the concentration of interstitials and vacancies are fixed at their thermal equilibrium values by:

$$C_i(t,0) = exp\left(\frac{-H^f_i}{kT}\right) \quad \text{(A-20)}$$

and,

$$C_v(t,0) = exp\left(\frac{-S^f_v}{k}\right) exp\left(\frac{-H^f_v}{kT}\right) \quad \text{(A-21)}$$

where $H^f_i$ and $H^f_v$ are the formation energies of interstitials and vacancies in the alloy and $S^f_v$ is the effective entropy for vacancy formation.

The model was further developed by Duh *et al.* to capture the structure dependence of a grain boundary on the point defect flux [91]. The modified model assumes the grain boundary dislocations act as perfect sinks for defects and explicitly determines the flux of point defects to the dislocations. The flux of point defects near a grain boundary in Eq. A-14 and Eq. A-15 are partitioned into two fluxes, $J^0_{v,i}$, which is the flux of defects within the interaction distance of the grain boundary, and $J^1_{v,i}$, which is the flux of defects outside the interaction distance of the grain boundary. The model assumes point defects leaving the region within the interaction distance of a boundary is due to the diffusion of point defects along secondary grain boundary dislocations for general high angle grain boundaries and direct diffusion to primary grain boundary dislocations for low angle grain boundaries. This is shown schematically in Figure A-1. The flux, $J^0_{v,i}$, can be related to the flux along a grain boundary, $J^{gb}_{v,i}$, using:

$$J^0_{v,i} = \frac{2J^{gb}_{v,i}\delta}{d} \quad \text{(A-22)}$$

for general high angle grain boundaries and,

$$J_{v,i}^{0} = \frac{J_{v,i}^{gb}}{d} \tag{A-23}$$

for low angle grain boundaries, where $d$ is the distance between grain boundary dislocations and $\delta$ is the grain boundary thickness. The distance between grain boundary dislocations can be defined using Eqs. 2.1 and 2.6. The flux along the grain boundary mimics the definition for the flux through the bulk to the grain boundary in Eq. A-8 and Eq. A-9 where:

$$J_{i}^{gb} = J_{Fe}^{i,gb} + J_{Cr}^{i,gb} \tag{A-24}$$

$$J_{v}^{gb} = -\left(J_{Fe}^{v,gb} + J_{Cr}^{v,gb}\right) \tag{A-25}$$

where $J_{Fe/Cr}^{v/i,gb}$ is the flux of vacancies or interstitials via Fe or Cr atoms in the grain boundary. The model assumes the flux of the defects via Fe or Cr atoms in the grain boundary can be described using an effective partial grain boundary diffusion coefficient and sink strength using the form:

$$J_{Cr}^{i,gb} = \frac{Sd_{Cr}^{i,gb} C_{Cr}(C_i - C_i^{eq})}{\Omega} \tag{A-26}$$

$$J_{Cr}^{v,gb} = \frac{Sd_{Cr}^{v,gb} C_{Cr}(C_v - C_v^{eq})}{\Omega} \tag{A-27}$$

$$J_{Fe}^{i,gb} = \frac{Sd_{Fe}^{i,gb} C_{Fe}(C_i - C_i^{eq})}{\Omega} \tag{A-28}$$

$$J_{Fe}^{v,gb} = \frac{Sd_{Fe}^{v,gb} C_{Fe}(C_v - C_v^{eq})}{\Omega} \tag{A-29}$$

where $\Omega$ is the average alloy atomic volume, $S$ is the sink strength of the grain boundary dislocations and $d_{Fe/Cr}^{v/i,gb}$ is the effective grain boundary diffusivity coefficient for vacancies or interstitials of a specified element. The sink strength, $S$, can be written as [137]:

$$S = g_o z m \tag{A-30}$$

where $g_o$ is a geometrical parameter based on grain boundary structure, $z$ is the sink capture efficiency and $m$ is a multiple sink correction factor. For simplicity, $z$ and $m$ are set to equal one as the grain boundary dislocations are considered perfect sinks and interactions between grain

boundary dislocations are ignored. The geometrical parameter, $g_o$, can be related to the grain boundary structure by:

$$g_o = \frac{1}{(d/2 - \alpha b)} \tag{A-31}$$

for general high angle grain boundaries and,

$$g_o = \frac{1}{ln\,(d/2\alpha r_o)} \tag{A-32}$$

for low angle grain boundaries where $\alpha$ is a constant assumed to be equal to one and $b$ is the Burgers vector of the grain boundary dislocations which comprise the grain boundary. To solve each defect-atom grain boundary flux, the partial diffusion coefficients of each defect-atom must be defined. The grain boundary diffusion coefficients are assumed to follow an Arrhenius-type temperature-dependence based on empirical evidence [138]:

$$d^{v/i,gb}_{Fe/Cr} = d^{v/i,gb}_{Fe/Cr,0} exp\left(\frac{E^{v/i,gb}_{Fe/Cr}}{kT}\right) \tag{A-33}$$

where $E^{v/i,gb}_{Fe/Cr}$ is the activation energy for grain boundary diffusion of a specific defect-atom species, $d^{v/i,gb}_{Fe/Cr,0}$ is the pre-exponential factor for a specific species , $k$ is Boltzmann constant and $T$ is the temperature. Eq. A-33 can be rewritten assuming the diffusion along a grain boundary is proportional to the rate of a characteristic jump of a marked defect within the boundary. Therefore, the partial diffusivity is proportional to the jump distance squared, the rate of jumping, and the partial correlation factor of its characteristic jump [37]. The result is Eq. A-33 can be written as [37]:

$$d^{v/i,gb}_{Fe/Cr} = g_{v/i} a^2 Z f^{GB}_{v/i} \nu_o exp\left(\frac{E^{v/i,gb}_{Fe/Cr}}{kT}\right) \tag{A-34}$$

where $g_{v/i}$ is a dimensionless constant based on the structure, $a$ is the lattice parameter, $Z$ is the coordination number, $f^{GB}_{v/i}$ is the correlation factor for the specific defect type, and $\nu_o$ is the attempt frequency. The quantities are adjusted to represent the average effect of all jumps possible in the boundary core of a specific defect which contribute to the grain boundary diffusivity of an atom-defect in the boundary. For grain boundary diffusion in metals the activation energy for grain boundary diffusion is typically lower than the activation energy for lattice diffusion [138]. The activation energy of a defect in a grain boundary was not explicitly used within the model. The assumptions of Aleshin *et al.* was used to find an approximate value [139]. Aleshin assumed the bulk and boundary diffusion differ by the grain boundary energy where:

$$E_{Fe/Cr}^{v/i,gb} \approx E_{Fe/Cr}^{v/i,bulk} - a^2\gamma_{gb} \tag{A-35}$$

where $\gamma_{gb}$ is the grain boundary energy based on dislocation theory. This approximation is not explicitly based on physical values and the grain boundary diffusivities are only a first-order approximation of the realistic value. Substituting Eq. A-35 into Eq. A-34 the grain boundary diffusivity can be determined by:

$$d_{Fe/Cr}^{v/i,gb} \approx g_{v/i}a^2 Z f_{v/i}^{GB} \nu_o exp\left(\frac{E_{Fe/Cr}^{v/i,bulk} - a^2\gamma_{gb}}{kT}\right). \tag{A-36}$$

The grain boundary diffusivity for each species can then be substituted into the Eqs. A-26 - A-29 to get the grain boundary flux as a function of the grain boundary dislocation separation and grain boundary diffusivity. Simple analysis shows general high angle grain boundaries diffusivity coefficients are very large compared to the bulk lattice value. This results in $J_{v,i}^0$ being much higher than $J_{v,i}^1$ under irradiation resulting in the general high angle grain boundaries absorbing defects rapidly and meeting the perfect sink condition. For low angle or special grain boundaries the defect flux in the boundaries is lower than general high angle grain boundaries due to the lower defect diffusivity in the boundary and the defect concentration is not strictly maintained at the thermal equilibrium value. The defect concentration gradients for specific misorientation angles can be seen in the main text in Figure 2.24.

The derivation for the grain boundary diffusivities have some limitations. First, the grain boundary diffusivities are not well known and an approximation is used based on bulk values. Any errors in the calculation in the bulk values, such as the bulk activation energies, would propagate to the values used in the grain boundary approximations. Also, the single degree of freedom description of the grain boundary energy has well known issues. In the model, the grain boundary misorientation angle is solely used to describe the grain boundary energy. As discussed in the main text, the grain boundary is dependent on all five degrees of freedom for the boundary. This is particularly problematic when considering grain boundary twin structures as coherent twins energy are very different to those of incoherent twins. Furthermore, the grain boundary dislocations are treated as perfect sinks but the absorption of point defects in itself is a complex process and the behavior of grain boundary dislocations could deviate from the ideal sink condition [36].

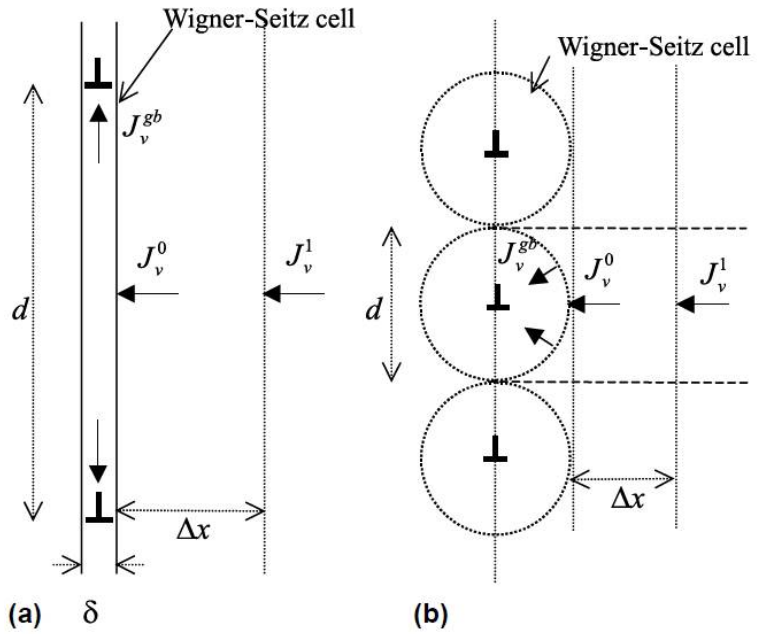


Figure A-1: Schematic showing the partitioning of defect fluxes at grain boundaries used in the RIS model. (a) The defects interacting with a general high angle grain boundary. (b) Defects interacting with a low angle grain boundary and diffusing directly to grain boundary dislocations. From [91].

# Appendix B

Summary of STEM-EDS results for investigated lath boundaries in the 9 wt. % Cr model F/M steel. Concentration values are calculated using 32 pixel binning.

| Boundary ID | Sample ID | Incident Particle | Dose (dpa) | Dose Rate (dpa/s) | Temp. (ºC) | Mis. Angle | Mis. Axis | Wt. % Cr at Boundary | FWHM of Profile (nm) | Area of Profile (wt.%·nm) |
|---|---|---|---|---|---|---|---|---|---|---|
| ASR_1 | 9CrM_As_Received_2 | n/a | n/a | n/a | n/a | 5.1º | <$\bar{2}\,\bar{2}\,3$> | 8.7 | n/a | n/a |
| ASR_2 | 9CrM_As_Received_2 | n/a | n/a | n/a | n/a | 6.4º | <$\bar{3}\,\bar{4}\,1$> | 8.7 | n/a | n/a |
| ASR_3 | 9CrM_As_Received_2 | n/a | n/a | n/a | n/a | 5.0º | <$\bar{2}\,\bar{4}\,3$> | 8.7 | n/a | n/a |
| ASR_4 | 9CrM_ASR_CAES | n/a | n/a | n/a | n/a | 8.9º | <$6\,\bar{1}\,\bar{2}$> | 8.7 | n/a | n/a |
| ASR_5 | 9CrM_ASR_CAES | n/a | n/a | n/a | n/a | 3.5º | <$\bar{3}\,\bar{2}\,3$> | 8.7 | n/a | n/a |
| Lath_1.C | 9CrM_1_400C_1.ep.1 | Protons | 1 | $5.9x10^{-6}$ | 400 | 5.0º | <$1\,\bar{1}\,\bar{1}$> | 8.7 | n/a | n/a |
| Lath_1.1 | 9CrM_1_400C_1.1 | Protons | 1 | $5.9x10^{-6}$ | 400 | 56.3º | <$\bar{1}\,3\,\bar{3}$> | 7.9 | 17.9 | 15 |
| Lath_1.2 | 9CrM_1_400C_1.1 | Protons | 1 | $5.9x10^{-6}$ | 400 | 1.9º | <$2\,\bar{3}\,2$> | 8.7 | n/a | n/a |
| Lath_1.3 | 9CrM_1_400C_1.1 | Protons | 1 | $5.9x10^{-6}$ | 400 | 2.3º | <$2\,2\,1$> | 8.7 | n/a | n/a |
| Lath_1.4 | 9CrM_1_400C_1.1 | Protons | 1 | $5.9x10^{-6}$ | 400 | 7.2º | <$0\,1\,\bar{1}$> | 8.7 | n/a | n/a |
| Lath_1.5 | 9CrM_1_400C_1.1 | Protons | 1 | $5.9x10^{-6}$ | 400 | 59.9º | <$\bar{1}\,\bar{1}\,\bar{1}$> | 9.9 | 2.7 | 3.5 |
| Lath_1.6 | 9CrM_1_400C_1.1 | Protons | 1 | $5.9x10^{-6}$ | 400 | 1.5º | <$5\,\bar{1}\,\bar{7}$> | 8.7 | n/a | n/a |
| Lath_1.7 | 9CrM_1_400C_1.1 | Protons | 1 | $5.9x10^{-6}$ | 400 | 9.2º | <$1\,\bar{1}\,\bar{2}$> | 10.2 | 2.0 | 3.2 |
| Lath_1.8 | 9CrM_1_400C_1.2 | Protons | 1 | $5.9x10^{-6}$ | 400 | 5.1º | <$\bar{1}\,1\,0$> | 7.9 | 16.1 | 20.4 |
| Lath_1.9 | 9CrM_1_400C_1.2 | Protons | 1 | $5.9x10^{-6}$ | 400 | 7.0º | <$4\,3\,\bar{1}$> | 7.9 | 19.9 | 15.8 |
| Lath_1.10 | 9CrM_1_400C_1.2 | Protons | 1 | $5.9x10^{-6}$ | 400 | 1.0º | <$\bar{3}\,1\,1$> | 8.7 | n/a | n/a |
| Lath_1.11 | 9CrM_1_400C_1.2 | Protons | 1 | $5.9x10^{-6}$ | 400 | 3.6º | <$\bar{4}\,\bar{1}\,3$> | 8.7 | n/a | n/a |
| Lath_1.12 | 9CrM_1_400C_1.2 | Protons | 1 | $5.9x10^{-6}$ | 400 | 2.7º | <$\bar{2}\,0\,\bar{3}$> | 8.7 | n/a | n/a |
| Lath_1.13 | 9CrM_1_400C_1.3 | Protons | 1 | $5.9x10^{-6}$ | 400 | 4.4º | <$1\,\bar{3}\,9$> | 8.7 | n/a | n/a |
| Lath_1.14 | 9CrM_1_400C_1.3 | Protons | 1 | $5.9x10^{-6}$ | 400 | 3.8º | <$2\,1\,\bar{6}$> | 8.8 | 7.7 | 1.3 |
| Lath_1.15 | 9CrM_1_400C_1.4 | Protons | 1 | $5.9x10^{-6}$ | 400 | 3.2º | <$2\,5\,3$> | 8.7 | n/a | n/a |

| Boundary ID | Sample ID | Incident Particle | Dose (dpa) | Dose Rate (dpa/s) | Temp. (ºC) | Mis. Angle | Mis. Axis | Wt. % Cr at Boundary | FWHM of Profile (nm) | Area of Profile (wt.%·nm) |
|---|---|---|---|---|---|---|---|---|---|---|
| Lath_1.16 | 9CrM_1_400C_1.4 | Protons | 1 | $5.9x10^{-6}$ | 400 | 48º | <$\bar{3}$2$\bar{3}$> | 11.9 | 4.4 | 15.1 |
| Lath_1.17 | 9CrM_1_400C_1.4 | Protons | 1 | $5.9x10^{-6}$ | 400 | 58.7º | <3$\bar{2}\bar{2}$> | 10.1 | 3.0 | 4.7 |
| Lath_1.18 | 9CrM_1_400C_1.4 | Protons | 1 | $5.9x10^{-6}$ | 400 | 5.6º | <1$\bar{6}\bar{4}$> | 8.7 | n/a | n/a |
| Lath_2.1 | 9CrM_2_400C_2.1 | Protons | 2 | $4.4x10^{-6}$ | 400 | 8.6º | <$\bar{2}\bar{3}$6> | 9.9 | 12.9 | 17.1 |
| Lath_2.2 | 9CrM_2_400C_2.1 | Protons | 2 | $4.4x10^{-6}$ | 400 | 5.1º | <32$\bar{1}$> | 9.4 | 15.7 | 11.6 |
| Lath_2.3 | 9CrM_2_400C_2.1 | Protons | 2 | $4.4x10^{-6}$ | 400 | 3.5º | <$\bar{2}$63> | 9.8 | 18.5 | 21.6 |
| Lath_2.4 | 9CrM_2_400C_2.1 | Protons | 2 | $4.4x10^{-6}$ | 400 | 3.7º | <$\bar{1}\bar{1}$4> | 10.0 | 14.7 | 20.1 |
| Lath_2.5 | 9CrM_2_400C_2.2 | Protons | 2 | $4.4x10^{-6}$ | 400 | 1.8º | <312> | 9.1 | 23.4 | 9.3 |
| Lath_2.6 | 9CrM_2_400C_2.2 | Protons | 2 | $4.4x10^{-6}$ | 400 | 49.1º | <2$\bar{2}\bar{3}$> | 12.2 | 6.0 | 22.2 |
| Lath_2.7 | 9CrM_2_400C_2.2 | Protons | 2 | $4.4x10^{-6}$ | 400 | 0.1º | <$\bar{3}\bar{2}$4> | 9.0 | 17.8 | 6.8 |
| Lath_2.8 | 9CrM_2_400C_2.2 | Protons | 2 | $4.4x10^{-6}$ | 400 | 8.8º | <$\bar{1}\bar{5}$4> | 9.9 | 14.5 | 18.7 |
| Lath_2.9 | 9CrM_2_400C_2.3 | Protons | 2 | $4.4x10^{-6}$ | 400 | 3.3º | <$\bar{8}$32> | 9.5 | 13.9 | 12.9 |
| Lath_2.10 | 9CrM_2_400C_2.3 | Protons | 2 | $4.4x10^{-6}$ | 400 | 53.3º | <1$\bar{5}$5> | 12.5 | 7.7 | 30.9 |
| Lath_2.11 | 9CrM_2_400C_2.3 | Protons | 2 | $4.4x10^{-6}$ | 400 | 4.3º | <02$\bar{3}$> | 10.1 | 15.6 | 24.1 |
| Lath_2.12 | 9CrM_2_400C_2.3 | Protons | 2 | $4.4x10^{-6}$ | 400 | 0.9º | <$\bar{3}\bar{2}$3> | 9.1 | 21.4 | 10.1 |
| Lath_2.13 | 9CrM_2_400C_2.3 | Protons | 2 | $4.4x10^{-6}$ | 400 | 1.1º | <$\bar{2}\bar{3}$3> | 9.4 | 21.8 | 15.4 |
| Lath_2.14 | 9CrM_2_400C_2.3 | Protons | 2 | $4.4x10^{-6}$ | 400 | 1.4º | <21$\bar{2}$> | 9.4 | 20.4 | 16.2 |
| Lath_2.15 | 9CrM_2_400C_2.3 | Protons | 2 | $4.4x10^{-6}$ | 400 | 1.4º | <$\bar{4}$32> | 9.4 | 13.3 | 10.4 |
| Lath_2.16 | 9CrM_2_400C_2.4 | Protons | 2 | $4.4x10^{-6}$ | 400 | 2.7º | <0$\bar{2}\bar{3}$> | 8.68 | n/a | n/a |
| Lath_3.1 | 9CrM_3_400C_3.1 | Protons | 3 | $4.8x10^{-6}$ | 400 | 0.4º | <131> | 9.1 | 21.6 | 10.5 |
| Lath_3.2 | 9CrM_3_400C_3.1 | Protons | 3 | $4.8x10^{-6}$ | 400 | 1.2º | <$\bar{3}$02> | 9.8 | 15.9 | 19.3 |
| Lath_3.3 | 9CrM_3_400C_3.1 | Protons | 3 | $4.8x10^{-6}$ | 400 | 3.7º | <$\bar{2}\bar{1}\bar{6}$> | 11.2 | 15.6 | 41.4 |
| Lath_3.4 | 9CrM_3_400C_3.1 | Protons | 3 | $4.8x10^{-6}$ | 400 | 2.1º | <$\bar{1}\bar{2}$2> | 9.2 | 24.2 | 12.9 |
| Lath_3.5 | 9CrM_3_400C_3.2 | Protons | 3 | $4.8x10^{-6}$ | 400 | 1.4º | <$\bar{2}$21> | 9.7 | 15.8 | 16.4 |
| Lath_3.6 | 9CrM_3_400C_3.2 | Protons | 3 | $4.8x10^{-6}$ | 400 | 56.8º | <111> | 10.0 | 15.2 | 21.1 |
| Lath_3.7 | 9CrM_3_400C_3.2 | Protons | 3 | $4.8x10^{-6}$ | 400 | 7.3º | <$\bar{4}$14> | 10.2 | 17.8 | 27.8 |
| Lath_3.8 | 9CrM_3_400C_3.2 | Protons | 3 | $4.8x10^{-6}$ | 400 | 3.7º | <3$\bar{2}\bar{3}$> | 9.4 | 18.7 | 15.1 |

| Boundary ID | Sample ID | Incident Particle | Dose (dpa) | Dose Rate (dpa/s) | Temp. (ºC) | Mis. Angle | Mis. Axis | Wt. % Cr at Boundary | FWHM of Profile (nm) | Area of Profile (wt.%·nm) |
|---|---|---|---|---|---|---|---|---|---|---|
| Lath_3.9 | 9CrM_3_400C_3.3 | Protons | 3 | $4.8x10^{-6}$ | 400 | 59.7º | <$\bar{7}$61> | 9.9 | 16.0 | 21.6 |
| Lath_3.10 | 9CrM_3_400C_3.3 | Protons | 3 | $4.8x10^{-6}$ | 400 | 2.2º | <$\bar{1}$11> | 9.3 | 18.7 | 11.6 |
| Lath_3.11 | 9CrM_3_400C_3.3 | Protons | 3 | $4.8x10^{-6}$ | 400 | 5.6º | <100> | 9.8 | 20.7 | 23.5 |
| Lath_3.12 | 9CrM_3_400C_3.4 | Protons | 3 | $4.8x10^{-6}$ | 400 | 59.4º | <011> | 10.6 | 12.1 | 24.9 |
| Lath_3.13 | 9CrM_3_400C_3.4 | Protons | 3 | $4.8x10^{-6}$ | 400 | 58.5º | <$\bar{1}$1$\bar{1}$> | 9.7 | 12.5 | 13.8 |
| Lath_3.14 | 9CrM_3_400C_3.4 | Protons | 3 | $4.8x10^{-6}$ | 400 | 59.9º | <$\bar{1}\,\bar{1}\,\bar{1}$> | 9.7 | 14.2 | 14.8 |
| Lath_1.1 | 9CrM_1_500C_1.1 | Protons | 1 | $1.2x10^{-5}$ | 500 | 1.5º | <02$\bar{1}$> | 8.7 | n/a | n/a |
| Lath_1.2 | 9CrM_1_500C_1.2 | Protons | 1 | $1.2x10^{-5}$ | 500 | 56.2º | <$\bar{1}\bar{3}$3> | 14.5 | 4.2 | 26.1 |
| Lath_1.3 | 9CrM_1_500C_1.2 | Protons | 1 | $1.2x10^{-5}$ | 500 | 2.3º | <$\bar{3}$23> | 9.6 | 13.8 | 13.1 |
| Lath_1.4 | 9CrM_1_500C_1.2 | Protons | 1 | $1.2x10^{-5}$ | 500 | 60.0º | <$\bar{1}$11> | 9.6 | 6.1 | 6.0 |
| Lath_1.5 | 9CrM_1_500C_1.2 | Protons | 1 | $1.2x10^{-5}$ | 500 | 1.4º | <263$\bar{}$> | 9.1 | 11.8 | 4.6 |
| Lath_1.6 | 9CrM_1_500C_1.2 | Protons | 1 | $1.2x10^{-5}$ | 500 | 5.8º | <$\bar{1}$56$\bar{}$> | 8.7 | n/a | n/a |
| Lath_2.1 | 9CrM_2_500C_2.1 | Protons | 2 | $1.2x10^{-5}$ | 500 | 2.5º | <324$\bar{}$> | 9.1 | 14.0 | 6.4 |
| Lath_2.2 | 9CrM_2_500C_2.1 | Protons | 2 | $1.2x10^{-5}$ | 500 | 3.9º | <3$\bar{2}\bar{3}$> | 8.7 | n/a | n/a |
| Lath_2.3 | 9CrM_2_500C_2.1 | Protons | 2 | $1.2x10^{-5}$ | 500 | 4.9º | <$\bar{2}\bar{7}$1> | 9.5 | 10.3 | 9.3 |
| Lath_2.4 | 9CrM_2_500C_2.1 | Protons | 2 | $1.2x10^{-5}$ | 500 | 2.4º | <12$\bar{2}$> | 9.4 | 11.1 | 8.5 |
| Lath_2.5 | 9CrM_2_500C_2.1 | Protons | 2 | $1.2x10^{-5}$ | 500 | 2.9º | <013> | 9.2 | 11.3 | 3.1 |
| Lath_2.6 | 9CrM_2_500C_2.2 | Protons | 2 | $1.2x10^{-5}$ | 500 | 6.7º | <08$\bar{1}$> | 9.1 | 18.2 | 8.2 |
| Lath_2.7 | 9CrM_2_500C_2.2 | Protons | 2 | $1.2x10^{-5}$ | 500 | 59.5º | <$\bar{1}\,\bar{1}\,\bar{1}$> | 9.3 | 12 | 7.3 |
| Lath_2.8 | 9CrM_2_500C_2.2 | Protons | 2 | $1.2x10^{-5}$ | 500 | 1.5º | <$\bar{1}$21> | 8.7 | n/a | n/a |
| Lath_2.9 | 9CrM_2_500C_2.2 | Protons | 2 | $1.2x10^{-5}$ | 500 | 6.3º | <$\bar{1}\bar{4}$4> | 9.0 | 6.8 | 2.5 |
| Lath_3.1 | 9CrM_3_500C_3.1 | Protons | 3 | $1.2x10^{-5}$ | 500 | 2.3º | <$\bar{3}$1$\bar{8}$> | 8.7 | n/a | n/a |
| Lath_3.2 | 9CrM_3_500C_3.1 | Protons | 3 | $1.2x10^{-5}$ | 500 | 60.2º | <232> | 9.8 | 13.9 | 15.8 |
| Lath_3.3 | 9CrM_3_500C_3.1 | Protons | 3 | $1.2x10^{-5}$ | 500 | 2.3º | <325$\bar{}$> | 9.3 | 16.4 | 10.6 |
| Lath_3.4 | 9CrM_3_500C_3.1 | Protons | 3 | $1.2x10^{-5}$ | 500 | 1.9º | <113> | 8.7 | n/a | n/a |
| Lath_3.5 | 9CrM_3_500C_3.2 | Protons | 3 | $1.2x10^{-5}$ | 500 | 2.1º | <$\bar{7}$23> | 8.7 | n/a | n/a |
| Lath_3.6 | 9CrM_3_500C_3.2 | Protons | 3 | $1.2x10^{-5}$ | 500 | 50.1º | <$\bar{1}\,\bar{1}\bar{2}$> | 12.1 | 5.7 | 20.9 |

| Boundary ID | Sample ID | Incident Particle | Dose (dpa) | Dose Rate (dpa/s) | Temp. (ºC) | Mis. Angle | Mis. Axis | Wt. % Cr at Boundary | FWHM of Profile (nm) | Area of Profile (wt.%·nm) |
|---|---|---|---|---|---|---|---|---|---|---|
| Lath_3.7 | 9CrM_3_500C_3.2 | Protons | 3 | $1.2x10^{-5}$ | 500 | 10.7º | <$\bar{1}$42> | 9.6 | 13.7 | 12.7 |
| Lath_3.8 | 9CrM_3_500C_3.2 | Protons | 3 | $1.2x10^{-5}$ | 500 | 51.3º | <$\bar{2}\bar{2}\bar{3}$> | 12.8 | 4.0 | 17.6 |
| Lath_3.1n | 9CrM_3_500C_3.1.n | Neutrons | 3 | $1.0x10^{-7}$ | ~500 | 5.5º | <$\bar{3}$11> | 12.7 | 5.2 | 22.2 |
| Lath_3.2n | 9CrM_3_500C_3.1.n | Neutrons | 3 | $1.0x10^{-7}$ | ~500 | 3.3º | <$\bar{4}$23> | 13.5 | 5.5 | 28.0 |
| Lath_3.3n | 9CrM_3_500C_3.1.n | Neutrons | 3 | $1.0x10^{-7}$ | ~500 | 59.1º | <0$\bar{1}$1> | 15.3 | 5.5 | 39.0 |
| Lath_3.4n | 9CrM_3_500C_3.1.n | Neutrons | 3 | $1.0x10^{-7}$ | ~500 | 59.6º | <$\bar{2}$32> | 10.7 | 7.8 | 16.8 |
| Lath_3.5n | 9CrM_3_500C_3.1.n | Neutrons | 3 | $1.0x10^{-7}$ | ~500 | 58.7º | <01$\bar{1}$> | 15.5 | 4.5 | 32.8 |
| Lath_3.6n | 9CrM_3_500C_3.1.n | Neutrons | 3 | $1.0x10^{-7}$ | ~500 | 59.4º | <$\bar{1}\bar{1}\bar{1}$> | 16.1 | 7.7 | 60.8 |
| Lath_3.7n | 9CrM_3_500C_3.1.n | Neutrons | 3 | $1.0x10^{-7}$ | ~500 | 47.1º | <$\bar{1}$01> | 16.7 | 4.3 | 36.5 |
| Lath_3.8n | 9CrM_3_500C_3.1.n | Neutrons | 3 | $1.0x10^{-7}$ | ~500 | 7.5º | <32$\bar{2}$> | 15.5 | 4.9 | 35.6 |
| Lath_3.9n | 9CrM_3_500C_3.1.n | Neutrons | 3 | $1.0x10^{-7}$ | ~500 | 56.1º | <$\bar{2}\bar{2}$3> | 16.4 | 4.6 | 37.9 |
| Lath_3.10n | 9CrM_3_500C_3.1.n | Neutrons | 3 | $1.0x10^{-7}$ | ~500 | 51.8º | <12$\bar{2}$> | 16.6 | 6.1 | 51.7 |
| Lath_3.11n | 9CrM_3_500C_3.1.n | Neutrons | 3 | $1.0x10^{-7}$ | ~500 | 59.8º | <1$\bar{1}$1> | 11.6 | 4.9 | 15.0 |

# Appendix C

Summary of STEM-EDS results for investigated grain boundaries in the 14YWT-SM10 specimens.

| Boundary ID | Sample ID | Incident Particle | Dose (dpa) | Dose Rate (dpa/s) | Temp. (ºC) | Mis. Angle | Mis. Axis | Wt. % Cr at Boundary | FWHM of Profile (nm) | Cr Profile Shape |
|---|---|---|---|---|---|---|---|---|---|---|
| ASR_1 | 14YWT_As_Received_1 | n/a | n/a | n/a | n/a | 52.6º | <$\bar{3}$ 1 $\bar{3}$> | 21.6 | 2.8 | v-shape |
| ASR_2 | 14YWT_As_Received_1 | n/a | n/a | n/a | n/a | 0.1º | <1 $\bar{1}$ $\bar{1}$> | 20.5 | 2.6 | v-shape |
| ASR_3 | 14YWT_As_Received_1 | n/a | n/a | n/a | n/a | 25.5º | <$\bar{3}$ 2 $\bar{1}$> | 22.8 | 1.9 | v-shape |
| ASR_4 | 14YWT_As_Received_1 | n/a | n/a | n/a | n/a | Not indexed | | 20.8 | 2.2 | v-shape |
| ASR_5 | 14YWT_As_Received_1 | n/a | n/a | n/a | n/a | Not indexed | | 20 | 1.8 | v-shape |
| GB_n75.1 | 14YWT_100_n75_100.1 | $Ni^{2+}$ | 100 | $2.3x10^{-3}$ | -75 | 59.4º | <2 $\bar{1}$ $\bar{2}$> | 13.3 | n/a | flat |
| GB_n75.2 | 14YWT_100_n75_100.1 | $Ni^{2+}$ | 100 | $2.3x10^{-3}$ | -75 | 24.5º | <$\bar{1}$ 1 1> | 13.3 | n/a | flat |
| GB_100.1 | 14YWT_100_100C_1 | $Ni^{2+}$ | 100 | $2.3x10^{-3}$ | 100 | 50.0º | <5 2 $\bar{3}$> | 11.6 | 5.0 | slight w |
| GB_100.2 | 14YWT_100_100C_1 | $Ni^{2+}$ | 100 | $2.3x10^{-3}$ | 100 | 58.3º | <1 $\bar{5}$ $\bar{5}$> | 10.9 | 5.8 | slight w |
| GB_100.3 | 14YWT_100_100C_1 | $Ni^{2+}$ | 100 | $2.3x10^{-3}$ | 100 | 52.4º | <$\bar{1}$ 1 1> | 11.5 | 6.0 | v-shape |
| GB_100.4 | 14YWT_100_100C_1 | $Ni^{2+}$ | 100 | $2.3x10^{-3}$ | 100 | 44.1º | <$\bar{2}$ 1 4> | 10.6 | 6.4 | v-shape |
| GB_300.1 | 14YWT_100_300C_1 | $Ni^{2+}$ | 100 | $2.3x10^{-3}$ | 300 | 17.8º | <1 $\bar{3}$ $\bar{6}$> | 13.3 | 5.7 | w-shape |
| GB_300.2 | 14YWT_100_300C_1 | $Ni^{2+}$ | 100 | $2.3x10^{-3}$ | 300 | 44.5º | <$\bar{1}$ 1 3> | 13.2 | - | v-shape |
| GB_300.3 | 14YWT_100_300C_1 | $Ni^{2+}$ | 100 | $2.3x10^{-3}$ | 300 | 58.9º | <1 $\bar{4}$ 4> | 12.8 | 3.9 | v-shape |
| GB_300.4 | 14YWT_100_300C_1 | $Ni^{2+}$ | 100 | $2.3x10^{-3}$ | 300 | 53.7º | <4 4 1> | 13.1 | 7.3 | w-shape |
| GB_300.5 | 14YWT_100_300C_1 | $Ni^{2+}$ | 100 | $2.3x10^{-3}$ | 300 | Not indexed | | 12.1 | 11 | w-shape |
| GB_450.1 | 14YWT_100_450C_1 | $Ni^{2+}$ | 100 | $2.3x10^{-3}$ | 450 | 55.1º | <1 0 1> | 21.5 | 2.3 | v-shape |
| GB_450.2 | 14YWT_100_450C_1 | $Ni^{2+}$ | 100 | $2.3x10^{-3}$ | 450 | 41.5º | <$\bar{5}$ $\bar{2}$ $\bar{3}$> | 18.2 | 3.7 | v-shape |
| GB_450.3 | 14YWT_100_450C_1 | $Ni^{2+}$ | 100 | $2.3x10^{-3}$ | 450 | 39.9º | <6 1 $\bar{6}$> | 20.2 | 1.8 | v-shape |
| GB_450.4 | 14YWT_100_450C_1 | $Ni^{2+}$ | 100 | $2.3x10^{-3}$ | 450 | 48.1º | <3 1 3> | 18.9 | 2.7 | v-shape |
| GB_450.5 | 14YWT_100_450C_1 | $Ni^{2+}$ | 100 | $2.3x10^{-3}$ | 450 | 44.6º | <1 0 $\bar{3}$> | 17.7 | 2.7 | v-shape |

| Boundary ID | Sample ID | Incident Particle | Dose (dpa) | Dose Rate (dpa/s) | Temp. (ºC) | Mis. Angle | Mis. Axis | Wt. % Cr at Boundary | FWHM of Profile (nm) | Cr Profile Shape |
|---|---|---|---|---|---|---|---|---|---|---|
| GB_600.1 | 14YWT_100_600C_1 | $Ni^{2+}$ | 100 | $2.3x10^{-3}$ | 600 | 27.1º | <0 6 $\bar{1}$> | 19.3 | 1.6 | v-shape |
| GB_600.2 | 14YWT_100_600C_1 | $Ni^{2+}$ | 100 | $2.3x10^{-3}$ | 600 | 45.0º | <$\bar{2}\,\bar{2}$ 3> | 18.4 | 1.6 | v-shape |
| GB_600.3 | 14YWT_100_600C_1 | $Ni^{2+}$ | 100 | $2.3x10^{-3}$ | 600 | 47.4º | <2 3 0> | 17.1 | 1.8 | v-shape |
| GB_600.4 | 14YWT_100_600C_1 | $Ni^{2+}$ | 100 | $2.3x10^{-3}$ | 600 | 30.8º | <0 2 1> | 18.3 | 1.8 | v-shape |